

University of Southampton Research Repository ePrints Soton

Copyright © and Moral Rights for this thesis are retained by the author and/or other copyright owners. A copy can be downloaded for personal non-commercial research or study, without prior permission or charge. This thesis cannot be reproduced or quoted extensively from without first obtaining permission in writing from the copyright holder/s. The content must not be changed in any way or sold commercially in any format or medium without the formal permission of the copyright holders.

When referring to this work, full bibliographic details including the author, title, awarding institution and date of the thesis must be given e.g.

AUTHOR (year of submission) "Full thesis title", University of Southampton, name of the University School or Department, PhD Thesis, pagination

UNIVERSITY OF SOUTHAMPTON

FACULTY OF ENGINEERING AND APPLIED SCIENCES

School of Electronics and Computer Science



**DESIGN, FABRICATION AND OPTIMIZATION OF LARGE AREA
CHEMICAL SENSOR BASED ON SURFACE-ENHANCED RAMAN
SCATTERING (SERS) MECHANISM**

by

Swe Zin Oo

Thesis for the degree of Doctor of Philosophy

16th March 2015

UNIVERSITY OF SOUTHAMPTON

ABSTRACT

FACULTY OF ENGINEERING AND APPLIED SCIENCES

School of Electronics and Computer Science

Thesis for the degree of Doctor of Philosophy

DESIGN, FABRICATION AND OPTIMIZATION OF LARGE AREA CHEMICAL SENSOR BASED ON SURFACE-ENHANCED RAMAN SCATTERING (SERS) MECHANISM

Swe Zin Oo

In recent years there has been an increasing interest in analysis and identification of complex molecules for the medical diagnostics, pharmaceutical research and homeland security applications. If these molecules are present in high concentration, a technique known as Raman spectroscopy can be utilized. Unfortunately, only one in every 10^{12} photon incidence on molecule undergoes Raman scattering resulting in weak Raman absorption. An efficient technique to overcome this limitation is to utilize surface-enhanced Raman scattering (SERS) whereby molecules are placed on the surface of nanostructured metallic substrate which performs the function of transducing photons into and out of the molecules. SERS extends the scope of Raman scattering to detect molecules at low concentrations to few/single molecule level. Previously the 'KlariteTM' substrate consisting of an inverted array of square based pyramidal nanostructures patterned onto a Silicon substrate has been demonstrated to afford highly reproducible SERS signals with approximately 10^7 enhancement factor.

In this report, the effect of geometrical parameters associated with the inverted pyramidal array on SERS effect for sensing applications was investigated. Geometrical parameters studied include pitch length, pit size, aspect ratio of the base of pyramid and fill factor. 3D computational modelling based on Rigorous Coupled Wave Analysis (RCWA) is used to bridge with theory. From these observations, the geometrical parameters of inverted pyramid nanostructures have been optimized for better sensing ability. A test chip is fabricated for the purpose of performing a matrix experiment, allowing deconvolution of geometrical variables: lattice pitch (1000nm-3000nm), pit size (500nm-2500nm), pit

aspect ratio [width to length]. Fabrication steps include electron-beam lithography, anisotropic wet etching and metallization.

Computational and experimental reflectometry systems were applied to enable the identification and analysis of a variety of dispersive features including propagating surface plasmons, localized surface plasmons and diffraction dispersion. From the study of inverted pyramid, plasmonic behaviors are observed: 1. the surface plasmon polariton depends strongly on polarization. 2. Highly dispersive features arising from simple surface diffraction effects appear insensitive to polarization state. 3. As the pit size gets bigger, the diffraction efficiency decreases but the wavelength/angular position remain the same. 4. Diffractive features are relatively sharp and clearly defined (narrow bandwidth), and are highly dependent on lattice pitch. Hence they move in wavelength and angle (e.g. highly dispersive) as pitch is varied. These features relate to the coupling of light into or out of the sensor chip. 5. Localized surface plasmons have characteristic of small wavelength shift over wide angular range (low dispersion), and are generally broader in bandwidth. Plasmon features can conclusively be identified over diffractive features by making comparisons between simulations 'with' and 'without' the top metal coating.

In order to derive the optimal geometry for SERS sensor, a highly stable test molecule which is known to form a monolayer coating on gold is required. For this purpose benzenethiol was used as standard in this work. Devices were tested using a Renishaw Invia Raman system. The main wavelength of interest here is 785nm where this laser is readily available and compatible with the end user Raman system. Full details of the optical and Raman measurements are carried out on the silicon test platform. Results show that the averaged SERS enhancement factor was only slightly dependent upon lattice pitch, but was highly dependent on pit size and aspect ratio. Density of the pits plays a further role simply by increasing the number of pits/unit area and so provides extra increase in SERS signal. The experimental data shows this is not simply a surface area dependent effect, but the optimal SERS signal can be obtained by close packing as tightly as possible pits of the optimal size. Minimum spacing (between adjacent pits) of 250nm is found to give the highest SERS enhancement. The optimal aspect ratio was found to be 1:1.2 and the optimal pit size determined to be 1000nm. This new optimized design shows 10-fold improvement in sensitivity compared to current available benchmark Klarite. The study has also explored the possibility of replicating the optimized design to a cost effective and

disposable polymer for the purpose of mass production. This was carried out using nanoimprint lithography. The replicated plastic sensor is comparable to the benchmark silicon Klarite. As a proof of principle, the qualitative performance in two demonstrator molecules such as ibuprofen and melamine has been carried out. The disposable plastic sensor was demonstrated for the possibility of dual sensing mechanisms such as surface plasmon resonance (SPR) and surface-enhanced Raman scattering (SERS). The sensitivity of plastic sensor using SPR mechanism is 225.83nm/RIU on thiol molecule. The work has also been carried out for an alternative SERS sensor design by changing the sidewall profile to 90° angle from (100) silicon etched plane. Changing the sidewall profile makes impact on the plasmonic behaviour. The straight sidewalls are favourable to the localized plasmon mode. The structures with slope sidewalls are favourable to both localized and propagating plasmons inside the cavities. This work was conducted as part of the FP7 “PHOTOSENSE” consortium project.

Table of Contents

ABSTRACT	i
Table of Contents	i
List of tables	v
List of figures.....	vii
List of Publications	xix
DECLARATION OF AUTHORSHIP.....	xxi
Acknowledgements	xxiii
Definitions and Abbreviations.....	xxv
Chapter 1.Introduction	1
1.1 Motivation and structures of the thesis	3
Chapter 2.Literature review	7
2.1 Outlook for SERS substrates.....	7
2.1.1 Unconventional Nano-clusters.....	12
2.1.2 Review on fabrication techniques for SERS substrates	16
2.2 Overview of Surface Plasmon Resonance (SPR) sensors	17
2.2.1 Optical working system of a SPR sensor	19
2.2.2 Outlook of commercialized SPR instruments	20
Chapter 3.Background Theory	25
3.1 Introduction	25
3.2 What is Raman scattering/Raman effect?	26
3.3 Surface-enhanced Raman Scattering	28
3.3.1 Surface plasmon and surface plasmon resonance	28
3.3.2 Enhancement mechanism.....	30
3.3.3 The Various Metals used in SERS	33
Chapter 4.Tools for assessing the behaviour of SERS active substrate	35
4.1 Design and simulation	35
4.1.1 Design considerations and simulation parameters	37

4.2	Optical measurement using a bespoke reflectometry system.....	41
4.3	Raman measurement protocol	43
4.3.1	Test Molecule Coating.....	44
4.4	Conclusion	44
Chapter 5. Inverted Pyramidal SERS sensor: Silicon Platform.....		45
5.1	Fabrication Process.....	45
5.1.1	Materials, Chemicals and Tools.....	45
5.1.2	Preparation of inverted pyramid on silicon platform	47
5.1.3	Angled gold deposition.....	51
5.2	Modelling for optimization of SERS substrate on Si platform	54
5.2.1	Optical Response from the silicon inverted pyramid before metallization	55
5.2.2	Geometrical parameters of rectangular inverted pyramidal SERS substrates versus its plasmonic behavior after metallization	59
5.3	Experimental results and discussion	68
5.3.1	Characterization.....	68
5.3.2	Pitch dependent delocalized plasmon	71
5.3.3	Pit size dependent localized plasmon	72
5.3.4	Inverted pyramid with high fill factor	74
5.4	SERS intensity analysis with Raman spectroscopy	76
5.5	SERS comparison of an optimized design with standard Klarite	78
5.6	Effect of polarization	81
5.6.1	Raman SERS counts	81
5.6.2	Polarization Conversion.....	83
5.7	Conclusion	85
Chapter 6. Inverted Pyramid SERS sensor: Plastic Platform.....		87
6.1	Transfer from silicon to plastic base platform of SERS substrates.....	87
6.1.1	Sheet-level processing.....	88
6.1.2	Roll-to-roll processing.....	90
6.2	Disposable plasmonic SERS sensor.....	92

6.2.1	Discrepancies between the plastic substrates and the silicon master	97
6.3	Heading to real world application?	102
6.3.1	Pharmaceutical cleaning verification.....	102
6.3.2	Food monitoring	103
6.4	Optimization of Au coating for plastic.....	106
6.5	Molecule vs. no-molecules on the plastic substrate leading to dual sensing mechanism, SPR and SERS	110
6.6	Conclusion	114
Chapter 7. Analysis on gold layer		117
7.1	Effect of Gold layer thickness.....	117
7.2	Effect of non-conformality gold deposition on Plasmonic properties	121
7.2.1	Design variation and discussion on results	122
7.2.2	Conclusion	127
Chapter 8. Next generation designs.....		129
8.1	Consideration of surface abilities with straight sidewalls	129
8.1.1	Simulation studies.....	132
8.1.2	Experimental studies using optical methods.....	139
8.1.3	Raman measurement	143
8.2	Conclusion	146
Chapter 9. Conclusion and future work		149
9.1	Conclusion	149
9.2	Some suggestions for future work.....	153
9.2.1	Integrated SERS sensor.....	153
9.2.2	Free standing inverted pyramid with nanopore leading to DNA sequencing via optical method	155
Appendices.....		159
Appendix A : Rigorous Coupled Wave Analysis (RCWA)		159
Appendix B Calculation of enhancement factor		163
B.1	Area multiplication factor.....	163
B.2	Enhancement factor	163

Appendix C	Experimental Results	165
C.1	Analytical data from the Reflectometry measurement	165
C.1.1	Pit size effect for Au 400nm	165
C.1.2	Pitch length effect for Au 400nm.....	165
C.1.3	Different Gold thickness	166
Appendix D	Straight Sidewall Structure	167
D.1	Simulation Results	167
D.1.1	Difference in Depth together with pit size	167
Bibliography		169

List of tables

<i>Table 2-1 Summary of a variety of engineered metallic structures for SERS detection.....</i>	<i>9</i>
<i>Table 2-2 Summary of parameters that influence the enhancement factor in the conventional nanostructures</i>	<i>12</i>
<i>Table 5-1 List of chemicals, materials and tools used</i>	<i>45</i>
<i>Table 5-2 Outline for the fabrication steps.....</i>	<i>49</i>
<i>Table 5-3 List for the improved SERS counts by the optimized design compared to standard Klarite for Benzenethiol test molecules and respective stokes wavelengths for the vibrational mode of molecules.....</i>	<i>80</i>
<i>Table 5-4: Comparison of Raman intensity from trigonal ring breathing mode of BTh for different input polarization</i>	<i>82</i>
<i>Table 6-1 Optimization progress for the polymer SERS substrates by R2R imprinting process</i>	<i>95</i>
<i>Table 6-2 Performance of the different SERS substrates</i>	<i>97</i>
<i>Table 6-3 Tabulation for the RMS roughness for the different base substrate for an optimized design</i>	<i>99</i>
<i>Table 6-4 Average Raman intensity for the characteristic vibrational modes of BTh molecules for different angle deposition showing the enhanced factor in SERS counts by optimized angle deposition</i>	<i>109</i>
<i>Table 6-5 List of SPR sensitivity (nm/RIU) corresponding to the shift in wavelength for different incident angles from plastic SERS sensor (1000P500D)</i>	<i>111</i>
<i>Table 6-6 List of SPR sensitivity (nm/RIU) corresponding to the shift in wavelength for different incident angles from plastic SERS sensor, 1250P1000D for different gold thickness: 200nm and 100nm.....</i>	<i>113</i>
<i>Table 7-1 List of pyramidal geometric data with ‘apex angle decreased non-conformality’ condition</i>	<i>123</i>
<i>Table 8-1 Details of the fabricated parameters of the anisotropic dry etchfor the straight sidewall cavities</i>	<i>130</i>

<i>Table 9-1 Comparison of average Raman intensity for the characteristic vibrational modes of BTh molecules on the different substrates.....</i>	<i>152</i>
<i>Table 9-2 Qualitative and quantitative performance of the different SERS substrates at C-C stretch mode of BThs</i>	<i>152</i>
<i>Table 9-3 Plasmon response to the change in depth and pit size at the constant pitch, 1500nm.....</i>	<i>167</i>

List of figures

<i>Figure 2.1 SEM images of several SERS platforms [4,7-9 for 1st row, 28-29, 32-33 for 2nd row, 58, [22], 99-100 for 3rd row, 49, 55, 9, 123 for 4th row, left to right][3-10,23-32]</i>	<i>8</i>
<i>Figure 2.2 SEM images of unconventional nano-clusters: (i) the nested VNT(Vortex Nanogear Transmissions) array, (ii) the genetic nanoarray (GNA), (iii) concentric necklace nanolens (CNNLs), (iv) Oligomer nano-cluster (undecamer) [79-82]</i>	<i>12</i>
<i>Figure 2.3 (i) schematic cross-section view through the pits with pitch=2000nm, (ii) Top view of SEM image, (iii) cross-sectional view of SEM image before metallization[13]</i>	<i>15</i>
<i>Figure 2.4 SERS intensity from different active SERS substrates: (a) Raman spectra of the analyte pMA (30minutes incubation time) on the nested VNTs substrate. (b) Raman spectra of the analyte pMA (10mM concentration with 12 hours incubation time) on the GNA substrate, (c) Raman spectra of the analyte pMA (10mM concentration with 12 hours incubation time) on the CNNLs, (d) Raman spectra of the analyte pMA (5mM concentration) on the Au oligomers substrate, (e) Raman spectra of the analyte rhodamine B, RhB ($10^{-5}M$ of RhB for 30minutes incubated) on ozone-oxidized graphene platform (red represent after 5min ozone treatment), (f) Raman spectrum of 0.5mM L-Alanine on commercialized pyramidal Klarite.....</i>	<i>16</i>
<i>Figure 2.5 Left: General layout of the SPR sensor working system. Right: line graph shows the measured light intensity from SPR sensor with wavelength or angle modulation[115].....</i>	<i>19</i>
<i>Figure 2.6 Left: outside view of SPIRIT, Right: inside view of SPRIT with SPREETA sensor chip[116].....</i>	<i>21</i>
<i>Figure 2.7 Cross-sectional view of integrated-waveguide of TiO₂ with microfluidic channel[120]....</i>	<i>22</i>
<i>Figure 3.1Energy level diagram involves in Rayleigh scattering, Stokes and Anti-Stokes Raman scattering. A photon with energy E_L excites the vibrational modes of molecules.[14]</i>	<i>26</i>
<i>Figure 3.2(a) Illustrative representation of localized and delocalized plasmons on the SERS active nanostructure. (b) Reflection spectra taken on gold coated inverted pyramidal structure with 1250nm pit size. Incident angle is set to 3° and sample orientation is varied by 10° as shown, spectrum is vertically offset by 2000.</i>	<i>30</i>
<i>Figure 3.3 Surface-enhanced mechanism: a) electromagnetic enhancement, b) chemical enhancement</i>	<i>32</i>

<i>Figure 3.4 Optical properties of metal in visible range[129]</i>	<i>33</i>
<i>Figure 4.1 Optical properties of gold in visible and near infrared region.....</i>	<i>36</i>
<i>Figure 4.2 SEM image showing the definition of geometrical parameters</i>	<i>37</i>
<i>Figure 4.3 A schematic layout for microscopic view of generation-1 chip; different grey scale represents the change in scattering intensity due to the different pit size. Changes in absorption intensity can be seen in the photograph of the fabricated chip after gold coating: chip dimension is 3.8cmx3.2cm.....</i>	<i>38</i>
<i>Figure 4.4 A picture for simulation design for the gold coated inverted pyramid showing the cross-sectional and 3-dimensional views: Light is launched from the bottom/opening of the pyramid.....</i>	<i>38</i>
<i>Figure 4.5 Transformation of graphical data to a reflection map. a) showing reflection efficiency as a function of wavelength for each angle (0.25°-70°); b) the dispersion map of (a) with identification of localized Plasmon, propagating Plasmon and the subtle diffraction features</i>	<i>39</i>
<i>Figure 4.6 Diagram showing the charge oscillation direction under different polarization state</i>	<i>40</i>
<i>Figure 4.7 Simulated normalized electric field of gold coated inverted pyramid (top-view) at 785nm excitation wavelength: a) TE- polarization (rectangular aspect ratio), b) TM-polarization (rectangular aspect ratio), c) TE-polarization (square aspect ratio), d) TM-polarization (square aspect ratio).....</i>	<i>41</i>
<i>Figure 4.8 (a) Schematic diagram for a fully automated reflectometry system (red dotted line represents the incoming light source and orange straight line refers to the collection of light by the spectrometer (b) Sketch shows the sample stage geometry in which θ and ϕ are defined as the collection/detection angle and azimuthal angle/sample rotation respectively while X, Y and Z are defined as the three dimensional movements.</i>	<i>42</i>
<i>Figure 4.9 Comparison of Raman spectrum for benzyl mercaptan molecule between the inverted pyramid area and the unpattern area</i>	<i>44</i>
<i>Figure 5.1 Diagram for fabrication process flow.....</i>	<i>48</i>
<i>Figure 5.2 SEM image shows the profile of oxide layer.....</i>	<i>50</i>
<i>Figure 5.3(a) Photograph of the fabricated test chip after gold deposition, (b) Chip layout with the geometrical parameters.....</i>	<i>50</i>

<i>Figure 5.4 SEM images for KOH etched pyramids, (a) and (b) show the potassium re-deposition and (c) after cleaning with FNA for 30sec of (b).</i>	<i>51</i>
<i>Figure 5.5 SEM images of pyramid after gold deposition showing gold spitting: (a) in low magnification on silicon platform, (b) in high magnification on plastic platform</i>	<i>52</i>
<i>Figure 5.6 Photograph showing (a) basket made by tantalum wire, (b) the tungsten liner with basket</i>	<i>53</i>
<i>Figure 5.7 SEM image showing the gold deposition without gold spit after cleaning procedure</i>	<i>53</i>
<i>Figure 5.8 SEM images showing the different thickness of gold and their variation of the roughness on the sidewall (a) 400nm (b) 300nm (c) 200nm (d) cross-sectional image of Au 400nm</i>	<i>54</i>
<i>Figure 5.9(a) a double-y line graph characterizes the geometrical properties of inverted pyramid: the left y-axis shows the fill factor of each pitch length as a function of pit size and the right y-axis defines the normalized depth to the largest pit size as a function of pit size shown by a series of black diamond symbol, (b) a microscopic layout for the rectangular based inverted pyramid: vertical black arrow guides the patterns changing with pitch at 1000nm pit size, horizontal back arrow guides the patterns changing with pit size at 1500nm pitch length, the red-dotted diagonal arrow guides the patterns with high fill factor as shown in (a) with the dotted ellipse.</i>	<i>55</i>
<i>Figure 5.10 Reflection maps of pitch effect under TM-polarization from the simulation: (a) 1250P1000D; (b) 1500P1000D; (c) 1750P1000D; (d) 2000P1000D; (e) Distribution of zero order diffraction of 1000nm pit size along with different pitch, before metallization. Series of colored arrows indicate the shift of diffraction lines to infrared range corresponding to the longer pitch length</i>	<i>57</i>
<i>Figure 5.11 Reflection maps of pit effect under TM-polarization: (a) 1500P500D; (b) 1500P750D; (c) 1500P1000D; (d) 1500P1250D; (e) Distribution of zero order diffraction of 1500nm pitch along with various pit sizes; (f) Comparison of reflection efficiency of the plain Si with the different pit size under normal incident. Black arrows are indicating that resonance dips are shifting to the longer wavelength together with the larger pit size.</i>	<i>58</i>
<i>Figure 5.12 Dispersion maps of pitch effect showing the change in reflection with the excitation wavelength as a function of incident angle for 1000nm pit size with 400nm gold thickness at TM polarization (a) 1250nm pitch, (b) 1500nm pitch, (c) 1750nm pitch (d) 2000nm pitch. Green dotted are the guide lines for showing the shift in diffraction features corresponding with the pitch and hence tuning the propagating surface plasmon while the yellow dotted lines are guiding to follow the broadband localized plasmon which is resistant to the variation of the pitch and the white dotted lines</i>	

are for the guidance to the mix plasmon mode. (e) a line graph for normalized absorption of 2 different plasmon resonances (750nm and 815nm) @1000D as a function of pitch length which gives an evidence that the fill factor affects the absorption intensity. 61

Figure 5.13 Dispersion maps for the different pit size at the fixed pitch length of 1500nm under TM polarization with the 400nm gold thickness (a) 500D (b) 750D (c)1000D (d) 1250D. Colour scale represents from dark blue to dark red for the high absorption to high reflection, respectively. The position of the colour schemes of dark blue and blue range which is related to the plasmons, is varied with the pit size. Note that the value of the color scale is different for the each dispersion maps and hence the absorption intensity is highest at the 1250nm pit size with high fill factor. 63

Figure 5.14 Line graph showing the normalized e-energy as a function of the operation wavelength for different pit size inverted pyramidal designs. Two sets of arrows (black and red-dotted arrows) are guiding the shift of the resonance wavelength with the high e-energy as a result of larger pit size. Each line of e-field (related to the different pit) shows the nature of plasmon that the incoming light which is larger than the pit can be squeezed into the pit coupling to the e-field at the interface and leads to the high e-energy. The position of the monitor (green) within the pit can be seen in the right side. 64

Figure 5.15 Images showing the e-field distribution within the cavity at 785nm excitation wavelength for pit sizes (a) 500D (b) 750D (c)1000D (d)1250D (the yellow line is guiding the area of a cavity. The colour scale is ranging violet to red and red represents the high e-field density. (e) A double Y-axis graph which is the extraction an information from the field distribution at 785nm (a, b, c, d) about how far the maximum e-field is occurred away from the tip of the inverted pyramid, as a function of pit size and another Y-axis gives the information about the depth varied with the pit size and it can be used to find out where the 785nm line couple with the plasmons and hence forms the e-field. 65

Figure 5.16 Dispersion maps for different high periodicity: (a) 1000P750D (b) 1250P1000D (c) 1500P1250D (d) 1750P1500D (e) 2000P1750D. Red dotted lines mainly concerns for the propagating plasmon varied with the diffraction distribution and the white dotted lines represent to the localized plasmon resulting from the respective pit size. 66

Figure 5.17 A graphic representation for the normalized reflection as a function of wavelength for the high periodicity with different geometrical parameter. Data are collected at the angle of incidence 3° under TM-polarization. Green dotted lines with the black arrows are concerned for the longer shift of the plasmon resonance with the larger pit size and the red circles are guiding for the propagating plasmon occurs along with the diffraction distribution related to the different in pitch. 67

Figure 5.18 Angled resolved reflection map giving the dispersion characteristics of the rectangular inverted pyramid, 1250P1000D, the colour map represent the strong absorption (dark) towards the strong reflection (red/white) (a) simulation result; (b) experimental measurement result; (c) the diffraction bands of simulation is overlaid with those of experiment (red dotted line-simulation, black-dotted line-experiment); (d) Normalized reflection spectra at normal incident angle, y axis is in log value, indicating the separation of absorption dip due to symmetry breaking to rectangle instead of square.....69

Figure 5.19 (a) a three dimensional AFM image of the rectangular based inverted pyramid (inset is the 2D FFT of the pyramidal array); (b) a depth profile extracted from the 3D AFM image giving the depth value (713nm) for the 1000nm pit size; (c) the gold surface morphology for the flat surface; (d) the morphology of gold deposition on the sidewall; (e) the profile taking from the single gold grain located on the sidewall and fitting with Gaussian function.71

Figure 5.20 Dispersion maps for different pitch length at 1000nm pit size; (a) 1250P (b) 1500P (c) 1750P (d) 2000P (e) 3000P (f) Line graph of the normalized reflection as a function of wavelength at the 3° incident angle for different pitch. Blue dotted lines show the tuning of the localized plasmon for 1000nm pit size. White dotted lines are guiding the examples of the dispersive plasmons propagating along with the diffraction lines. Each set of black dotted lines are guiding the shift of wavelength to the infrared region when the pitch is increased.72

Figure 5.21 Dispersion maps for different pit sizes with 1500nm pitch length (a) 500D; (b) 750D; (c) 1000D (d) 1250D.....73

Figure 5.22 Left: Characterization for the normalized reflection as a function of wavelength for the different pit sizes (the data are collected at 3° incident angle under TM-polarization). The arrows are guiding for the shift in wavelength of the plasmon resonance corresponding to the pit size. Right: Table 5.3: Analytical data representing the plasmon mode with their change in resonance and absorption intensity for the different pit size.74

Figure 5.23 Characterization for the normalized reflection as a function of wavelength for the high fill factor with different combination of pitch and pit size (the data are collected at 3° incident angle under TM-polarization).....75

Figure 5.24 Dispersion maps for the different SERS substrates maintaining the fixed spacing between the pyramids as 250nm: (a) 1000P750D, (b) 1250P1000D (c) 1500P1250D. Yellow dotted lines are guiding for the shift of plasmon mode.75

Figure 5.25 Line graphs showing for the Raman intensity of the trigonal ring breathing mode of thiol molecules are given for different aspect ratio. Raman intensity is represented as a function of the pitch length for different pit sizes. (a) REC1:1.0 (b) REC1:1.1 (c) REC1:1.2 (d) REC1:1.3. The black arrows are guiding for the enhanced Raman intensity by increasing the pit size. The star symbols are markers for the SERS active substrates which are composed of pitch and pit size for the high fill factor.	76
Figure 5.26 Line graph composed by two sets of axes: black axes represent the Raman intensity of the different aspect ratio as a function of fill factor (dotted lines) and red axes act for the normalized Raman intensity of the inverted pyramid made up of 80% fill factor, as a function of the different aspect ratio.....	78
Figure 5.27 Comparison of SERS counts between standard Klarite and the optimized inverted pyramidal structure: (a) Raman spectrum of BTh molecules, (b) Reflection spectrum at 3° incident angle without azimuth angle.	79
Figure 5.28 Diagram which shows the Raman intensity as a function of change in pitch length and pit size. Raman count is extracted from the Raman spectrum of BTh molecules for the trigonal ring breathing mode. The red symbol is for the Raman intensity of the pit size effect and the red-dotted line refers to the exponential fitted curve. The green symbol is for the Raman intensity of the pitch length effect and the green dotted line represents the exponential fitted curve.	81
Figure 5.29 Schematic diagram gives a brief view of laser path to sample in Raman system	82
Figure 5.30 Column chart gives Raman intensity corresponding to the input polarization state for Klarite and the optimized pyramidal structure.....	82
Figure 5.31 Schematic diagram shows the condition of reflection measurement system with the sample.....	84
Figure 5.32 Dispersion maps after processing with the incident TM-polarized light; (a) azimuth angle, $\phi=0^\circ$, (b) $\phi=45^\circ$, (c) $\phi=90^\circ$, (i) co-polarization, (ii) cross-polarization, (iii) polarization conversion	84
Figure 6.1 Sheet-level imprinting process flow.....	89
Figure 6.2 SEM images of the negative copy of silicon master, i.e., pyramids.....	89

<i>Figure 6.3 SEM images of the plastic replica of silicon SERS substrates (a) cross section image (b) image is viewed at the tilted angle</i>	<i>89</i>
<i>Figure 6.4 (a) Diagram for R2R imprinting process, (b) the work flow for recombination of Ni-shim for large area scale</i>	<i>90</i>
<i>Figure 6.5 (a) SEM image of the inverted pyramid structure imprinting by UV embossed with large-area nickel shim, (b) SEM image of cross-sectional view of plastic inverted pyramid after replication</i>	<i>91</i>
<i>Figure 6.6 Line graph showing for the Raman intensity of the trigonal ring breathing mode of thiol molecules are given for the plastic SERS substrates. Raman intensity is represented as a function of the pitch length for different pit sizes. The red dotted circle is marked for the highest Raman count for the 1250P1000D active SERS substrate.</i>	<i>92</i>
<i>Figure 6.7 (a) line graph showing Raman intensity at 1003cm^{-1} Raman shift of 1000nm pit as a function of pitch length for different base substrates, (b) Raman intensity spectra of thiol molecules for different base substrates of an optimized design (1250P1000D_REC1:1.2).....</i>	<i>93</i>
<i>Figure 6.8 Bar chart for the comparison of SERS performance among the various plastic SERS substrates. Raman intensity is averaged for the the trigonal ring breathing of thiol ($990\text{-}110\text{cm}^{-1}$). Final demonstrator, 5G is improved by a factor of 7 compared to the 1st generation.</i>	<i>96</i>
<i>Figure 6.9 (a) Line graph for the cross-sectional profile for the width of the rectangular based inverted pyramid for the different SERS substrates. Y-axis represents the depth for each substrate profile and the x-axis gives the width of each inverted pyramid version. These profiles are extracted from the 3D AFM image as shown in the arrow direction of (b). (b) AFM 3D image for the final demonstrator, 5G.</i>	<i>98</i>
<i>Figure 6.10 Line graph shows the deterioration in depth of the replicated plastic substrates from the silicon master. Depth is normalized to the optimized design, silicon master.....</i>	<i>99</i>
<i>Figure 6.11 Line graph shows the roughness for the different base substrates for an optimized design.</i>	<i>99</i>
<i>Figure 6.12 SEM images (a) silicon substrate, (b) plastic substrate, sheet-level processing, (c) plastic substrate, R2R processing. Insets are the Fourier/reciprocal space representation of the respective substrate.</i>	<i>100</i>

Figure 6.13 The specular reflection maps as a function of the excitation wavelength for different substrates: (a) plastic substrate, (b) the silicon master. (c) Comparison of the normalized reflection as a function of the excitation wavelength at 3° incident angle between the plastic and silicon platform.	101
Figure 6.14 Raman spectra of various concentrations of ibuprofen solutions. The dotted circle is guiding the peak which is presence of ibuprofen.	103
Figure 6.15 1mM melamine and milk samples. The characteristic melamine peak is at 680cm^{-1} shown by the black dotted circle.	104
Figure 6.16 Spectra form various concentrations of melamine extracted from milk using acetonitrile	105
Figure 6.17 SEM images of inverted rectangular based optimized pyramidal design after 400nm gold deposition. (a) standard angle deposition at 25° , (b) optimized angle deposition at 34° . Insets are the high magnification of SEM images and (c) SEM image confirms the conformal Au coating on the sidewall at the optimized angle deposition.	107
Figure 6.18 Dispersion maps for plastic SERS substrates for the optimized design under p-polarization. (a) Standard angle Au deposition, (b) Optimized angle Au deposition, (c) Normalized Reflection for the different angle deposition at $\theta=3^\circ$. Standard deposition shows the plasmon resonance at 769nm and optimized deposition tunes the plasmon resonance at 791nm.	108
Figure 6.19 Raman SERS measurement for different angle deposition. (a) Average Raman spectra of BTh molecules after measuring 36 random points on the each substrate (b) Reproducibility calculated at the 1075cm^{-1} Raman vibrational frequency of BTh molecules. Error bars represent the relative standard deviation from the average Raman intensity.	109
Figure 6.20 Reflection maps for 1000P500D substrate with 200nm gold thickness (a) without molecule (b) with BZM molecule (c) Overlay plot for diffraction distribution of sample both before and after molecule, numbers on the plot refers the position where the detail analysis on the reflection spectra as shown in (d). (d) Comparison of the reflectivity difference before and after molecule coating at the angle of incidence, 30° .	111
Figure 6.21 Comparison of reflection spectrum before and after application of molecule from 1250P1000D inverted pyramid, plastic (a) Au200nm, $\theta=20^\circ$ (b) Au200nm, $\theta=30^\circ$ (c) Au100nm, $\theta=20^\circ$ (d) Au100nm, $\theta=30^\circ$	112

Figure 6.22 Reflection maps for 1250P1000D substrate with 100nm gold thickness (a) before molecule (b) after application of PMMA (c) Comparison of the reflectivity difference before and after molecule coating at the angle of incidence, 10°	114
Figure 7.1 Illustration of the simulated design for the different gold thickness showing that just change in gold thickness in the conformal coating , not effect on the geometrical parameter.....	118
Figure 7.2 Dispersion map as a function of the excitation wavelength for different gold thickness (a) 50nm, (b) 100nm, (c) 200nm, (d) 300nm and (e) 400nm. The inverted pyramidal is designed using the optimized geometrical parameter. Simulation is performed at TM-polarization.	118
Figure 7.3 Normalized reflectivity for different gold thickness (a) at normal incidence, (b) at 45° incident angle.....	119
Figure 7.4 Normalized field intensity for different gold thickness at the 785nm operation wavelength (a) 50nm, (b) 100nm, (c) 200nm, (d) 300nm and (e) 400nm.	120
Figure 7.5 (a) Line graph shows that the field density as a function of gold thickness. (b) Normalized field distribution plot for 400nm gold thickness with the created roughness at the height of 300nm by using the 50nm sphere. (c) Illustration of the simulated design with the roughness at 300nm height.	120
Figure 7.6 Simulation results shows the effect of non-conformal gold coating resulted from decrease in apex angle of pyramid	124
Figure 7.7 Normalized reflectivity spectra for non-conformal gold coating shows the changes in Plasmon behavior and its energy at (a) 5° incident angle (b) 10° incident angle (c) 15° incident angle (d) 20° incident angle.	125
Figure 7.8 Dispersion maps for reducing pith length by 200nm at noncon-7 condition at TM polarization (a) 900P261D (b) 700P261D.....	126
Figure 7.9 Effect of apex angle increased non-conformality coating on Plasmon properties: (a) index profile (b) dispersion map. Green box shows the high plasmon absorption over wide angular spectrum in visible and near infrared region and yellow box shows the high energy plasmons in part of infrared region. (c) e-field energy within the pit.....	126
Figure 8.1 SEM images cleaved devices with different angle metallization of the straight sidewall cavities: (a) 25° glancing angle deposition provides gold of 220nm thickness on the sidewall and	

180nm thickness at the bottom, (b) 34° glancing angle deposition provides that 83nm thick gold on the sidewall and 105nm thick at the bottom of the cavity. 131

Figure 8.2 Dispersion maps of the normalized reflection efficiency for the nanostructure cavity composed of the straight sidewall profile, for the 1000nm pit size and 782nm depth with the different periods ranging from 1250nm to 2000nm by 250nm steps. The gold layer is deposited as 400nm thick on the flat surface and 220nm on the sidewall surface. The simulation is performed with TM-polarization for the specular measurement. 133

Figure 8.3(a). Distribution of zero order diffraction of 1000nm pit size along with various pitch length ranging from 1250nm to 2000nm. The colour arrows indicate to the shift of the diffraction lines and the red circles with arrows for the shift of bandgap. (b) Normalized reflection at 3° incident angle as a function of the excitation wavelength for pitch effect. The red dotted lines are guided to the plasmon resonance. 133

Figure 8.4 Dispersion maps for the 90SW cavity devices composed of the straight sidewall profiles, with the 1500nm pitch length and 782nm depth of a different pit size ranging from the 500nm to 1250nm by 250nm step. The gold layer is deposited 400nm on the flat surface and 220nm on the sidewalls. The simulation is performed under TM-polarization for the specular measurement. 135

Figure 8.5 (a) Normalized reflection at a 3° incident angle as a function of the excitation wavelength for various pit sizes with a 1500nm pitch length. (b) A double-y axis graph shows that the amount of wavelength shift and the change in the absorption efficiency varied with pit size. 135

Figure 8.6 Dispersion maps of normalised reflection efficiency 1250P1000D straight sidewall structures of different depths, (a) Depth = 782nm, (b) Depth = 1048nm. The reflection efficiency is collected at TM-polarization and the scale bar scaled from the dark blue to the dark red for the complete absorption to complete reflection of the light at each wavelength, respectively. White-dotted lines show the different plasmon modes between the two structures with different depths. 136

Figure 8.7 (a) Normalized Reflection spectrum of 1250P1000D with different depths as a function of wavelength. The coloured region refers to the range of wavelengths where the plasmon behaviour is distinctly affected by the change in device depth. (b) The line graph shows the total integral of the e-field intensity over the monitored area as a function of wavelength. The inset graph shows the close view of the field intensity at the near infrared region. 137

Figure 8.8 Field Distribution across the cavity as a function of height for the different depth, the 1st column represents the shallow depth 782nm, and the 2nd column refers to the deeper depth 1048nm.

Each row represents the particular excitation wavelength where the plasmon absorption occurred, as shown Fig 8.7(a). The lower two plots are the high resolution contour maps for the variation of e-field intensity as a function of height for different excitation wavelengths. Left is for shallow depth and right is for the deeper depth.....139

Figure 8.9 Dispersion maps for the various pit sizes at constant of pitch lengths and depths (a)500nm, (b) 750nm, (c) 1000nm, (d) 1250nm (e) Normalized reflection as a function of wavelength at 3° incident angle illumination for different pit sizes. Dotted lines are present as guides for the shift of the plasmon resonance with the pit size.140

Figure 8.10 Dispersion maps of the normalized reflection efficiency for the different pitch length while maintaining the depth and pit size; (a) 1250nm, (b) 1500nm, (c) 1750P, (d) 2000nm, (e) line plot of the normalized reflection as a function of wavelength for different pitch length so that plasmon is confined at the fixed resonance due to the constant pit size (shown by the dotted line).....141

Figure 8.11 Reflection analysis for different depth. (a) Dispersion map for the depth of 782nm. (b) Dispersion map for the depth of 1048nm. Normalized Reflection at 3° incident angle for different depth with a separation distance of 250nm between adjacent structure such that (c) 1250P1000D, (d) 1500P1250D, (e) 1750P1500D, (f) 2000P1750D. (g) Comparison of normalized reflection (@ 3° incident angle) between different depths as a function of tuneable plasmon resonance for different pyramidal structures.....142

Figure 8.12 Comparison of average Raman intensity for trigonal ring breathing: (a) and (c) shows the effect of pit size and pitch length, for 1048nm depth respectively. (b) And (d) represents the effect of pit size and pitch length, for 782nm depth respectively.144

Figure 8.13 Comparison of average Raman intensity for BTh molecule between the optimized deeper depth structure (blue spectrum) and the optimized shallow one (red spectrum).145

Figure 8.14 SEM images cleaved devices with different angle metallization of the straight sidewall cavities: (a) 28° glancing angle deposition of titanium, (b) 34° glancing angle deposition of titanium, (c) 37° glancing angle deposition of silver.146

Figure 9.1 (a) photo of silicon stamp, (b) layout diagram, (c) replicated plastic substrate, using R2R imprinting.151

Figure 9.2 (a) Schematic diagram for free-space SERS sensor, (b) Raman spectra of BTh shows that an optimized inverted pyramid has higher enhancement compared to standard Klarite.....154

<i>Figure 9.3 Schematic diagram for the proposed design of integrated SERS substrate</i>	<i>154</i>
<i>Figure 9.4 Schematic diagram shows that double stranded DNA passing through a nanopore of micro-cavity structure.....</i>	<i>156</i>
<i>Figure 9.5(a) Helium ion microscope image of fabricated free standing microcavity with nanopore, (b) High magnification image highlights the nanopore structure with red box.</i>	<i>156</i>
<i>Figure 9.6 (a) a cross-sectional view of inverted pyramid indicating where a square hole and its spatial monitor are allocated; (b) a cross-sectional view of index profile where the red colour refers to the medium of air with $RI=1$</i>	<i>158</i>
<i>Figure 9.7 Calculated electric field above the nanopore within 3D gold microcavity for different excitation wavelength using the water background media.</i>	<i>158</i>
<i>Figure 9.8 Geometry of metallic rectangular-groove grating [151]</i>	<i>160</i>
<i>Figure 9.10 Line graph shows that the shift in plasmon resonance on the depth variation for different plasmon mode.</i>	<i>167</i>

List of Publications

- 1) S.Z. Oo, R. Y. Chen, S. Siitonen, V. Kontturi, D. A. Eustace, J. Tuominen, S. Aikio and M.D.B. Charlton, “Disposable plasmonic plastic SERS sensor,” *Optics Express* 21, 18484-18491 (2013)
- 2) S.Z. Oo, S. Siitonen, V. Kontturi, D. A. Eustace and M.D.B. Charlton, “Disposable gold coated non-inverted pyramidal SERS sensor on the plastic platform” (to be submitted)
- 3) S.Z. Oo, M.D.B. Charlton, “Effect of non-conformality gold deposition on SERS related plasmonic effects” (to be submitted)
- 4) Swe Zin Oo et al., “Optimization of SERS enhancement from nanostructured metallic substrate based on arrays of inverted rectangular pyramids and investigation of effect of lattice non-symmetry,” *Proc. SPIE 8234, Plasmonics in Biology and Medicine IX* (2012)
- 5) Swe Zin Oo et al., “3D analysis of surface plasmon dispersion for SERS sensor based on inverted pyramid nanostructures,” *Proc. SPIE 8269, Photonic and Phononic properties of Engineered Nanostructures II* (2012)
- 6) M. Firdaus A. Muttalib, S.Z. Oo and M. D. B. Charlton, “Experimental measurement of photonic/plasmonic crystal dispersion, applied to the investigation of surface plasmon dispersion for SERS sensing applications,” *Proc. SPIE 8264, Integrated Optics: Devices, Materials and Technologies XVI* (2012)
- 7) M. E. Pollard, S. J. Pearce, R. Chen, S.Z. Oo and M. D. B. Charlton, “Polymer waveguide grating couplers for low-cost nanoimprinted integrated optics,” *Proc. SPIE 8264, Integrated Optics: Devices, Materials, and Technologies XVI* (2012)
- 8) S.J. Pearce, M.E. Pollard, S. Z. Oo, R. Chen and M.D.B. Charlton, “Nanostructured surface enhanced Raman scattering sensor platform with integrated waveguide core”, *Applied Physics Letters* 105, 181101 (2014)
- 9) S. J. Pearce, S.Z. Oo, M.E. Pollard and M. D. B. Charlton, “Integration of nanostructures and waveguide core for surface enhanced Raman spectroscopy: a novel excitation method,” *Proc. SPIE 8264, Integrated Optics: Devices, Materials, and Technologies XVI* (2012)
- 10) S. J. Pearce, S.Z. Oo, M.E. Pollard and M. D. B. Charlton, “FDTD modelling of waveguide core integrated etched nanostructures,” *Proc. SPIE 8818, Nanostructured Thin Films VI* (2013)

- 11) S. J. Pearce, S.Z. Oo, M. E. Pollard, R. Chen, S. Kalsi and M.D. B. Charlton,
“Waveguide core integrated nanostructured SERS sensor platform,” Proc. SPIE
8818, Nanostructured Thin Films VI (2013)

Conference Presentations

1. Speaker: “Effect of non-conformality gold deposition on SERS related plasmonic effects,” SPIE Photonics West, San Francisco, CA, USA (2013)
2. Speaker: “Disposable plasmonic plastic SERS sensor”, SPIE Photonics West, San Francisco, CA, USA (2013)

DECLARATION OF AUTHORSHIP

I, Swe Zin Oo declare that this thesis and the work presented in it are my own and have been generated by me as the result of my own original research.

DESIGN, FABRICATION AND OPTIMIZATION OF LARGE AREA CHEMICAL SENSOR
BASED ON SURFACE-ENHANCED RAMAN SCATTERING (SERS) MECHANISM

I confirm that:

1. This work was done wholly or mainly while in candidature for a research degree at this University;
2. Where any part of this thesis has previously been submitted for a degree or any other qualification at this University or any other institution, this has been clearly stated;
3. Where I have consulted the published work of others, this is always clearly attributed;
4. Where I have quoted from the work of others, the source is always given.
With the exception of such quotations, this thesis is entirely my own work;
5. I have acknowledged all main sources of help;
6. Where the thesis is based on work done by myself jointly with others, I have made clear exactly what was done by others and what I have contributed myself;
7. Parts of this work have been published.

Signed:.....

Date:.....

Acknowledgements

First of all I would like to thank my supervisor Dr. Martin D.B. Charlton for giving me an opportunity to pursue the research project, part of consortium project collaborating with VTT- technical Research Centre of Finland, TNO-ORGANISATIE VOOR TOEGEPAST NATUURITENSCHAPPELIJK ONDERZOEK-TNO, Philips- Philips Electronics Nederland B.V., Renishaw Diagnostics-United Kingdom, Nanocomp Ltd-Finland, Momentive performance materials GmbH-Germany, Universitaet Wien-Austria, 3D AG-Switzerland. I am deeply indebted to him as his hard work helped me in all aspects that the project touched upon in all studied years. I would like to thank Dr.Ruiqi Chen for assisting with the electron-beam lithography whenever I was in urgent condition and Dr. Mike Edward Pollard for assisting with the modelling and simulation of the design. My gratitude also goes to Dr. Stuart J. Pearce for giving a hand whenever I have got an issue with metal evaporator and also for his assist of oxide deposition. Further thanks are given to Chirenjeevi Krishnan who encouraged me and gave me valuable discussion from starting to the end of this project. I would also like to thank everyone in Nano Research group and nanofabrication centre for all their support and discussions. In addition, I would also like to thank the European commission for providing the funding for the research.

I would also like to give my special thanks to my parents for their encouragement and patience, along with everyone else who has helped me to fulfil this goal.

Definitions and Abbreviations

1. Ag=silver
2. Al=aluminium
3. Au=gold
4. BTh=Benzene thiol molecules (C_6H_5SH)
5. BZM=Benzyl Mercaptan ($C_6H_5CH_2SH$)
6. CdS=Cadmium sulfide
7. Cu=Copper
8. CVD=Chemical vapor deposition
9. D=Pit Size
10. EF= Enhancement Factor
11. FNA= Fuming nitric acid
12. Ga=Gallium
13. GNR= Graphene nano-ribbon
14. HF=Hydrofluoric acid
15. In=Indium
16. IPA=Isopropyl alcohol
17. KOH=Potassium Hydroxide
18. NC=Nano-crystals
19. P=Pitch Length
20. PB=Post Baking
21. PbSe=Lead Selenide
22. Pd=Palladium
23. PET=Polyethylene Terephthalate
24. PMMA=Poly methyl methacrylate
25. Pt=Platinum
26. QDR= Quick dense rinsing
27. SERS=Surface-Enhanced Raman Scattering
28. SiO_2 =Silicon dioxide
29. SPP=Surface Plasmon Polariton
30. SPR=Surface Plasmon Resonance

31. SW= Straight Side-Wall

32. TiO₂=Titanium dioxide

Chapter 1. Introduction

The advent of surface-enhanced Raman scattering (SERS) has redefined Raman scattering to new heights and provides greater expectation in the field of medicine, forensics, environmental monitoring and drug detection. Even though SERS has great potential, it has been prevented from emerging laboratory based research to everyday use. This hindrance was caused by poor reproducibility of SERS substrate on large scale, high enhancement, cost-effective high throughput. Recent advances in these fields along with increasing interest in fabricating nanostructures for different SERS platforms are bringing great hopes to SERS technique. Since Fleischmann et al [1] observed SERS on electro-chemically roughened silver electrodes various SERS substrates including colloids [2], nanorods [2,3], nanowire [1,4], nanospheres [3,5], nanoring [6] and tetrahedral nanocrystals [7] have been proposed. In addition to the different shapes, various materials including silver [8], gold [2,7], platinum [9] and chalcogenide [10] have been used and claimed to have electromagnetic enhancement in the range 10^8 - 10^{13} [11,12]. Even though various SERS substrates and enhancement mechanisms have been proposed, the main challenge faced by all of them is lack of repeatability over the large area scale and ultrahigh sensitivity. In addition, hot-spots (region producing high SERS enhancement) produced by these techniques are random and vary fabrication to fabrication even using the same methods. Moreover, conventional analytical techniques are usually expensive both in terms of personnel, time and equipment. One of the principal requirements is to perform screening tests without specialized infrastructure. Limitations of current sensors include large dimensions, sometimes limited sensitivity and inherent single-parameter measurement capability. However, the full utilization of nano-structured sensors is hindered by the lack of fabrication methods for low-cost, highly reproducible nano-structured surfaces. SERS technology potentially allows single molecule detection for applications in biotechnology, process control, environmental monitoring and clinical diagnostics.

Therefore the objectives of the SERS sensors are:

- To provide nano-structured sensor surfaces for multi-parameter and high resolution sensing
- To provide low-cost, high-volume, large area production process for nano-structured sensors

- To evaluate SERS technology for multi-parameter sensing in different application area with varying requirements

Recently, Klarite™ SERS substrates have claimed to be highly reproducible with less than 10% standard deviation in peak heights from measurement to measurement and along the substrate[13]. This substrate is a 3D gold coated inverted pyramid composed of 2000nm pitch and 1500nm pits width with the length to width aspect ratio 1:1.

Here the next generation of Klarite on silicon platform was fabricated by varying its pyramidal geometrical parameters such as pitch length, pit width and base aspect ratio (width to length). Studying the plasmonic and SERS effect in relating to the geometrical parameters, an optimized Klarite substrate geometry was achieved composed of 1250nm pitch 1000nm pit size with the rectangular aspect ratio (1:1.2). This non-symmetry lattice structure enables the optimized design to support more localized plasmons than its predecessor Klarite. In addition to that, it also enables coupling between different Plasmon modes at critical incident angles and geometries. The fabrication was performed using electron-beam lithography and simple anisotropic potassium hydroxide (KOH) wet etching to pattern the highly reproducible SERS substrate. Comprehensive spectroscopic measurements are performed on gold coated samples as a function of incident angle and wavelength to understand the behavior of light and surface plasmon within the graded pyramidal pits. Simultaneously RCWA (Rigorous Coupled Wave Analysis) based Photonic Suite is used to design 3D modeling on these pits to understand complex spectroscopic measurements and bridge it with theory. Electric field analysis was also performed within the pit for TE and TM incident light, for constant pitch varying pit width and constant pit width (hole) varying pitch. Additionally, effect of gold thickness was resolved through 3D simulation.

After deriving the optimized design on the silicon platform, the structures are transferred to the plastic platform utilizing sheet-level and roll-to-roll (R2R) Nanoimprinting or Nanoimprint Lithography (NIL) to aim for large volume processing. The objectives of transferring to the plastic platform are to utilize the abilities of comparatively cost-effective manufacturing process for high throughput, easy to dispose of and nature of flexibility. The study was also carried out on the dual sensing mechanisms on the plastic sensor including the surface-enhanced Raman scattering (SERS) and surface-plasmon resonance (SPR).

Finally the alternative SERS sensor composed of 90° straight sidewall holes was investigated. This is different from the pyramidal slope sidewall on the same silicon platform. And its performance on SERS effect was assessed. The reason of studying the alternative design for sensing is that in the case of integrating SERS sensor with waveguide, this alternative design is comparatively easy to integrate with waveguide compared to the pyramidal slope sidewall.

1.1 Motivation and structures of the thesis

There is interest in being able to detect and analyze complex molecules such as proteins, DNA, chemicals, narcotics, explosives and chemical/biological warfare agents for homeland security applications. Other applications are in water purity monitoring or food quality control during long distance shipping.

The challenge then is how to detect these complex molecules. If molecules are present in very high concentration then a technique known as Raman spectroscopy can be utilized. This involves putting the unknown substance on a (glass) slide and focusing a high power laser onto it. Energy gets absorbed by the molecule and so reflected light loses a bit of energy. By measuring this energy change in wavelength of reflected light then information can be gained about the strength of the chemical bonds between molecules. Characteristic peaks then appear at different energies which allow identification of the unknown molecule. The problem is that RAMAN process of absorption of energy by the molecules is very inefficient.

One efficient technique to overcome this limitation is to utilize Surface-Enhanced Raman Scattering (SERS). In this case the molecule is not merely placed on any surface but on top of a nano structured metallic substrate which performs the job of transducing the optical radiation in and out of molecules as a result the scope of Raman scattering is extended to detect molecules at low concentration to few/single molecule level.

Despite its huge potential, several factors that inhibit SERS adoption outside the research community are

- Inability to replicate SERS substrate at low cost
- Randomness and disorder in films of nano particles deposited over the base substrate

- Lack of systematic method in comparison between different SERS substrates

However, the benchmark substrate Klarite is very promising for mass-manufacturing at low cost using nanoimprint lithography due to the ease of embossing with the nature of slope sidewall. Klarite demonstrates the uniform gold particle deposition resulting in the less than 10% reproducibility of intra-sample measurement. Active surface area of Klarite can be excited using 633nm and 785nm operation wavelength. The reason of tuning the infrared wavelengths is to be compatible with commercially available Raman system and these infrared diode lasers are cheap compared to UV and other laser systems.

Therefore, this thesis aims to investigate the optical properties of pyramidal structures on both silicon and plastic substrate platforms with an emphasis on its geometrical parameters. In particular, the plasmonic behavior and its related SERS effect are explored as they are critical to the enhancement of the SERS sensor. Hence an optimized geometrical combination can be determined to support the highest enhancement.

This thesis is divided into literature reviews, background theory and five chapters of original results. Chapter 2 reviews recent research to SERS sensing mechanism in chemical and biological field and recent progress in fabrication and applications of various SERS sensors. Chapter 3 introduces the reader to the theoretical background of Raman scattering and surface-enhanced Raman scattering and surface plasmon polariton and describes the geometry of SERS substrate to be studied. Chapter 4 outlines the numerous tools, apparatus and techniques used to attain the experimental and simulated data presented in this thesis.

Chapter 5 provides the detail of fabrication process for master silicon SERS substrate, an in-depth analysis of plasmonic behavior varied with the geometrical parameters of inverted pyramid. Finally an optimized design of inverted pyramid is assessed via using both optical and SERS Raman measurements. Chapter 6 discusses the transfer of SERS sensor to plastic platform, accesses the qualitative and quantitative properties of plastic sensor and compared with the silicon master. Since the plastic sensor is dedicated to utilize in dual sensing mechanism (SERS/SPR), the preliminary demonstrations of surface-plasmon resonance, SPR sensing on the benzene thiol molecules and PMMA are presented.

Chapter 7 details the effect of gold layer thickness and the effect of non-conformality of gold deposition on the plasmonic behavior of the inverted pyramid, silicon platform.

Chapter 8 provides the alternative SERS design which is dedicated to integrate with waveguide in future. Here assessment of its SERS effect compared to the inverted pyramid is performed. Chapter 9 summarizes the results of the thesis and suggests the possible future direction of the current project.

Chapter 2. Literature review

This chapter highlights the different SERS substrates with various engineered nanostructures, fabrication methods, material and their respective sensitivities. Sensitivity of the SERS sensor is based on the various parameters such as architectural design, metals, and surface roughness. The aim is to realize the nature of SERS substrates and their respective controlled parameters to achieve high sensitivity. Based on these findings, this chapter discusses the limitation of current SERS substrate on the real world applications. The surface plasmon resonance, SPR sensors are also discussed since a fabricated nanostructure in this thesis has the potential of dual (SERS/SPR) sensing mechanism.

2.1 Outlook for SERS substrates

Surface-enhanced Raman Scattering (SERS) is an optical sensing technique that utilizes and enhances Raman scattering from molecules adsorbed on specific nanostructure active SERS substrate. Many researches have been carried out to find out the origin of higher enhancement factor (EF) and hence developed different SERS structures with various fabrication methods and materials. Up to date, it has been believed that the reason which is responsible for the higher Raman scattering and EF is the electromagnetic enhancement mechanism which is basically related to the plasmonic effects. This plasmonic effect is generally achieved by supporting via the selective metal and composite architectural design of nanostructures. However the enhancement is too sensitive in every slight change of geometrical parameters and metal condition and therefore understanding the dependence of EF on the physical parameters is very essential to achieve the ideal SERS substrates. Handling the fabrication technique is also challenged to attain a hot-spot free substrate providing reproducibility and repeatability. Although SERS has the challenges and limitations, it has the unique advantages including rich in information of Raman spectra[14-16], high spatial resolution[17,18], ultrahigh sensitivity[19-21], label-free identification and the elimination of time-consuming sample preparation. Therefore, SERS has the potential for biosensing, food and safety, environmental monitoring, pharmaceuticals and biological and chemical warfare.

SEM images of some developed SERS substrates are shown in Fig 2.1. In order to facilitate the achievement of reproducibility and sensitivity, several SERS mechanisms have been developed using various sizes, shapes and morphologies based on different based-materials (Silicon, Polymer(polystyrene, polyethylene), chalcogenide glass, zinc oxide) and diverse of coated metals (gold, silver, platinum, palladium) regarding with various lithography methodologies and deposition techniques. Table 2.1 summarizes a variety of engineered SERS substrates over the architectures, fabrication techniques, materials, enhancement factor and some of their limitations.

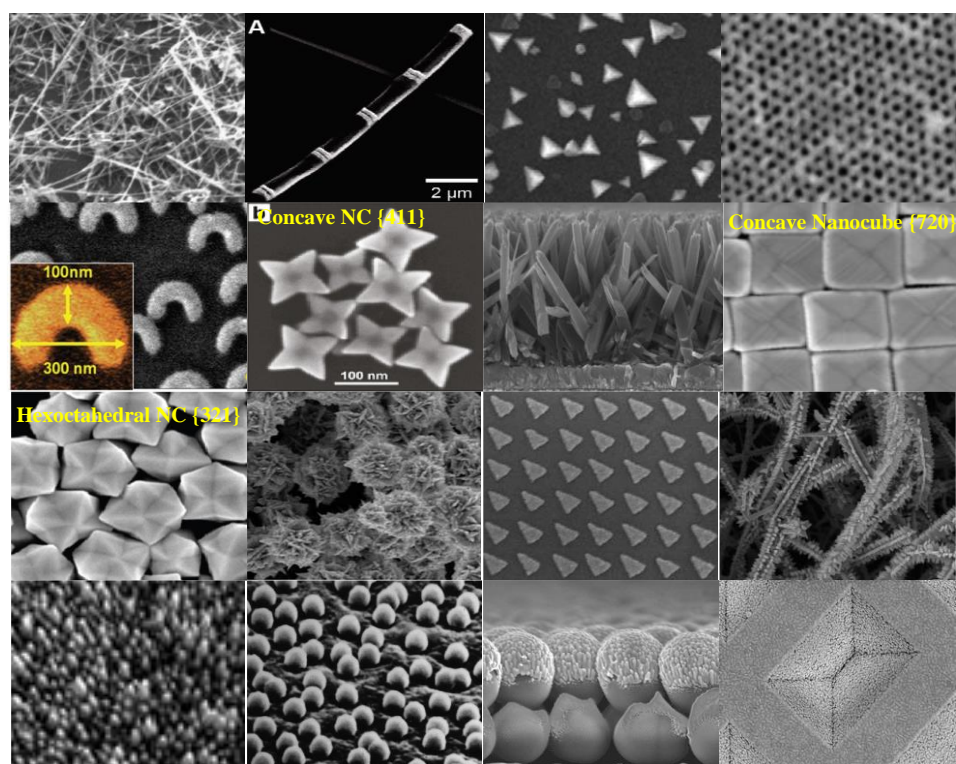


Figure 2.1 SEM images of several SERS platforms [4,7-9 for 1st row, 28-29, 32-33 for 2nd row, 58, 22 , 99-100 for 3rd row, 49, 55, 9, 123 for 4th row, left to right]

Table 2-1 Summary of a variety of engineered metallic structures for SERS detection

Architecture	Fabrication Methods	Substrate material	Metals	Remarks
Nano-rods[26,31,33-36]	<ul style="list-style-type: none"> ➤ Hydrothermal ➤ On wire lithography ➤ Seed-mediated growth ➤ Oblique angle deposition ➤ Electroless deposition by the reduction of $[\text{Ag}(\text{NH}_3)_2]^+$ with glucose 	<ul style="list-style-type: none"> ➤ Fluorine-doped tin oxide (FTO) substrates ➤ TiO_2 ➤ SiO_2 	<ul style="list-style-type: none"> ➤ Gold (Au) ➤ Silver (Ag) 	<ul style="list-style-type: none"> ➤ Reproducibility (<10%) in testing of PMBA ➤ 10^{-12}M detection limit of malachite green ➤ 6.8×10^8 EF in detection of thiol molecule
Nano-voids/hole[37-42]	<ul style="list-style-type: none"> ➤ E-beam lithography ➤ Thermal evaporation ➤ Nanosphere lithography ➤ Electrochemical deposition ➤ Focused Ion Beam 	<ul style="list-style-type: none"> ➤ Silicon ➤ Polystyrene 	<ul style="list-style-type: none"> ➤ Au ➤ Ag ➤ Cu 	Controlling the ratio of diameter/periodicity can tune the surface plasmon resonance
Nano-wires[43-48]	<ul style="list-style-type: none"> ➤ 3D electrochemical deposition system ➤ Anodic Aluminium Oxidation ➤ Glancing Angle deposition ➤ Langmuir-Blodgett 	-	Ag	EF = $> 10^8$ for crystal violet EF of the dense corrugated nanowire is higher 2.6 times than the sparse nanowire
Nano-sphere[31,49-55]	<ul style="list-style-type: none"> ➤ Spin Coating ➤ Nanosphere lithography ➤ CTAB-assisted growth process with iodide ions 	Glass	<ul style="list-style-type: none"> ➤ Au ➤ Ag 	SERS intensity significantly increased by the size of spheres
Nano-pillars	<ul style="list-style-type: none"> ➤ E-beam lithography 	Glass/Quartz	<ul style="list-style-type: none"> ➤ Au 	EF = 4.7×10^5 in detection of para-mercaptoaniline analyte
Nano-crystal (NCs) [28-30,56-59]	Chemosynthesis method <ul style="list-style-type: none"> ➤ Tetrahedral NCs ➤ Concave NCs ➤ Concave Nanocubes ➤ Hexoctahedral NCs 		Pt/Au/Ag /Au- Pd/CdS/PbSe/ZnO	-

Architecture	Fabrication methods	Core material	Shell material	Remark
Core@shell nanostructures[60-65]	<p>Chemical Reduction</p> <p>Au@SiO₂</p> <ul style="list-style-type: none"> ➤ Synthesized by citrate reduction techniques for metal NPs ➤ Modifying the sodium silicate concentration for silica shell <p>Ag@C</p> <ul style="list-style-type: none"> ➤ Synthesized by the hydrothermal route and the low temperature heating-stirring method <p>Ag@Au/Au@Ag</p> <ul style="list-style-type: none"> ➤ Synthesized by citrate reduction techniques and continuous stirring 	Au/Ag	SiO ₂ /C/Au/Ag	<ul style="list-style-type: none"> ➤ Solution-phase NPs is difficult to control the SERS intensities and replication due to the inherent instabilities in molecular addition and surface chemistry of structural defects including of pinholes and edges ➤ Providing long SERS-active shelf life (six months) due to the protection of carbon shell from oxidation ➤ Ag@Au NPs owe more advantages than Au@Ag NPs because Au is inherit of more controllable surface morphology, more sensitive due to the binding properties of functional groups including -SH, -NH₂ and finally Ag has the problem of stability due to its oxidation property
<p>Graphene SERS[66-70]</p> <p>Graphene nano-ribbon (GNR)</p> <p>Armchair GNR</p> <p>Zigzag GNR</p>	<ul style="list-style-type: none"> ➤ CVD-grown graphene surface ➤ E-beam lithography ➤ Lift off ozone, ➤ UV induced oxidation treatment 	Si/SiO ₂	Graphene	<ul style="list-style-type: none"> ➤ Highest chemical enhancement factor 10³ to 10⁴ after ozone treatment due to both high oxidation and doping effects ➤ Raman intensity depends on the polarization, chemical bond type and ribbon width

The amplification of Raman scattering is highly dependent on the different architectures of SERS substrates and its metallization providing the fingerprint of the small amount of biological and chemical molecules even for the single molecule like DNA and the complex

sample (e.g. a biological cell). The fact that the roughness of the SERS substrate is playing the main role for high enhancement factor is widely believed although the detail relationships such as between the plasmons resonance and EF, between the metal roughness and EF, have not been theoretically and rigorously proved. Therefore, the researchers have studied the fabrication techniques to get the suitable metal roughness for SERS enhancement either on the based substrate by various patterning or the different metallization techniques. Metallization on the nanostructures has been claimed to improve the amplification of Raman scattering 10^6 to 10^{14} times providing sensitive detection and analysis of a single molecule [20,71-75]. Most of the substrates have used gold (Au) and silver (Ag) more than other metals of aluminium (Al), copper (Cu), indium (In) and gallium (Ga). This is because Au is a simple process and resistance to the oxidation and Ag has the highest enhancement of Raman cross section for an excitation in the visible region. But all latter metals are challenging to process because of rapid formation of unwanted oxide layers and chemical stability.

Most of the SERS substrates are multi-scale nanoparticles and nanocrystals. The nanoparticles were classified 1-dimensional, 2-dimensional and 3-dimensional nanoparticles into nanorods, nanocrescent and nanopyramids respectively. The nanocrystals were categorized by its different index crystals. The index crystal is composed of well-defined tips and edges supporting large electric field and resulting in strong enhancement although it has fabrication challenges in controlling high-energy surfaces during the synthesis of nanocrystals and the cost. The multi-scale nanoparticle has the challenge in fabrication to achieve high index nanoparticle templates although they possess a reasonable sensitivity to detect the small amount of molecule due to a major contribution of its size and periodicity. Table 2.2 summarizes the parameters of conventional SERS structures that can control the Raman amplification. In addition to these conventional structures, research has been carried out non-conventional structure to achieve the high plasmon resonance and electric field that are cast for the high SERS enhancement factor.

Table 2-2 Summary of parameters that influence the enhancement factor in the conventional nanostructures

Conventional Nanostructures	Parameters which cause Raman Enhancement factor
Nanotriangle/Nanoprism[76,77]	Corner truncation and roundness, metal thickness, edge length, perpendicular bisector
Nanosphere[49-55,78]	Size, spacing between dimmers, periodicity
Nanovoid[37-39]	Ratio of diameter to depth, depend on metal thickness
Nanowire/Nanorod[31,33-36,43-48]	Controlling wire and gap diameters and the length

2.1.1 Unconventional Nano-clusters

There are three different compositions of nanoparticles: 1. clusters [49,79-82], 2.reshaping the nanostructures [83-85] and 3.applying new materials[44,66-70,86-88] in order to get the high plasmon energy with high enhancement factor of Raman scattering.

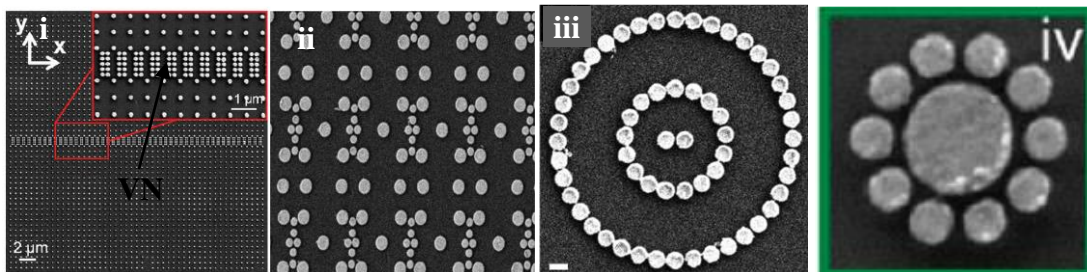


Figure 2.2 SEM images of unconventional nano-clusters: (i) the nested VNT(Vortex Nanogear Transmissions) array, (ii) the genetic nanoarray (GNA), (iii) concentric necklace nanolens (CNNLs), (iv) Oligomer nano-cluster (undecamer) [79-82]

In the composition of clusters/arrays, nanoparticles called nanodiscs/nanodisks, nanolens and nanocylinders are arranged in a manner to produce the high electric-field between the coupling of the radiative photonics and near-field photonics. But the electric-field concentration is varied with geometry, interparticle spacing and cluster size as the conventional nanostructures. Different arrays of nanoclusters as shown in Fig 2.2 are fabricated using the electron-beam lithography on the quartz substrate followed by lift-off of PMMA resist. In order to give the interaction of the recirculated light with the surface

plasmon polaritons in nanoparticles (NPs), an array of Au nanodiscs (Fig 2.2 (i)) was created enabling the optical vortices to route the optical power around the NPs. These optical vortices can route the high e-field through the nanodiscs. Therefore, the nanostructure maintaining coupled optical vortices is defined as “Vortex Nanogear Transmissions” (VNTs). In order to achieve a wider bandwidth of e-field spectrum for VNTs, the VNT was integrated with regular nanoparticles (NPs) arrays and is called as the nested VNT design. These adjacent NPs arrays were used as collector panels to route the incident light into the central VNT where the e-field intensity was further enhanced.

An array called the genetic nanoarray (GNA) (Fig 2.2(ii)) which is designed by the genetic algorithm (GA) to find both the spatial arrangement and the radii of N spheres promising the maximum field enhancement. To find the radius of a sphere, GA applies the generalized multi-particle Mie (GMM) theory. GMM is the expansion of the single particle Mie theory using the vector spherical wave functions (VSWF) on each sphere. The genetically optimized array with $N=16$ setting the central diameter separation of 25nm, achieves the optimum distance between the near-field plasmons of dimer and radiative photonic contributions of the nearby NPs.

Alyssa J. Pasquale et.al also arranged Au nanocylinders in loops like a necklace in which a nanoparticle dimer is positioned at the centre of one or more concentric necklace nanolenses, so called CNNLs (Fig. 2.2(iii)). CNNLs are composed of Au nanolens with constant diameter of 150nm and 25nm edge-to-edge spacing. The general idea of CNNLs is to enhance the near-field intensity occurred in the dimer gap using the higher-order radiative coupling from surrounding necklaces. In practice, the optimization accomplishes only when the outer necklace has the diameter twice of the inner necklace. As a result, the near-field intensity is increased by the geometry moving from the isolated dimer to single-necklace (dimer/enneadecagon (19 particles)) and double-necklace (dimer/enneagecagon/tetracontagon (40 particles)). But there is saturation once a third necklace is added.

Jian Ye et.al study the modification in the relative size of central and surrounding particles of a cluster along with interparticle spacing and size of NPs which all affect the tailoring of plasmonic resonance. First they studied the different sizes of Au heptamers variations in the diameter from 85nm to 170nm under the constant interparticle distance at 15nm and 30nm fixed heights. It showed that the resonance can be tuned by varying the size of NPs. The larger the cluster dimension, further the Plasmon resonance is red shifted. They also

studied the response from the variation of interparticle spacing of Au heptamers by changing the gap size of 15nm to 60nm with 130nm constant diameter. The maximum Raman intensity was achieved by the smallest gap size of 15nm and dramatically decreased and disappeared with increasing gap size due to the detuning of Plasmon resonance between the excitation wavelength and Stokes wavelengths. Finally they fabricated different oligomer clusters (Fig. 2.2 (iv)) including octamer, nonamer, decamer and undecamer to study the effect of modification in the relative size of central NPs with respect to surrounded NPs' size. In the clusters, the peripheral NPs' diameter and interparticle gap are controlled at constant of 85nm and 15nm respectively. The highest SERS signal is achieved by nonamer while the undecamer shows the lowest SERS enhancement.

The studies are still going on the new material like graphene[66-68,86], graphene-oxide [69] and alloy nanoparticles for optimizing of plasmonic related e-field or using alternative membrane for substrate to solve the binding problem rather than fixing the architectures of nanostructures. Graphene is widely believed to give high SERS enhancement due to its remarkable mechanical, electronic and photonic properties [89-91]. Now most of graphene-based SERS substrates are related to charge transfer of chemical enhancement and get the highest chemical enhancement of 10^4 [67].

However the conventional nanostructures have accomplished the requirement of the SERS community with their unique properties. For example, Mesophotonics Ltd has developed a commercialized SERS substrate called Klarite™ giving a uniform enhancement throughout the substrate with reproducibility better than 10% for benzenethiol and aminothiophenol molecules as chemical markers. It consists of square lattice inverted pyramid pit along $\langle 111 \rangle$ plane with a constant pitch 2000nm and pit size 1500nm. Circular and square apertures are produced onto SiO₂ hard mask through conventional optical lithography followed by anisotropic KOH etching to etch along $\langle 110 \rangle$ planes resulting in array of inverted square pyramidal pits (Fig 2.3). The substrate is made SERS active by gold sputtering resulting in physical electrical connection of pit side walls to flat surface between the pits[13]. This is simple fabrication technique but a more reliable one. In this report Klarite will be considered as a starting point towards the production of idealized substrate.

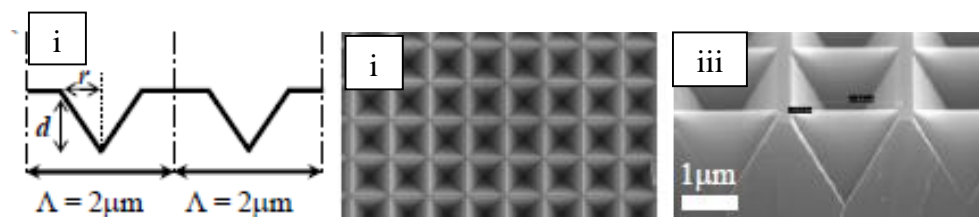


Figure 2.3 (i) schematic cross-section view through the pits with pitch=2000nm, (ii) Top view of SEM image, (iii) cross-sectional view of SEM image before metallization[13]

Other than the architecture of SERS substrate, the enhancement factor also depends on how well the molecules are adhered to substrate. In order to make a good SERS probe molecule, it must be adhered within 10nm distance from SERS substrate. For gold and silver metal surfaces, thiol molecules or triazole moieties display strong chemical affinity. Hence in order to test the efficiency of SERS substrates, two commonly used analytes are Benzenethiol (BTh) and Rhodamine 6G (R6G). Also, a self-assembled monolayer of p-mercaptoaniline (pMA) absorbed on the gold nanoclusters with different incubation time and concentration. In order to experimentally validate of the above unconventional nanoclusters and the commercialized Klarite, Raman measurement were proceeded with a 785nm excitation wavelength to quantify the SERS counts (as shown in Fig 2.4). In fact, comparing the enhancement factor of the different SERS active substrate is tricky due to the different Raman cross-section of analyte with their respective concentration and active area of the substrate. Regarding to the instrumentation, Raman intensity are highly sensitive to the magnification of objective lens, the integration time with the accumulation, the laser power and the quality of the blazed grating.

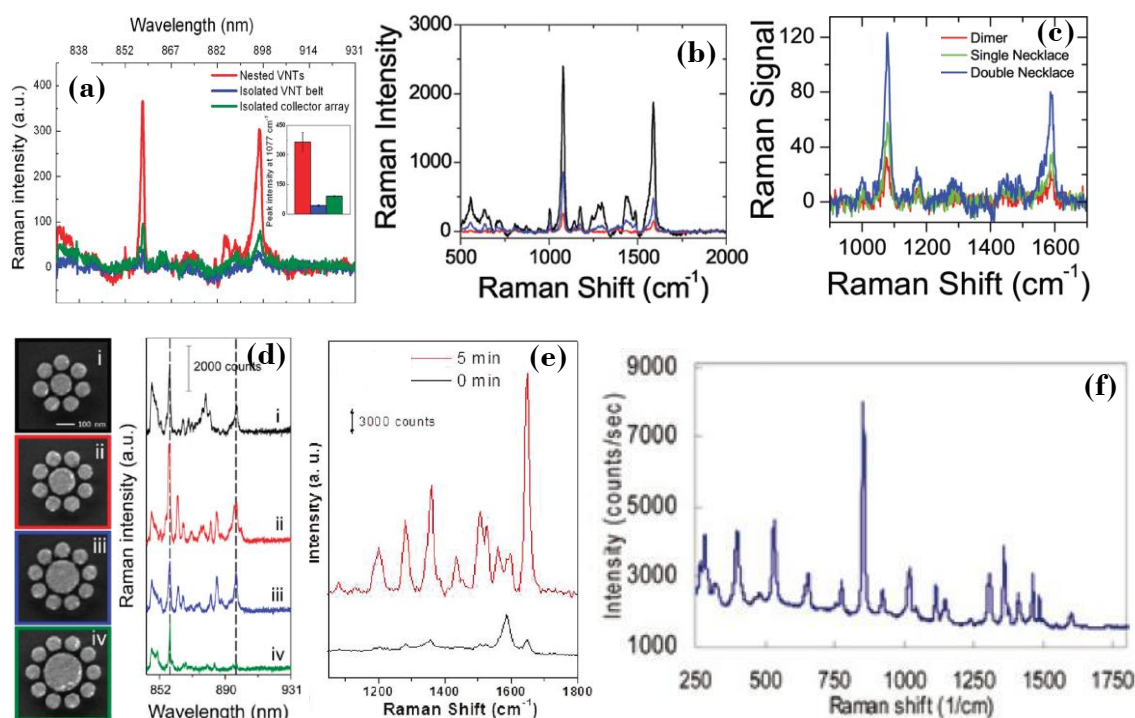


Figure 2.4 SERS intensity from different active SERS substrates: (a) Raman spectra of the analyte pMA (30minutes incubation time) on the nested VNTs substrate, (b) Raman spectra of the analyte pMA (10mM concentration with 12 hours incubation time) on the GNA substrate, (c) Raman spectra of the analyte pMA (10mM concentration with 12 hours incubation time) on the CNNs, (d) Raman spectra of the analyte pMA (5mM concentration) on the Au oligomers substrate, (e) Raman spectra of the analyte rhodamine B, RhB (10^{-5} M of RhB for 30minutes incubated) on ozone-oxidized graphene platform (red represent after 5min ozone treatment), (f) Raman spectrum of 0.5mM L-Alanine on commercialized pyramidal Klarite

2.1.2 Review on fabrication techniques for SERS substrates

There are a lot of studies on SERS substrates. There is still limitation on good reproducibility, durability, enhancement and cost so that lots of experiments are ongoing with various fabrication methods to fulfil these needs for the real applications. Some of this fabrication methodologies are electron-beam lithography (EBL)[92,93], nanosphere lithography (NSL) [94,95], electron spinning technique [96], chemosynthesis method [22,97,98], nanoimprint lithography (NIL)[99-103], scanning-probe-based lithography [104] and template synthesis technique[105]. NIL is recently developed lithography from conventional contact printing technique which can produce large-area homogenously patterned SERS active substrates and followed by physical vapour deposition for metallization. The example of scanning-probe-based lithography is dip-pen nanolithography which fabricates the structures by using point-by-point approaches so that

it will take long time to fabricate and consequently is hard to attain large area substrates as well as mass production. Moreover, there is limitation to get high aspect ratio structures. One more nanofabrication technique for SERS substrate is template synthesis technique. Template materials such as Anodic aluminum oxide and indium tin oxide are synthesized by electrodeposition or electrochemical method. This technique has been found to be low cost and high throughput for production of nanowires and nanorods arrays although challenges in reproducible fabrication. The Ag nanoparticle arrays with Nanosphere lithography indicates the electromagnetic coupling is sensitive to the nanoparticle dimension whereas in the case of Au-coated Nanorod arrays, SERS sensitivity depends on thickness of Au coating, tilt angle of oblique deposition and height of nanorod. These two mechanisms need relatively sophisticated fabrication process. Nanowire is capable of producing hotspots due to its unique geometry (high density facets). The main challenge of its implementation is difficult to produce nanowire with uniform length and diameter. In addition to the growth of nanowire, deposition of metal on nanowire is difficult. . However, these techniques are far below the development of silicon fabrication technology [3]. Therefore, if SERS substrate fabrication techniques are compatible with silicon fabrication technology, it would be possible to manufacture the inexpensive, high throughput and sustainable SERS active substrates. One successful Silicon SERS active substrate has been established is KlariteTM[13]. This is a simple fabrication technique but powerful one. In this report Klarite was therefore considered as a starting point towards the production of idealized SERS substrate.

2.2 Overview of Surface Plasmon Resonance (SPR) sensors

In 1975, D.W. Lubbers and co-workers had achieved the first optical chemical sensor for the measurement of CO₂ and O₂ concentration through absorption spectrum changes. Since then, a large variety of optical sensors have been used in chemical and biological sensing including spectroscopy, interferometry, ellipsometry and surface plasmon resonance. All these sensors are based on the measurement of changes in the refractive index, absorbance and fluorescence properties of analyte molecules. The potential of surface plasmon resonance (SPR) for characterization of thin films and monitoring processes at metal interfaces was recognized in the late seventies. In 1982 Nylander and Liedberg successfully demonstrated SPR as viable technique for biological and gas molecule

detection [106]. Since then SPR has been explored in various scientific communities as detection and imaging technique. Surface plasmon resonance, SPR sensors are optical sensors exploiting the coherent oscillation of electromagnetic waves called–surface plasmon polariton at the interface between metal and dielectric and SPR are also classified into localized surface plasmons and propagating surface plasmon[107]. As a surface-based technique SPR has shown a great promise in affinity biosensors and imaging allowing real-time analysis of bio specific interactions without the use of labelled molecules. Even though SPR based sensor technology has been commercialized, there is gap between research and application to be bridged to exploit its full potential.

SPR sensors have driven an essential role in detection and identification of chemical and biological substances and their interactions [108-114]. The SPR sensors has potential application in numerous area including:

- food safety : portable detection systems can be used to detect food borne pathogens which would benefit food producers, processors, distributors and regulator agencies
- pharmaceutical research: requires high throughput with parallel screening
- security and defense : field detection of biological warfare agents
- medical diagnostics : SPR sensors can pave way from centralized laboratories screening to selected diagnostics sensors which can be used at local clinics
- environmental monitoring: detection of pesticides in water, detection of environmental toxic, detection of spores and bacteria.

Multi channel SPR sensor which has widely importance in pharmaceutical and medical diagnostics is limited to centralized laboratory due to their huge size and power requirements. Hence require a portable SPR sensor. Over last decades various researches have proposed portable SPR sensors in combination with microfluidic channels, but resolution to determine refractive index change is far below the laboratory SPR sensors. Before prototype SPR sensors can be implemented as a field sensors the refractive index resolution and the ability to detect short oligonucleotides should match that of laboratory sensors.

2.2.1 Optical working system of a SPR sensor

Generally, SPR optical system consists of light source, SPR coupler/sensor and a detector as shown in Fig 2.5. When the beam of light is radiated to the SPR sensor, surface plasmon wave is excited and hence optically interrogated by the detector. Since the propagation constant of surface plasmon wave is always higher than that of optical wave propagation at metal-dielectric interface and thus the surface plasmon wave cannot be coupled with an incident wave at a planar metal-dielectric interface. Therefore the momentum of the incident wave should be matched with momentum of surface plasmon wave which can be achieved by via prism coupling based on attenuated total reflection, grating coupling based on diffraction on periodic metallic grating and waveguide coupling based on evanescent wave coupling between the dielectric and plasmonic waveguides.

Any coupling method (grating coupling, waveguide coupling and prism coupling) works generally with the same procedure: light source radiate to SPR coupler to excite a surface plasmon and the reflected or diffracted light is detected and analysed by the detector. Depending on which modulation approach is used, the detector records the amplitude intensity of the (reflected or diffracted) light (usually used in SPR imaging application) or its wavelength spectrum or its angular spectrum. As a change in the refractive index at the metal-dielectric interface results in a change in momentum of the surface plasmon. Any change in refractive index is measured by measuring changes in the intensity, angular and wavelength spectrum of the light coupled to surface plasmon.

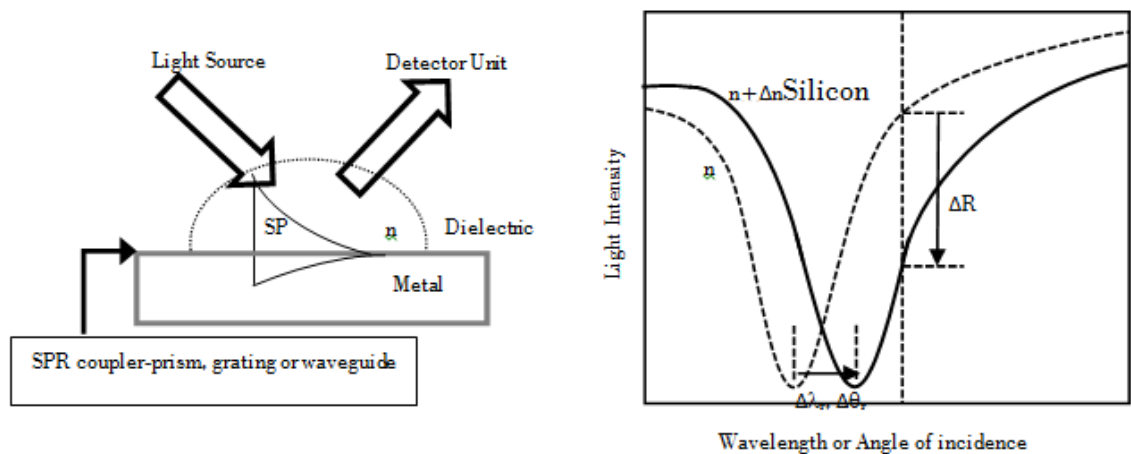


Figure 2.5 Left: General layout of the SPR sensor working system. Right: line graph shows the measured light intensity from SPR sensor with wavelength or angle modulation[115].

Main performance characteristics of SPR sensors are determined by its sensitivity, resolution, linearity, accuracy, reproducibility and dynamic range. Sensitivity is the ratio of the change in sensor output to the change in the quantity to be measured. The resolution quantifies the change in the refractive index that produces a detectable change in the sensor output. The current resolution is restricted by the properties of the surface plasmon and optical components. Hence various approaches are being investigated to tune the properties of surface plasmon. One such approach is use of hybrid surface plasmons propagating along a thin symmetric metal waveguide, which yields narrower resonances and higher sensitivity which is of significant importance in SPR sensing platform.

2.2.2 Outlook of commercialized SPR instruments

During this last decade, the trend of SPR sensor is moving towards portable and miniaturize SPR system from the lab-based systems to facilitate the detection of low-levels environmental pollutants and warfare chemicals on the fields. Some of the commercialized portable SPR sensors manufactures are:

- Texas Instrument (Spreeta)
 - 50nm Au coated Prism coupling with angle modulation
- K-MAC (Biochip Analyzer, SPRmicro)
- Seattle Sensor Systems (SPIRIT)
 - Based on Spreeta sensing chip
- Möbius advanced technology (handheld SPR)
- Sensia β -SPR system
- Biacore system

The typical refractive index resolution of these miniaturized SPR sensors is in the range of 2×10^{-6} [116] while the performance of laboratory SPR sensors is couple of order of magnitude higher 2×10^{-7} [117] and 3×10^{-8} [118]. This poor resolution makes portable SPR system less efficient the competitive labelling immunoassay systems. Other than resolution what makes the portable systems challenging is sample preparation. The most efficient solution is use of microfluidic channels but again would increase the complexity and analysis time. Currently, available commercialized SPR sensor system is the size of lunch box compared to table-top and lab-based SPR instruments. Figure 2.6 shows SPIRIT SPR system based on SPREETA sensing chip.

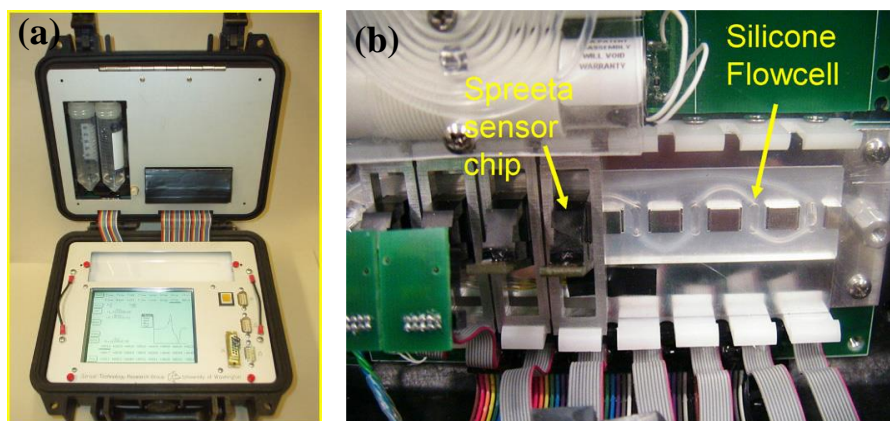


Figure 2.6 Left: outside view of SPIRIT, Right: inside view of SPIRIT with SPREETA sensor chip[116]

The portable SPR instruments comprise of a light source, optics, a fluidic cell, SPR sensor chip, a detector, and electronics for data acquisition and processing. Nowadays the commercial portable SPR devices utilize a multichannel fluidic cell in which one channel is act as reference and remaining for different analysis. This kind of cell is suitable for the several targets analysis with single injection of the sample. To use miniaturised SPR system as efficient as an field system, the sensitivity and resolution should be increased while complexity should be reduced so it can be used by non-technical personnel.

To increase the sensitivity and resolution, various methods have been proposed in the literature:

- Use of planar gold thin film ($\sim 50\text{nm}$) sensitivity as high as 620nm/RIU can be obtained
- The use of corrugated grating with prism coupling: it is theoretical possible to obtain 6 to 7 times sensitivity than thin films but practically realised sensitivity is lower (500nm/RIU) than thin films
- the use of micro holes in gold film with diameter of 500nm to $2\mu\text{m}$ which is possible to achieve 2 times that of current state of planar[119]. The excitation of holes with dove prism gives refractive index resolution (1.5×10^{-6}) equivalent to that of current state of planar thin film SPR sensors. The draw back of micro holes is slightly higher in the noise level than planar, for which efficient most signal processing may provide solutions. In addition the micro hole arrays has integration

capability with waveguides which may provide effective coupling of incoming light with surface plasmons.

- Another approach is waveguide biosensor system integrated with microfluidic channel as shown in Fig 2.7. It has been reported that this is possible to measure the concentration of antibody (*L.monocytogenes*) as low as 10^6 CFU/mL by using birefringence measurement system measuring the phase difference between two orthogonal polarization[120].

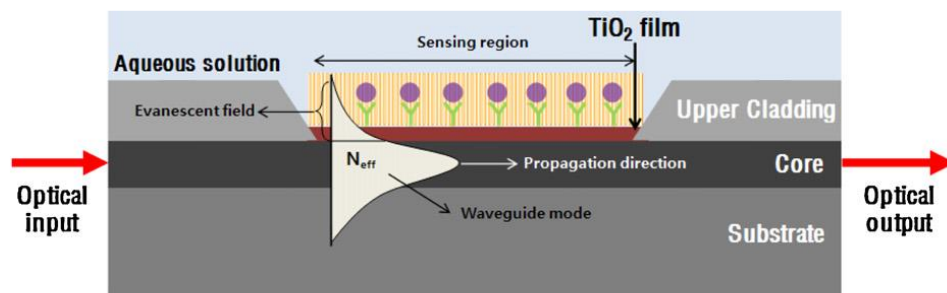


Figure 2.7 Cross-sectional view of integrated-waveguide of TiO_2 with microfluidic channel[120]

To reduce complexity, the traditionally colourmetric paper and test-strip based method with SPR sensors may provide as an alternative for very remote locations. Most available SPR sensors can be excited by single wavelength like 633nm, 850nm and 1064nm individually. Improving techniques includes of changing metal composition and structuring and coupling method to get better excitation of surface plasmon. For example, the use of chalcogenide prism with graphene multilayer (six layers) SPR sensor which can sense over a broad wavelength range in visible and near infrared regime [121]. It is possible to get increased sensitivity due to the use of graphene and detection accuracy increases much higher (100%) when silica glass is replaced by high index chalcogenide glass. The detection accuracy of this sensor in near infrared is 16 times higher than in visible region. One simple alternative way of improving SPR sensors for multiple resonance excitation wavelengths can be promised with the higher sensitivity by integrating pyramidal based SPR-like SERS sensor with waveguide. Currently our conventional rectangular based pyramidal SERS sensor has comparable sensitivity to the current commercial Klarite sensor over a broad wavelength range[122]. That is based on the low-cost imprinted disposable sensor platform[123]. After multiplexing with wave-guiding excitation of

plasmon, the system can lead to the higher sensitivity than current result due to the fine tuning of plasmon resonance. The disposable plastic SERS sensor will demonstrate as SPR sensor using the shift in wavelength specification for sensitivity.

Chapter 3. Background Theory

This chapter explores the background physics which can be applied to surface-enhanced Raman scattering (SERS) and surface plasmon resonance (SPR) sensors. Generally discussion is the Raman effect and enhancement mechanisms which are inter-related with the surface plasmon and its behaviour.

3.1 Introduction

In recent years there has been an increasing interest in detection and analysis of complex molecules such as protein, deoxyribonucleic acid (DNA), chemicals, narcotics and chemical/biological warfare agents for homeland security applications. If these molecules are present in high concentration, a technique known as Raman spectroscopy can be utilized. This involves dispensing the unknown substance on a slide or other sample holder and focusing high power laser onto it and measuring re-emitted Raman photon. Unfortunately, only one in 10^{12} photon incidence on molecule undergoes Raman scattering resulting in weak Raman absorption. An efficient technique to overcome this limitation is to utilize surface-enhanced Raman scattering (SERS) whereby molecules are placed on the surface of nanostructured metallic substrate which performs the function of transducing photon into and out of the molecules. SERS extends the scope of Raman scattering to detect molecules at low concentrations to few/single molecule level. Literally, SERS is not a technique based on Raman theory which is the first reported in 1974 by Fleischmann et al who detected pyridine on electro-chemical roughened silver electrodes, observing high count rates of vibration band of molecules (~ 500 - 1000 per second). This work is the first ever reported observation of the SERS effect. However, there are limitations for SERS technique to be commercialized mainly due to reproducibility/repeatability with high enhancement Raman amplification, comparably cost-effective high throughput manufacturing, easy disposable and reusable. Over the years, different architectural design and material have been researched to seek the possible solution to fulfil these limitations. SERS enhancement depends significantly on the characteristics of excitation laser (wavelength, polarization and angle of incidence), detection mechanism, surface material (usually gold or silver), surface morphology, geometry, analyte properties (molecular affinity for surface), surface coverage and distance of molecule from the metal surface.

However, the exact origins of SERS enhancement from these factors are a topic of current debate.

SERS technique provides the fingerprint of the test molecules and it can work well with many excitation wavelengths provided when an appropriate substrate is used as base of the molecule whereas this would not be feasible for IR/Near-IR spectroscopy and fluorescence technique. Moreover SERS would require less to no sample preparation and can be inherently used to study plasmon behaviour of metallic substrates. This vast potential makes SERS attractive to real world and research applications in optics, biology, chemical analysis, homeland security, medical science and forensics.

3.2 What is Raman scattering/Raman effect?

The process involves the simultaneous absorption of an incident photon and emission of another photon is called a scattering process where the emitted photon is called a scattered photon. There are two types of scattering such as elastic and inelastic scattering. For elastic scattering (as shown in Fig 3.1) incident and scattered photons have the same energy but different direction and/or polarization. Elastic scattering leaves the molecules in the same energy level after scattering have occurred meaning that no transfer of energy happens between the molecule and photon. The elastic scattering is also known as Rayleigh scattering.

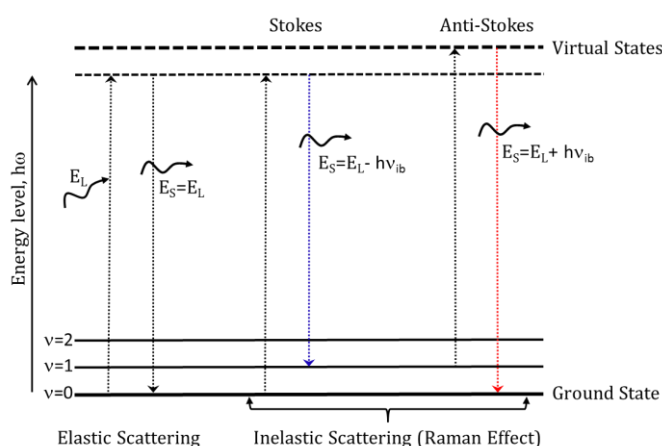


Figure 3.1 Energy level diagram involves in Rayleigh scattering, Stokes and Anti-Stokes Raman scattering. A photon with energy E_L excites the vibrational modes of molecules.[14]

In an inelastic scattering, the scattered photon and incident photon has different energy. The most important form of inelastic scattering in molecules is Raman scattering which involves transactions between the vibrational/rotational levels. Raman scattering is similar to fluorescence but an incident photon is replaced by a scattered photon or fluorescence photon. The main difference is that Raman scattering processes are instantaneous while fluorescence involves an intermediate step which is electronic excitation followed by emission with a finite life time. Raman scattering can happen without direct absorption of the photon (as required for fluorescence). It can also occur even when no electronic transitions exist in the molecule at the incident wavelength however it is a weak phenomenon under typical condition. Alternatively, from a quantum mechanical view, Raman process is considered as two separate steps: absorption of the incident photon and spontaneous emission of the scattered photon. There is an intermediate virtual state (Fig 3.1) to depict a higher energy level in order for optical absorption to occur. If the intermediate virtual state coincides with one of the real electronic (vibronic) levels in the molecule, resonant scattering can occur. Such resonant effects can increase the scattering efficiency by several orders of magnitude. In the case of $E_S < E_L$, a molecule is excited from the ground state to a higher energy level ($E_L - E_S$) and after short period in the higher energy level, relaxed to the vibrational energy level and this is called Stoke process. Therefore in stoke process, a photon is losing energy to the molecule's vibration, the frequency decreases and the wavelength increases. In the case of $E_S > E_L$, the molecule has relaxed from an excited vibrational state ($v=1$) to vibrational ground state ($v=0$) and hence the energy of vibration $h\omega_v = E_S - E_L$. This reverse process is called Anti-Stoke Process. The energy lost by the photons in the scattering event is called Raman shift and defined in energy as $\Delta E_R = E_L - E_S$. Therefore, positive Raman shift represents Stokes event and negative Raman shift for Anti-Stokes events[14]. The Raman shift is expressed in wavenumbers and in units of " cm^{-1} ". The Raman scattering is weak due to the low absorption cross section, between 10^{-31} and $10^{-29} \text{cm}^2/\text{molecule}$. Therefore, surface-enhanced Raman scattering become alternative technique to amplify the Raman effect. Raman output is also determined by the lattice energy and volume of material.

3.3 Surface-enhanced Raman Scattering

The Raman effect can be amplified by the several orders of magnitude using the metallic roughened electrodes where the molecules was attached. This technique was discovered by Fleischmann et al. Since then many researches on SERS have been processed to achieve the unique roughness and SERS is believed to be used as an enhanced mechanism for Raman analytical technique investigating the identification of fingerprints of molecule absorbed on a metallic nanoparticles or structured metallic substrates. From the literature review, it is observed that large enhancement is highly dependent on the roughness, particle/structural shape, size and separation between the structures. In this work, the structure has been optimized to tune a specific resonance (generally for common Raman excitation wavelength) by coupling the incident light to a resonant plasmon. Moreover the metal roughness inside the cavity creates an additional local electric field enhancement to amplify the Raman scattering.

It is widely suggested from current theories that Raman scattering has been enhanced from two contributions such as electromagnetic field effect and chemical effect. The electromagnetic enhancement is much higher than the chemical enhancement[124]. The electromagnetic effect is intimately related to the surface plasmon behavior of the structure. Therefore the surface plasmon and surface plasmon resonance has been described before going to the enhancement mechanisms.

3.3.1 Surface plasmon and surface plasmon resonance

The term ‘plasmon’ was first used by Pines in 1956 to denote collective oscillations of electrons which resemble plasma oscillation observed in gaseous discharge[125]. In SERS, a plasmon is a quantum quasi-particle of the charge density oscillation in the metal [126]. As plasmon is a quasi-particle it is always lossy and highly interacting. If not maintained by an external source of energy it will start to decay exponentially due to its nature of quasi-particle. At the metal-dielectric interface, the longitudinal oscillations of charge density are called surface plasmons. Surface plasmon polaritons are a particular type of electromagnetic wave that is propagating at an interface of metal and dielectric media due to their interaction with the free electrons of the metal. This surface plasmon wave (SPW) is a transverse magnetic (TM-polarized) with magnetic vector parallel to the plane of

interface. These evanescent field vectors of SPW reach their maxima at the interface and decay exponentially into both media such as in the metal it extends to the negative z region and has a negative and real dielectric constant ϵ_m and in the dielectric it extends to the positive z region and has real and positive dielectric constant ϵ_d . SPW is characterized by its propagation constant and electromagnetic field distribution.

$$\beta_{SP} = \frac{\omega}{c} \sqrt{\frac{\epsilon_m \epsilon_d}{\epsilon_m + \epsilon_d}} \quad (3-1)$$

β_{SP} is the propagating constant of SPW along a planar boundary between the semi-infinite metal with a complex dielectric constant ($\epsilon_m = \epsilon'_m + i\epsilon''_m$) and a semi-infinite dielectric with a refractive index, n . ω is the angular frequency, c denotes the speed of light in vacuum. This equation denotes that a SPW can exist at metal-dielectric interface if the real part of ϵ_m is negative and its absolute value is smaller than refractive index of the dielectric medium. At optical wavelengths, this condition is satisfied by metals like chromium, gold, silver, aluminium, platinum and palladium. Among them, gold and silver are widely used due to excitation of plasmon at visible and near-infra red range because this wavelength laser is readily available.

This resonant interaction between the surface charge oscillation and electromagnetic field of light constitutes surface plasmon polariton and hence gives rise to unique characteristic like helping to concentrate and channel light using subwavelength structures formed by the different relative permittivity of the metals and neighbouring non-conducting media. Guiding light in this way results in an electric field enhancement that can be used to operate light-matter interactions allowing the advance of new sensing methods such as surface-enhanced Raman scattering, SERS and surface plasmon resonance, SPR. For example, metallic structures much smaller than the wavelength of light are essential for the massive signal enhancement achieved in SERS. Here two types of plasmons are concerned and known as delocalized and localized plasmons. The delocalized surface plasmon polaritons, SPP freely propagate over the top surface of the sample which is excited through the periodicity of the surface and its energy highly depends on the incident angle and the sample orientation as shown in Fig 3.2. The localized plasmons are the electric field distributions confined inside the cavity and hence it is expected to be independent of sample orientation and incident angle. Figure 3.2 gives the geometrical representation of

localized and delocalized plasmons on the nanostructures and their reflection spectra relates to the sample orientation.

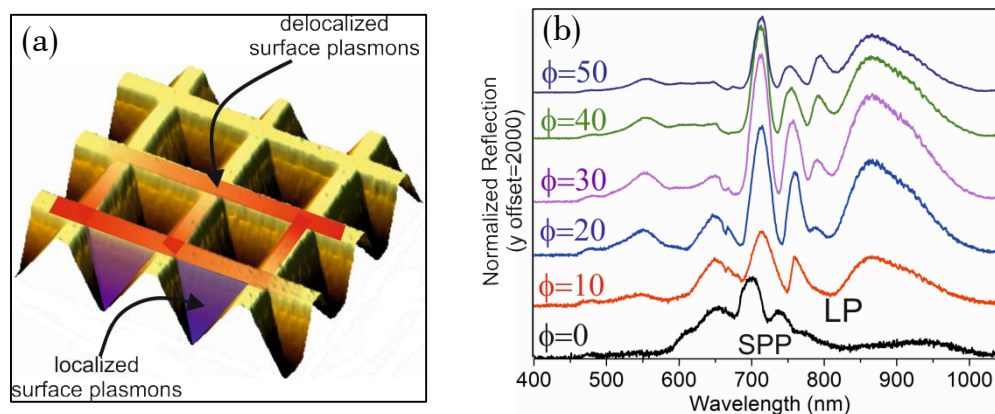


Figure 3.2(a) Illustrative representation of localized and delocalized plasmons on the SERS active nanostructure. (b) Reflection spectra taken on gold coated inverted pyramidal structure with 1250nm pit size. Incident angle is set to 3° and sample orientation is varied by 10° as shown, spectrum is vertically offset by 2000.

3.3.2 Enhancement mechanism

Two enhancement mechanisms which are contributed to the enhancement of Raman scattering; electromagnetic field localization and chemical enhancement have been discussed.

3.3.2.1 Electromagnetic enhancement

When the nanoparticles are exposed by a laser, the electron cloud (Plasmon) is displaced from the respective nuclei, as a counter active force arising from the Coulomb interaction between the electrons and nuclei that leads to the oscillation of electron cloud relative to the nuclei. This collective oscillation of the electrons is called the dipole plasmon resonance of the particle in Fig 3.3 (a); this excitation that can occur in bulk metal or metal surfaces. Surface plasmon resonance can either be propagating (for example, on the surface of a grating) or localized (for example, on the surface of a spherical particle). Surface roughness or curvature is required for the excitation of surface plasmon by light because the electric field can be more confined on that kind of surface compared to smooth surface. The electromagnetic field of the light at the surface can be greatly enhanced under

conditions of surface plasmon excitation by amplifying both the incident laser field and the scattered Raman field through their interaction at the surface, so called electromagnetic SERS enhancement. Excitation of the surface Plasmon greatly increases the local field experienced by a molecule adsorbed on the surface of the particle. Since the Raman intensity of a molecule varies with local field enhancement (excitation) and radiation enhancement (re-emission), enhancement factor is considered as

$$EF \approx \frac{|E_{Loc}(\omega_L)|^2}{|E_{Inc}|^2} \frac{|E_{Loc}(\omega_R)|^2}{|E_{Inc}|^2} \quad (3.1)$$

Since the Raman shift is small and an approximation is made that $\omega_R \approx \omega_L$ and the enhancement factor becomes

$$EF \approx \frac{|E_{Loc}(\omega_L)|^4}{|E_{Inc}|^4} \quad (3.2)$$

This enhancement factor is electromagnetic enhancement factor. This EF can be limited by excitation wavelength, mode vibrational energy, molecular orientation, scattering configuration and the substrate orientation with respect to incident polarization [127]. Also this enhancement decreases as $[r/(r+d)]^{10}$ for a monolayer of molecules where 'r' is radius of sphere and 'd' is the distance in z-direction. If the radius of curvature, r (sphere) is bigger, the starting point of the fall off distance will be long-ranged whereas for small radii, it can be near surface effect. Although the enhancement factor can be optimized with larger radius, other factors (particle size, shape and particle morphologies and their inter-particle distance and coupling effect and so on) should be taken into account during preparation of SERS substrate[128].

3.3.2.2 Chemical enhancement

It is very difficult to study the chemical enhancement mechanism compared to the electromagnetic enhancement for two reasons: first, its enhancement is small (10^1 - 10^2) compared with the factor of electromagnetic enhancement (10^4 - 10^7). Second almost any experimental parameter will influence both mechanisms, making the separation of effects difficult. Even though electromagnetic mechanism is a non-selective amplifier for Raman scattering, the molecules CO and N₂ give a difference in a factor of 200 in their SERS intensities. The highest occupied molecular orbital (HOMO) and the lowest unoccupied molecular orbital (LUMO) of adsorbate are equally formed in energy with respect to the Fermi level of the metal. When the molecule gained the energy of half the intrinsic intra

molecular excitation from an incident laser, the charge transfer is occurred either from the metal to the molecules or vice versa as shown in Fig 3.3 (b).

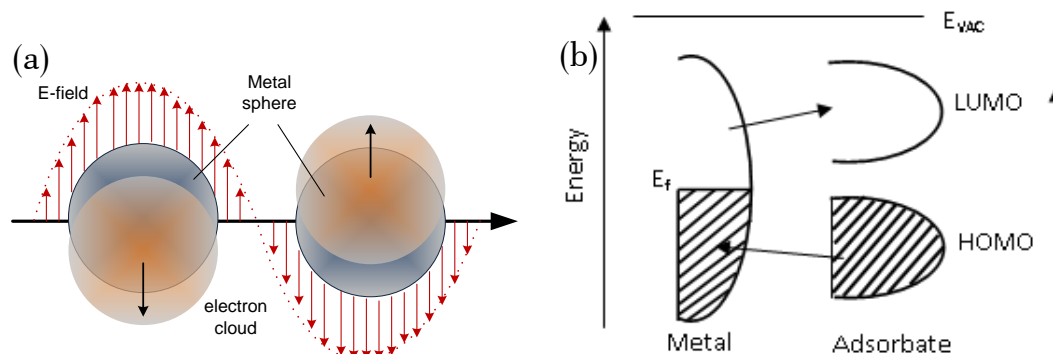


Figure 3.3 Surface-enhanced mechanism: a) electromagnetic enhancement, b) chemical enhancement

The chemical enhancement depends not only on pure intra-molecular interaction, but also on other factors like screening, orienting, damping properties of the metal surface [128]. Furthermore, the surface bonding and their effects (smooth, uniform and very stable structured surfaces) on the electronic structure of the adsorbate are critical in determining chemical enhancement.

Other than chemical enhancement and electromagnetic enhancement there are few other factors which influence the SERS enhancement. Some of these factors are given below

- Characteristics of the laser excitation e.g. wavelength, polarization, angle of incidence
- Detection setup, e.g. scattering configuration (back scattering configuration), solid angle for collection, polarized and/or unpolarized detection
- SERS substrate, e.g. material (usually silver or gold), geometry orientation with respect to incident beam direction and polarization, and refractive index of the environment, the dimensionality of the substrate
- Intrinsic properties of the analyte, e.g. Raman polarizability tensors of the modes
- Analyte adsorption properties, e.g. adsorption efficiency and analyte concentration (surface coverage), distance from the surface, adsorption orientation (fixed or random) [127]

This work will focus on the factor of SERS substrate and analyte adsorption properties.

3.3.3 The Various Metals used in SERS

In general two metals gold and silver are widely used for SERS and plasmonics due to their inherent optical properties to maintain good plasmon resonances in the visible/near-infrared range which is the most interesting range for SERS. In the case of amplification, the flat metallic surface is lower than the rough metallic one, this effect was observed in copper and platinum also but lower than silver or gold.

A metal is suitable to observe SERS effect if it satisfies these criterions:

- The real part of dielectric function $\text{Re}(\epsilon)$ should be negative in the visible and infrared region of spectrum.
- The imaginary part of dielectric function $\text{Im}(\epsilon)$ should be within the range of interest 600nm-800nm which is compatible with the commercially available Raman system.

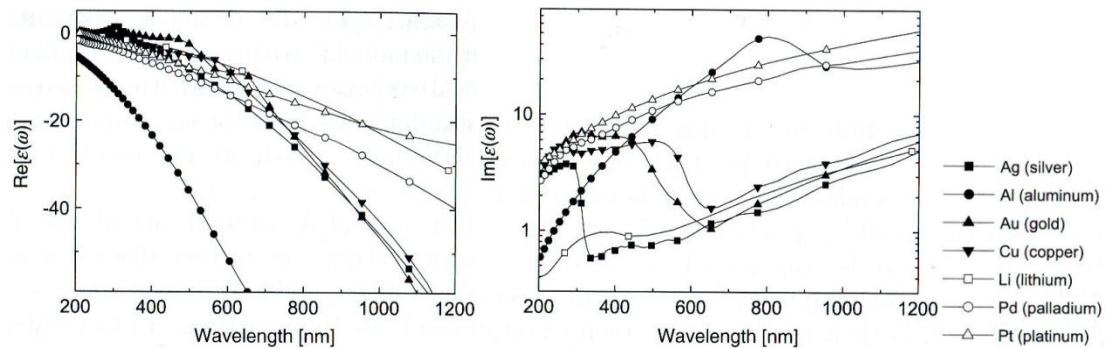


Figure 3.4 Optical properties of metal in visible range[129]

From Fig 3.4, it is evident that number of metal particles such as aluminium, palladium and platinum can be ruled out from the group of metals suitable for SERS detection in the range of interest (600nm-800nm). The latter two present too much absorption, while aluminium would only be suitable for applications in the UV. These metals do show a good metallic behavior including their optical properties but are not expected to exhibit any plasmonic properties. It means that, SERS has been observed on these, but the enhancements are either ‘chemical’ or small electromagnetic enhancements not arising from plasmon resonances[127].

Among all metals, silver is a promising candidate and has been widely used for SERS and plasmonics applications. Gold and copper also exhibit plasmon resonance, but only at wavelengths greater than $\sim 600\text{nm}$. At such wavelengths, the plasmon resonance of gold becomes comparable to that of silver. The main difference between gold and silver is the presence of inter-band transitions for gold. It increases the real part of dielectric function in the region where plasmon resonances have occurred, and hence shifts them to longer wavelength compared to silver. The inter-band transition also increases the optical absorption in the near infrared region, and make the optical absorption much larger for gold than for silver in the region where $\text{Re}(\epsilon) < 0$. It is observed that higher absorption for gold at $\lambda < 600\text{nm}$ provides more 'lossy' plasmon resonances that lead to fewer enhancements. But this is no longer true at longer wavelengths, typically $\lambda > 600\text{-}650\text{nm}$. Therefore gold should produce comparable plasmonic properties as silver particularly for local field enhancement in the longer wavelength range. Finally, some alkali metals like lithium also exhibits resonance across the whole visible range, but has not been used widely over the past as lithium reacts easily with water and is scarce in nature due to its strong chemical activity. Silver is a good candidate as plasmon active material but it has oxidation issue resulting in poor stability and lower bio-compatibility. Moreover, practical issues like ease of manipulation, especially for the fabrication of nanostructures, cost, toxicity, availability and durability must be taken into consideration. Therefore gold seems to be the most suitable plasmon-supporting material [130].

Chapter 4.

Tools for assessing the behaviour of SERS active substrate

This chapter discusses the main tools which were used for evaluation of the sensor's behaviour in terms of optics, particularly behaviour of surface plasmons. A large part of this study was carried out by simulation. Here the designs were defined and the figure of merits was explained in dispersion map. Secondly this chapter mentions that how the optical measurement can be carried out experimentally using a bespoke reflectometry system after the sensor is fabricated. Finally the section ends by describing how the sensor sensitivity is evaluated with Raman spectroscopy and test molecule coating method for the Raman measurement.

4.1 Design and simulation

Direct computation of the plasmonic properties as a function of angle of incidence for broadband wavelength range taking into account absorption and dispersion properties of metals remain challenging for currently available simulation software. In particular, the simulator hardly recognises the small features of the sensor when run under conditions of low computational cost and time. For example, Lumerical FDTD solution requires small mesh with very long computation time to define the exact structure of the sensor surface and does not allow illumination of the sensor with broadband light for a range of incident angles within a single simulation run. Fortunately RSoft DiffractMOD can satisfy those requirements with relatively low computational cost using multi-variable optimization and scanning tool (MOST).

This section discusses the design and simulation models developed for inverted pyramidal SERS sensor using the commercialized photonic suite, RSOFT DiffractMOD which employs Rigorous Coupled Wave Algorithm (RCWA)[seen in Appendix A] to obtain the backward diffraction efficiency using the periodic boundary condition. The sensor features a 3D pyramid which is inverted and makes it arrays on the silicon substrate with different spaces between each pyramid. As a plasmon active layer, gold is angle deposited on the structures and then the laser (with broadband range) is illuminated at the opening of the pyramid. The optical property of gold has been used from built-in material database of the

simulator as shown in Fig 4.1. The three dimensional sensor without gold coating is first designed for the various pyramids with the different depths and line width to study the interaction of light with the inverted pyramid on silicon platform. The different thickness of gold are then coated on the structure and collect the zero order diffraction of the inverted pyramidal sensor to observe the contribution of plasmons with the different thickness of gold, for which their localized e-fields are believed to be important for SERS enhancement. From the observation of the spatial electric field and its related plasmon resonance, the geometrical parameters of inverted pyramid would be optimized for the surface plasmon resonance, its energy and hence SERS enhancement factor.

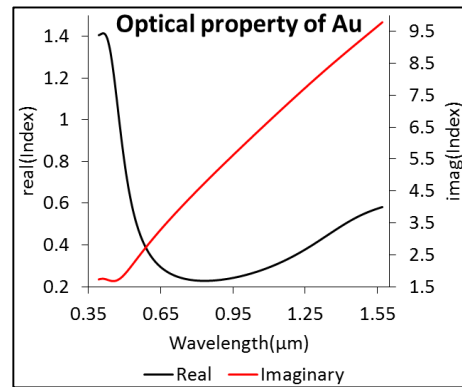


Figure 4.1 Optical properties of gold in visible and near infrared region

After achieving the optimized inverted pyramid on the silicon platform, the simulation is run for the optimized design on the plastic platform (PMMA substrate) in order to examine whether plastic platform sensor can achieve the same or better enhancement since the plastic platform sensor would be easy for large area fabrication with low cost and be flexible in handling and disposable easily after every use.

4.1.1 Design considerations and simulation parameters

The sensor is designed from the starting point of a commercialized Klarite™SERS sensor, featuring a square based inverted pyramid array with gold coating. As shown in Fig 4.2, the sensor is a form of inverted pyramid which has the geometrical parameters in nanometer scale naming Pitch, Pit size and depth corresponding to the pit size. The Klarite is composed of 2000nm pitch length and 1500nm pit size on the square base aspect ratio (width: length). In this thesis, the inverted pyramids are designed by varying their geometrical parameters such as: pit size ranges from 500nm to 2500nm, pitch starts from 1000nm to 3000nm and the depth is formed according to the relationship: $depth = \tan 54.7^\circ \times \frac{1}{2} \text{ of pit size}$ (the angle is measured from the wet etch of 100 silicon plane). Also those sensors are designed for the different aspect ratio (width: length) such as square (1:1.0) to rectangle (1:1.3) increased by 0.1 in the length (1:1.0, 1:1.1, 1:1.2, 1:1.3). For clarification of the different designs of inverted pyramid, a schematic diagram for all geometrical variations is shown in Fig 4.3. These dimensions and parameters were chosen to achieve a SERS sensor from the electromagnetic enhancement mechanism which can provide higher sensitivity and compatibility with the readily available Raman laser. As shown in the layout (Fig 4.3), there are four groups of matrix corresponding to the different aspect ratio: each group consists of the various inverted pyramidal arrays changing the pitch length with pit size. Each block contains an array of inverted pyramid specified by pit size and pitch length as shown in inset of Fig 4.3. The grey colour scale in schematic layout represents the scattering intensity varied with different pit sizes.

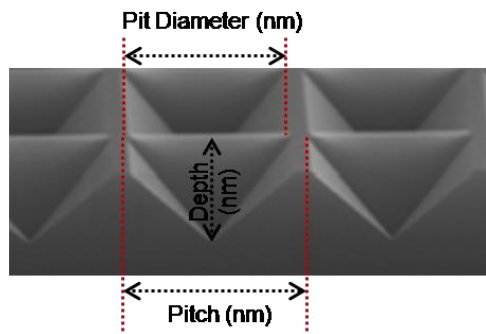


Figure 4.2 SEM image showing the definition of geometrical parameters

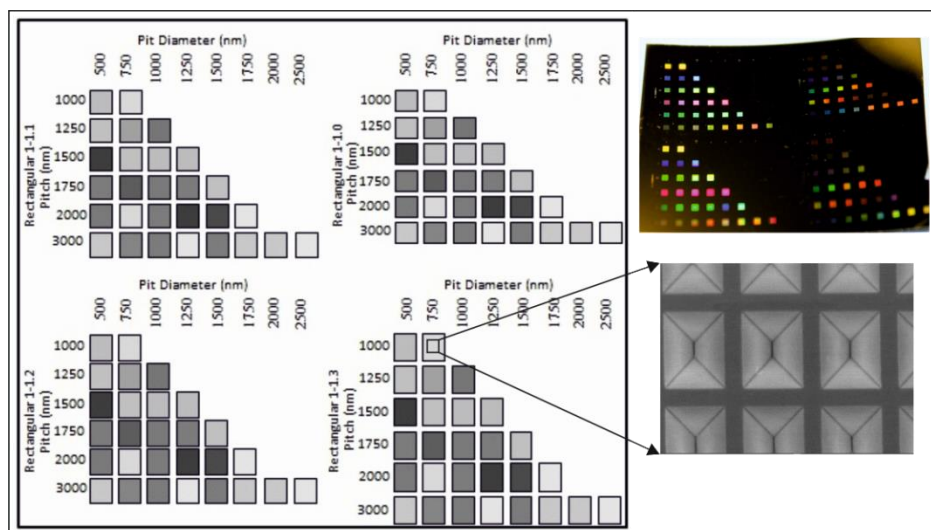


Figure 4.3 A schematic layout for microscopic view of generation-1 chip; different grey scale represents the change in scattering intensity due to the different pit size. Changes in absorption intensity can be seen in the photograph of the fabricated chip after gold coating: chip dimension is 3.8cmx3.2cm

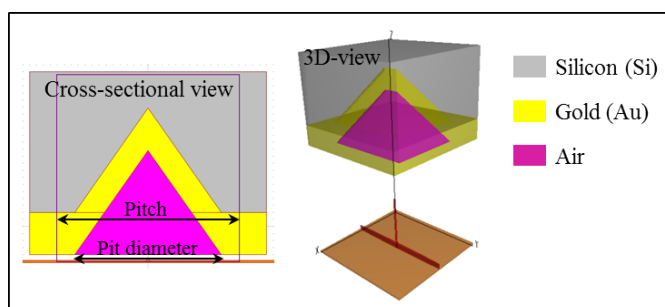


Figure 4.4 A picture for simulation design for the gold coated inverted pyramid showing the cross-sectional and 3-dimensional views: Light is launched from the bottom/opening of the pyramid.

Figure 4.4 shows the cross-sectional and 3-dimensional views of the rectangular pyramid design after gold coating. Since the aspect ratio is rectangular the longer side of the pyramid is truncated in design (as shown in 3D-view) due to the limitation of KOH wet etching. DiffractMOD treats a unit cell (each inverted pyramid) as a periodic array and uses a transmission line formulation for boundary conditions. The z-direction is defined as the launch field (as shown in 3D view). The polarization is mainly set up for TM-polarization since the plasmon is excited when the electric field is perpendicular to the interface of the inverted pyramid. The dispersive properties of the gold are included in a built-in material database within RSoft simulator and the optical properties of the silicon are taken from [131]. The simulation results shown here are for rectangular aspect ratio

1:1.2 unless otherwise stated and hereafter the geometrical parameters, pitch is denoted as “P” and pit width is termed as “D”. The simulation is run to collect the zero order diffraction (specular reflection) spectra from the inverted pyramid for all incident angles (0° to 70°). The input light source is defined to be a broadband excitation wavelength ranging from 400nm to 1500nm.

A dispersion map (e.g. Fig 4.5) is formed by mapping a group of graphical data (reflection efficiency vs wavelength) for various incident angles together in a single colour map. Wavelength varies along the y-axis and the incident angle varies along the x-axis. The reflection efficiency is represented on the plot in terms of colour ranging from dark blue to dark red. The dark blue relates to plasmon/high absorption due to the electric field being concentrated at the interface between dielectric and metal. Dark red corresponds to entire/high reflection. Figure 4.5 describes the transformation of graphical data to the reflection map. This kind of reflection map allows easy identification of diffraction, non-dispersive localized plasmon and propagating plasmon properties since the localized plasmon has flat band and does not vary with incident angle while the propagating plasmon has sharp narrow band and varies with incident angle.

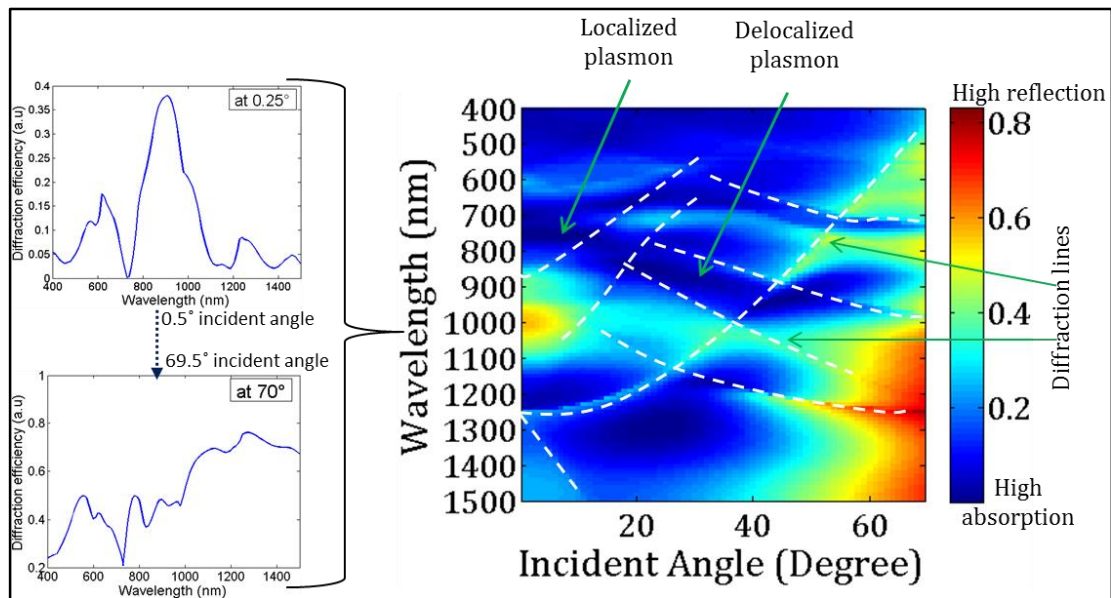


Figure 4.5 Transformation of graphical data to a reflection map. a) showing reflection efficiency as a function of wavelength for each angle (0.25° - 70°); b) the dispersion map of (a) with identification of localized Plasmon, propagating Plasmon and the subtle diffraction features

4.1.1.1 Polarization definition

Understanding the polarization in relation to the structure will give a hand in the understanding and interpretation of the reflection map and plasmonic behavior. Figure 4.6 shows a top view of a rectangular inverted pyramid with a guidance of e-field direction for different polarizations at normal incidence ($\theta=0^\circ$) and azimuth angle, ($\phi=0^\circ$). For TE-polarization, the wave of e-field is perpendicular to the incident plane and the charge oscillation occurs across the sidewalls C to D while for TM-polarization the wave of e-field is parallel to the incident plane and creates charges between the sidewalls A and B. Since the rectangular inverted pyramid is asymmetric, the electric-field density and hence the diffraction efficiency is sensitive to the polarization state while the square inverted pyramid is less sensitive to polarization due to the symmetric structure. For TM-polarization state, the interaction of incident light to the inverted pyramid allows e-field charge oscillation over the short distance between sidewall A and B. This interaction would be expected for all specular incident angle (θ), up to $\theta=70^\circ$. This can't happen for all specular angles in TE-polarization because the charge oscillation passes through the longer distance from the sidewall C to D. This results in a reduction of electromagnetic interaction as the area subtended by the incident light varies with incident angle, providing high reflectivity for incident angles larger than 60° .

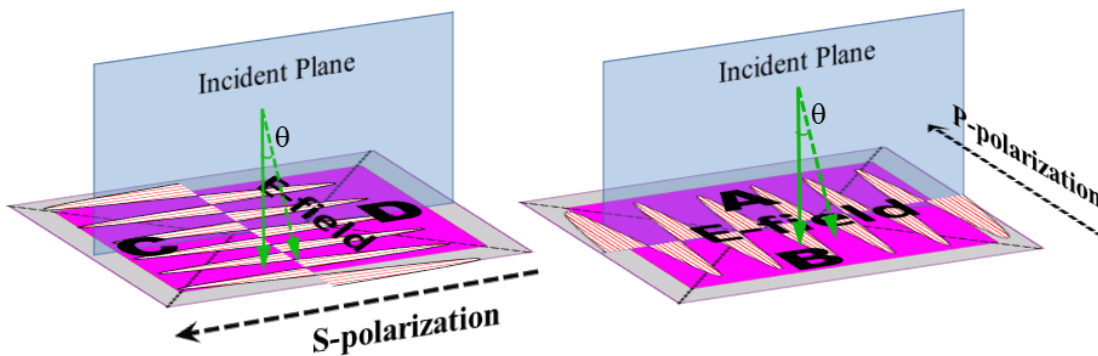


Figure 4.6 Diagram showing the charge oscillation direction under different polarization state

For example, the difference in e-field between TE and TM polarizations for square and rectangle aspect ratio inverted pyramids is shown in Fig 4.7. As expected the e-field density is different for TE and TM polarization due to the non-symmetry of the lattice

structure for the rectangular inverted pyramid but have same e-field density in the case of square base structure due to the symmetry of the lattice structure. However the field orientation is orthogonal to each other due to the direction of incidence.

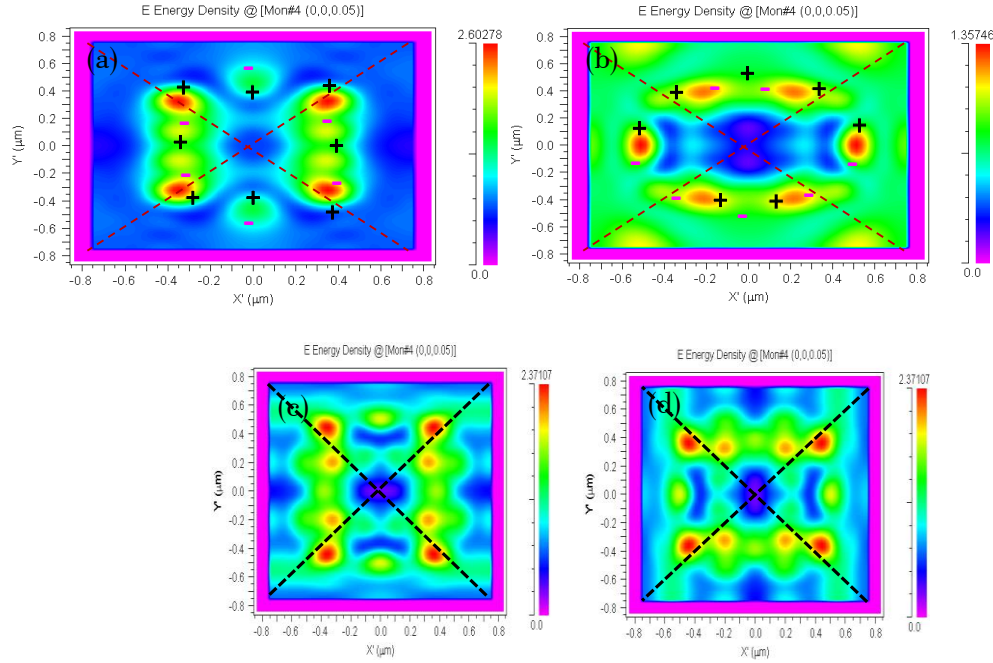


Figure 4.7 Simulated normalized electric field of gold coated inverted pyramid (top-view) at 785nm excitation wavelength: a) TE- polarization (rectangular aspect ratio), b) TM-polarization (rectangular aspect ratio), c) TE-polarization (square aspect ratio), d) TM-polarization (square aspect ratio).

4.2 Optical measurement using a bespoke reflectometry system

This section describes an automated experimental reflection system which was used for measuring the specular reflection, giving information associated with dielectric photonic crystals or surface plasmon polariton dispersion corresponding to the nanostructure metallo-dielectric surfaces. This fully automated system employs a broadband spectroscopic reflectometry method to acquire polarization resolved data. This measurement system can also be used for analysis of waveguide grating couplers, mapping far field profiles of LEDs, mapping angular absorption properties of solar cells. This bespoke system was built by Dr. Martin D.B Charlton and programmed using LABVIEW by Dr. Michael E. Pollard.

The experimental setup is comprised of the broadband laser source (Fianium), a computer controlled motorized stage (Newport), a spectrometer (BWTEK-visible range), a set of motorized polarizers, a focusing lens placed before a silver mirror which focus light onto a sample mounted on computer controlled rotation and positioning stages. The reflected signal is collected by a moving fiber detector, which has collimating lenses placed in front of the detector. An overview of the setup is shown in Fig 4.8(a).

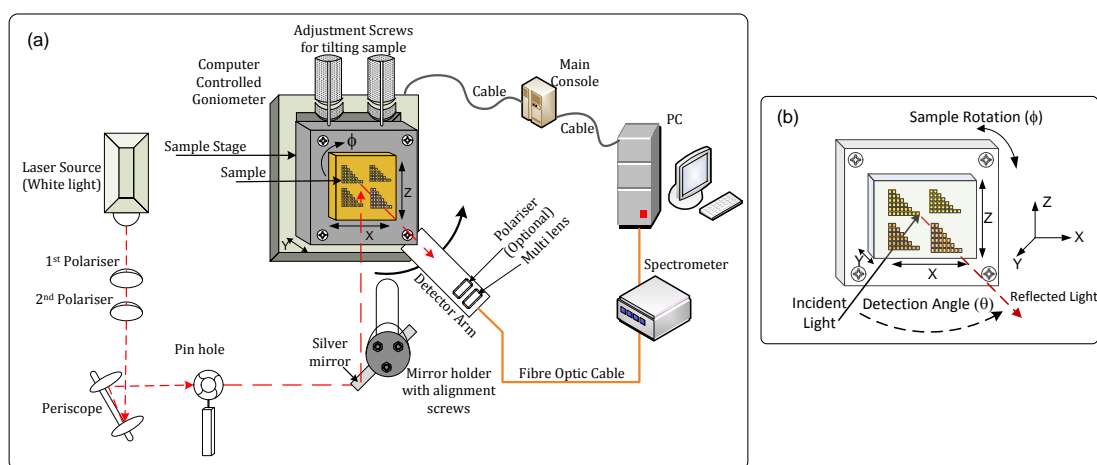


Figure 4.8 (a) Schematic diagram for a fully automated reflectometry system (red dotted line represents the incoming light source and orange straight line refers to the collection of light by the spectrometer (b) Sketch shows the sample stage geometry in which θ and ϕ are defined as the collection/detection angle and azimuthal angle/sample rotation respectively while X, Y and Z are defined as the three dimensional movements.

The desired polarization(TM/TE) and power level can be set from the software by controlling a pair of polarizers. The 1st polarizer controls the laser power while 2nd polarizer sets the polarization state. The beam path is fully aligned at each step of the system (incoming/out coming beam paths) and this alignment procedure is very tedious and tricky for samples like photonic crystals. The sample is loaded at the sample stage as shown in Fig 4.8(b), and the sample can be shifted in three dimensions X, Y and Z as well as it can be rotated in azimuth angle rotation, ϕ in both direction. The tilt of the sample can be controlled either by manually adjusting the two screws located at the top of the sample stage or by automatically rotate the motor via software. The reflection is collected by rotating the detector arm with the detection angle starting from 0° to 180° which is twice the incident angle. Reflection results are plotted as a color map of intensity as a function of incident angle over a visible and near infrared range due to the limitation of the

spectrometer. The spectra are normalized to the reflection off unpattern gold for all respective incident angle and polarization to remove the effects of the absorption of gold and to enhance the plasmonic features.

4.3 Raman measurement protocol

In order to investigate the sensing ability to test molecules from the plasmon enhanced Raman mechanism of the inverted pyramidal structures, Raman measurement is carried out using a RENISHAW Invia Raman Spectrometer system. All Raman measurements are taken at 785nm unless otherwise stated and all the collected spectra are baseline corrected to reveal the absolute Raman counts of the vibrational structure of test molecules. It is generally believed that by improving the coupling between surface plasmon polaritons and incident photons, Raman signals can be amplified by several orders of magnitude. This can be done using surface-enhanced Raman scattering, active nanostructures. A standard test molecule is needed for this purpose. Figure 4.9 shows the Raman fingerprint of benzyl mercaptan test molecule from the rectangular based pyramidal SERS substrate and EF provides 10^9 . This example spectrum is obtained from inverted pyramidal area and the unpatterned gold area, meaning that the e-field trapped inside the inverted pyramid (called localized plasmon or mix plasmon mode) amplifies the Raman scattering interaction with the molecule resulting in the significant Raman signature of molecules while the unpattern gold surface gives no information about the molecules for the low concentration. The gold coating is uniform enough to avoid any SERS signal from the unpatterned surface due to the random hot-spot. The geometrical parameters of the inverted pyramid which is the reason for tuning/controlling the diffraction and hence the plasmons increase the Raman scattering process, will be characterized through the analysis of the Raman response of test molecules at the Raman vibrational frequency of 990 cm^{-1} - 1010 cm^{-1} which is a trigonal Ring breathing of mode of test molecules.

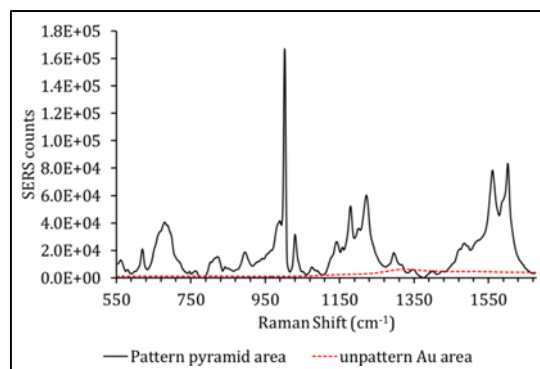


Figure 4.9 Comparison of Raman spectrum for benzyl mercaptan molecule between the inverted pyramid area and the unpattern area

4.3.1 Test Molecule Coating

The SERS substrates in this report are coated with two types of thiol molecules. One is benzyl mercaptan ($\text{C}_6\text{H}_5\text{CH}_2\text{SH}$) with an hour incubation time, prepared at the university laboratory and another is a benzenethiol ($\text{C}_6\text{H}_5\text{SH}$) test molecule with 24 hours (overnight) incubation time, carried out at RENISHAW Diagnostics, Glasgow. But the coating method is the same in such a way that making 5mM solution in ethanol in which substrates are kept with the dedicated incubation time, allowing the SH group to bind with the gold surface as a closely packed monolayer. The excess molecules are then washed off by thoroughly rinsing in ethanol solution. Although samples are coated with different molecules, the relative assessment of SERS enhancement is still conducted by analysing SERS counts of trigonal ring breathing (990 cm^{-1} - 1010 cm^{-1} Raman shift) since both molecules are from the same group of thiols.

4.4 Conclusion

This chapter introduces three subjects. First the modelling and the simulation are described using the commercially available RSoft photonic and followed by the how the results will be collected and assessed for the plasmon behavior and e-field density related on the polarization status. Second the function of the experimental reflectometry system is discussed. Finally the testing parameters for the Raman spectroscopy and the way of test molecule coating are discussed.

Chapter 5. Inverted Pyramidal SERS sensor: Silicon Platform

This chapter discusses the fabrication process in detail for the inverted pyramidal SERS sensor based on a silicon material platform. Design and simulation of the sensor for with and without metallization is undertaken to study the effect of geometrical parameters on the plasmonic behaviour. This allows us to find the optimized geometrical parameters to achieve the highest plasmon absorption for the sensing application. Characterization of the fabricated silicon inverted pyramid is performed using an atomic force microscopy (to measure surface roughness), a bespoke Reflectometry system (to measure absorption of light by the sensor surface), and Raman measurement using Benzene Thiol as a test molecule to assess the SERS enhancement from the inverted pyramidal SERS sensor.

5.1 Fabrication Process

5.1.1 Materials, Chemicals and Tools

Table 5-1 List of chemicals, materials and tools used

Chemical/Material/Tools	Purity/Specification /Composition	Supplier
<100> 6" Silicon wafer (n or p doped)	Low resistivity (1-20 Ω /cm)	IDB Technologies Ltd.
Acetone	HPLC grade	OM group ULTRA PURE CHEMICAL Ltd.
Isopropyl alcohol	HPLC grade	OM group ULTRA PURE CHEMICAL Ltd.
Silicon dioxide pellets	99.995%	Testbourne Ltd.
ZEP520A	High resolution positive electron beam resist	ZEON CORPORATION
ESPACER 300Z	Weak acidic solution Charge dissipating Agent	Showa Denko K.K
ZED-N50 developer	n-Amyl acetate	ZEON CORPORATION

Argon	99.988%	Boc Gases
Trifluoromethane	CHF ₃	Boc Gases
Potassium Hydroxide	99.99%	OM group ULTRA PURE CHEMICAL Ltd.
Buffered Hydrofluoric Acid	7:1	Microchemicals
Fuming Nitric Acid	HNO ₃ >90%	Sigma-Aldrich
Titanium pellets	99.99%	Testbourne Ltd.
Chromium pellets	99.6%	Umicore Materials AG
Gold pellets	(5N) 99.999%	American Elements
Hydrogen peroxide 31%	Ultrapure ACS reagent	Sigma-Aldrich
Tantalum Wire	0.5mm diameter,99.9%	GoodFellow
Tungsten Liner	-	-
Graphite Liner	-	-
Ethanol	HPLC grade	Rathburn Chemicals
Benzyl Mercaptan	C ₆ H ₅ CH ₂ SH	-
Benzenethiol	C ₆ H ₅ SH	-
HELIOS sputtering tool	-	Leybold Optics GmbH
Spectroscopic Ellipsometer	M-2000	J.A Woollam Co., Inc.
Spin Coater	Model 200	Brewer Science Cee
Electron Beam Lithography	JBX-9300FS	JEOL Ltd.
Reactive Ion Etcher	Plasmalab 80 Plus	OXFORD Instruments
Plasma Asher	Model 300	PVA TePla
Scanning Electron Microscope	JSM 7500F	JEOL Ltd.
Evaporator	LAB 700H	Leybold Optics GmbH
Microscope	Eclipse L200	Nikon
Atomic force microscopy	Multimode V	Bruker

5.1.2 Preparation of inverted pyramid on silicon platform

This section describes in detail the fabrication process and the control parameters to produce an inverted pyramidal silicon substrate. In order to achieve a defect free sample, each step of process should be carried out with intermediate cleaning process. The fabrication of inverted pyramid involves several steps, which are described as a schematic diagram of process flow in Fig 5.1. An extensive list of the fabrication process is provided orderly in Table 5.2.

Table 5.2 provides the detail procedures for sensor fabrication. A 6 inch silicon wafer is first cleaned with fuming nitric acid. If there is any dust on the wafer, an extra sonication cleaning step can be used. After drying the wafer in an oven for 30 minutes for the elimination of moisture to assist in adhering the next layer, the deposition of silicon dioxide (SiO_2) can be sputtered by HELIOS sputtering tool. Deposition of oxide can be performed with different methods such as thermal deposition, evaporating and sputtering. For this project, oxide is deposited for the thickness of 250nm by sputtering as it gives the fairly uniform oxide layer throughout the wafer. The oxide recipe (SiO2_KAG_lowloss) is developed by Dr. Stuart Pearce, a member of project group and the deposition rate is 2.8Å/sec. The uniformity and thickness have been checked by ellipsometer and the variation in uniformity is less than sub-nanometer. The wafer is then resist coated as described in Table 5.2 (step-3) for the e-beam exposure. The positive e-beam resist is prepared for 400nm thickness and followed by a thin film conducting layer, Espacer 300Z (~15nm) to avoid problems of positional error due to the charge of oxide layer during exposure time.

The wafer is ready to be exposed for the described pattern as discussed in the section 4.1.1 and Fig 4.3. The e-beam lithography is carried out by Dr. Ruiqi Chen, a member of project group. In this thesis, the inverted pyramids have different geometrical parameters and line spacing between the adjacent pyramids ranging from maximum 2.5μm to minimum 250nm. In order to achieve the uniform patterning with minimum line spacing, the proximity correction has been carried out during exposure time. The exposed wafer is thoroughly rinsed in deionized water to remove the conducting layer (ESPACER). The wafer is then developed as described in Table 5.2, step-4(ii). The next step of fabrication process is to open the exposed oxide area using the plasma dry etching method as written in Table 5.2,

step-5. The etch rate, 19.38nm/min, is achieved within the 12.5 min etching time. In this recipe, an extra N₂ cooling step (for the substrate) is added to the standard oxide recipe to increase the quality of the profile structure with long lasting of the mask and hence increases the selectivity. This cooling step is good to be used if the high aspect ratio anisotropic dry etching has to be performed. The oxide profile structure is shown in Fig 5.2. The remaining e-beam resist have to be stripped off by O₂ plasma asher before continuing to the anisotropic wet etching otherwise the residual resist will redeposit on the wafer and make the surface dirty and contaminated.

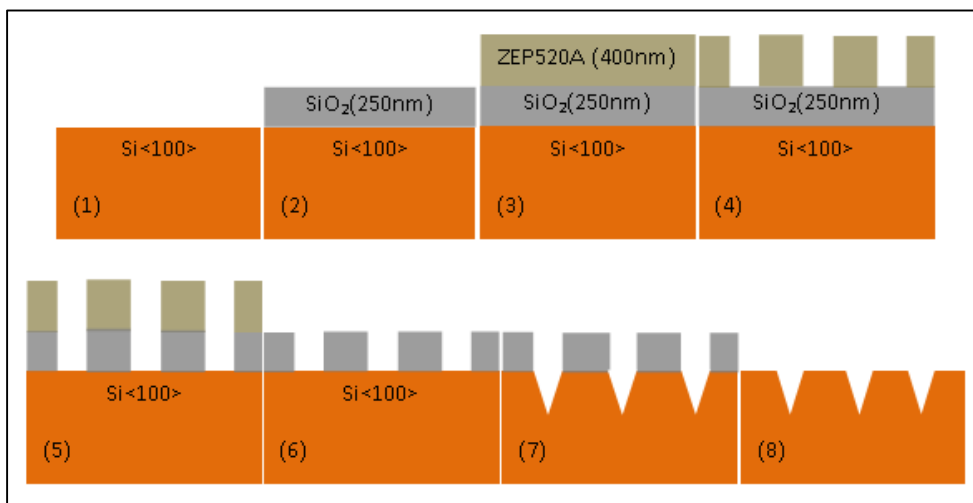


Figure 5.1 Diagram for fabrication process flow

In order to get the inverted pyramidal structure, potassium hydroxide (KOH) wet etching is performed with the 40% concentration at the temperature of 70°C. The etch rate is achieved at 77.6nm/min. The etch rate strongly depends on the temperature compared to the concentration. The higher the temperature, the faster the etch rate but the faster etching may harm the atomically smooth sidewalls. For this thesis, the different geometry pyramidal structures are patterned together on the single wafer. Due to the wide range of patterns on the same mask, in practice very small pit structures had to be sacrificed due to over etching in order to achieve the correct depth of the largest pyramid. The etch rate along the <100> plane is however approximately 40 times faster than the slow etching <111> plane as the latter has tightly packed crystal structure. Finally, the oxide (hard mask) can be removed by dipping the wafer in the oxide etchant (7:1 buffered HF acid) for

1-2 minutes. The removal of oxide is clearly noticeable due to the hydrophobic nature of silicon.

Table 5-2 Outline for the fabrication steps

No.	Fabrication Process	Controlled Parameters		
1	Cleaning wafer	(1)FNA-15min QDR-2 cycles HF-10sec QDR-4cycles	(2) Sonication Acetone-30sec IPA-20sec	
2	Deposition of SiO ₂ hard mask (250nm thickness)	SiO ₂ _KAG_lowloss - Thickness controlled by time - Deposition rate=0.28nm/sec		
3	Spin Coating 1.ZEP520A~400nm 2.Espacer300Z~15nm	<u>ZEP520A</u> Speed-3370rpm Acceleration-20,000 Time-180sec PB temp-180°C PB time-2min	<u>Espacer300Z</u> Speed-2000rpm Acceleration-20,000 Time-90sec	
4(i)	E-beam expose the pattern	Acceleration voltage=100kV, beam current=25nA Aperture=200μm Resist sensitivity=190μC/cm ² Used proximity correction		
4(ii)	Developing the exposed area	ZED-N50 (undiluted solution) – 90secs IPA-30secs		
5	Dry etching for SiO ₂ hard mask etch rate=19.38nm/min Selectivity(SiO ₂ :ZEP)=1.3:1	Ar-38sccm CHF ₃ -25sccm	Press: - 30mT RF-200W Time-30sec	REPEAT- 25times
		N ₂ -68sccm	Time-1min	
6	Strip off the resist	O ₂ =800ml/min	Power=800W	Time-5min
7	Anisotropic wet etching	40% KOH solution Temp -70°C, Time-11mins		
8	Removal of SiO ₂ hard mask	7:1 Buffered HF acid Time-2mins, QDR-2cycles		

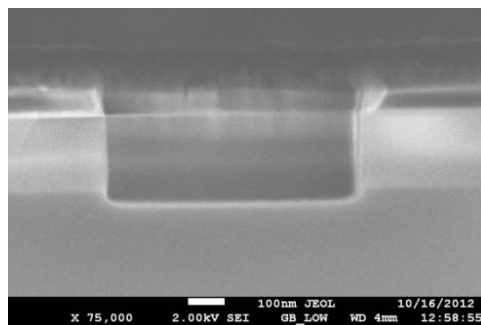


Figure 5.2 SEM image shows the profile of oxide layer

5.1.2.1 KOH wet etching issues

The maximum available depth of the pyramids depends on the pit size with the trigonometric relation ($\text{depth} = \tan 54.7^\circ \times \frac{1}{2}$ of pit size) and the pyramid profile whether the sharp or truncated pyramid is decided by the aspect ratio of the pyramid. The square aspect ratio gives the sharp tip pyramid while the rectangular one forms the truncated pyramid. Since the different geometrical pyramids are patterned on one chip as shown in Fig 5.3, the smallest feature (500nm pit size) will give the 580nm pit size due to the over etching to achieve the largest pit size, 2500nm. However, all pyramids are formed with nice shape and suitable quality to continue to test and characterization. A problem is random re-deposition of potassium after etching. Figure 5.4 (a) and (b) show examples of potassium re-deposition on the chip. SEM image Fig 5.4(c) shows an example after overcoming the issue by dipping the chip into fuming nitric acid for 20 to 30secs followed by thoroughly rinsing with the deionized water. An alternative solution is to sonicate the samples in warm water immediately after etching is finished.

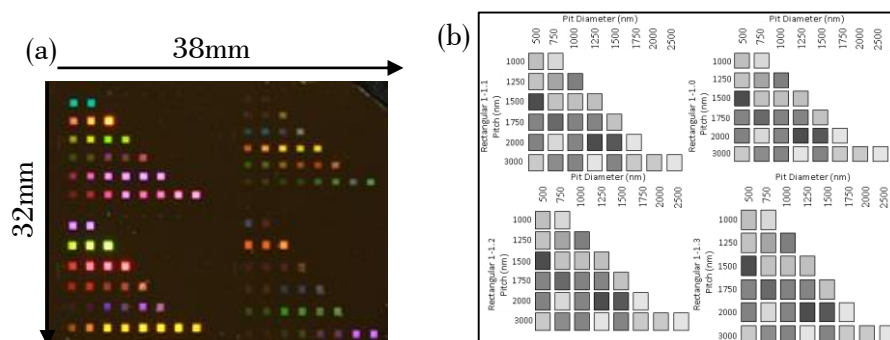


Figure 5.3(a) Photograph of the fabricated test chip after gold deposition, (b) Chip layout with the geometrical parameters

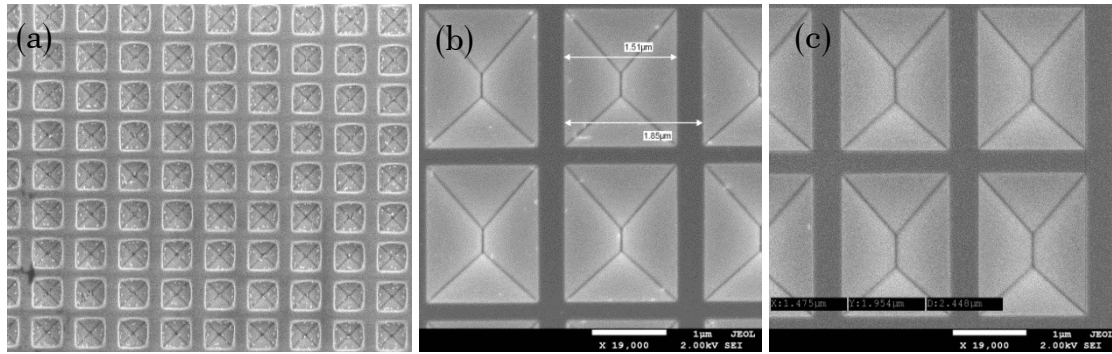


Figure 5.4 SEM images for KOH etched pyramids, (a) and (b) show the potassium re-deposition and (c) after cleaning with FNA for 30sec of (b).

5.1.3 Angled gold deposition

For the purpose of investigating the effect of gold thickness (deposited on the inverted pyramids) on the plasmonic behavior and Raman sensitivity, gold is deposited onto a set of test chips with thickness ranging from 25nm to 400nm (25, 50, 100, 200, 300 and 400nm) using an electron-beam evaporator. Gold deposition is conducted utilizing glancing angle deposition at the deposition angle of $25^{\circ} \sim 27^{\circ}$ to achieve a uniform surface roughness on the slope side wall. The uniform deposition is succeeded by continuously spinning the substrate holder at 20 rpm during the gold evaporation. The deposition rate of $5\text{\AA}/\text{sec}$ is gained by 13% soak power at 136mA current. A thin chromium layer is applied beforehand as an adhesive layer. This is deposited at $2\text{\AA}/\text{sec}$ to achieve the small grain size. The ratio of thickness in gold to chromium is 20:1. Before gold deposition, the chamber is conditioned by depositing 700nm of titanium to make a clean environment as the SERS substrate requires ultra-clean metallization.

5.1.3.1 Metallization issue

The main issue in metallization for the chemical sensor is gold spitting during evaporating gold which is kept inside the graphite crucible liner. What is gold spitting? Gold spitting is an event that various sizes of spherical gold balls, are randomly depositing on the substrate as shown in Fig 5.5. During the evaporation of gold, carbon impurities float to the surface of gold melt inside the crucible in such a way that carbon becomes concentrated as dark color on the surface of the melt gold. If this carbon is not removed before the next deposition, there will be a high spit density of gold on the evaporated film. Generally, this

is not an issue for the deposition of metal contacts but for the chemical sensor which analyzes the spectrum of vibrational molecules needs super clean gold deposition. In order to achieve high quality gold films with low spit density, the carbon issue has to be eliminated. The source of the carbon is believed to be: 1) the incoming gold pellets used to replenish the melt and 2) the graphite liner. Therefore gold cleaning process has to be carried out before running the evaporation. The cleaning procedure has been given by Mr Peter Ayliffe (E-beam engineer). Throughout the cleaning process the source has to be handled only with clean metal tweezers or lint free cleanroom cloth. The gold cleaning process has two parts such that cleaning gold melt and the replenished gold pellets. For gold melt, rub the melt using acetone-soaked lint-free cloth until no further traces of carbon can be seen on the cloth because a dark stain of carbon can be seen initially on the cloth. Care should be taken to avoid snagging pieces of cloth on the rough surface when the sides and base of the melt have been rubbed. The melt is then cleaned by sonication with acetone for 30 minutes and rinse twice with IPA, followed by immersing in hydrogen peroxide (31%, as supplied) for 45 minutes. The melt needs agitation in every 15 minutes to disperse bubbles. Finally rinse the melt in dunk tank and blow dry using nitrogen gun. The new gold pellets have to be cleaned in the same way prior to replenishing the melt.

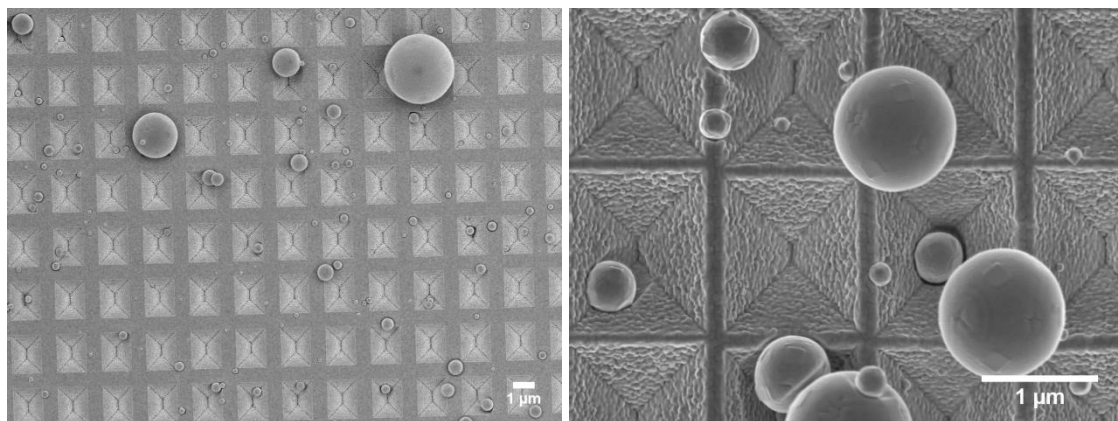


Figure 5.5 SEM images of pyramid after gold deposition showing gold spitting: (a) in low magnification on silicon platform, (b) in high magnification on plastic platform

Another source of carbon is believed to be the graphite liner. For this process, a tungsten liner is substituted and wiped around the inside of the liner using a lint-free cloth soaked in acetone, IPA and dry for few minutes. One problem with a tungsten liner is that the electron beam cannot supply enough heat to melt gold inside the liner due to high thermal conductivity of the liner. Consequently it is difficult to achieve the $5\text{\AA}/\text{sec}$ deposition rate

within the maximum power limit (150mAx10kV) of the machine. In order to achieve adequate heat dissipation around the liner to melt gold, the liner is placed inside a basket made up of tantalum wire (which is more resistance to heat compared to tungsten wire). This arrangement is shown in Fig 5.6.



Figure 5.6 Photograph showing (a) basket made by tantalum wire, (b) the tungsten liner with basket

Finally the gold has to be melted slowly allowing sufficient rise and soak time to attain a clean evaporated film because an abrupt increase in power can cause high spit density. High quality gold film free of gold spitting is shown in Fig 5.7.

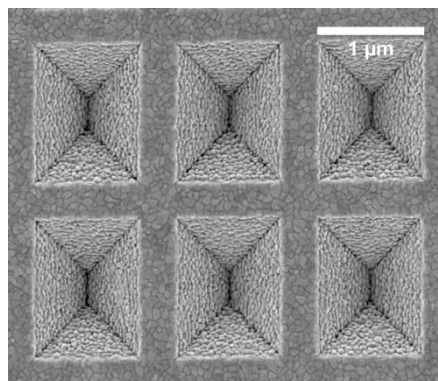


Figure 5.7 SEM image showing the gold deposition without gold spit after cleaning procedure

5.1.3.2 Characterization for the quality of metalization

The metallization quality is examined with the scanning electron microscopy (SEM) as shown in Fig 5.8. The gold is uniformly deposited on the flat surface and the roughness on the sidewall is varied with the thickness of the gold such that the higher the gold thickness the more the roughness is formed on the sidewall. The thickness of the gold deposited on

the sidewall is approximately two-third of the thickness on top surface due to the facet inclination 35.3° . The cross-section image Fig 5.8(d) confirms the conformal coating on the sidewall of the inverted pyramid.

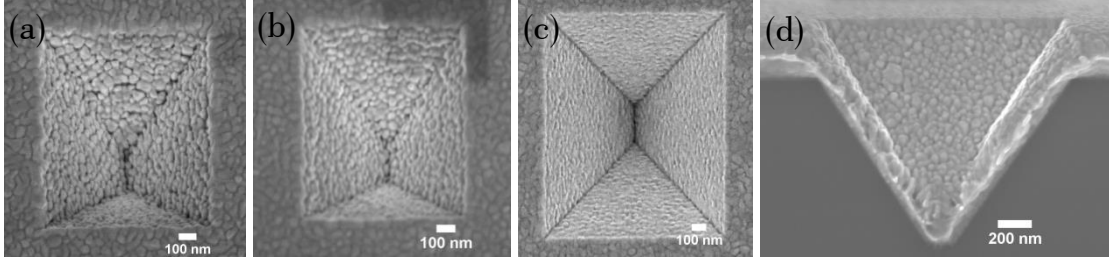


Figure 5.8 SEM images showing the different thickness of gold and their variation of the roughness on the sidewall (a) 400nm (b) 300nm (c) 200nm (d) cross-sectional image of Au 400nm

5.2 Modelling for optimization of SERS substrate on Si platform

In order to reduce the computational cost and time, the inverted pyramids are selectively designed and simulated (instead of modelling all 28 designs included in the fabricated test chip layout). To gain the effective selection for design a double-y line graph is plotted for the fill factor ($\frac{\text{pit size}}{\text{pitch length}} \times 100\%$) and the variation of depth as a function of pit size as shown in Fig 5.9 in which the x-axis refers to the pit size varied from 500nm to 2500nm and the left y-axis is about the fill factor of inverted pyramid while the right y-axis indicates the normalized depth to the largest pit size. Surface plasmons are said to be delocalized (propagating) surface plasmon polaritons (SPPs) if they travel along the interface of the metal and dielectric medium at the top surface of the substrate. They can be excited via scattering from the periodicity of the structure and have sharp (narrowband) absorption properties. Their plasmon energies are highly dependent on incident angle as well as lattice orientation.

Surface plasmons can also be localized within the cavity/pit of inverted pyramid, such that its electric field distribution is strongly confined inside the pit. These are known as the localized plasmons. Its plasmons bands are broader than the propagating plasmons (as shown in Fig 3.2)[107,132]. Since its electric field distributions are kept within the pit, the depth of the pyramid will determine e-field formation and distribution. This relates to the

effective refractive index of plasmon mode, which in turn relates to the shape and geometry of the pit. Therefore, propagating plasmons scale with fill factor (spatial periodicity of the pyramids) whereas localized plasmons scale with pits size.

In Fig 5.9 (a), the geometrical parameters shown by a dotted ellipse are assured to meet the aforementioned rigorous hypothesis because these geometrical combinations (pitch and pit size) hold the high fill factor with the deeper depth. In the layout (Fig 5.9 (b)), a red dotted arrow indicates patches of the inverted pyramids which are relevant to the designs with the high fill factor within the dotted ellipse in Fig 5.9(a). In order to get better understanding of plasmonic behavior in relation to the geometrical parameters of inverted pyramid, another two sets of pyramids are selected (shown by black arrows in Fig 5.9(b)) which show the effect of pitch length and pit size as well.

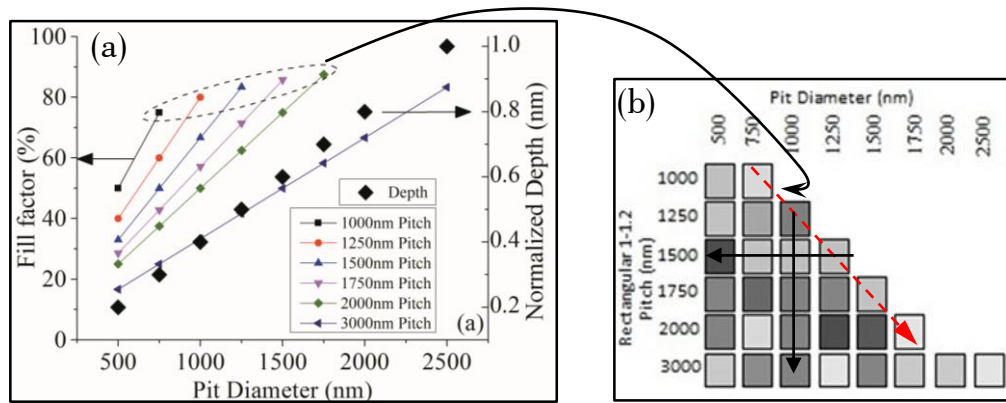


Figure 5.9(a) a double-y line graph characterizes the geometrical properties of inverted pyramid: the left y-axis shows the fill factor of each pitch length as a function of pit size and the right y-axis defines the normalized depth to the largest pit size as a function of pit size shown by a series of black diamond symbol, (b) a microscopic layout for the rectangular based inverted pyramid: vertical black arrow guides the patterns changing with pitch at 1000nm pit size, horizontal black arrow guides the patterns changing with pit size at 1500nm pitch length, the red-dotted diagonal arrow guides the patterns with high fill factor as shown in (a) with the dotted ellipse.

5.2.1 Optical Response from the silicon inverted pyramid before metallization

This section gives the investigation on incident broadband wavelength illumination on silicon inverted pyramid without gold coating in order to study the effect of geometrical parameters on optical response such as pit size and pitch of the rectangular aspect ratio

1:1.2. The broadband source is considered to find out the better excitation wavelength for the inverted pyramid device.

5.2.1.1 Effect of Pitch length

In order to understand the diffraction related effects resulting from the periodicity (pitch effect) for uncoated silicon, a design with fixed (1000nm) pit size is selected, and pitch length is varied from 1250nm to 2000nm increasing by 250nm step. These geometries are selected to prove the hypothesis discussed in section 5.2 and Fig 5.9. The zero order diffraction (reflection) is collected as the outcome and prepared reflection map as discussed in the section 4.1.1. Note that these diffraction patterns are without metal coating and the color code represents the reflection efficiency while the dark blue just simply refers to the scattering of incident light at the interface. The change in pitch length is a reason for the different diffraction patterns and distribution. Generally longer the pitch length, the more shift in diffraction lines to the longer wavelength (red-shift). This phenomenon can be easily seen with the guidance of the series of colored arrows in Fig 5.10(d). Particularly, two main diffraction lines distinctly appear; one is at the wavelength which is half of the pitch length and other is at the wavelength which is the pitch length for every pitch of structures which will be responsible for the propagating surface plasmon when the device is SERS active after metallization. For example 1250nm pitch, two noticeable diffraction lines occur at wavelength of 625nm and 1250nm (black dotted lines in Fig 5.10 (d)) and for 1500nm pitch, lines are at 750nm and 1500nm (black straight lines) respectively. The formation of these two diffractive lines from the periodicity effect is believed to support the surface plasmon polaritons (the propagating plasmons) along with scattering after metallization on top of it.

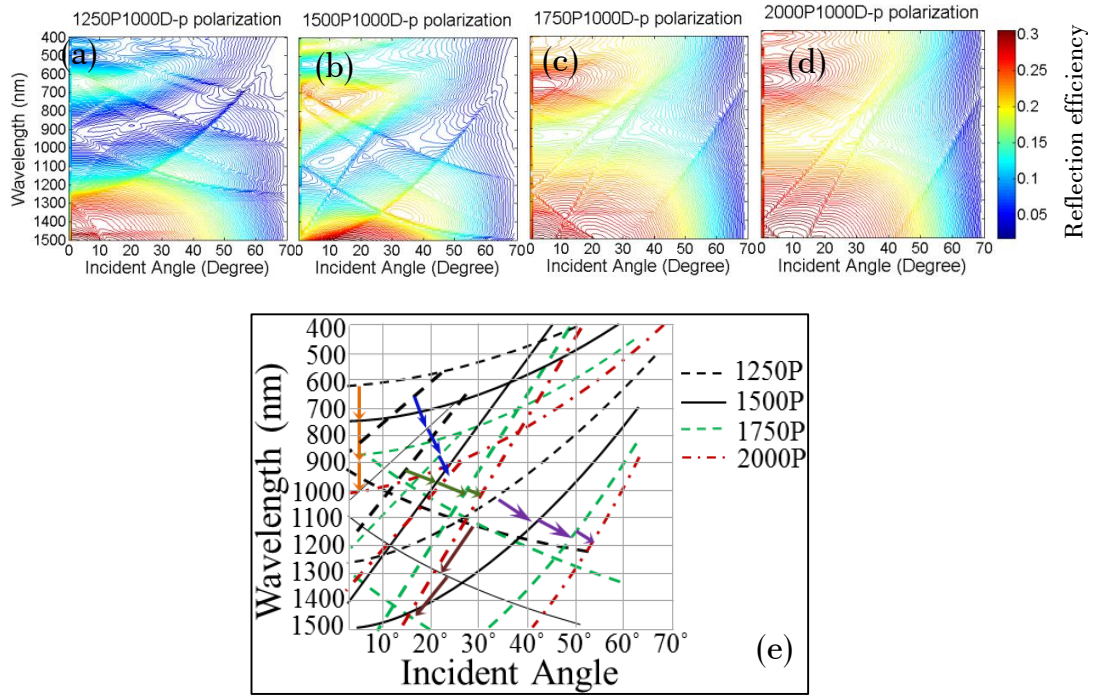


Figure 5.10 Reflection maps of pitch effect under TM-polarization from the simulation: (a) 1250P1000D; (b) 1500P1000D; (c) 1750P1000D; (d) 2000P1000D; (e) Distribution of zero order diffraction of 1000nm pit size along with different pitch, before metallization. Series of colored arrows indicate the shift of diffraction lines to infrared range corresponding to the longer pitch length

Moreover, the pit size and its related depth are believed to control the e-field confinement and density within the pits. This will be discussed in the following section. This diagram of pitch effect leads to two essential intuitive properties of plasmons relating to the geometrical parameters. First, these diffractive lines can give a clue at which excitation wavelength the plasmons can be directly coupled to the incoming photons when the beam of light irradiates on the substrate after metallization. Second the diffraction lines are shifted within the visible to near-infrared range. By controlling the pitch length, plasmons coupling to the incoming light will occur within that range of wavelength which is of interest to current Raman laser and spectroscopy system for visible and near infrared region. From this observation, the diffraction pattern is concluded that to be highly sensitive to the pitch length.

5.2.1.2 Effect of pit size

Now the effect of pit size is investigated using geometry at 1500nmpitch length with varying pit size from 500nm to 1250nm via 250nm step. As before, reflection efficiencies are represented as a dispersion map as described in section 4.1.1 and the color bar scales

the reflection from red to dark blue (maps are shown in Fig5.11 (a, b, c and d). As expected, (since pitch is constant) dispersion maps for the different pits are almost identical as shown in Fig 5.11(e). The effect of pit size on the optical response therefore follows the aforementioned hypothesis discussed in section 5.2.1.

It is observed in the dispersion maps that the larger the pit size, the less the reflection efficiency is and hence absorption energy can be assumed to be improved. For example, the dispersion map for the smallest pit size (500nm) is occupied with the high reflection (red) while the largest pit (1250nm) is influenced by the less reflection (blue).

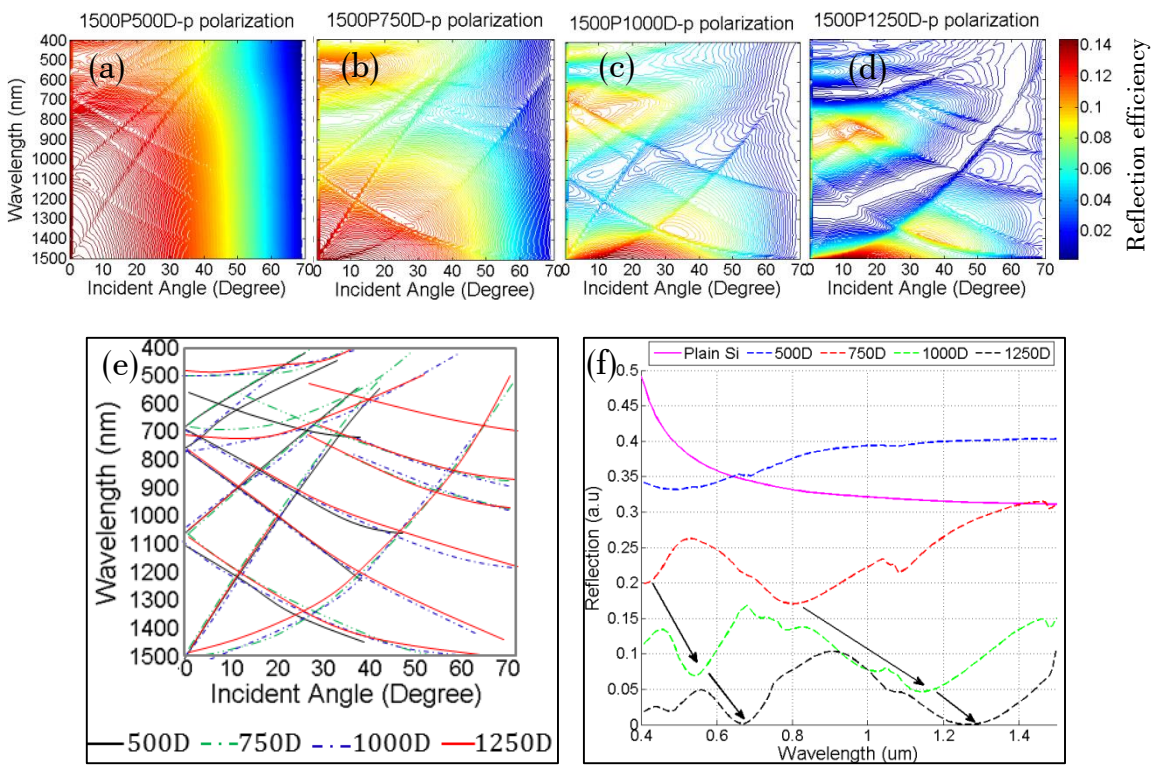


Figure 5.11 Reflection maps of pit effect under TM-polarization: (a) 1500P500D; (b) 1500P750D; (c) 1500P1000D; (d) 1500P1250D; (e) Distribution of zero order diffraction of 1500nm pitch along with various pit sizes; (f) Comparison of reflection efficiency of the plain Si with the different pit size under normal incident. Black arrows are indicating that resonance dips are shifting to the longer wavelength together with the larger pit size.

To get better understanding, the reflection spectrum of each pit size as a function of wavelength is compared at the normal incident angle using the flat Si as a reference (shown in Fig 5.11(f)). Again this comparison follows the proposed hypothesis given that in Fig 5.11(f), the flat silicon does not give any absorption dip whilst the textured structure

produces absorption assuming that silicon is optically thick to prevent the incoming light pass through it.

Thorough analysis shows that the larger the pit size, the less reflection and the absorption wavelength becomes red-shifted (shown by the black arrows). This will become the source for plasmonic coupling to incoming light after metallization.

From this understanding, it is believed that the variation of pit size is possible to tune the absorption resonance for the desired excitation wavelength which is the origin of the localized standing plasmon.

5.2.2 Geometrical parameters of rectangular inverted pyramidal SERS substrates versus its plasmonic behavior after metallization

In this section, genuine properties of plasmons are studied through variations of geometrical parameters of rectangular based pyramid nanostructures using a 3D model based on RCWA method. Simulation results clearly indicate that tailoring the geometrical parameters of pyramids can tune and enhance the plasmon resonances either through localization or mixing of localized and propagating plasmons. The mix-mode of plasmons is one of the reasons for the enhanced plasmon absorption in the rectangular pyramidal SERS substrate. From an analysis of geometrical parameters (pitch length, pit size and fill factor) the 1250nm pitch-1000nm pit size pyramid shows the highest plasmon absorption than other geometrical parameters of pyramid in near infra-red region.

The SERS structure is modelled as an asymmetrical inverted pyramidal structure with the 1:1.2 (width: length) aspect ratio instead of commercial symmetrical design. From the simulation results of section 5.2.1, the optical properties of inverted rectangular pyramidal pits are studied and they are highly dependent on the pit size, pitch length and shape. Although these properties are sensitive to gold thickness and its non-conformality, roughness and local dielectric environment, their effects on plasmonic behaviour is not discussed in this section. Here the coupling of plasmon (localized and propagating) with incident and reflected laser beam as well as the mixture of plasmon (either localized plasmons to propagating ones or to same plasmonic mix modes) are examined. The simulation results give the sense of possibility to selectively tune plasmon properties to achieve high SERS enhancement. All simulations are based on the 1:1.2 aspect ratio of

rectangular pyramid and TM polarization using with 400nm thickness of gold with zero roughness unless other is mentioned.

5.2.2.1 Pitch dependent delocalized plasmons

The pitch dependent diffraction patterns have been discussed in section 5.2.1.1 before gold coating and proposed that these tunable diffraction lines can guide an excitation wavelength at which the surface plasmon polaritons could occur. In order to make clear hypothesis, reflection maps for the effect of pitch after gold deposition are plotted in Fig 5.12 which is zoomed in for the visible and near-infrared region of wavelength. Fig 5.12 represents the reflection maps for the constant pit size varying with the pitch length of the inverted rectangular pyramid. The reflection map is formed by mapping a group of reflection efficiency over a broad wavelength range in visible and near infrared regime for function of incident angles together in a single color map. The color map is represented in the color scale: scaling from dark to white corresponding to complete absorption (dark) to the complete reflection (white).

In each map, the green dotted/straight lines represent the diffraction lines shifting with variation of the pitch length and indicate the propagating surface plasmon polariton. Results are in good agreement to the aforementioned hypothesis and hence the propagating plasmon can be selectively tuned by changing the pitch length. For example, the propagating plasmon mode in 1250nm pitch is shifted to longer excitation wavelength in 1500nm pitch (as shown in green straight lines in Fig 5.12 (a) and (b)). From the dispersion maps, the localized plasmons are observed approximately at 750nm and 815nm for 1000nm pit size (marked by yellow dotted lines). It is evident that the tuning of localized plasmons inside the pyramid cannot be dominated by the varying pitch but their respective intensities are highly dependent on fill factor as shown in Fig 5.12(e). E.g. in 1250P1000D with the 80% fill factor, the strong propagating plasmon absorption supports to couple with the localized plasmon and become the mixed plasmonic modes resulting in the highly localized plasmons for wider incident angles (shown by white dotted lines) and hence this mixed plasmon mode for wider angle could give larger collection angle in Raman Spectroscopy system. In 3000P1000D which has the lower fill factor (30%) the propagating plasmon cannot support to couple with the localized plasmon and hence the latter occupies only the low absorption efficiency and hence the low plasmon energy.

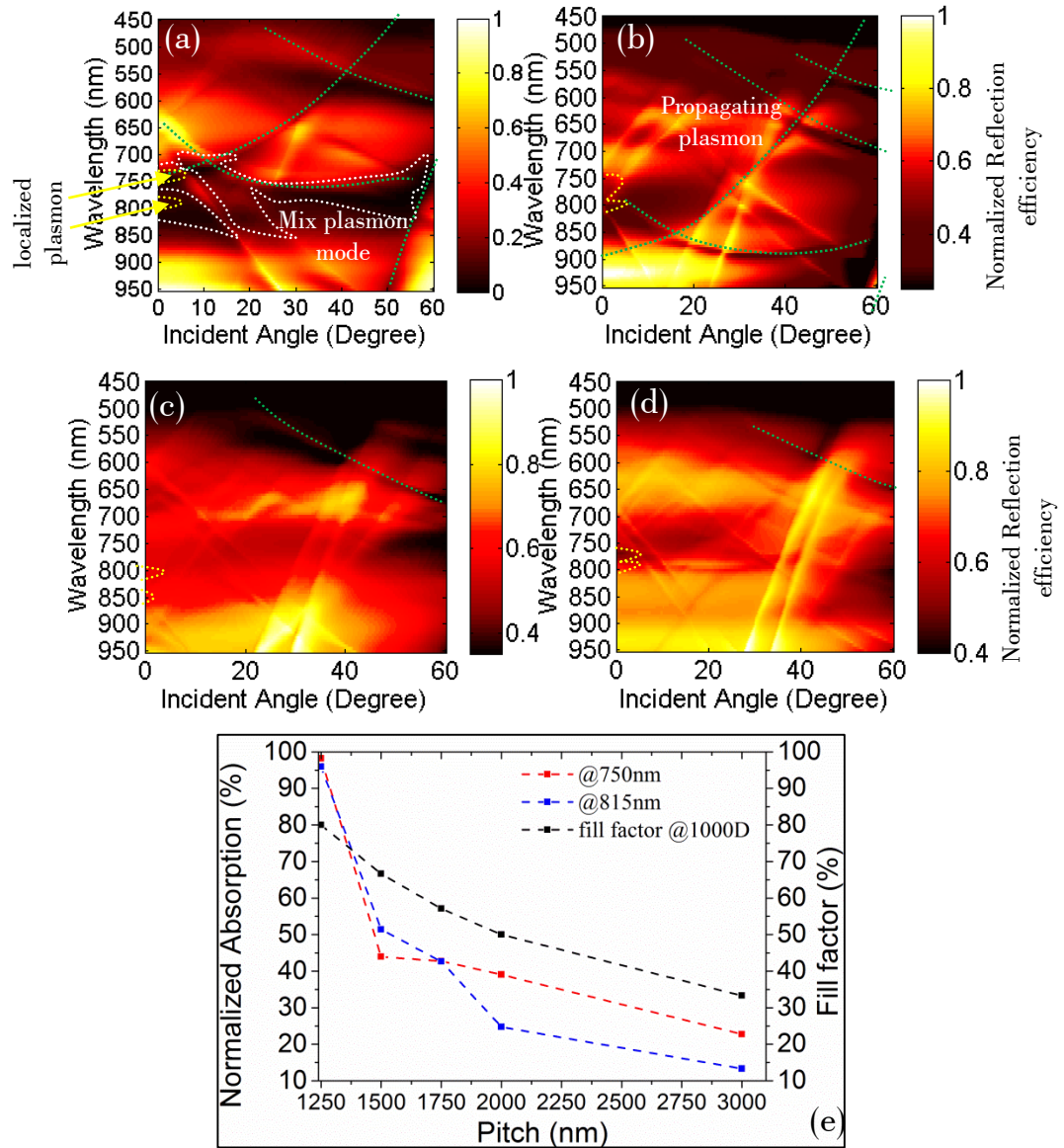


Figure 5.12 Dispersion maps of pitch effect showing the change in reflection with the excitation wavelength as a function of incident angle for 1000nm pit size with 400nm gold thickness at TM polarization (a) 1250nm pitch, (b) 1500nm pitch, (c) 1750nm pitch (d) 2000nm pitch. Green dotted are the guide lines for showing the shift in diffraction features corresponding with the pitch and hence tuning the propagating surface plasmon while the yellow dotted lines are guiding to follow the broadband localized plasmon which is resistant to the variation of the pitch and the white dotted lines are for the guidance to the mix plasmon mode. (e) a line graph for normalized absorption of 2 different plasmon resonances (750nm and 815nm) @1000D as a function of pitch length which gives an evidence that the fill factor affects the absorption intensity.

Figure 5.12(e) clearly shows that the lines of each plasmon absorption profile exactly follow the fill factor profile in the pitch effect. A fact is observed that the fill factor can control the coupling mode of plasmon either between localized to propagating plasmons or between their own kind and makes the plasmon energy higher. As a result the localized

plasmon absorption of 1250P1000D (98.21% @750nm excitation wavelength and 95.93% @815nm operation wavelength) is four times higher than that of 3000P1000D (22.76% @750nm and 13.31% @815nm). From these simulation results of pitch effect, the optimized design for sensing function could be 1250nm pitch-1000nm pit size pyramidal structure due to three reasons. First, Raman lasers are commonly available in visible and near-infrared line for spectroscopy system. Second, the actual excitations and collection cone of Raman microscope are quite handy in the narrow acute incident angles with the reasonable laser energy density at small numerical aperture. Third, it gives the 98.21% plasmon absorption (white-dotted line in Fig 5.12(a)) due to the mix coupling mode of localized and propagating plasmons within the visible region of wavelength with narrow range of incident angles, which can support surface plasmon polaritons to go further distance and better sensitivity.

5.2.2.2 Pit size dependent localized plasmons

To study the plasmonic behavior related to the pit geometry, dispersion maps for various pit size (500nm to 1250nm with a 250nm step) while maintaining fixed pitch length (1500nm) are shown in Fig 5.13. The simulation is carried out for TM polarization and 400nm gold thickness. The color scale represents from the dark blue (high absorption) to dark red (high reflection). The different absorption intensities together with the different tuning wavelength occur for different pit sizes. From the dispersion maps, it is difficult to clearly understand the effect of pit size on plasmon behavior. Different pit sizes are tuning the localized plasmons at different wavelength and the fill factor still support the mixed plasmonic mode to cause the high plasmonic absorption.

Since it is believed that the localized plasmons correspond to high e-field distribution within the pit (cavity), in the simulation the spatial e-field density is investigated further, using monitors which measures maximum intensity over the entire cross-sectional area placed through the centre of the cavity for the XZ and YZ plane, as indicated in Fig. (5.14) inset.

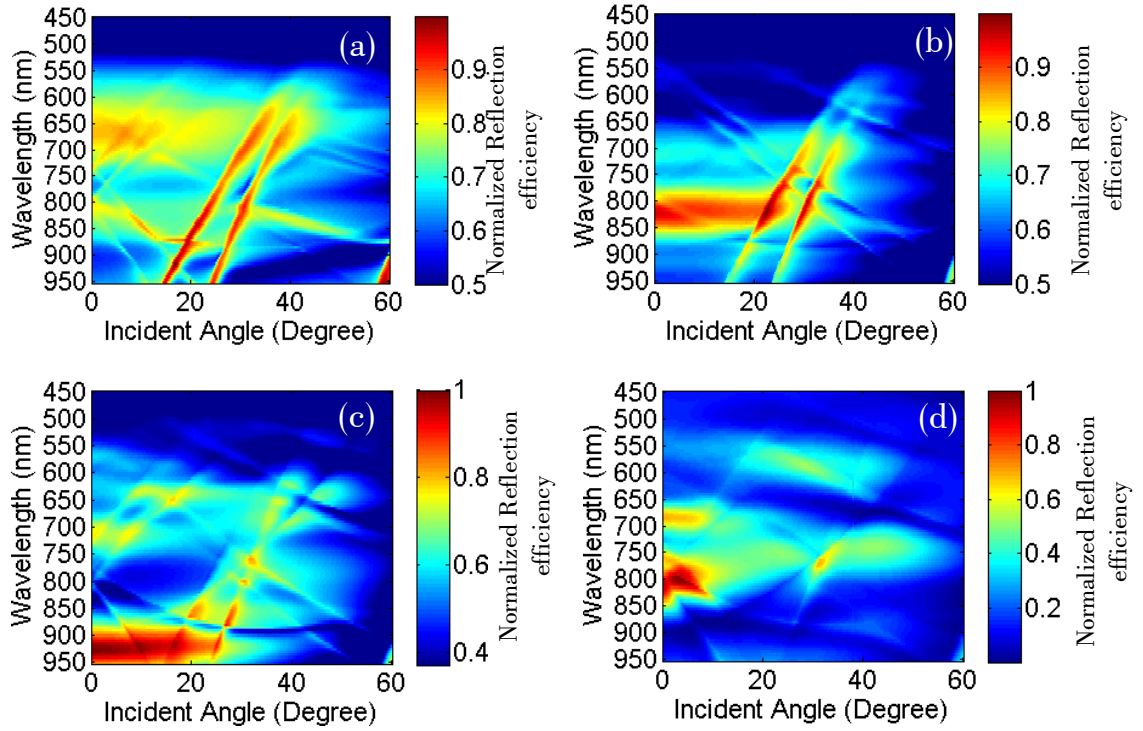


Figure 5.13 Dispersion maps for the different pit size at the fixed pitch length of 1500nm under TM polarization with the 400nm gold thickness (a) 500D (b) 750D (c) 1000D (d) 1250D. Colour scale represents from dark blue to dark red for the high absorption to high reflection, respectively. The position of the colour schemes of dark blue and blue range which is related to the plasmons, is varied with the pit size. Note that the value of the color scale is different for the each dispersion maps and hence the absorption intensity is highest at the 1250nm pit size with high fill factor.

The monitor records e-field as function of space using an equation:

$$U_E(r') = \frac{1}{2} Re[\varepsilon(r')] |E(r')|^2 \quad (5.1),$$

where E is the electric field, ε is the spatially dependent index and r' are spatial coordinates. The monitor grid size is the same as the pyramid grid size. The e-field density is collected at 1° angle of incidence for the visible and near infrared region.

Using this method, variation of maximum e- field energy within the pit can be analysed as a function of the operation wavelength for different pit sizes. The result is shown as a line graph Fig 5.14 in which the y-axis refers to the e-field energy normalized by the largest value of e-field. The high e-field shifts to longer wavelength along with pit size, in agreement with the hypothesis discussed previously. Those shifts are marked by the arrows (black and red) in Fig 5.14.

Maximum e-field energy however does not represent the localized plasmon, particularly for the 500nm pit size for which the high energy occur at the corner of opening which mostly

contributes to propagating surface plasmons rather than the localized plasmon (e.g is mixed mode plasmon). Figure 5.15(e) represents the distance away from the tip of the pyramid where the maximum e-field density (only for the operation wavelength of 785nm) occurs as the function of pit size and the respective e-field distribution at 785nm for different pit size are shown in Fig 5.15(a-d). It can be observed that the strong electric field can be selectively confined at the different depth at 785nm excitation wavelength. The maximum e-field occurs at the depth smaller than the respective maximum depth of the pit (the depth can be seen in Fig 5.15(e) as a reference). Plasmons are believed to possess the ability that the conventional light can be confined into the nanoscopic volumes which is much smaller than the excitation wavelength. This phenomenon can be observed in detail in Fig 5.15 (a, b, c and d) and Fig 5.15 (e) extract the information about the distance where 785nm wavelength has been squeezed and confined as the e-field and hence the pit size can selectively tune the excitation wavelength conforming to the localized plasmons within the pit. E.g. 500D forms the high localized plasmon at 354nm away from the tip while 750D, 1000D and 1250D forms the high localized plasmon at 190nm, 150nm and 267nm away from the tip respectively for the 785nm wavelength. The resonance wavelength and energy of localized plasmons are highly dependent on the pit size of the pyramid.

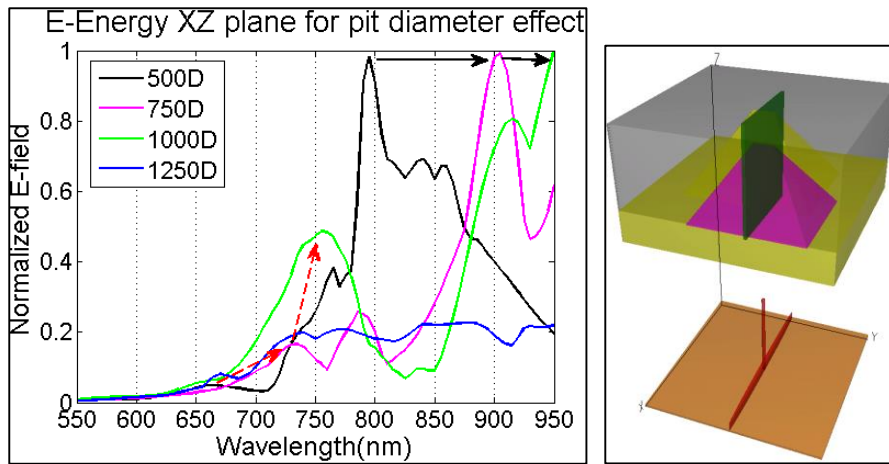


Figure 5.14 Line graph showing the normalized e-energy as a function of the operation wavelength for different pit size inverted pyramidal designs. Two sets of arrows (black and red-dotted arrows) are guiding the shift of the resonance wavelength with the high e-energy as a result of larger pit size. Each line of e-field (related to the different pit) shows the nature of plasmon that the incoming light which is larger than the pit can be squeezed into the pit coupling to the e-field at the interface and leads to the high e-energy. The position of the monitor (green) within the pit can be seen in the right side.

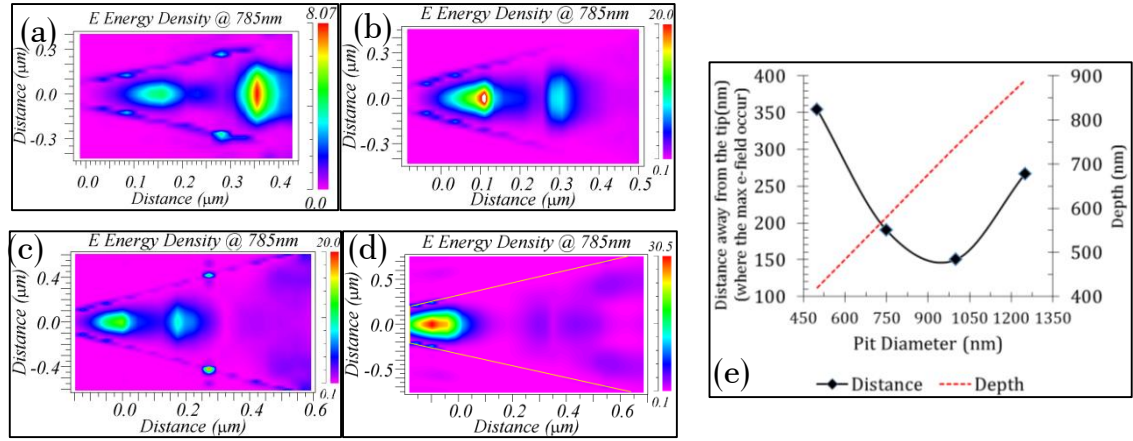


Figure 5.15 Images showing the e-field distribution within the cavity at 785nm excitation wavelength for pit sizes (a) 500D (b) 750D (c) 1000D (d) 1250D (the yellow line is guiding the area of a cavity). The colour scale is ranging violet to red and red represents the high e-field density. (e) A double Y-axis graph which is the extraction an information from the field distribution at 785nm (a, b, c, d) about how far the maximum e-field is occurred away from the tip of the inverted pyramid, as a function of pit size and another Y-axis gives the information about the depth varied with the pit size and it can be used to find out where the 785nm line couple with the plasmons and hence forms the e-field.

5.2.2.3 Inverted Pyramid sensors with high fill factor

Generally, the high periodicity structures (which means the space between the adjacent pyramids becomes narrower), overwhelms with stronger surface plasmon polariton (red-dotted lines in Fig 5.16) creating more opportunities to offer the mixed plasmon modes by coupling with either the localized plasmons (white dotted lines) or the SPP itself. To observe this event dispersion maps are formed for the 250nm spacing between adjacent pyramids with different combination of pitch and pit size such as 1000P750D, 1250P1000D, 1500P1250D, 1750P1500D and 2000P1750D and are shown in Fig 5.16. The polarization condition is TM and Au thickness is 400nm. Mostly, surface plasmons modes are tuned in near infra-red region corresponding to the optical properties of the metal (gold). Thus, all these patterns could give the higher Raman intensity with the near infra-red excitation wavelength. Detailed analysis on the high fill factor response to the plasmonic behavior (in terms of reflection) is performed at the 3° incident angle as a function of excitation wavelength and is shown in Fig 5.17.

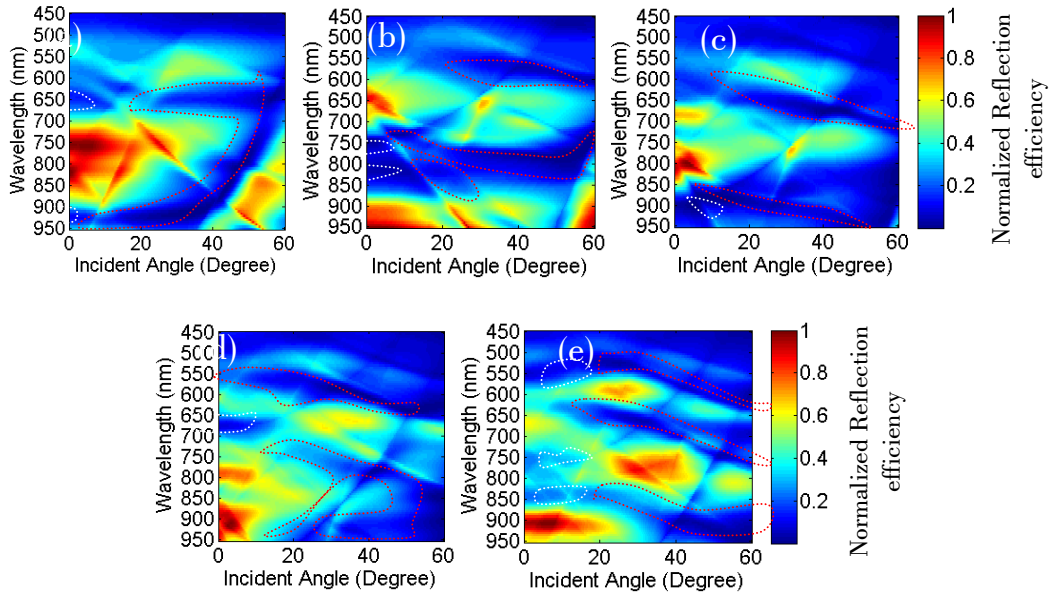


Figure 5.16 Dispersion maps for different high periodicity: (a) 1000P750D (b) 1250P1000D (c) 1500P1250D (d) 1750P1500D (e) 2000P1750D. Red dotted lines mainly concerns for the propagating plasmon varied with the diffraction distribution and the white dotted lines represent to the localized plasmon resulting from the respective pit size.

Since the pit size changes the resonance profiles of the rectangular based inverted pyramid shift to longer wavelength (shown in Fig 5.17 with green dotted circle and black arrows). Each resonance provides almost complete absorption as a result of the mixed plasmon mode coming from the advantage of the effect of high periodicity. However the pitch is altered and hence the diffraction distribution becomes different leading to different tuning for the propagating surface plasmon polariton which is marked by a red circle. Therefore some pattern designs (1500P1250D, 1750P1500D) could still work for sensing application even though they lack highly localized plasmon at common Raman excitation wavelengths such as 785nm and 633nm. Among these patterns, only the 1250P1000D structure provides the high energy plasmon mode around the wavelength of 780nm which is available in the common Raman laser system. As a result, this rectangular based inverted pyramid structure (1250P1000D) will enhance Raman intensity over other pyramid geometries.

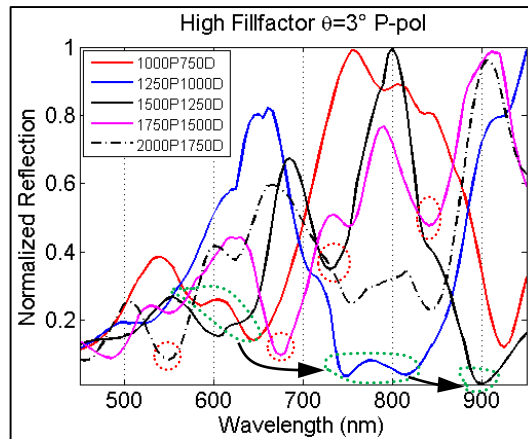


Figure 5.17 A graphic representation for the normalized reflection as a function of wavelength for the high periodicity with different geometrical parameter. Data are collected at the angle of incidence 3° under TM-polarization. Green dotted lines with the black arrows are concerned for the longer shift of the plasmon resonance with the larger pit size and the red circles are guiding for the propagating plasmon occurs along with the diffraction distribution related to the different in pitch.

5.2.2.4 Conclusion

In this section, a model was designed for rectangular based pyramid structures as an active SERS substrate and was simulated for the zero order diffraction (corresponding to specular reflection) for visible and near infrared region. Geometrical design parameters of pyramidal structures were varied in order to study fill factor, pitch and pit size dependence on plasmon absorption efficiency. From this rigorous analysis, the geometrical effects on the coupling of plasmonics behavior were understood. Changing the structural pitch length controls the distribution of the diffraction features and its periodicity tunes the density of the propagation plasmons energy and opportunity of the mixed plasmon mode. Although changes of pit size cannot dominate the order of diffraction, it mainly overwhelms the trapping of localized plasmons for selective excitation wavelengths due to the depth variation of pyramidal profile. Finally the fill factor plays the major role in efficiency of coupling to localized plasmon modes and so increases the localized plasmon absorption.

5.3 Experimental results and discussion

5.3.1 Characterization

Now the actual experimental optical behavior of nano-textured inverted pyramids is examined through characterization using the automated Reflectometry system described in chapter 4.

The fabricated inverted pyramid design is composed of 1250nm pitch and 1000nm pit size at the rectangular aspect ratio, 1:1.2. Angular reflection characteristics for wavelength ranging from 450nm to 950nm as function of incident angle 0° to 60° are shown in Fig 5.18(b) and Fig 5.18 (a) is its respective simulation result. The incident light is TM-polarized resulting in electric field oriented perpendicular to the surface of the substrate. Both the simulation and experiment reflection maps clearly determine the sharp diffraction bands with different energy. Figure 5.18 (c) shows a good fit of diffraction bands between the simulation and experiment.

The closer observation of the reflection diagrams reveals that some absorption modes follow along with the diffraction lines and some are found between diffraction bands. As discussed in chapter 3 the latter can form as the localized plasmon inside the cavity while the former is known as the delocalized plasmon propagating over the periodic surface. The localized plasmon is observed as the flat band at 720nm from $\theta=0^\circ$ to 10° and the coupling between localized and delocalized plasmon occurs from $\theta =10^\circ$ to 20° leading to the localized plasmon till $\theta=45^\circ$. However, the detailed examination of the localized plasmon bands indicates the interaction with the diffraction lines, especially at the larger incident angles produces the coupling between the localized and delocalized plasmon.

Since the inverted pyramid is the rectangular based and the symmetry is broken resulting in the two plasmon resonances separately. The resonance is 30 nm different between the simulation and experiment due to an error in pit size which is due to a small difference in actual gold thickness at the top surface of the pyramid. In simulation the gold thickness on sidewall was designed using the relationship: gold thickness at top surface $\times \sin 35.3^\circ =$ the thickness at the sidewall. In the simulation the top surface gold thickness is used as the defined value 400nm and hence the sidewall thickness becomes 231nm while the former is 331nm and the latter gets ~ 200 nm in the fabrication design leading to the approximately

30nm difference compared to the simulation. The difference in the absorption is possibly due to the depth difference where the simulation applies the 741nm according to the equation described in section 4.1.1 and the fabrication has the 713nm only in the depth as shown in the depth profile (Fig 5.19 (b)) which is extracted from the 3D AFM image of the 1250P1000D rectangular inverted pyramid (Fig 5.19(a) in which the inset is the Fourier transformation from the pyramid array showing the scattering directions of the rectangular lattice).

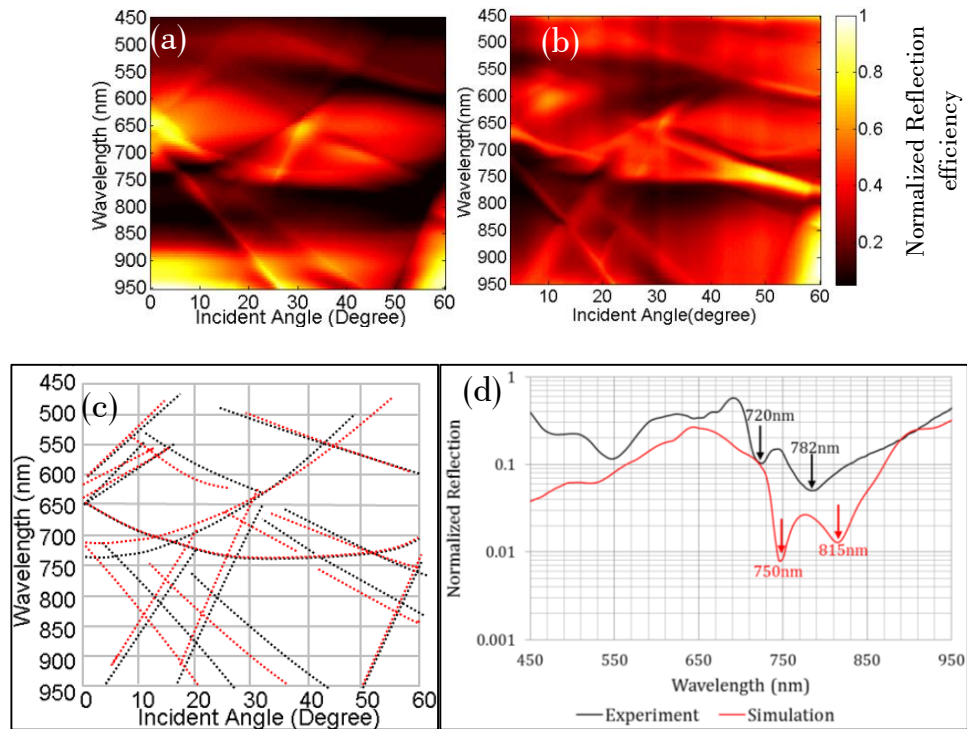


Figure 5.18 Angled resolved reflection map giving the dispersion characteristics of the rectangular inverted pyramid, 1250P1000D, the colour map represent the strong absorption (dark) towards the strong reflection (red/white) (a) simulation result; (b) experimental measurement result; (c) the diffraction bands of simulation is overlaid with those of experiment (red dotted line-simulation, black-dotted line-experiment); (d) Normalized reflection spectra at normal incident angle, y axis is in log value, indicating the separation of absorption dip due to symmetry breaking to rectangle instead of square.

Also the fabrication design has the roughness in the gold morphology Fig (5.19 (b) and (c)) while the simulation utilizes the built-in gold properties without roughness. The analysis for the gold surface roughness is done using a software called Gwyddion and the surface roughness was extracted using with Ra or RMS whereby Ra is the arithmetic average of height deviations from the mean height over the evaluation length and RMS is the root

mean square of the average of height deviation according to ISO 4287/1 and ASME B46.1. At the flat surface area (562nm \times 562nm) on the flat, RMS roughness is (2.9 \pm 0.43) nm in rows scan and (2.78 \pm 0.40) nm in columns scan. For the cavity of the inverted pyramid, the four sloped sidewalls have been processed using the same order of polynomial function on each to achieve the flat sidewalls. The RMS roughness for each sidewall has been examined and then averaged. Therefore the deviation of surface height inside the pit is (8.31 \pm 1.57) nm in rows scan and (7.93 \pm 1.35) nm in columns scan.

The difference RMS roughness between flat surface and cavity is obvious whereby RMS roughness inside the inverted pyramid is approximately three times higher than that of the flat surface. It can be concluded that RMS roughness inside the cavity is higher than top surface and hence supports the improvement of SERS effect with the coated molecule existed on the sidewalls. The variation of roughness proved that SERS enhancement of inverted pyramid device using the angled metallization technique would not result from the random hotspots and hence increase the reproducibility of intra-sample. The grain structure of the gold has been looked into regarding size and profile as shown in Fig 5.19 (e). The length of gold grain is 65.5nm in average after processing over 10 grains and the grain profile is well fitted with the Gaussian meaning that the profile of the grain is quite similar to that of the gold nanosphere. Thus, the angled gold coated inverted pyramid has an additional advantage having Mie plasmons from those spheres like gold grain structure and their high degree in roughness within the pit over their nature advantage of the rectangular inverted pyramidal design to result in the better sensitivity action for the low concentration molecules.

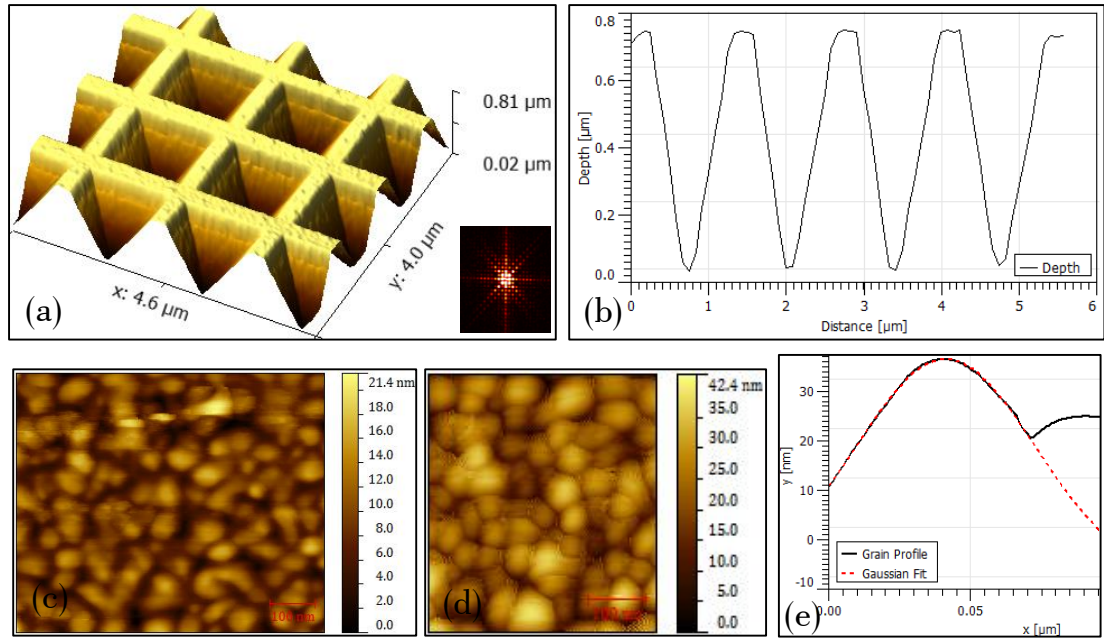


Figure 5.19 (a) a three dimensional AFM image of the rectangular based inverted pyramid (inset is the 2D FFT of the pyramidal array); (b) a depth profile extracted from the 3D AFM image giving the depth value (713nm) for the 1000nm pit size; (c) the gold surface morphology for the flat surface; (d) the morphology of gold deposition on the sidewall; (e) the profile taking from the single gold grain located on the sidewall and fitting with Gaussian function.

5.3.2 Pitch dependent delocalized plasmon

Pit size is fixed at 1000nm and pitch is varied in 250nm steps starting from 1250nm to 2000nm, then directly to 3000nm. Example reflectivity maps are shown in Fig 5.20 to observe the effect of pitch on plasmon behaviour. As expected, by varying the pitch has much effect on the diffraction distribution and resulted in more densely populated diffraction lines with increasing pitch length.

For example, the distribution of diffraction features in Fig 5.20(e) 3000nm pitch is denser compared with that of 1250nm pitch, Fig 5.20(a). The experimental results fit well with the observation in the simulation results showing that diffractive features shift to longer wavelength with increasing pitch (marked with the dotted black lines in 1250P, 1500P and 1750P). The dispersive propagating plasmons are believed to be dependent on the scaling of the pitch so that the pitch length and the distribution of diffraction features are correlated and hence the propagating plasmons can be observed along with the diffraction lines (marked with the white dotted lines in Fig). However the reason why the dispersive surface plasmons cannot be tuned on every diffraction line requires the thorough analysis of the structure even though it could be dependent on the pit size and the nature of

pyramid. The localized plasmons are maintained within the pit and the pit is constant, then the plasmons are fixed at around 550nm and 782nm (marked by blue dotted lines in Fig 5.20 (e)) although their intensities are related to the periodicity.

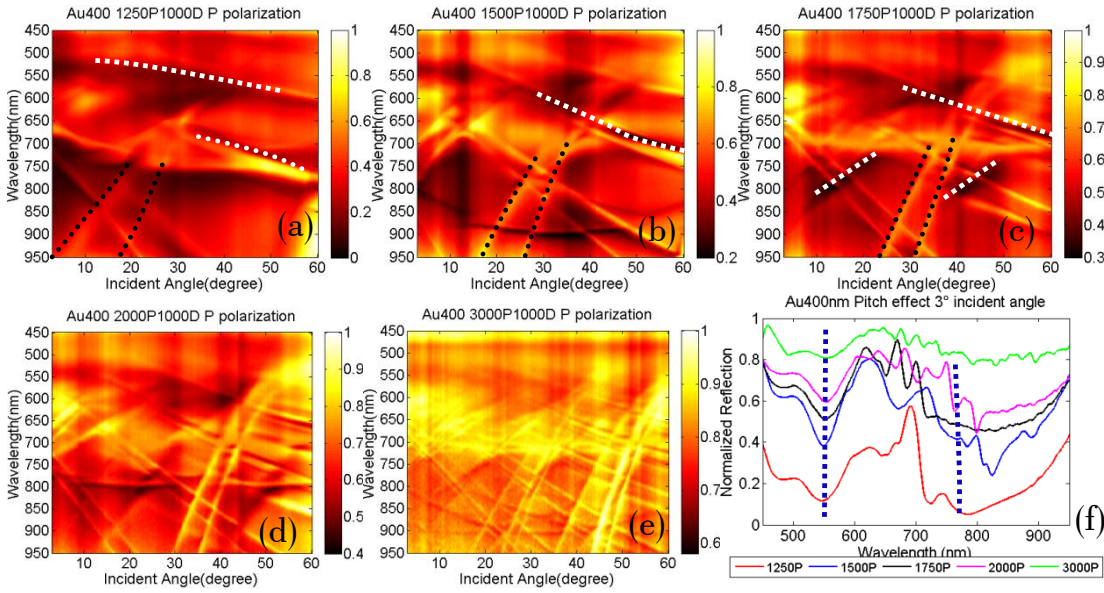


Figure 5.20 Dispersion maps for different pitch length at 1000nm pit size; (a) 1250P (b) 1500P (c) 1750P (d) 2000P (e) 3000P (f) Line graph of the normalized reflection as a function of wavelength at the 3° incident angle for different pitch. Blue dotted lines show the tuning of the localized plasmon for 1000nm pit size. White dotted lines are guiding the examples of the dispersive plasmons propagating along with the diffraction lines. Each set of black dotted lines are guiding the shift of wavelength to the infrared region when the pitch is increased.

5.3.3 Pit size dependent localized plasmon

Pit size of a fabricated test structure is varied from 500nm to 1250nm in 250nm steps with a constant pitch (1500nm). Hence pit depth will change by the relationship of $(\text{pit size}/2) \times \tan(54.7^\circ)$. By measuring the reflection map using the reflectometry system described in chapter 4, it is possible to identify the plasmon behavior in relation to the expectations of the simulations. As discussed before, changing the pit size does not affect the diffraction lines in the same way as change in pitch because the diffraction distribution for all pit sizes is very similar in the reflection maps (Fig 5.21 (a-d)). The tuning of the plasmon resonance however is effected by the pit size as shown in fig 5.22. This shows how the normalized reflection as a function of excitation wavelength varies with change in pit size. As the previous simulation suggested all plasmons modes become shifted to longer wavelengths

when increasing the pit size as shown in Fig 5.22. In Fig 5.22, three plasmon modes are analyzed named mode-1, 2 and 3 and data is tabulated in Table 5.3. At close inspection, the plasmon mode tuned at the near infrared region (mode1 and mode3) gives larger magnitude in shift to the infrared region when the pit becomes larger while the plasmon mode-2 at the visible region has smaller shift to the infrared region. The change in absorption intensities is dependent on the fill factor but the increase in absorption for the near infrared region is not linearly proportional to the fill factor, such that a small initial (250nm-step) increment in fill factor(varying the pit size from 750nm to 1000nm) results in 35% improvement in absorption whereas a second 250nm-increment in fill factor (1000D to 1250D) gives only 4.2% enhancement in absorption for the plasmonmode-1 while the mode-2 has only 1% improvement in the second increment in the fill factor. It is noticed that 250nm spacing between adjacent pyramids defines a limit for fill factor to obtain the maximum absorption in the near infrared region. There will be no great improvement in absorption by reducing the spacing to less than 250nm.

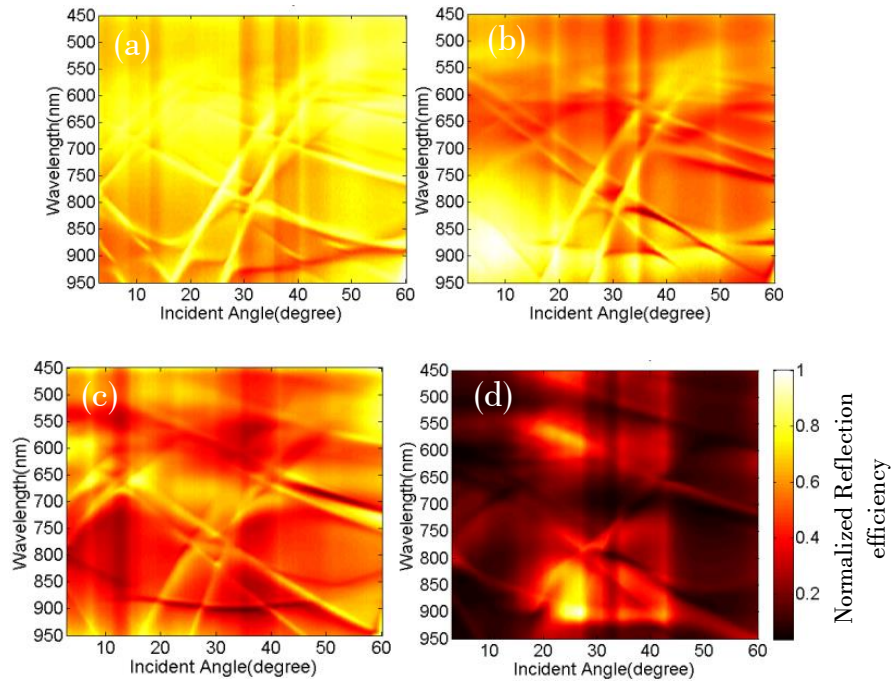


Figure 5.21 Dispersion maps for different pit sizes with 1500nm pitch length (a) 500D; (b) 750D; (c) 1000D (d) 1250D

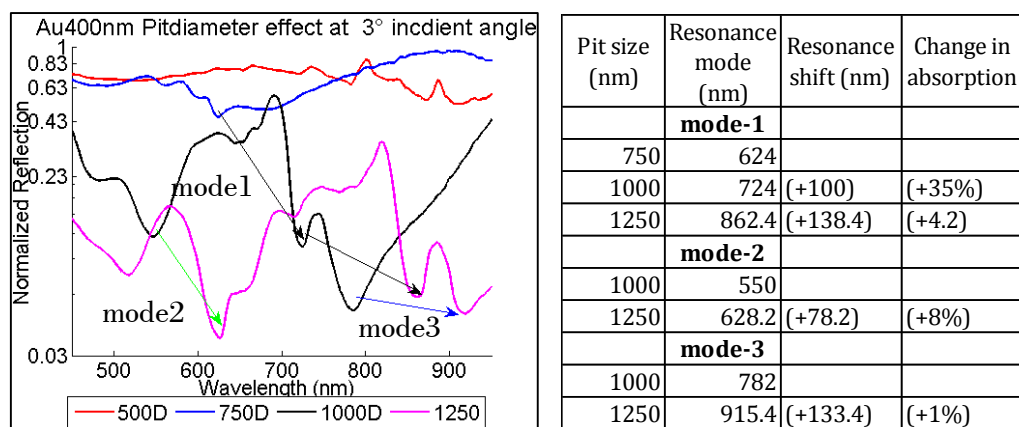


Figure 5.22 Left: Characterization for the normalized reflection as a function of wavelength for the different pit sizes (the data are collected at 3° incident angle under TM-polarization). The arrows are guiding for the shift in wavelength of the plasmon resonance corresponding to the pit size.

Right: Table 5.3: Analytical data representing the plasmon mode with their change in resonance and absorption intensity for the different pit size.

5.3.4 Inverted pyramid with high fill factor

Further investigation is carried out with the high fill factor design (250nm spacing between adjacent pyramids) for a range of pitch (1000P750D, 1250P1000D, 1500P1250D, 1750P1500D and 2000P1750D). The study is conducted for the normalized reflection at 3° incident angle under p-polarization. The fundamental plasmon mode of the inverted pyramid (which is marked by the black dotted circle in Fig 5.23) which is the reason to enhance the Raman scattering of molecules deposited on the SERS active substrate, shifts to the infrared region (the lower energy) due to the result of change in the pit size. However since the spacing between the pyramids is maintained at 250nm, the high absorption intensity can be achieved for the SERS active substrates such as the absorption intensities are 89.85%, 94.98% and 95.16% for the 1000P750D, 1250P1000D and 1500P1250D respectively. This fundamental plasmon mode consists of two simultaneous excitation resonances resulting from the nature of the asymmetric (rectangle) inverted pyramid and support to tune the scattering in and scattering out of photon in resonance concertedly which is a most necessary feature for SERS applications. This fundamental mode could not be maintained in the near infrared region for the 1750P1500D and 2000P1750D designs due to the consequence of the larger pitch effect. However those designs occupy the different plasmon resonance around near infrared region (marked by the red dash lines) which can be used as an excitation wavelength for the SERS applications although they

could not match the current Raman laser line and hence could not produce high enhancement in sensitivity for the available Raman lasers such as 532nm, 633nm and 785nm.

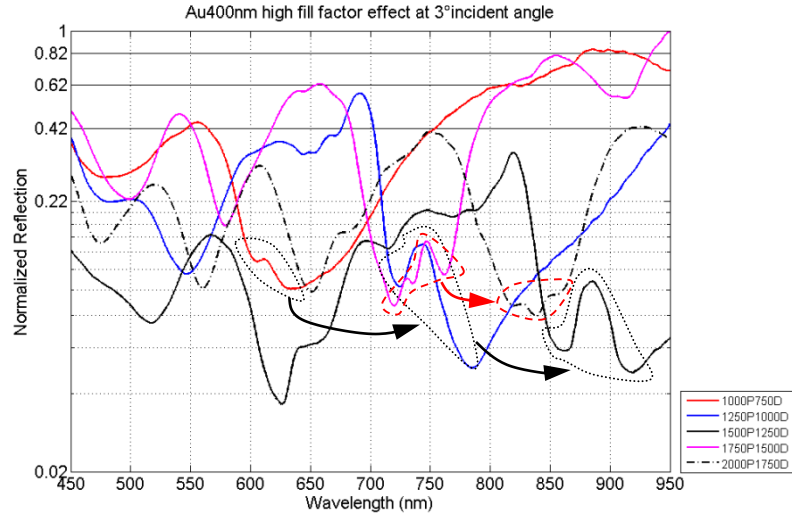


Figure 5.23 Characterization for the normalized reflection as a function of wavelength for the high fill factor with different combination of pitch and pit size (the data are collected at 3° incident angle under TM-polarization).

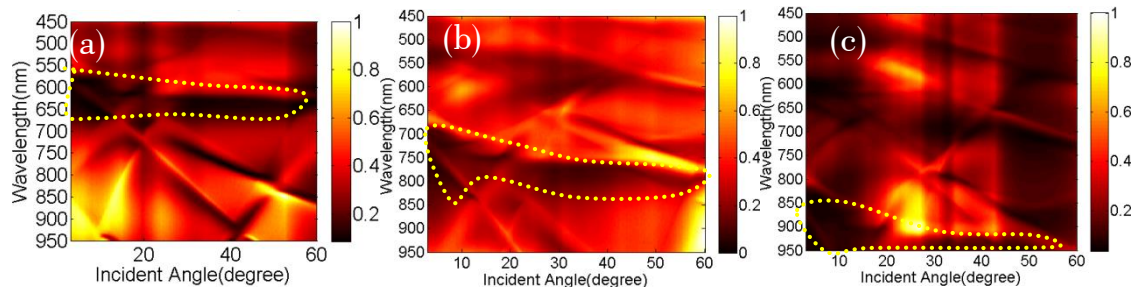


Figure 5.24 Dispersion maps for the different SERS substrates maintaining the fixed spacing between the pyramids as 250nm: (a) 1000P750D, (b) 1250P1000D (c) 1500P1250D. Yellow dotted lines are guiding for the shift of plasmon mode.

The fundamental plasmon modes which are shifted within the near infrared region for whole specular angles are shown in Fig 5.24 in which the yellow dotted lines are guiding the shift of the plasmon mode to the longer wavelength within the infrared region. Among all the high fill factor designs, the 1250P1000D design is recommended to achieve the high enhancement in SERS mechanism for sensor applications with Raman spectroscopy since it offers the high plasmon resonance tuning at the 785nm which is the excitation laser readily available in the Raman system.

5.4 SERS intensity analysis with Raman spectroscopy

First Raman measurements for the silicon based inverted pyramid SERS substrate are performed for all geometrical parameters with the respective aspect ratio (REC1:1.0, REC1:1.1, REC1:1.2, REC1:1.3). Measurement parameters are: x20 magnification (N.A=0.4, collection cone is the range from -14.5° to 14.5°), 0.2mW power with 10 seconds exposure time to increase the signal to noise ratio. The operational wavelength used for this measurement is 785nm. Give a care to the focus to obtain the signal from the center of the pit/cavity if the measurement is carried out with high magnification. Measurements are always collected in 7 different positions and averaged. Test molecules used here is benzenethiol which is deposited as described in section 4.3.1.

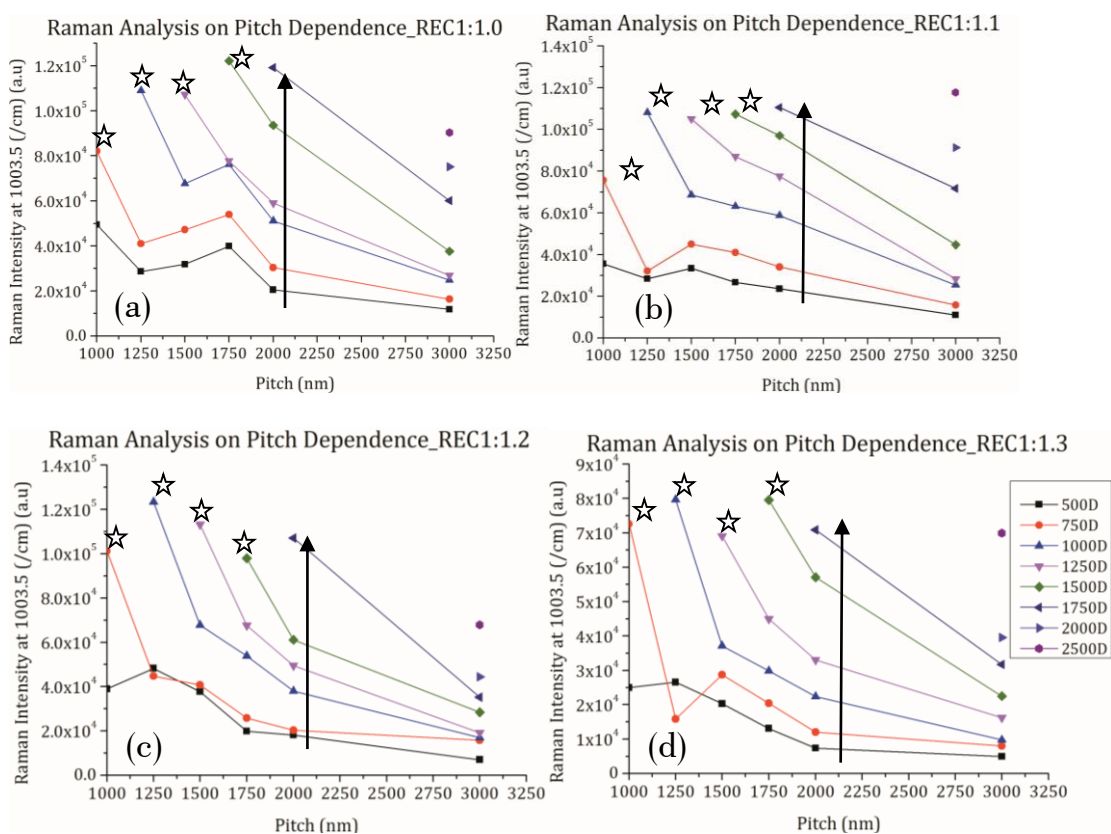


Figure 5.25 Line graphs showing for the Raman intensity of the trigonal ring breathing mode of thiol molecules are given for different aspect ratio. Raman intensity is represented as a function of the pitch length for different pit sizes. (a) REC1:1.0 (b) REC1:1.1 (c) REC1:1.2 (d) REC1:1.3. The black arrows are guiding for the enhanced Raman intensity by increasing the pit size. The star symbols are markers for the SERS active substrates which are composed of pitch and pit size for the high fill factor.

In Fig 5.25, each graph describes the Raman response of test molecules to the geometrical parameters of the inverted pyramid in such a way that the x-axis is the pitch length for each

aspect ratio and the y-axis is set for Raman intensity of every pit size influenced by the pitch. Therefore, the effect of pitch with constant pit size on the Raman effect could be easily observed such as Raman intensities of each pit size are scaled with the pitch length/periodicity. For example, the intensity from 750nm pit pyramid (Fig 5.25 (c) REC1:1.2) shown by red-line is sharply decreasing with increasing the pitch length. In addition, a fact is also observed that, increasing the pit size allows to increase the Raman intensity due to the formation of large area to confine the more localized trapped plasmon/e-field within the cavity and the another reason is the tuning plasmon resonance is shifted to the near infrared region as large as the pit size and hence matching with the current excitation wavelength, 785nm for Raman measurement. As for example, the black arrows are given as a guide for increasing Raman intensity together with the increased pit size. Also the graph allows us to observe that the Raman SERS counts rise together with the fill factor ($\frac{\text{pit size}}{\text{pitch length}} \times 100\%$). In Fig 5.25, the star symbols mark the developed Raman intensity due to the influence of the fill factor ranging from 75% to 85%. From Fig 5.25, a fact is clearly confirmed that SERS intensity is highly dependent on the geometrical parameters of pit size, pitch length and their fill factor.

Since the assessments from Fig 5.25 point out that the high fill factor with large pit size could enhance the Raman scattering process in every aspect ratio, the questions is how high the fill factor should be and which aspect ratio for inverted rectangular pyramid should be used to enhance Raman intensity more. To answer the questions and achieve the correct parameters for the highest enhancement, Raman data are analyzed for the fill factor with the aspect ratio in Fig 5.26 which is comprised of the two sets of axes in such a way that one set (black axes connected to the colorful dotted line plots) is corresponding to the Raman intensity of the trigonal ring breathing mode of thiol molecules for each aspect ratio varied with the fill factor and an another set (red axes related to the red straight line) is considered for the normalized Raman counts only for the 80% fill factor as a function of aspect ratio. The Raman intensity is not linearly increased with the fill factor. The intensity is increasingly improved till the 80% fill factor and drop down then till the 86% fill factor after that rising again. The behavior of the Raman intensity profiles for the different aspect ratios are mostly in the same trend. Comparing the effect of fill factor among the inverted pyramids with different aspect ratios, the SERS counts are distinctly gained by increasing the aspect ratio at 1:1.2 but when the aspect ratio is increased to 1:1.3, the inverted

pyramid does not follow the aforementioned principle probably due to the deformation of the localized dipole e-field supporting the coupling efficiency. According to the fill factor analysis the 80% fill factor offers the highest enhancement, the normalized Raman intensity of the inverted pyramid with 80% fill factor is therefore particularly examined for the different aspect ratio (shown by red-marker-line). It proves again that the highest Raman SERS counts belongs to the design made by 80% fill factor based on the 1:1.2 aspect ratio. The optimized geometrical parameters of the inverted pyramid have finally concluded such as the aspect ratio of 1:1.2 with the 80% fill factor composed by the 1250nm pitch and 1000nm pit size.

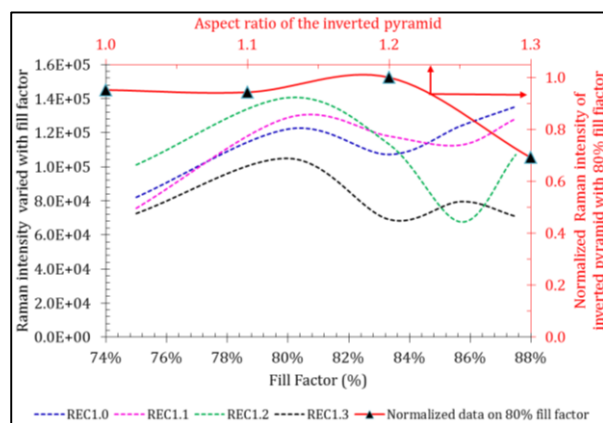


Figure 5.26 Line graph composed by two sets of axes: black axes represent the Raman intensity of the different aspect ratio as a function of fill factor (dotted lines) and red axes act for the normalized Raman intensity of the inverted pyramid made up of 80% fill factor, as a function of the different aspect ratio.

5.5 SERS comparison of an optimized design with standard Klarite

Figure 5.27 shows the comparison of SERS spectra recorded for benzenethiol between standard Klarite and an optimized inverted pyramid which is a 1250P1000D with the 1:1.2 aspect ratio. Measurements are performed using x20 magnification and 10 seconds exposure time with 0.2mW power and 785nm excitation wavelength. Table 5-3 describes a list of improved SERS counts for individual vibrational frequency of test molecule, by the optimized design. The overall average improved intensity by the optimized design is 8 times higher than standard Klarite although the intensity of in-plane CH deformation is

improved by 10 times. This developed enhancement is mainly due to the mixmode of the plasmon, coupling of the localized trapped plasmon inside the cavity to the delocalized plasmon evanescent on the slope sidewall as discussed in section 5.2.2.1. Another reason of improving enhancement by the optimized design is due to the asymmetric rectangular based inverted pyramid providing two simultaneous plasmon resonances at 724nm and 782-820nm in experimental result and at 750nm and 815nm in simulation result (as discussed in section 5.3.4 and as shown in Fig 5.23) to support the coupling photon in both direction of scattering in and out of the molecules. Figure 5.27(b) gives the comparison of normalized reflection between standard Klarite and the optimized design from which the aforementioned phenomenon can be clearly seen. The symmetric square base Klarite has only single resonance at around 750nm while the asymmetric rectangular based inverted pyramid has double resonance (one is at 724nm and other is from 782nm to 820nm) which could support to couple the incoming light with the light of both scattered in and out of the molecule. As a supporting evidence, the scattering wavelength, λ_{stokes} for each Raman shift of the vibrational mode of BTh molecules using the equation:

$$\text{Stokes wavenumber shift, } \Delta\omega = \left(\frac{1}{\lambda_0} - \frac{1}{\lambda_{\text{Stokes}}} \right) \times 10^7 \left(\frac{\text{nm}}{\text{cm}} \right) \quad (5.1)$$

where λ_0 is the excitation wavelength, 785nm. The solved scattered wavelength for each Raman shift is tabulated in Table 5.3, 3rd column and those wavelength are pretty much close to the broad absorption mode of the localized plasmons.

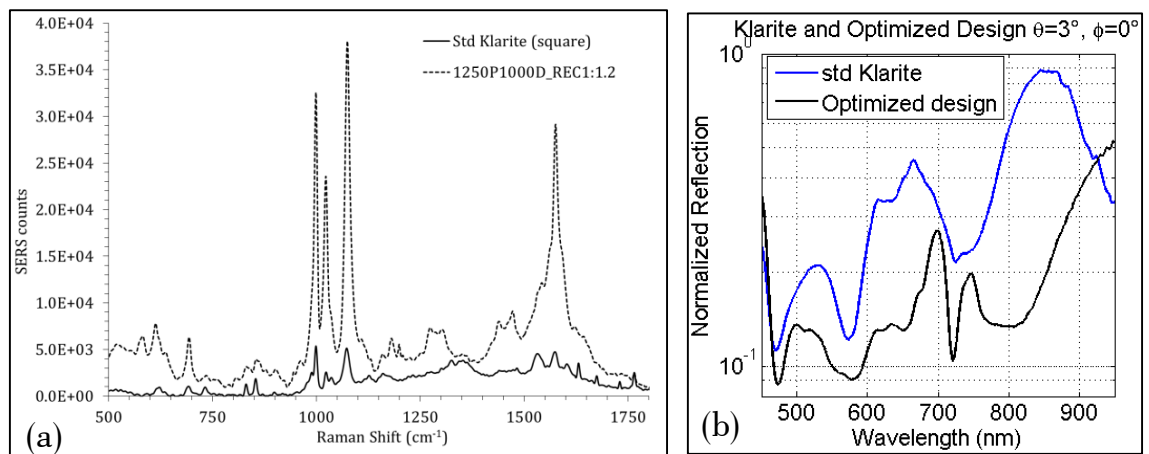


Figure 5.27 Comparison of SERS counts between standard Klarite and the optimized inverted pyramidal structure: (a) Raman spectrum of BTh molecules, (b) Reflection spectrum at 3° incident angle without azimuth angle.

Table 5-3 List for the improved SERS counts by the optimized design compared to standard Klarite for Benzenethiol test molecules and respective stokes wavelengths for the vibrational mode of molecules

Raman vibrational frequencies (cm^{-1})	Improved SERS counts	Scattered Wavelength, λ_{stokes} (nm)
Ring deformation (615-630)	931%	824.95
Trigonal Ring Breathing (990-1010)	636.4%	851.91
In-plane CH deformation (1015-1030)	1050.85%	853.643
CC stretches, 1075	780%	857.38
Ring stretches (1550-1630)	648.24%	895.97
Average	809.298%	

To understand the relationship between SERS counts and the geometrical parameters of the inverted pyramid, pitch and pit effect are analysed for the Raman counts of the trigonal ring breathing mode of the test molecule. And the geometrical effect on the SERS counts is shown in Fig 5.28 in which the x-axis represents the change in pitch length for the 1000nm pit size and the change in pit size for the 1500nm pitch length in the nanometer scale and the y-axis represents their Raman intensity of trigonal ring breathing mode of BTh. Remaining the pitch length at 1500nm and increasing the pit size result in the increase in Raman intensity exponentially (shown by red symbol and the red dotted line). However, maintaining the pit size at 1000nm and increasing the pitch length lead to the decrease in Raman intensity exponentially (shown by green symbol and the green dotted line). The coefficients of the exponential fitted curves are 1.53×10^4 and 3.85×10^5 for the pit effect and for the pitch effect respectively. Therefore, a fact can be observed that the pitch effect on the SERS counts is more influenced than the pit effect as the coefficient of the pitch effect is 10-fold larger than that of the pit effect at the excitation wavelength of 785nm, near infrared region.

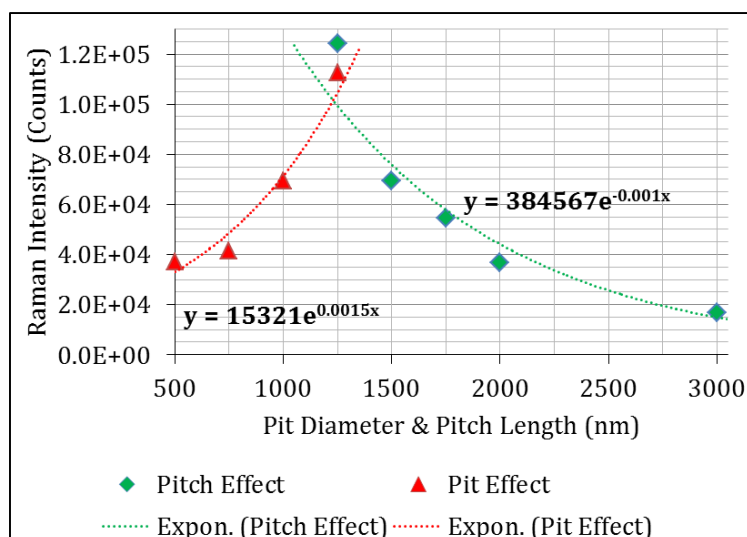


Figure 5.28 Diagram which shows the Raman intensity as a function of change in pitch length and pit size. Raman count is extracted from the Raman spectrum of BTh molecules for the trigonal ring breathing mode. The red symbol is for the Raman intensity of the pit size effect and the red-dotted line refers to the exponential fitted curve. The green symbol is for the Raman intensity of the pitch length effect and the green dotted line represents the exponential fitted curve.

5.6 Effect of polarization

5.6.1 Raman SERS counts

The Invia Raman system has a motorized polarizer which can be set for the three different polarization sets which affect the polarization of the laser such as the normal, the orthogonal and the circular. For the circular polarization, the quarter (1/4) waveplate has been fixed prior to the sample while the half (1/2) waveplate is fixed for the orthogonal condition. Under normal polarization, no waveplate is involved so that the lasers are all polarized from the source and this is equivalent to the x-axis of the sample. Note that there is no polarization setting on the detection scheme of this Raman setup. This can be seen in Fig 5.29 which is the schematic drawing for the laser path to the sample in Raman system. For simplicity, here only the normal polarization is applied to the sample so that the input polarization will act as TE-polarization to the sample at 0° sample rotation while the sample is rotated to 90° the input polarization will treat as TM-polarization to the sample. This polarization is defined as discussed in the section 4.1.1.1. Therefore, in Raman measurement, 0° sample rotation and 90° sample rotation can be defined as the TE- and TM-polarization, respectively. Raman measurement is carried out with 785nm excitation

wavelength for both standard Klarite and the optimized design using BTh test molecule and tabulated Raman intensity from trigonal ring breathing mode of BTh as shown in Table 5.4. Table provides the information of Raman intensity corresponding to the input polarization for both designs. Raman intensity of molecule from the optimized pyramid has over 2-fold improvement in the TM-polarization state, compared to the TE-polarization state. However, Raman intensity of molecule from Klarite does not respond significantly to the input polarization. From this observation, a fact can be concluded that the optimized design has a property that is sensitive to the polarization due to the asymmetric rectangular based structure while the symmetric square based Klarite does not own this property.

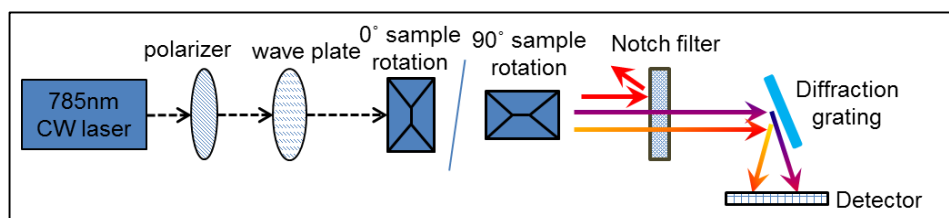


Figure 5.29 Schematic diagram gives a brief view of laser path to sample in Raman system

Table 5-4: Comparison of Raman intensity from trigonal ring breathing mode of BTh for different input polarization

Nanostructures	Raman Intensity from trigonal ring breathing mode of BTh	
	0° sample rotation	90° sample rotation
The Optimized design (rectangular based pyramid)	25000	60000
Standard Klarite (square based pyramid)	38504	34627.8

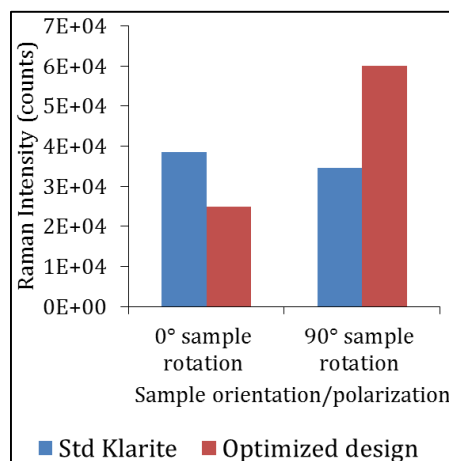


Figure5.30 Column chart gives Raman intensity corresponding to the input polarization state for Klarite and the optimized pyramidal structure

5.6.2 Polarization Conversion

The experimental arrangement used which was described detail in chapter-4, to examine the polarization effect is schematically described in Fig 5.31 where radiation from the broadband laser is TM-polarized and directed onto the rectangular inverted pyramid and the spectrometer collect the zeroth order specular beam passing through a second polarizer which can be set to pass either the TE-polarized or TM-polarized component. The dispersion map is the result of processing the ratio of the TE-polarized reflected intensity to the incident TM-polarized intensity as a function of θ , called as TMTE while the TMTM dispersion map is treated at the second polarizer set to collect the TM-polarization. By comparing the signal of TMTM to TMTE at 750nm resonance for different values of ϕ (azimuthal rotation/sample rotation), absolute magnitude of the TM to TE conversion can be observed as shown in Fig 5.32 (c) where the y-axis is represented in log scale. This section describes only the preliminary results of the polarization conversion from the inverted pyramidal grating, therefore the discussion will not go in depth analysis. The TM to TE conversion is measured for the gold coated inverted pyramid composed by 1250nm pitch 1000nm pit size, rectangular aspect ratio, as a function of incident angles for different values of azimuth angle, ϕ .

Figure 5.32 has the three rows and columns where the row represents the each azimuthal angle 0° , 45° and 90° while the first column refers to co-polarized reflection map, 2nd columns to cross-polarized reflection map and 3rd column shows the comparison of normalized reflection for co- and cross-polarization at 750nm resonance where the absolute magnitude of TM-TE conversion can be observed. Note that all these data in Fig 5.32 are already processed as described in the previous paragraph. Polarization conversion enriched by surface plasmon polariton in grating was studied and noted that polarization conversion is zero at $\phi=0^\circ$ and 90° as the grooves in 2 dimension are perpendicular and parallel to the incident plane respectively [133]. Unlike 2D grating, due to the 3D nature and pyramidal structure, the polarization conversion still can process at $\phi=0^\circ$ and 90° as shown in Fig 5.32. In 3D gold coated inverted pyramid, it can be clearly observed that the plasmonic distribution together with diffraction features in co- and cross-polarized reflection map perform very different for different azimuthal angles.

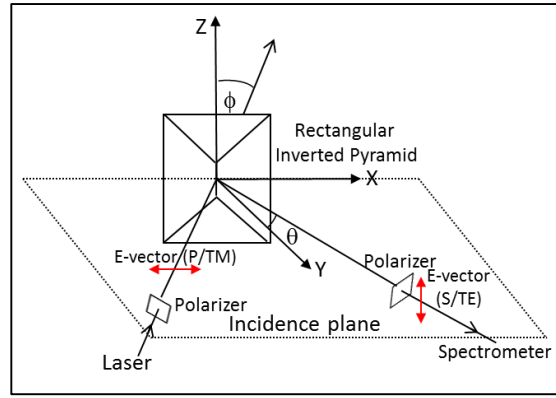


Figure 5.31 Schematic diagram shows the condition of reflection measurement system with the sample

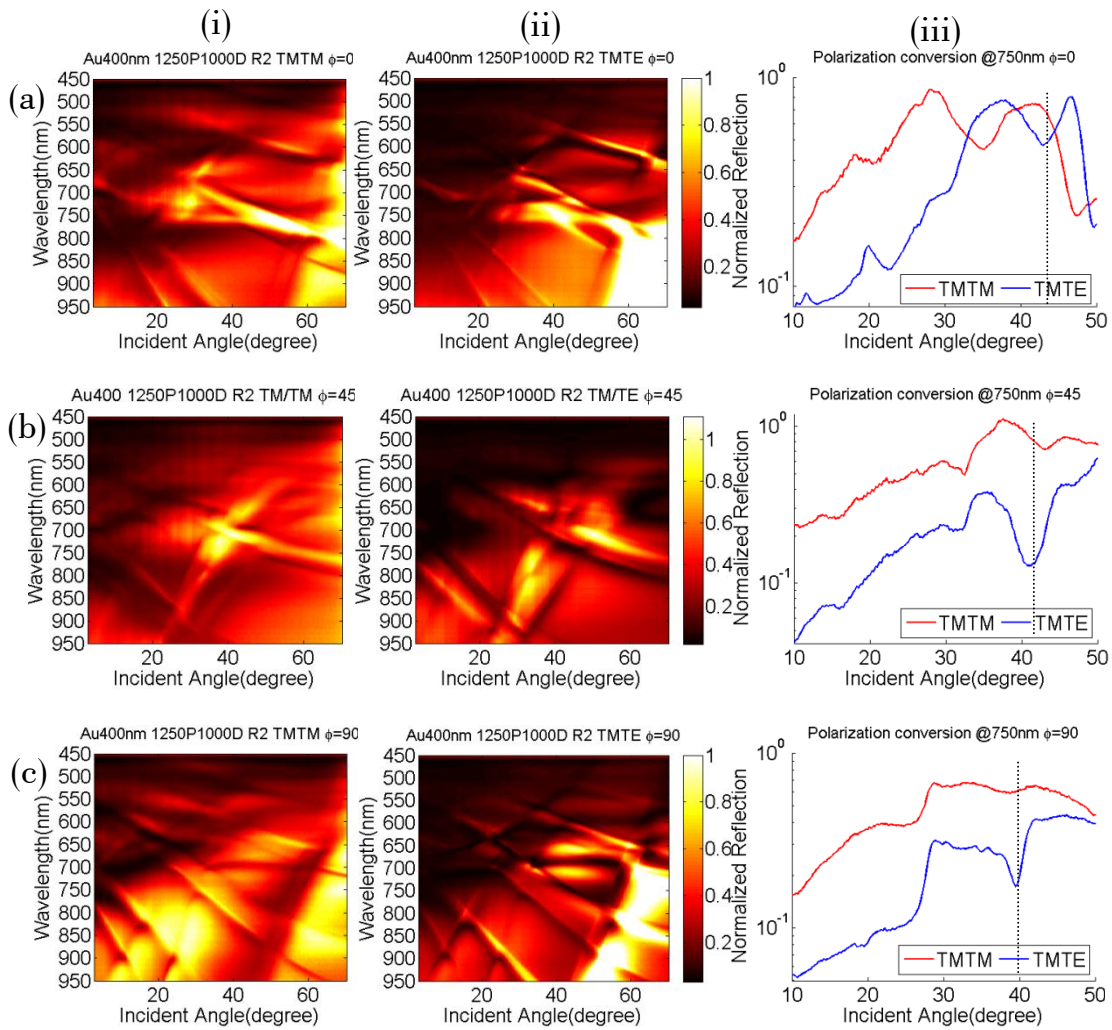


Figure 5.32 Dispersion maps after processing with the incident TM-polarized light; (a) azimuth angle, $\phi=0^\circ$, (b) $\phi=45^\circ$, (c) $\phi=90^\circ$, (i) co-polarization, (ii) cross-polarization, (iii) polarization conversion

From the dispersion maps of Fig 5.32, it can be seen that the localized resonance is simply located at 750nm for the various azimuth angles, although due to the asymmetrical lattice, the polarization has effect on the incidence field when the far from the normal incidence, resulting in the different coupling process between the incident photon and plasmon at the interface. In cross-polarization, the TM-TE conversion occurs at $\theta \approx 40^\circ$ for various azimuthal angles. At $\phi = 45^\circ$ the maximum TM-TE conversion, 72.41% is occurred through the surface plasmon absorption and then reradiate to the TE-radiation.

5.7 Conclusion

This chapter discussed about the detail fabrication process of the anisotropic KOH wet etching and angle gold deposition and issues with potassium redeposition in wet etching and gold spitting with the metallization. Design and simulation on the inverted pyramid was carried out to find out the effect of geometrical parameters on the plasmonic behaviour such as changing the pitch length affects on the diffraction distribution and hence propagating surface plasmon while the change in pit size has the responsibility of tuning the localized surface plasmon within the cavity. From this understanding, the optimal geometry combination is decided for the inverted pyramid as 1250nm pitch length and 1000nm pit size. This hypothesis from simulation is pretty much same with the experimental results. Again the fill factor ($\frac{\text{pit size}}{\text{pitch length}} \times 100\%$) plays a major role to provide the mix plasmon mode such as the coupling effect either between the delocalized to localized plasmon or between their own kind of plasmon.

Also the experimental results showed that the spacing between the adjacent pyramids, 250nm offers the highest plasmon absorption and the spacing smaller than 250nm will not give any distinct improvement in plasmon absorption expect for the high fabrication cost. In addition to these geometrical parameters, the aspect ratio (width to length) of the inverted pyramid plays in major role such that the inverted pyramid with the asymmetric lattice is highly sensitive to the polarization and showed that over 2-fold improvement in SERS measurement under the input TM-polarization light compared to the TE-polarized light. The inverted pyramid with the symmetric lattice however, showed that less to no sensitive to the polarization. Moreover, it was observed that this inverted pyramidal structure can offer the polarization conversion via plasmon coupling. Finally, it was

demonstrated that the optimized inverted pyramidal SERS sensor has average of 8 times improvement in Raman intensity of BTh molecules, compared to the benchmark standard Klarite.

Chapter 6.

Inverted Pyramid SERS sensor: Plastic Platform

This chapter describes a transfer technique of SERS sensor from silicon to plastic platform for large-area high throughput fabrication. A detail assessment of plastic SERS sensor in terms of qualitative and quantitative sensing quality will be followed on and then characterizes the difference between silicon substrate and plastic substrate. The plastic sensor is demonstrated for real world applications such as pharmaceutical cleaning verification and food monitoring process. The proof of concept for the applications has been achieved by project collaborator, Renishaw Diagnostics Ltd. Moreover, this section discusses about optimization of gold metallization for the plastic SERS sensor. Finally this chapter examines the possibility of dual-sensing configuration, SERS and SPR, for an inverted plastic sensor.

6.1 Transfer from silicon to plastic base platform of SERS substrates

In order to achieve the low-cost and high throughput manufacturing of SERS substrates with the ease of disposal, silicon base substrates are transferred to the polymer/plastic platform. Transfer is achieved using nanoimprinting or nanoimprint lithography (NIL) which has the potential for the low-cost production because it requires less-complicated equipment and is simple to fabricate compared with the conventional lithography system. Polymers are also well known material in fabricating photonic and optical devices due to their properties such as high optical transmittance and versatile process ability at relative low temperatures. The large-area inverted pyramidal nanostructures are fabricated by the use of sheet-level and roll-to-roll (R2R) UV-nanoimprinting manufacturing processes. The developing process for these nanoimprinting techniques are carried out by the project collaborators: VTT Technical Research Centre of Finland, NanocompOy Ltd. (Finland), 3D AG (Switzerland) and Momentive Performance Materials (Germany). In this section, the process flow of both nanoimprinting methods for fabricating large-area SERS structures is reported.

Nanoimprint lithography (NIL) is an embossing method whereby a surface relief pattern is replicated from a mould or template/stamp onto another surface. The pattern transfer process involves embossing a soft polymer layer followed by immediate UV curing. Compared to thermal imprint methods, UV-NIL gives better large-area scalability, feature accuracy and surface quality, all of which are important for optical components. To be able to replicate polymer SERS sensors, the template surface must first be fabricated. A master template fabricated in section 5.1 without metallization, is sent to the project collaborators. There are two steps to fabricate a replicated device. Firstly a master template is replicated onto a mould forming a negative copy master called as an intermediate master/stamp. This is then imprinted onto the final substrate to form the positive replica. For this project, sheet-level processing is used to validate the transfer principle of silicon to plastic platform, and gives also possibility to use plastic copies of the silicon master in the Ni shim fabrication which is the most critical part for successful roll-to-roll processing.

6.1.1 Sheet-level processing

The plastic nanostructures are replicated into Ormocer® plastic using UV imprinting equipment (Obducat Eitre 6). Ormocer lacquer has a refractive index of 1.5 to 1.55 at the near-infrared wavelength range (635nm-800nm). Sheet-level process is illustrated in Fig 6.1. First the silicon master stamp is cleaned and anti-adhesion treated with fluorosilane to ease mould separation after UV curing. UV-curable hybrid polymer material (Ormstamp/Ormocomp) is droplet deposited on 4" BK7 glass substrates. During the mould pressing step, imprint pressures are increased from low values up to around atmospheric pressure (<1bar) giving the several imprinting times to fill in all cavities and areas on the mould. UV curing of the samples is carried out with the exposure time 90-120 seconds resulting in 540-1000mJ/cm² exposure dose. Overexposure is normally allowed to give a secure UV curing of the full material layer, in the direct-patterning. Finally, separation of the glass substrate and silicon master stamp is performed by manually using a doctor blade to release a negative copy of master (also called the intermediate master). Care should be taken in the separation step because the small size of the mould pieces might have a possibility of breaking and chipping. The same procedure is used to fabricate a polymer replica onto the final polymer substrate using the intermediate plastic master instead of the silicon master as a mould.

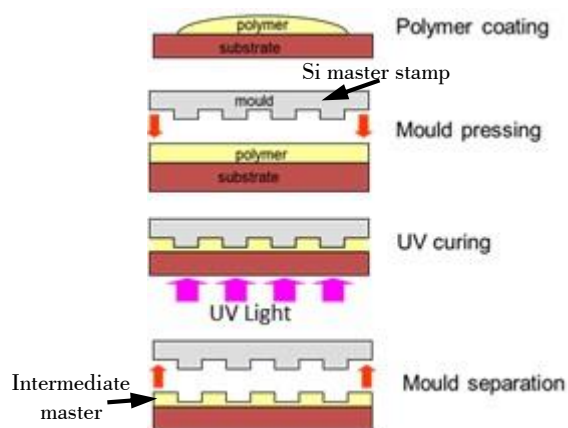


Figure 6.1 Sheet-level imprinting process flow

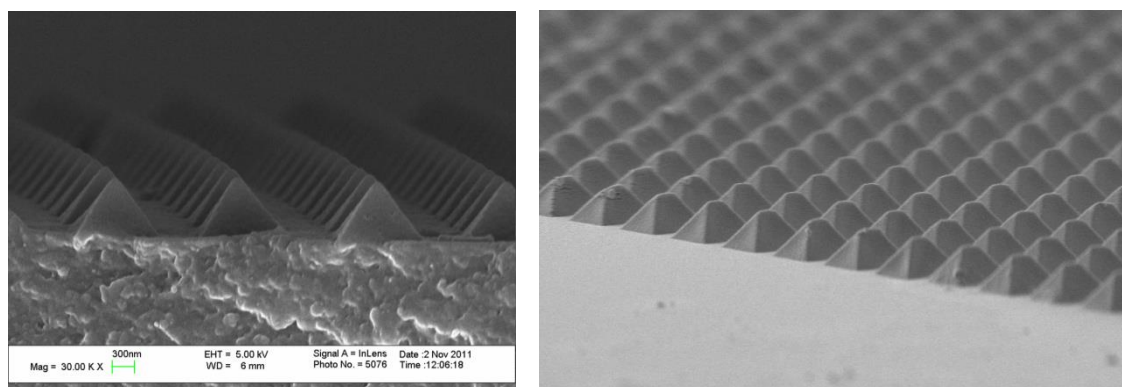


Figure 6.2 SEM images of the negative copy of silicon master, i.e., pyramids

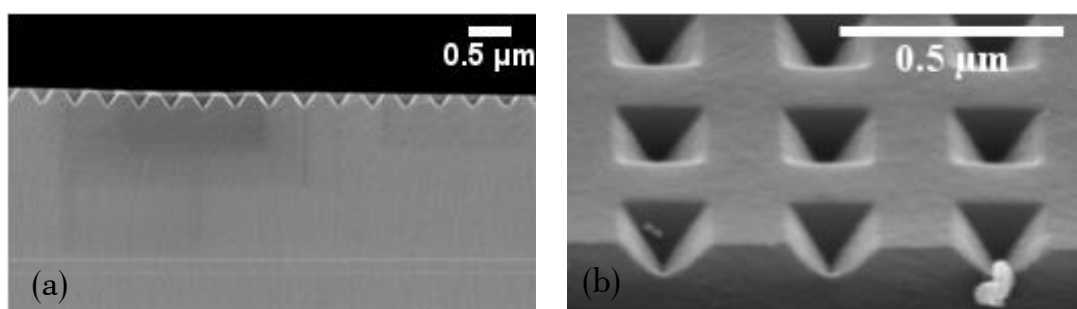


Figure 6.3 SEM images of the plastic replica of silicon SERS substrates (a) cross section image (b) image is viewed at the tilted angle

Imprint qualities of the polymer replica of SERS substrates and the intermediate master are inspected by SEM imaging and they are in good replication quality as shown in Fig 6.2 and Fig 6.3. The assessment of the replicated SERS substrates produced by sheet-level process revealed that nanoimprinting using this kind of plastic materials (Ormocomp/Ormostamp) is basically possible, although large areas of perfect and defect-free substrates could not be

obtained due to the curing issues and the possibility of originating from the high viscosity(2-6 Pa.s) of the polymer material.

6.1.2 Roll-to-roll processing

In roll-to-roll (R2R) UV imprinting process, the following steps are carried out to replicate SERS structure from silicon master to polymer replica such as master manufacturing, Ni-shim electroforming from the master, recombination of structure to large area shim, tool welding, process parameter evaluation, replication and post-processing. The final quality of the polymer replica depends upon each step of the product chain. The properties of UV-curable polymer, such as viscosity and adhesion, are also essential for imprinting processes to fabricate the qualified replicated structures. Therefore, UV lacquer and carrier web pair is experimentally chosen in laboratory by the small unit of UV-embossing manual test before starting the roll-to-roll processing. As the outcome, for the UV lacquers an acrylate polymer Nalax3 (RI=1.479...1.5 at the operation wavelength of 800nm) and for the substrate material PMMA (Poly methyl methacrylate) are introduced by Nanocomp Oy Ltd. The overview process of roll-to-roll UV imprinting process and the work flow of Ni-shim electroforming and large-area recombination are shown in Fig 6.4(a) and (b) , respectively.

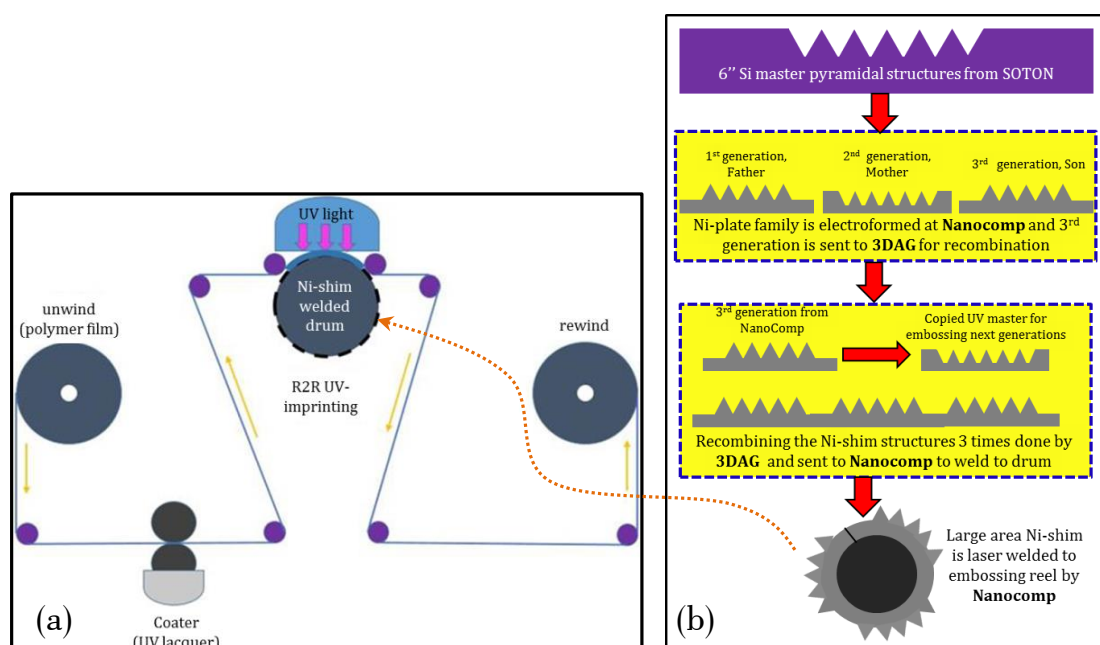


Figure 6.4 (a) Diagram for R2R imprinting process, (b) the work flow for recombination of Ni-shim for large area scale

First a Nickel-shim family is electroformed from the silicon master (without Au coating). In recombination process the UV-step-and-repeat replication of substrates to form a large area Ni-shim with minimum depth loss. A UV master is copied from the 3rd generation electroformed Ni-shim and then the step-and-repeat replication has been carried out with the transparent UV-master. After the replication is successful, the plate is pre-metallized with chemical reductive silvering based on silver nitrate and Hydrazine. The pre-metallized plate is then grown a 300 μm thickness of nickel onto the silver by electroforming. The silver-nickel master is then released from the step-and-repeat polymer plate and followed by passivation with a potassium bichromate on the silver side which is a structure side. An additional electroformed copying step has been made to the sub-master shim with the right polarity of the microstructures which has been laser welded to an embossing reel. Since a PMMA carrier web is used in the R2R process, the PMMA is corona treated to ensure good adhesion between UV lacquer and carrier web. Corona treatment is a process in which the high electrical voltage is created in close proximity to the substrate resulting in high electrical discharge/corona discharge thereby causing partial ionization of the surrounding environment.

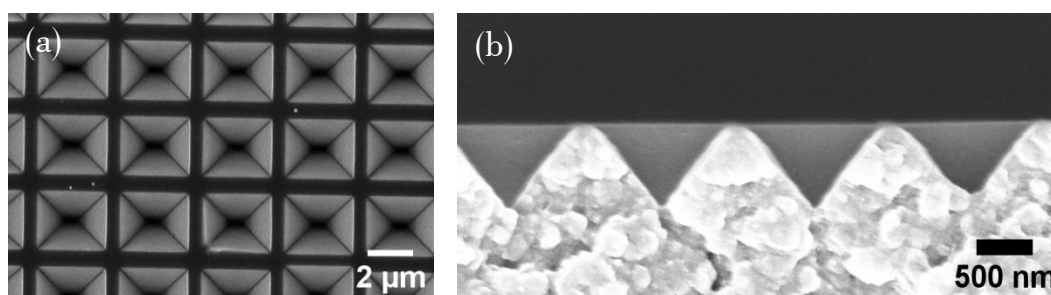


Figure 6.5 (a) SEM image of the inverted pyramid structure imprinting by UV embossed with large-area nickel shim, (b) SEM image of cross-sectional view of plastic inverted pyramid after replication

The resulting environment on the surface have a strong chemical attraction resulting in the enhanced surface energy and hence adhesion. In the second step, UV-curable lacquer is coated on top of the web using a reverse gravure coater. During the embossing phase the SERS structure is replicated onto the lacquer using the embossing reel while the lacquer is cured by UV light exposure through the PMMA carrier film. After embossing, the lacquer is post-cured and a protective foil laminated on top of SERS structure. Fig 6.5 shows the SEM

imaging of the plastic substrates replicated by R2R processing. It observes that the inverted pyramidal structure is very promising for mass-manufacturing due the ease of embossing with the nature of slop sidewall.

6.2 Disposable plasmonic SERS sensor

The successful transfer of SERS sensor from silicon to plastic platform was discussed in section 6.1. This section will evaluate those transfer plastic samples whether their optical response is similar to the silicon master samples and whether the plastic substrates is agreed with the silicon master in the selection of the optimized parameters for inverted pyramid.

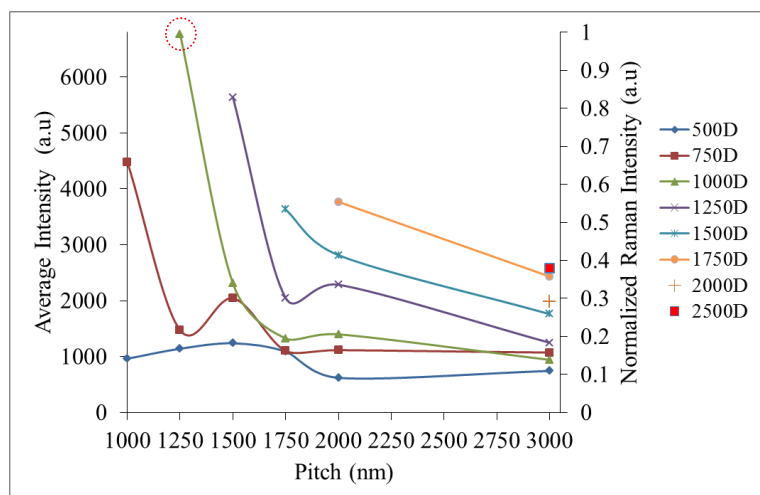


Figure 6.6 Line graph showing for the Raman intensity of the trigonal ring breathing mode of thiol molecules are given for the plastic SERS substrates. Raman intensity is represented as a function of the pitch length for different pit sizes. The red dotted circle is marked for the highest Raman count for the 1250P1000D active SERS substrate.

Raman measurements of benzyl mercaptan deposited on the plastic SERS substrates are carried out for different pitch and pit size at the aspect ratio 1:1.2. Test molecule is coated as discussed in the section 4.3.1. Measurement parameters are such as 785nm excitation wavelength, 44mW power, 10 seconds exposure time with 3 accumulations under x50 objective lens. Figure 6.6 gives the average Raman intensity of Trigonal Ring breathing for different pitch and pit size and follows the same trend as the silicon platform (as seen in Fig 5.25(c) -Raman intensity on pitch dependence for aspect ratio1:1.2) showing that the

identical geometrical parameter combination (1250P1000D-marked by the red circle) has the highest Raman intensity although its value is lower than the silicon optimized design.

Therefore, Raman measurements on the different substrates (Si-master, sheet-level processing and R2R processing) are therefore performed on (REC1:1.2) rectangular aspect ratio for 1000nm pit size varying with pitch length from 1250nm to 3000nm (shown in Fig 6.7(a)). Measurement parameters were: 10mW power, 10 second exposure time, 3 times accumulation and 50xmagnification in all cases. Although 50 times magnification ($N.A = 0.75$) gives an approximate calculated beam spot size is $0.66\mu\text{m}$, the spot size of 785nm line which is captured in the camera is actually of the 10 order of the size of a single pit (the image of spot size is shown in appendix B1). Hence the measured Raman counts are enhanced due to coupling to localized surface plasmons supported by an individual pit and include very limited contributions from propagating surface plasmons corresponding with coupling between neighboring pits although sideways scattering is certainly possible for periodic structures supporting propagating plasmons.

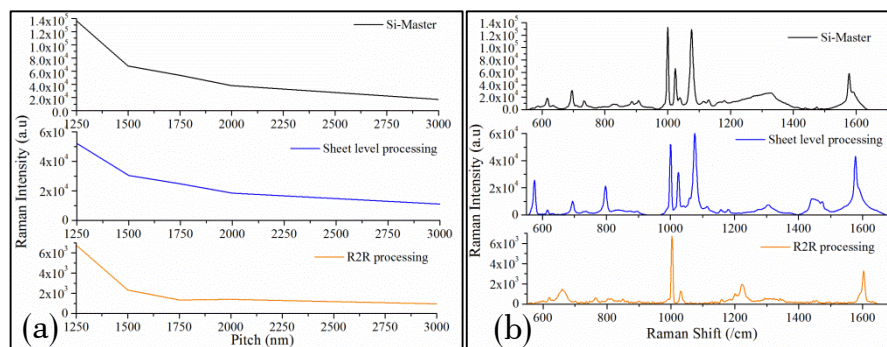


Figure 6.7 (a) line graph showing Raman intensity at 1003cm^{-1} Raman shift of 1000nm pit as a function of pitch length for different base substrates, (b) Raman intensity spectra of thiol molecules for different base substrates of an optimized design (1250P1000D_REC1:1.2)

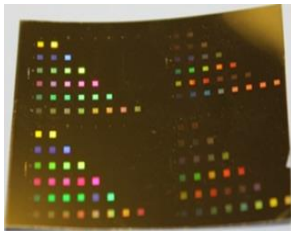
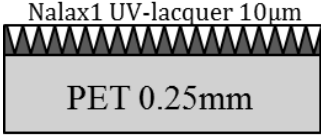
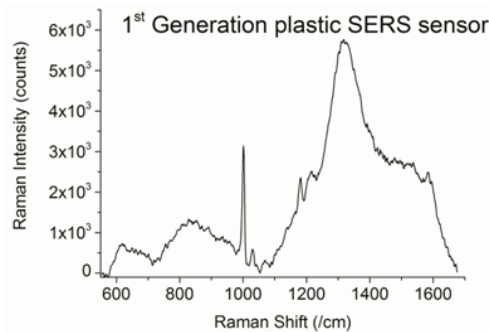
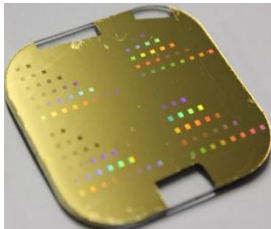
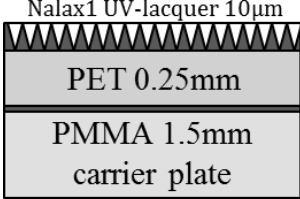
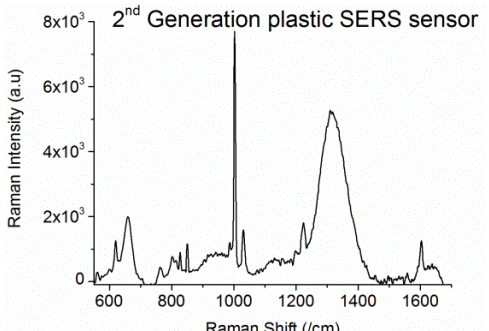
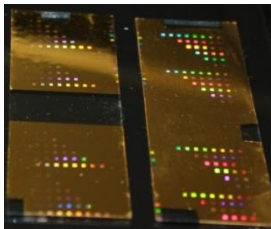
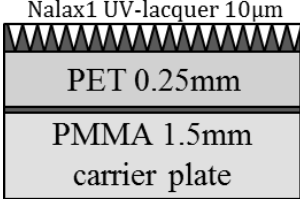
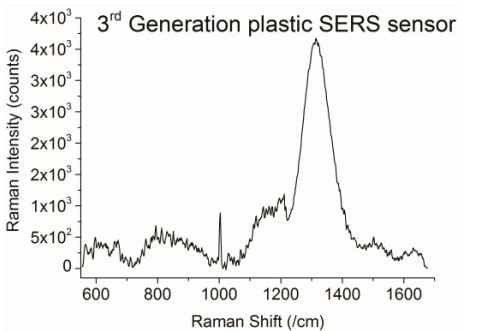
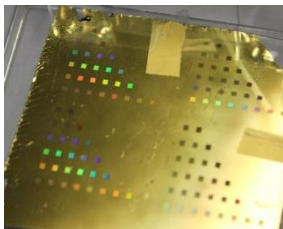
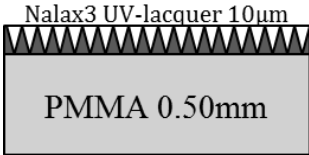
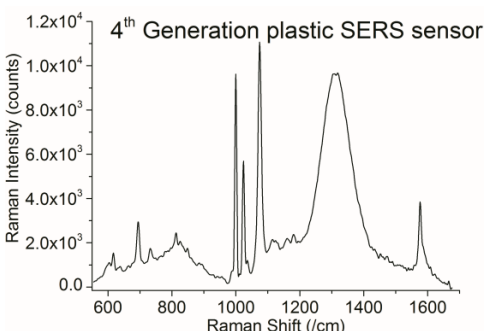
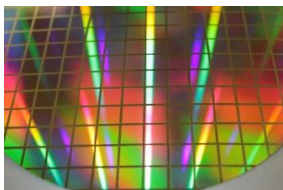
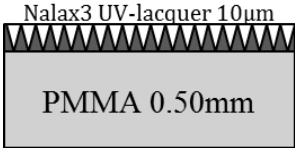
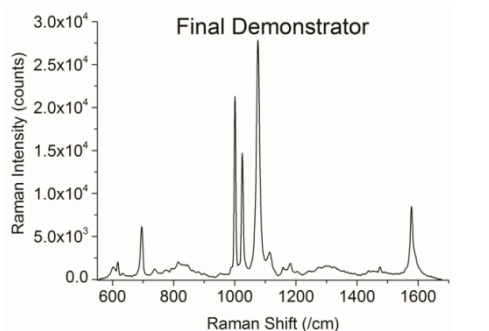
As expected, the trend of Raman intensity as a function of pitch is same for all substrates resulting in the effect of geometrical parameters of inverted pyramid is completely inherited by the plastic substrates. However, Raman intensity from the plastic substrates is lower than the optimized silicon master and the standard Klarite indicating that the sensitivity improvement of an optimized silicon substrate has not successfully transferred to the plastic substrates probably due to the difference in grain formation of gold between the silicon and plastic. The possible reasons will be discussed in the session 6.2.1.

Here the main transfer imprinting technique is considered as the roll-to-roll process for the plastic replica because the sheet-level process is dedicated to produce only for intermediate stamp. The optimization progress of R2R process for the polymer substrates is tabulated in Table6-1. In the table, the three columns represent the photograph of each generation of polymer replica, its schematic structure and the respective Raman spectrum of test molecules of an optimized pattern (1250P1000D) consecutively. Nanocomp Oy. Ltd attempted the total five generations for polymer replica. Three generations are based on the combination of 10 μ m Nalax1 UV-lacquer with PET (Polyethylene terephthalate). 1st generation polymer replica used the 0.25mm PET leading to the difficulty of levelness in metallization step to achieve the uniform metal layer resulting in the loss of improvement in the sensitivity. Therefore, 2nd and 3rd generation replica were attached to the carrier plate made up of 1.5mm PMMA (Polymethyl methacrylate) to attain the surface flatness but it can cause the loss of substrate flexibility. Difference between 2nd and 3rd generation is only the way of cutting the substrate. However, attaching to the carrier plate after imprinting cannot give promising solution to the surface flatness and related gold surface morphology resulting in the variation in the Raman intensity between 2nd and 3rd generation. The variation in Raman intensity can be seen clearly in Fig 6.8 which gives the average SERS counts calculated at the trigonal ring breathing of thiol (990-110cm⁻¹).

Therefore, Nanocomp tried the alternative combination of 10 μ m Nalax3-UV lacquer with 0.50mm PMMA. This alternative combination offers the balance between the flatness and flexibility and the improved Raman intensity. After that using this combination of UV lacquer and carrier web, an optimized design (1250P1000D) is transferred to plastic as a chip with 8x8mm dimension in larger area manufacturing using the Nickel shim welded to the roller and named as the 5th generation or the final demonstrator. Changing the combination of UV and carrier web in imprinting process affects the SERS counts improvement and proves that the intensity of 4G is higher than the previous generation and the final version in high throughput manufacturing eliminates the peak around at 1300cm⁻¹ due to the defect of substrate giving the factor of 7 improvement compared to the 1st generation polymer replica although it won't comparable to the SERS improvement of the optimized design on silicon platform. This improvement is the result of changing the UV lacquer to Nalax3 and the possible reason is below.

Chapter 6 Inverted Pyramid SERS sensor: Plastic Platform

Table 6-1 Optimization progress for the polymer SERS substrates by R2R imprinting process

R2R polymer replica	Schematic structure	Raman spectrum of test molecules
1st generation 	 <p>Nalax1 UV-lacquer 10µm</p> <p>PET 0.25mm</p>	 <p>1st Generation plastic SERS sensor</p>
2nd generation 	 <p>Nalax1 UV-lacquer 10µm</p> <p>PET 0.25mm</p> <p>PMMA 1.5mm carrier plate</p>	 <p>2nd Generation plastic SERS sensor</p>
3rd generation 	 <p>Nalax1 UV-lacquer 10µm</p> <p>PET 0.25mm</p> <p>PMMA 1.5mm carrier plate</p>	 <p>3rd Generation plastic SERS sensor</p>
4th generation 	 <p>Nalax3 UV-lacquer 10µm</p> <p>PMMA 0.50mm</p>	 <p>4th Generation plastic SERS sensor</p>
5th generation 	 <p>Nalax3 UV-lacquer 10µm</p> <p>PMMA 0.50mm</p>	 <p>Final Demonstrator</p>

Nalax1 and Nalax3 are non-commercial mixture, the former is fixed to PET-polymer and the latter is fixed to PMMA-polymer. Those are quite different in the point of chemical consistence. Typically both of lacquers based on the acrylate monomer and oligomer chain so molecular weight distribution is very large range. In mixture have also some aid chemicals for UV-curing function and adhesion promoter. Refractive index difference is quite minimal: RI of Nalax3=1.505 at 532nm and RI of Nalax1=1.500 at 532nm. The refractive index might be varied about ± 0.005 by reason of variation on UV-curing energy and material stability. In practice the surface energy level has some variation between Nalax1 and Nalax3 and hence it will impact on Au coating morphology.

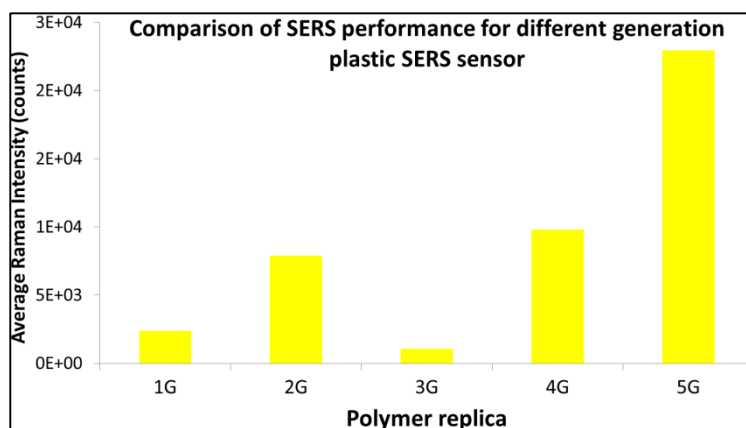


Figure 6.8 Bar chart for the comparison of SERS performance among the various plastic SERS substrates. Raman intensity is averaged for the the trigonal ring breathing of thiol ($990\text{-}110\text{cm}^{-1}$).

Final demonstrator, 5G is improved by a factor of 7 compared to the 1st generation.

Table 6-2 gives the list of performance (in terms of enhancement factor and the on-chip reproducibility) on different types of SERS substrate comparing to the benchmark SERS substrate, KlariteTM. The optimized design on silicon platform enhanced 10 fold in Raman intensity compared to standard Klarite although this SERS enhancement could not successfully transferred to the plastic platform and the possible reasons will be discussed in the section 6.2.1. The calculation of enhancement factor using the area multiplication factor is shown in appendix B. For the consistent of Raman intensity over the substrate area, the reproducibility is calculated over the substrate area approximately $600\mu\text{m}^2$ for the optimized design, Si and 4th generation plastic resulting in <10% reproducibility.

Table 6-2 Performance of the different SERS substrates

Substrate	Enhancement Factor	On chip reproducibility (%)
Klarite™, Si	$\sim 10^7$	8.8
Optimized design, Si	0.4×10^9	<8
Optimized design, R2R imprinting process UV lacquer on PMMA 4 th generation	2.6×10^7	9.4
Optimized design, R2R imprinting process UV lacquer on PMMA 5 th generation	5.23×10^7	59

For the large area fabrication of optimized design polymer replica, the on-chip reproducibility goes down to 59% over the (8x8mm) area and the variability between the chips from a single metallized wafer called chip-to-chip reproducibility also goes down to 63% due to the lack of control in the levelness of polymer wafer during the metallization. The preliminary large area fabrication polymer SERS substrates therefore may not be possible quantitative detection. However the alternative combination of UV and carrier web is offering the improvement compared to that of Nalax1 with PET. This plastic SERS substrate (5th generation) capable of qualitative exploitation in various sensing application and has been demonstrated in pharmaceutical cleaning and food monitoring applications. This demonstrating has been carried out by Renishaw Diagnostics, Glasgow.

6.2.1 Discrepancies between the plastic substrates and the silicon master

From Table 6.2, the qualitative and quantitative performance for the optimized design, the plastic SERS substrates cannot match with those from the silicon platform. Also the enhancement between the different versions of the plastic substrates varied distinctly for the optimized design as shown in Fig 6.8. Therefore the detail characterization on those substrates is performed using the atomic force microscopy and compared with the optimized design, silicon master. The characterization results are shown in Fig 6.9 which shows the extracted profile information across the width of the optimized design as a function of the depth for the different versions. As shown in Fig 6.9 (a), the plastic replica, 1G cannot be successfully transferred from the silicon platform. Its profile is pretty much

flat compared to the sharp tip of the Si master since it is a measurement of the width of the pyramid as shown in Fig 6.9 (b) where the arrow is guiding from which direction the profile is extracted. Also the depth is loss in large amount during the imprinting process. Nanocomp performed the development in the imprinting process and therefore the profile structure and depth of the inverted pyramid are gradually close to the silicon master as I can see in the 4G and 5G profile structures. Therefore the final demonstrator, 5G shows the higher enhancement among all plastic versions. But the final demonstrator still have to be improved its imprinting process to achieve the depth compared to the silicon master. Figure 6.10 gives the depth analysis between the plastic replica and the silicon master where the depth is normalized to the silicon master. The depth of the plastic replica increase generation to generation. However, the 5th generation still has the impairment in the depth quality compared to the silicon master.

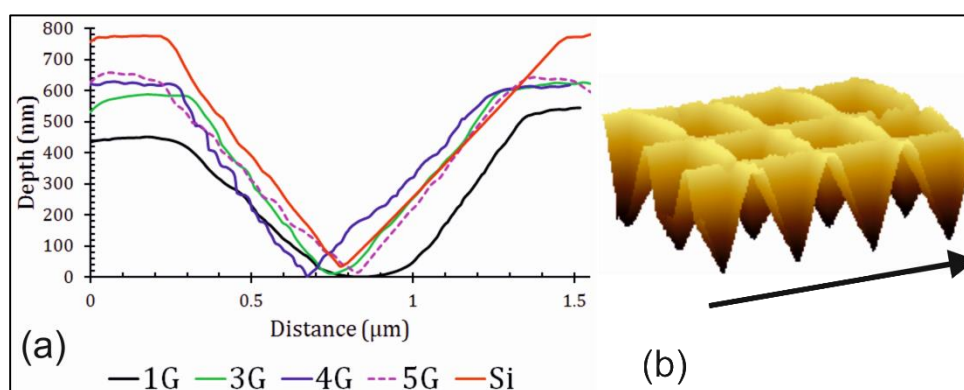


Figure 6.9 (a) Line graph for the cross-sectional profile for the width of the rectangular based inverted pyramid for the different SERS substrates. Y-axis represents the depth for each substrate profile and the x-axis gives the width of each inverted pyramid version. These profiles are extracted from the 3D AFM image as shown in the arrow direction of (b). (b) AFM 3D image for the final demonstrator, 5G.

In addition to the difference in the profile and the depth, the plastic platform SERS substrates have the difference in roughness to the silicon master. The variation of roughness is characterized for the different regions such as the flat surface and the region within the pyramid. For this purpose, AFM imaging and Gwyddion software are used for the AFM data processing. The difference in RMS roughness for the different SERS substrates is tabulated and plotted in Table 6-3 and Fig 6.11 respectively.

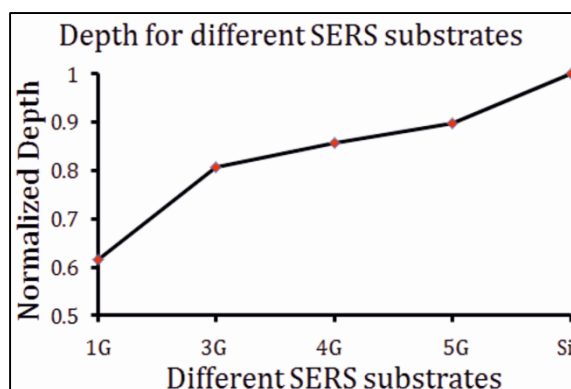


Figure 6.10 Line graph shows the deterioration in depth of the replicated plastic substrates from the silicon master. Depth is normalized to the optimized design, silicon master

Table 6-3 Tabulation for the RMS roughness for the different base substrate for an optimized design

Optimized SERS substrates	RMS roughness (nm)	
	Flat Surface	Inside the pyramid
1G	2.021	3.63
3G	2.307	5.19
4G	2.447	7.29
5G	2.909	5.52
Si, master	2.784	8.3115

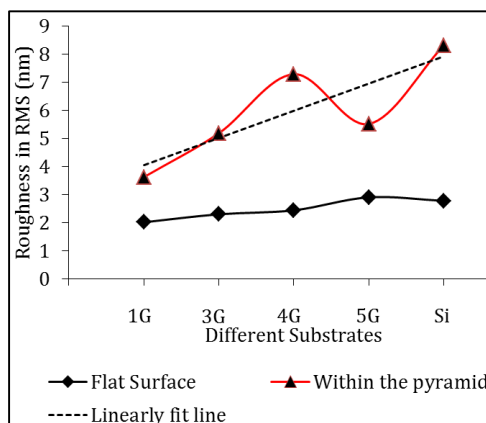


Figure 6.11 Line graph shows the roughness for the different base substrates for an optimized design.

As discussed before in the section 5.3.1, the gold grain height deviation between the flat surface and inside the pyramid is quite high in terms of sub-nanometer scale and therefore the Raman scattering of the molecules can be enhanced by the pyramidal structures rather than the flat surface. From the comparison of roughness for the different SERS substrates, there is no much variation for the flat surface. But the roughness within the pyramid is quite different among the SERS substrates. For example, RMS roughness from the 1G plastic substrate is over 2 times lower than the silicon master. The imprinting process has been developed giving an opportunity to control the waviness of the plastic during the metallization, and hence the gold roughness within the pyramid also improved generation by generation for the plastic platform. However for the 4G and 5G platform, there is still

challenge in metallization to achieve the optimized roughness compared to the silicon master due to the lack of constant flatness in plastic substrate compared to that of silicon. The deficiency in the roughness within the pyramid also leads to the lower enhancement factor for the plastic in addition the absence of the depth.

Also the FFT of the SEM image of Si substrate shows distinct, well-defined first-order peaks as shown in Fig 6.12. Eight first-order Bragg peaks can be observed in the FFT image of Si substrate which reveals the contributions from the ordering of the rectangular structure, which indicates that the image is constituted from the rectangular lattice with sharp edges of the inverted pyramid. The digital FFT of the SEM image for the plastic substrates demonstrate the impairment of gold grain structure on the rectangular inverted pyramid array. The scattering lines are not sharp and almost form only four scattering orders, which indicate the presence of defects in the formation of edges and facet line of the inverted pyramid structure. These defects from the FFT representation indicate the errors in the plastic transfer itself because these kinds of defects in FFT representation can be seen from the plastic substrates before gold deposition.

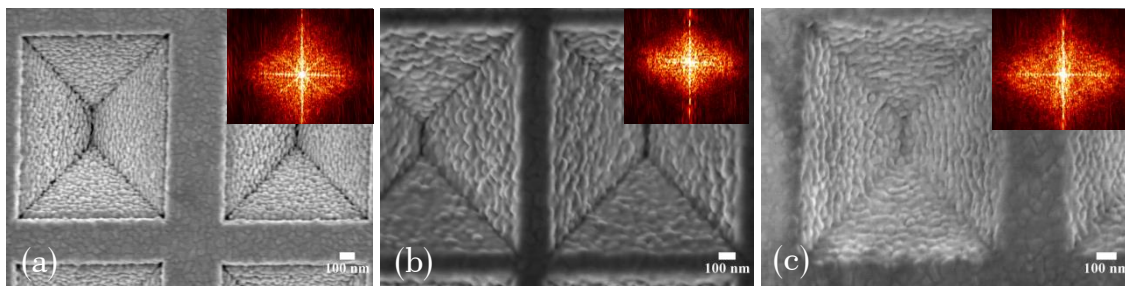


Figure 6.12 SEM images (a) silicon substrate, (b) plastic substrate, sheet-level processing, (c) plastic substrate, R2R processing. Insets are the Fourier/reciprocal space representation of the respective substrate.

The difference in the reflection efficiency between the plastic replica and the silicon master has been shown in Fig 6.13. As expected the plastic (PMMA) and silicon substrates has the difference in terms of the reflection efficiency in such a way that the PMMA has the low reflection as its refractive index is lower than the silicon. However the plasmon distribution is the pretty close between the plastic and the silicon master. Although the plasmon resonance is not exactly agreed with the silicon master, it shows the double

plasmon resonances at 720nm and 780nm of operation wavelength resulting in the possibility of performing Raman measurement using the 785nm excitation laser.

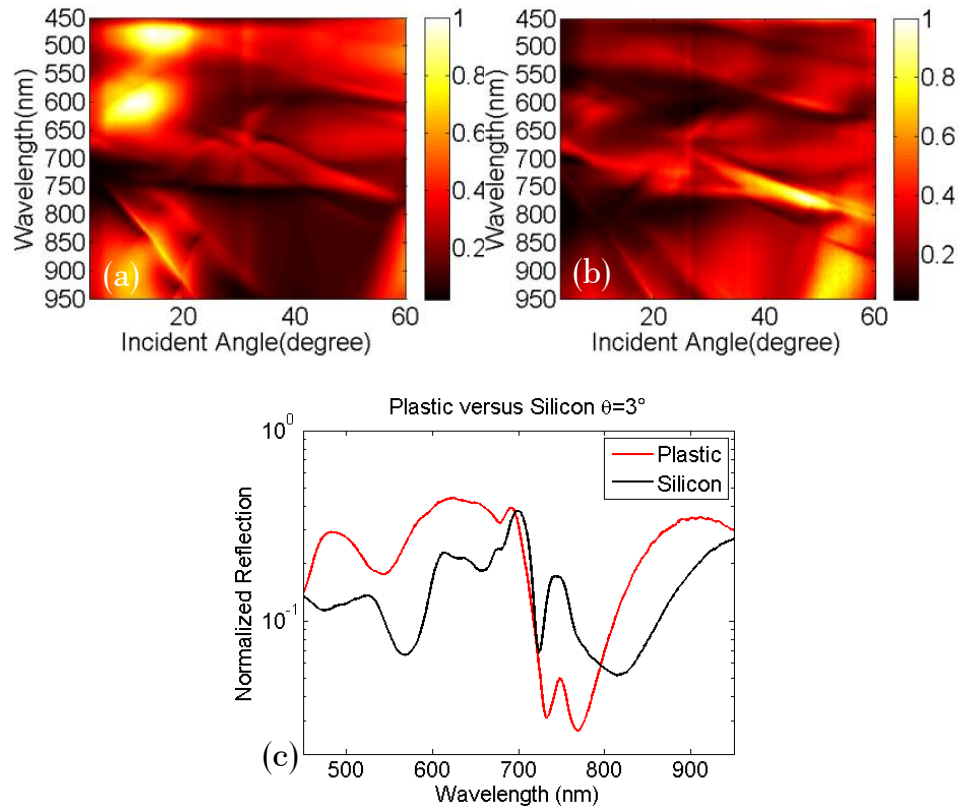


Figure 6.13 The specular reflection maps as a function of the excitation wavelength for different substrates: (a) plastic substrate, (b) the silicon master. (c) Comparison of the normalized reflection as a function of the excitation wavelength at 3° incident angle between the plastic and silicon platform.

6.3 Heading to real world application?

6.3.1 Pharmaceutical cleaning verification

Cleaning verification is essential in pharmaceutical production, as stringent cleaning protocols are extremely important in order to minimize the risk of contamination. There is an identified need for more rapid cleaning verification, which may be carried out away from the centralized testing lab. This section will explore whether or not these plastic substrates are a viable candidate for this application.

The experimental method was as follows. 2 ml of ibuprofen solution at a known concentration was pipetted across the surface of a 5x5 cm aluminium surface and dried on a hotplate at 80 °C. Once dry, a cotton bud (moistened with methanol) was run across the surface in a reproducible pattern. This bud was then placed in a 1.5ml tube containing 0.1 ml of methanol and agitated for 5 minutes to ensure extraction of the target molecules. 10 μ l of the solution was then extracted for analysis on a substrate. This method was repeated for a range of ibuprofen solutions in order to determine the limit of detection. The measurement was carried out using a Thermo Nicolet Almega microscope using a 20x objective lens and a 10 second acquisition time per spectrum and the measured spectra are baseline corrected.

From Fig 6.14, the good qualitative detection of ibuprofen was observed that the distinctive doublet peak at around 810 cm^{-1} is an indicator of the presence of ibuprofen shown by dotted circle. The limit of detection is 100 μM as the 10 μM ibuprofen doublet is not clearly defined, though chemometric data processing may prove to give a more reliable analysis. In further analysis, it should be noted that the cotton bud used to swab the surface was extremely absorbent, so when the bud is placed in methanol a small quantity of methanol is absorbed. Therefore, it is impractical to use an extraction volume below 0.1ml. Also, when pipetting the solution onto the substrate, instead of forming a droplet, the liquid covers the active area. This is due to the low surface tension of the methanol solvent used in swabbing and extraction. This deposited sample dries very quickly on the substrate surface (approximately one minute), giving a short sample preparation time with no need for additional solvent transfer.

Proof of concept for the application of cleaning verification has been achieved. An experimental method involving swabbing dried residue from an aluminium plate and detected the extracted material on demonstrator SERS substrates has been developed and shown to work repeatedly. This application is suitable for further investigation to allow portable Raman instrumentation.

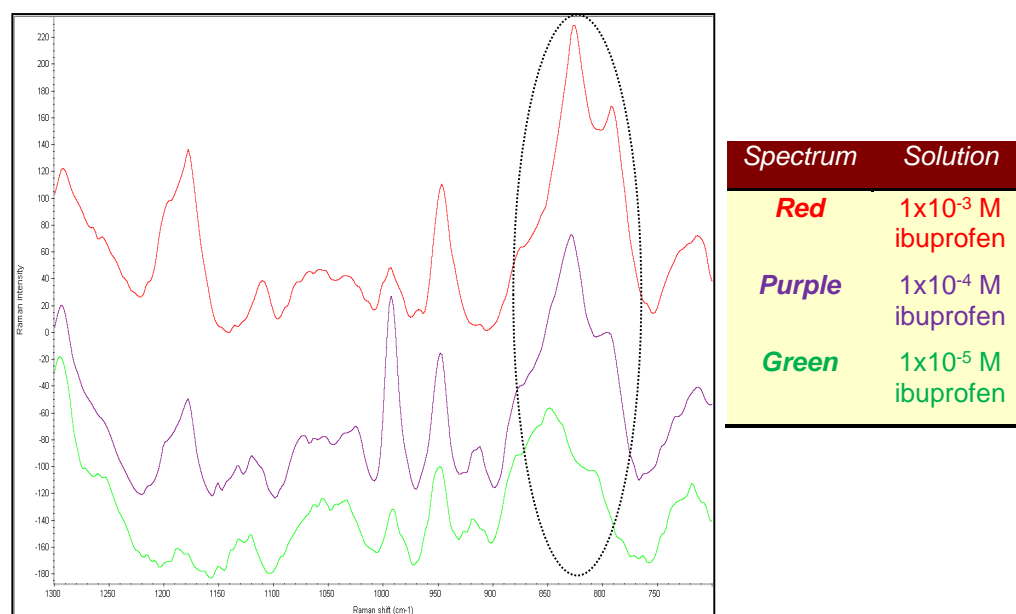


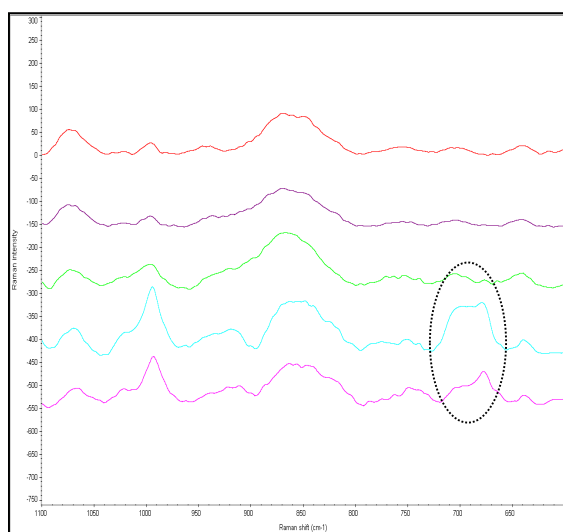
Figure 6.14 Raman spectra of various concentrations of ibuprofen solutions. The dotted circle is guiding the peak which is presence of ibuprofen.

6.3.2 Food monitoring

Milk products contaminated with melamine can lead to kidney disease and even death in infants. Typical detection techniques are High Performance Liquid Chromatography (HPLC), Gas Chromatography Mass Spectrometry (GCMS) and Enzyme-Linked Immunosorbent Assay (ELISA). However, these methods require time-consuming sample preparation steps and can only be done by highly trained personnel on expensive instruments. A series of experiments I designed to determine whether the demonstrator substrates and SERS are a viable candidate for use in food monitoring applications.

Initially, 0.1mL of semi skimmed milk was pipetted into a 1.5mL tube, and this was spiked with 10 μ L of 1mM melamine solution. The resulting solution was mixed and placed in the micro-centrifuge for one minute at 10000rpm. 10 μ L was then extracted and dried on a substrate with a measurement taken on the spectrometer afterward.

No melamine was detected, so 10 μ L of semi skimmed milk was pipetted onto a substrate and analysed. When the two spectra are compared, it was observed they were comparable. A reason for this could be that the milk components (e.g. proteins, fats or lactose) preferentially interact with the gold surface. These large molecules prefer to bond to the gold surface of the substrate because of chemically reactive functional groups (such as primary amine and sulphur linkages), thereby blocking the melamine molecules from binding to the gold and resulting in no melamine being detected. Therefore, sample pre-treatment is necessary to filter out these large molecules. After research, a new method was developed. 10 μ L of 1mM melamine solution was spiked into 0.1mL semi-skimmed milk, and to this 0.1mL of acetonitrile was added. The sample was then placed in the micro-centrifuge for 10 minutes at 14800rpm. Upon exiting the micro-centrifuge, there was a clear solution with a white solid. 10 μ L of this solution was extracted for analysis. Since the speed was at its highest setting, the time was altered to 20 and 30 minutes to determine if this would have an effect on the results.



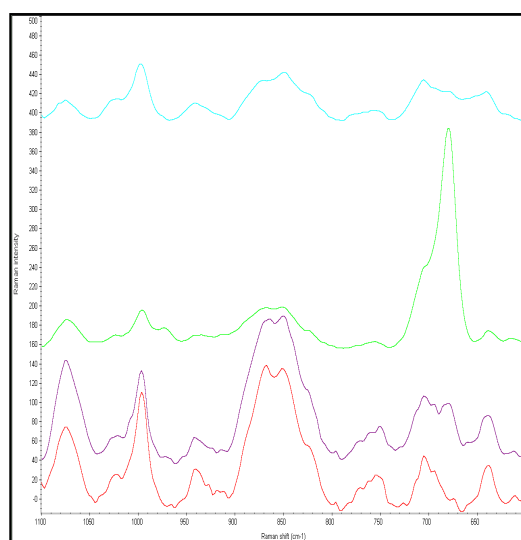
Spectrum	Solution
Red	1mM melamine
Purple	Semi Skimmed Milk
Green	10 minutes
Blue	20 minutes
Pink	30 minutes

Figure 6.15 1mM melamine and milk samples. The characteristic melamine peak is at 680cm⁻¹ shown by the black dotted circle.

On examination of Fig 6.15, it can be concluded that the 1mM melamine sample spectrum and the semi skimmed milk are comparable. This is evidence to support the theory that the large milk molecules are binding to the gold surface, thus preventing the melamine molecules from binding to the gold and being detected. This reinforced the need for an effective extraction method. Using acetonitrile and 10 minutes on the micro-centrifuge did

not result in melamine detection. However, after 20 minutes there is a singlet peak at approximately 680 cm^{-1} , and after 30 minutes there is a singlet peak observed shown by dotted circle. This is strong evidence for the presence of melamine.

It was determined that using acetonitrile and long centrifuge times does result in melamine being detected, however further work needs to be carried out in order to determine if there is a more effective extraction method. 10mM, 1mM, 0.1mM and 0.01mM melamine solutions were prepared. 0.1mL of semi skimmed milk and 0.1mL of melamine solution at various concentrations were added into an empty 1.5mL tube. The solution was mixed and then placed in an ultrasonic bath for 5 minutes, with the temperature set to 20°C . A control sample was also used, to allow a fair comparison. This control sample was semi skimmed milk subjected to the procedure with no addition of melamine. The sample was then removed from the sonic bath and 0.1mL of acetonitrile was pipetted into the tube. The solution was vortex mixed and then placed in the micro centrifuge for 10 minutes at 4000rpm. After centrifugation, there was a clear liquid with a white solid at the bottom, except for the 1mM and 0.01mM melamine solutions. These solutions had a white solid at the bottom but a cloudy liquid; it is unclear why this happened.



Spectrum	Solution
Blue	Control
Green	10mM melamine
Purple	1mM melamine
Red	0.1mM melamine

Figure 6.16 Spectra from various concentrations of melamine extracted from milk using acetonitrile

From Fig 6.16, it can be concluded that melamine can be detected with a limit of detection between 10 and 1mM. The limit of detection is high due to an inefficient extraction method. Proof of concept for the food monitoring application was observed, with melamine successfully extracted from milk samples and detected using the demonstrator substrates

although demonstrator plastic substrates must be developed to improve the limit of detection to a practical level.

6.4 Optimization of Au coating for plastic

Angle metallization is performed in such a way that the plastic substrate is held at a tilt angle and rotated so that the gold is deposited roughly on the surface rather than smoothly. This gold roughness is critical to the SERS effect since it provides regions of high electric field density, which allow coupling of the surface plasmon from the SERS substrate to couple to the target molecule. The enhanced e-field supported by the roughness will be discussed in the section 7.1.1 using the simulation. The gold deposition method is the same as mentioned in the section 5.1.3 in which the substrate holder is tilted to 25° with respect to the Au crucible and called as the standard angle deposition method in our thesis. After research, the angle is optimized to 34° and called as the optimized angle deposition in which Au grain is more spherical-like maintaining the conformal gold coating on the sidewall as shown in Fig 6.17(c). The SEM pictures (Fig 6.17 (a and b)) of the standard and optimized angle deposition shows good fidelity of the features indicating the successful transfer of the pattern by the imprint methods. However, the careful inspection of the SEM images for plastic substrates deposited by the two different angles Au grain reveals that a slight different in gold layer morphology. This is expected to slightly affect the electric-field localization along the side walls of the pit and hence the different Raman amplification. It is examined whether the plasmon resonance of the plastic substrate deposited by the optimized angle is maintained at the same excitation wavelength like in the standard angle deposition by comparing the reflection maps of the respective substrates as shown in Fig 6.18. Those dispersion maps are collected as discussed in the section 4.1.1 for the angular reflection as a function of the excitation wavelength and color scaled from the dark blue to dark red for the complete absorption to the complete reflection respectively. Therefore which wavelength excites the plasmon resonance can be identified easily in the color map. At a first glance, the dispersion lines attributed to features of the pyramidal design match well between different angle depositions of gold. The plasmon absorption region corresponding to the dark blue gives the solution of the incident angle and excitation wavelength where plasmon resonance occurs and hence Raman amplification for the SERS effect. However, the careful examination of the reflection

spectra at the 3° incident angle, the substrate with the standard angle deposition tunes the plasmon resonance at the 769nm while the plasmon resonance is excited at the 791nm for the optimized angle deposition. The latter is 6nm different from the Raman operating wavelength 785nm while the former is 16nm different. The difference in the plasmon resonance between the standard and optimized angle gold deposition is attributed to the exclusion of grain structure and morphology of the gold surface (inclusion of the information about the difference in resonance is needed further analysis). However this experimental angular reflection measurement serves as a guideline for observing plasmon resonances and determining the physical reason behind increased SERS counts.

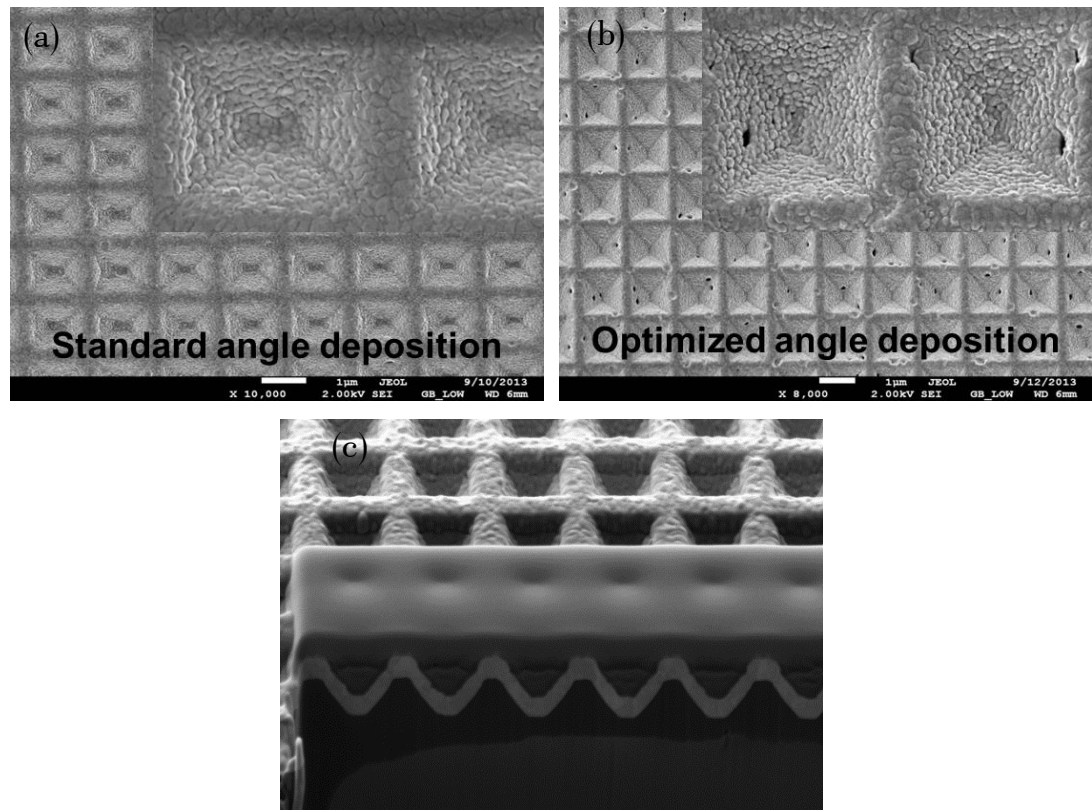


Figure 6.17 SEM images of inverted rectangular based optimized pyramidal design after 400nm gold deposition. (a) standard angle deposition at 25° , (b) optimized angle deposition at 34° . Insets are the high magnification of SEM images and (c) SEM image confirms the conformal Au coating on the sidewall at the optimized angle deposition.

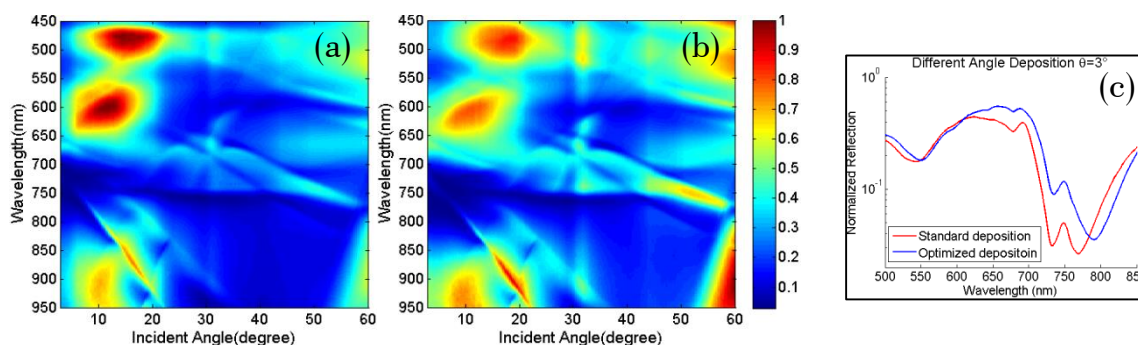


Figure 6.18 Dispersion maps for plastic SERS substrates for the optimized design under p-polarization. (a) Standard angle Au deposition, (b) Optimized angle Au deposition, (c) Normalized Reflection for the different angle deposition at $\theta=3^\circ$. Standard deposition shows the plasmon resonance at 769nm and optimized deposition tunes the plasmon resonance at 791nm.

The Raman measurement was performed using the parameters such as: 44mW power at 785nm operation wavelength, 3 seconds in exposure time, 2 times accumulation per scan and 20x objective lens with NA=0.4. The measurement was collected for the 36 random points over the substrate and averaged them and plotted the Raman spectra for both substrates of different angle deposition as shown in Fig 6.19 (a). The average Raman intensities of each Raman vibrational frequencies of BTh molecules for the respective SERS substrates are tabulated as shown in Table 6-4. As seen in Fig 6.19(a), the inverted pyramids with the optimized angle gold deposition has the higher Raman enhancement in sensing of test molecules compared to those with the standard angle deposition. The averaged improved factor in SERS counts by the optimized angle deposition is 3.52 although it reaches till 4.58 improvements especially for the ring stretches mode at the Raman vibrational frequencies of 1576cm^{-1} .

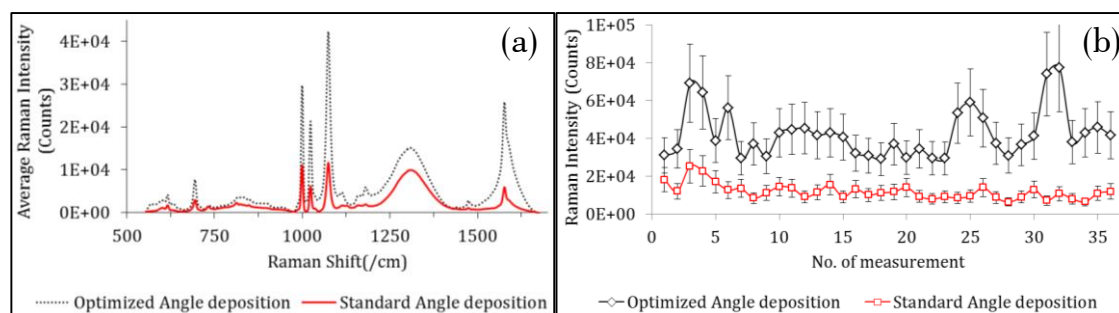


Figure 6.19 Raman SERS measurement for different angle deposition. (a) Average Raman spectra of BTh molecules after measuring 36 random points on the each substrate (b) Reproducibility calculated at the 1075cm^{-1} Raman vibrational frequency of BTh molecules. Error bars represent the relative standard deviation from the average Raman intensity.

Table 6-4 Average Raman intensity for the characteristic vibrational modes of BTh molecules for different angle deposition showing the enhanced factor in SERS counts by optimized angle deposition

Characteristic Raman Vibrational frequencies of BTh molecules (/cm)	Averaged Raman Intensity (Counts)		Enhanced factor in SERS Counts (by optimized angle deposition)
	Standard Angle Deposition	Optimized Angle Deposition	
Ring deformation (615-630)	1615.07	4136.69	2.561
Trigonal Ring Breathing (990-1010)	11088.34	29595.68	2.67
In-plane CH deformation (1015-1030)	5477.65	20858.97	3.81
CC stretches, 1075	10490.34	41559.8	3.96
Ring stretches (1550-1630)	5439.24	24965.66	4.58
Average Improved factor by optimized angle deposition			3.52

Figure 6.19 (b) gives the information about repeatability of Raman intensity from test molecules over the large area substrate. The variation of Raman intensity over the whole substrate was calculated for the C-C stretches mode of the test molecule and the on-chip reproducibility is not much different for both angle deposition methods. The reproducibility of the substrate deposited by the standard angle method is 35% in terms of relative standard deviation while the substrate deposited by the optimized angle method is 30% of reproducibility. The low reproducibility is due to the lack of control in the flatness of the substrate during metallization.

6.5 Molecule vs. no-molecules on the plastic substrate leading to dual sensing mechanism, SPR and SERS

In order to analyze the surface plasmon resonance, SPR sensing, the replicated plastic SERS sensor is probed by the Reflectometry system as described in section 4.2 without the need for any coupling mechanism, such as prism or waveguide. In this mechanism, small changes in the refractive index at the substrate interface would result in a shift in plasmon resonance wavelength and angle. Here I will emphasize on the shift in plasmon resonance and discuss the preliminary results. For these purpose first benzyl mercaptan (BZM) molecules is deposited on the sensor as described in the section 4.3.1. The 500nm pit size and 1000nm pit size plastic substrates with 200nm gold thickness are used as examples to study the SPR sensing capability.

Figure 6.20 gives the dispersion from the SERS plastic sensor before (Fig 6.20(a)) and after (Fig 6.20(b)) deposition of molecules to show SPR sensing capability. It is observed that the distinct shift of diffraction distribution and hence the plasmon mode after application of molecule and Fig 6.20 (c) provides the overlay of the diffraction features before and after depositing molecule from which change in position of diffraction lines and its respective surface plasmon have been observed. These can be exploited in SPR sensing configuration in terms of change in wavelength, $\Delta\lambda_{\max}$ as shown in the equation 6.1:

$$\Delta\lambda_{\max} = m\Delta n[1 - \exp(\frac{-2d}{l_d})] \quad 6.1$$

where m is the refractive index sensitivity (nm/RIU), Δn is the change in refractive index induced by the adsorbate $= n_{\text{ad}} - n_{\text{air}}$, d is the effective adsorbate layer thickness here for thiol molecules $d \approx 1.67\text{nm}$, l_d is the characteristic electromagnetic field decay length, 20nm is used for gold (Au)[132].

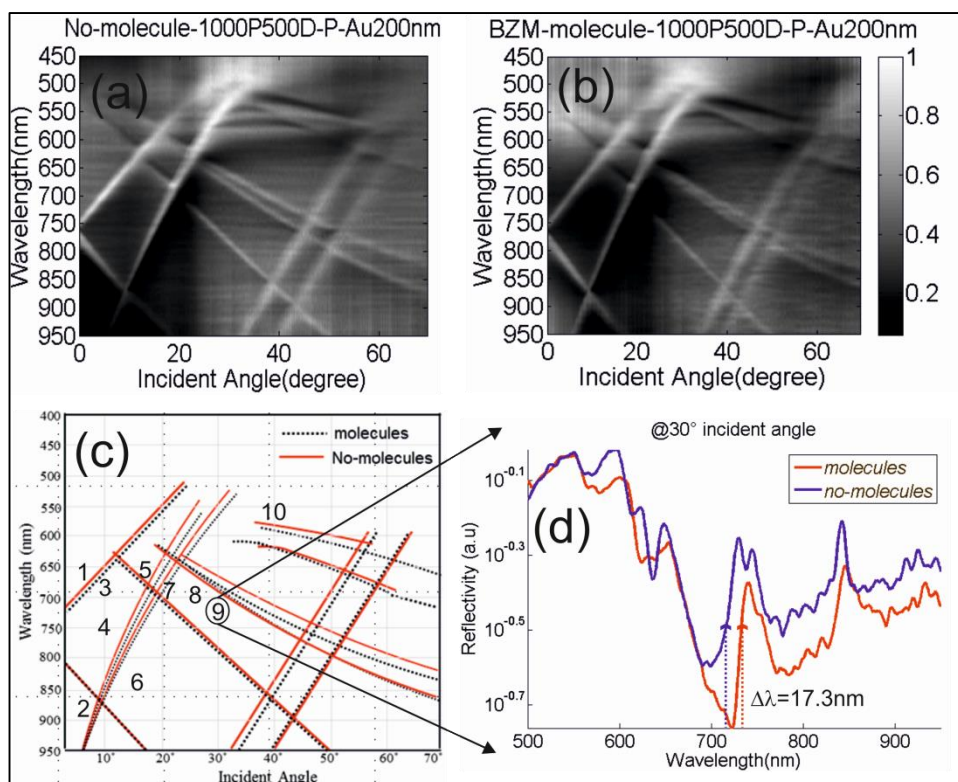


Figure 6.20 Reflection maps for 1000P500D substrate with 200nm gold thickness (a) without molecule (b) with BZM molecule (c) Overlay plot for diffraction distribution of sample both before and after molecule, numbers on the plot refers the position where the detail analysis on the reflection spectra as shown in (d). (d) Comparison of the reflectivity difference before and after molecule coating at the angle of incidence, 30°.

Table 6-5 List of SPR sensitivity (nm/RIU) corresponding to the shift in wavelength for different incident angles from plastic SERS sensor (1000P500D)

No. from fig 6.20(c)	Incident angle (Degree)	$\Delta\lambda_{\text{max}}$ (nm)	Refractive index sensitivity, 'm' (nm/RIU)
1	5	6.9	90.07437843
2	5	8.5	110.9611908
3	10	12	156.6510929
4	10	7.6	99.21235885
5	15	6.8	88.76895266
6	15	7.7	100.5177846
7	20	7.5	97.90693308
8	25	10.3	134.4588548
9	30	17.3	225.838659
10	40	5.1	66.57671449

From this equation, the sensitivity can be calculated using the $\Delta\lambda_{\max}$ from the comparison of reflection spectrum as shown in Fig 6.20(d). The sensitivity from the 500nm pit size inverted pyramid sensor device are calculated for different incident angles ranging from 5° to 40° and those measurements are marked with the number on Fig 6.20(c). From this detail analysis, $\Delta\lambda$ is appeared to be maximum, 17.3nm at the angle of incidence 30° and hence a maximum wavelength sensitivity of 225nm/RIU is achieved. Therefore, the 500nm pit size sensor at 30° input laser illumination can offer maximum wavelength sensitivity compared to the other incident angle.

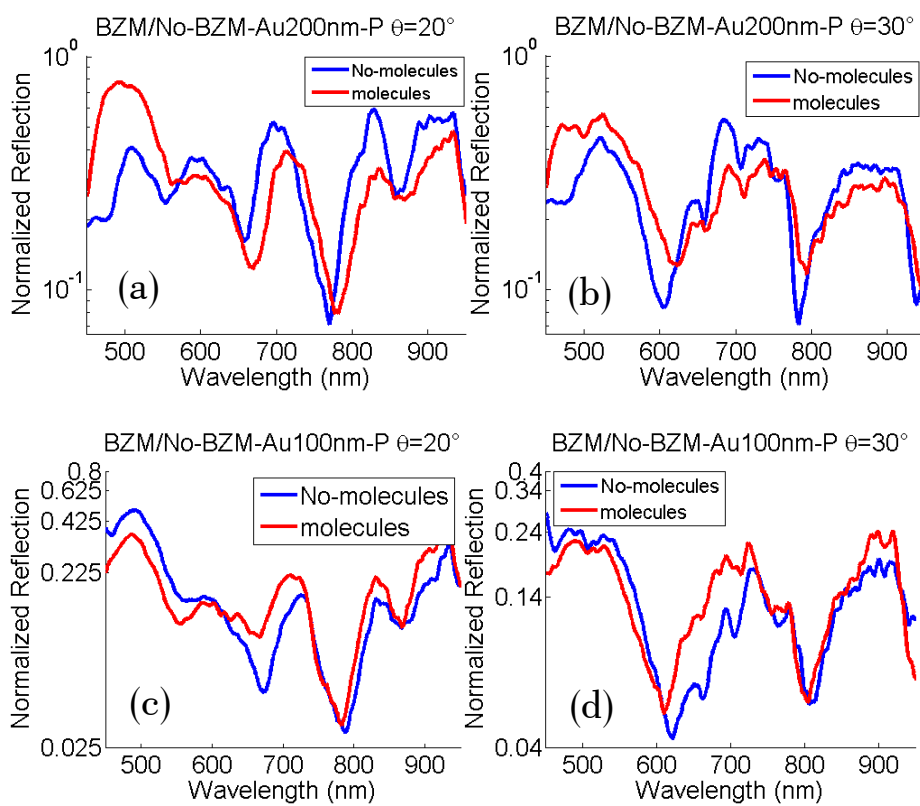


Figure 6.21 Comparison of reflection spectrum before and after application of molecule from 1250P1000D inverted pyramid, plastic (a) Au200nm, $\theta=20^\circ$ (b) Au200nm, $\theta=30^\circ$ (c) Au100nm, $\theta=20^\circ$ (d) Au100nm, $\theta=30^\circ$

SPR sensing ability in the larger pit size 1000nm is discovered as a best optimized design in SERS sensing configuration. In this design, analysis is carried on for different gold thickness (Au200nm and Au100nm) to see the effect of gold thickness on SPR sensing ability. Figure 6.21 provides the comparison of reflection spectrum before and after application of molecule for both gold thickness 200nm and 100nm at the incident angle of

20° and 30°. From figure, change in coupling wavelength is deduced and then calculated sensitivity is given in Table 6.6 for comparison of sensitivity. First thing noticed from the reflection spectra for different gold thickness is that the surface plasmon resonance after application of molecule is shifted to the longer wavelength in 200nm gold thickness while those is shifted to shorter wavelength in 100nm gold thickness. Second, the sensitivity from the 1000nm pit size (optimized SERS sensor design) gives the almost 2-fold improvement compared to smaller pit size, 500nm under same gold thickness. The 1250P1000D sensor device with 200nm gold thickness provides a wavelength sensitivity of 417nm/RIU at 30° incident angle. But the sensor with 100nm gold thickness demonstrates a wavelength sensitivity of 352nm/RIU at 20° incident angle. A fact is noticed that different gold thickness produces the difference not only in terms of sensitivity but also coupling angle of incidence.

Table 6-6 List of SPR sensitivity (nm/RIU) corresponding to the shift in wavelength for different incident angles from plastic SERS sensor, 1250P1000D for different gold thickness: 200nm and 100nm

Incident Angle (Degree)	Au200nm_1250P1000D		Au100nm_1250P1000D	
	$\Delta\lambda_{\max}$ (nm)	Refractive index sensitivity, 'm'	$\Delta\lambda_{\max}$ (nm)	Refractive index sensitivity, 'm' (nm/RIU)
20 (1 st dip)	22	287.1936704	27	352.4649591
20(2 nd dip)	11	143.5968352	8.5	110.9611908
30(1st dip)	32	417.7362478	24.4	318.5238889
30 (2 nd dip)	13	169.7053507	9.5	124.0154486

Finally the 1250P1000D plastic sensor with 100nm gold thickness is demonstrated with different molecule using PMMA which is spin-coated of 5 μ L droplet resulting in the adsorbate layer thickness of 156nm, confirmed by ellipsometry measurement. Figure 6.22 shows the dispersion from the sensor chip. Due to the thicker adsorbate layer, change in plasmon distribution is quite huge after application of PMMA. However their wavelength of sensitivity shows only 45nm/RIU and 54nm/RIU for the change in plasmon resonance wavelength of 22nm and 26nm, respectively. Nevertheless, the sensor can still give wavelength sensitivity for the adsorbate layer, 156nm which is far away from the sub-nm scale compared to the monolayer of BZM, 1.67nm.

The section describes the first step of SPR sensing application from the SERS sensor chip although the plastic sensors have to be characterized further for performance considerations such as resolution, accuracy, reproducibility and limit of detection. However, it is observed that all these shifts in plasmon resonance after application of molecule also depend on the type of molecules and their concentration and molecular affinity and on the other hand metal thickness, geometric parameters and polarization can alter the plasmon resonance energy. In conclusion, this plastic sensor is demonstrated the capability of simultaneous SERS and SPR sensing using a monolayer of thiol molecules.

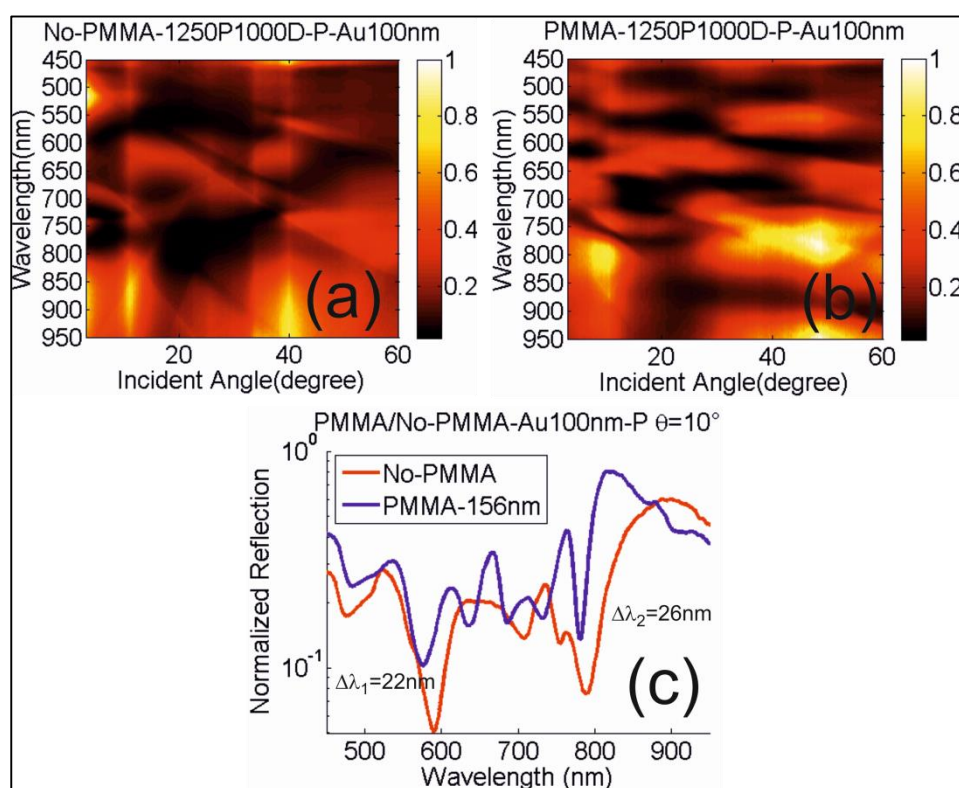


Figure 6.22 Reflection maps for 1250P1000D substrate with 100nm gold thickness (a) before molecule (b) after application of PMMA (c) Comparison of the reflectivity difference before and after molecule coating at the angle of incidence, 10°

6.6 Conclusion

For the purpose of the low-cost mass-manufacturing and easy disposal then the sensor is transferred to plastic base platform using the silicon platform as a stamp. Transfer is achieved using roll-to-roll and sheet-level nanoimprint fabrication techniques. The

replicated plastic sensor also follows the same geometrical combination for highest SERS enhancement such as 1250nm pitch length and 1000nm pit size with rectangular aspect ratio (1:1.2). However, EF of the replicated plastic sensor is 10-fold lower than its enhanced silicon master. Analysis using AFM imaging gives the clues to this error in sensitivity. They have the impairment in replication such as structural profile and depth accuracy and lack of waviness causing the difference in surface roughness of gold in the sidewall. Nonetheless, the plastic sensor still can demonstrate for the real world application such as pharmaceutical cleaning and food monitoring even though they don't have super high enhancement like silicon master. However the optimization of metallization makes the enhancement factor improved by the factor of 3.5. Finally these plastic sensors have the intuitive picture of dual sensing application using both of SERS and SPR sensing configuration.

Chapter 7. Analysis on gold layer

This chapter describes the influence of gold layer thickness on plasmon behaviour of inverted pyramid nanostructure for silicon using the rectangular inverted pyramid (1250P1000D) with the variation of gold thickness from 50nm to 400nm. Maintaining the inverted pyramid at fixed geometrical parameters, gold layer is deposited for different thickness. The non-conformality effect of gold deposition on plasmonic properties also has been studied.

7.1 Effect of Gold layer thickness

The silicon based inverted pyramid is coated with different gold thickness ranging from 50nm to 400nm to observe the plasmonic behaviour change with the effect of gold thickness. While the gold thickness is varied, maintaining the pit size, depth and the conformal coating are constant as shown in Fig 7.1 to examine only the effect of gold thickness on the plasmonic features rather than the effect of geometrical parameters. The reflection maps for the various gold thicknesses are shown in Fig 7.2, colour scaling with the dark blue to dark red representing the high plasmon absorption to the high reflection. Since the pitch and pit size and depth are fixed at constant, the diffraction features at the reflection map remain same for all thickness of gold. The plasmon resonance due to the geometrical parameter is tuned around the near infrared region from 700nm to 800nm. However, due to the effect of gold thickness, the plasmon resonance is shifted to the higher energy/shorter wavelength attributing to the increase of gold thickness. Under TM-polarization and normal incidence, particularly, the inverted pyramid with 50 nm Au thickness tunes the plasmon resonance at the wavelength of 775nm and then shift to the shorter wavelength with the increase of Au thickness and hence the plasmon resonance is tuned at 750nm wavelength at the 400nm Au thickness. In order to observe the above phenomenon in detail, the reflectivity of different Au thickness under normal and 45° incident angles is plotted as shown in Fig 7.3. For 45° incidence, the tuning of the plasmon resonance follows the same shifting flow of wavelength with normal incidence showing that 805nm at the 50nm Au thickness and shifted to lower energy of 785nm at the 400nm Au thickness. However, the absorption intensity related to the plasmon resonance is not linearly dependent on the gold thickness showing that 200nm Au thickness offers the high

plasmon intensity of 99.95% while the 300nm gold thickness gives the 99.6% plasmon intensity. At the normal incidence, the plasmon resonance becomes sharper with the increment of gold thickness till 200nm and then the influence of rectangular lattice separates it into two resonances: the distance between the resonances are longer with the thickness of the gold such that 50nm and 70nm away from each other for the 300nm and 400nm thickness of gold respectively as shown in Fig 7.3. However the plasmon resonance is resistant to the rectangular lattice effect at the 45° incident angle as the area subtended by the incident wave is not rectangular and the resonance peak is single and become sharper till the 300nm gold thickness. It is still not clear why the resonance becomes broaden again at 400nm gold thickness.

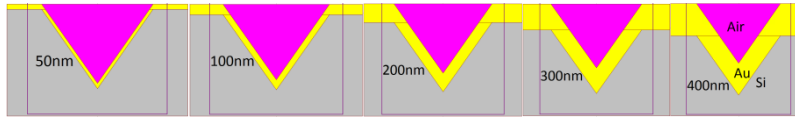


Figure 7.1 Illustration of the simulated design for the different gold thickness showing that just change in gold thickness in the conformal coating , not effect on the geometrical parameter.

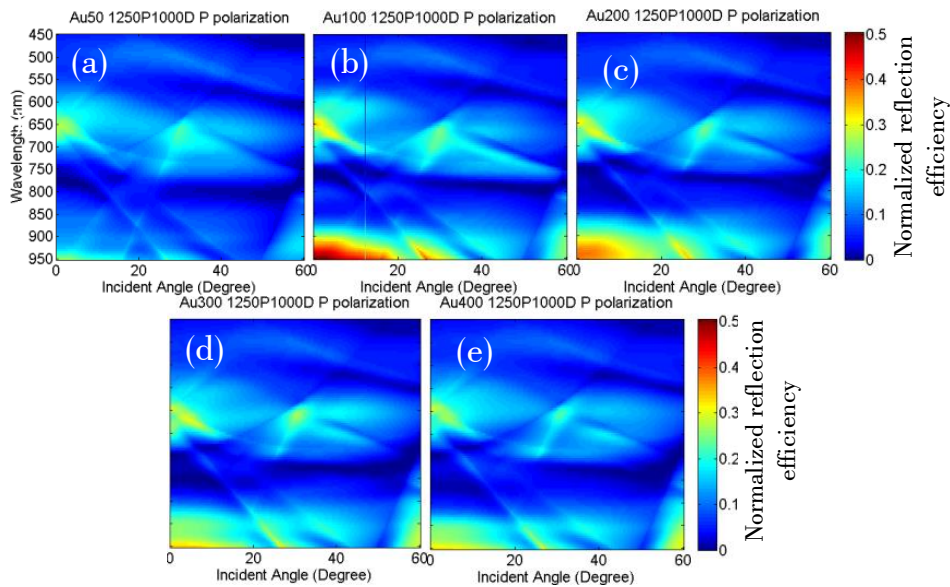


Figure 7.2 Dispersion map as a function of the excitation wavelength for different gold thickness (a) 50nm, (b) 100nm, (c) 200nm, (d) 300nm and (e) 400nm. The inverted pyramidal is designed using the optimized geometrical parameter. Simulation is performed at TM-polarization.

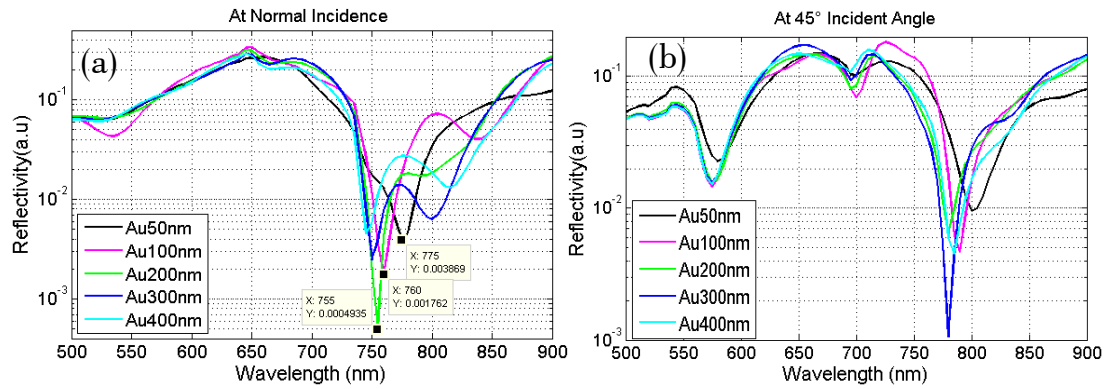


Figure 7.3 Normalized reflectivity for different gold thickness (a) at normal incidence, (b) at 45° incident angle

The monitor is placed across the inverted pyramid to observe the e-field density and distribution corresponding to the thickness of gold within the cavity. Field plots for different gold thickness are shown in Fig 7.4. The field distribution within the cavity is the same for all thickness of gold in such a way that the plasmon are propagated along the sidewall resulting in the standing localized plasmon around the immediate vicinity within the cavity although the field intensity is varied with the gold thickness. Since the 50nm gold thickness is thin enough for plasmon coupling, the e-field density which is the reason for plasmon, can occur in both sides of interface such as one side is at the interface of gold and air and the other side is at the interface of gold and silicon. Starting from the 100nm thick gold which is thick enough for plasmon to penetrate, the e-field density occurs only within the cavity (Au+Air). All electric fields(which are responsible for the propagating plasmon) form along the sidewall of the pyramid and hence support the e-field standing wave inside the cavity, particularly at 100nm Au thickness, the strong e-field standing wave can be seen in Fig 7.4 (b) in which the monitor is recorded for 785nm wavelength at normal incidence. The highest localized field density is occurred at height of 300nm away from the tip of the pyramid and the height (where the highest field intensity is confined) is independent from the gold thickness and is mainly dependent only on the pit size although the field intensity is partially dependent on the gold thickness. The field intensity varied with gold thickness at 785nm wavelength is shown as a line graph in Fig 7.5 (a). The field intensity is not linearly dependent on the gold thickness. At 50nm thickness, the Au is optically thin enough to couple the e-field between both sides of the layer of gold and develop the high e-field intensity compared with the thicker gold layer. However, a fact has

to be remembered that the gold layer considered here is the smooth gold coating with zero roughness. When the roughness is considered, field intensity will be different from the aforementioned phenomenon. For example, for 400nm gold thickness, the roughness is considered at the same distance (300nm) away from the tip to examine the change in the palsmon feature. The roughness is created by the 50nm sphere forming on the sidewall with no gap between them as shown in Fig 7.5 (c). Due to the effect of roughness the filed intensity becomes higher (as shown in Fig 7.5 (b)) compared to the field without roughness (Fig7.4(e)).

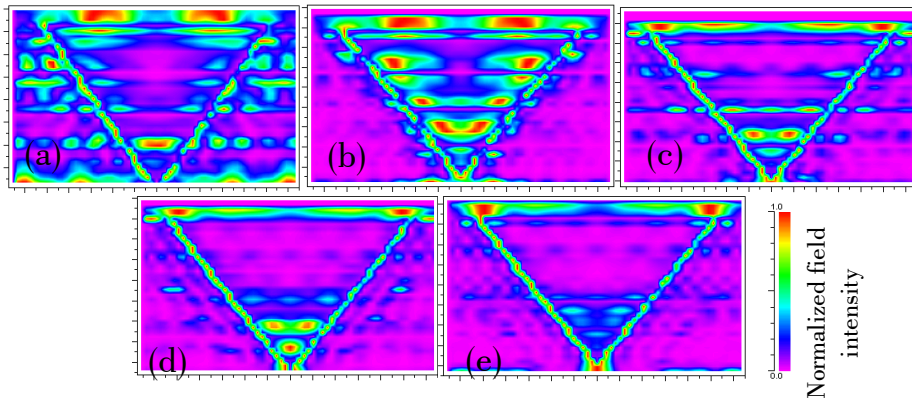


Figure 7.4 Normalized field intensity for different gold thickness at the 785nm operation wavelength (a) 50nm, (b) 100nm, (c) 200nm, (d) 300nm and (e) 400nm.

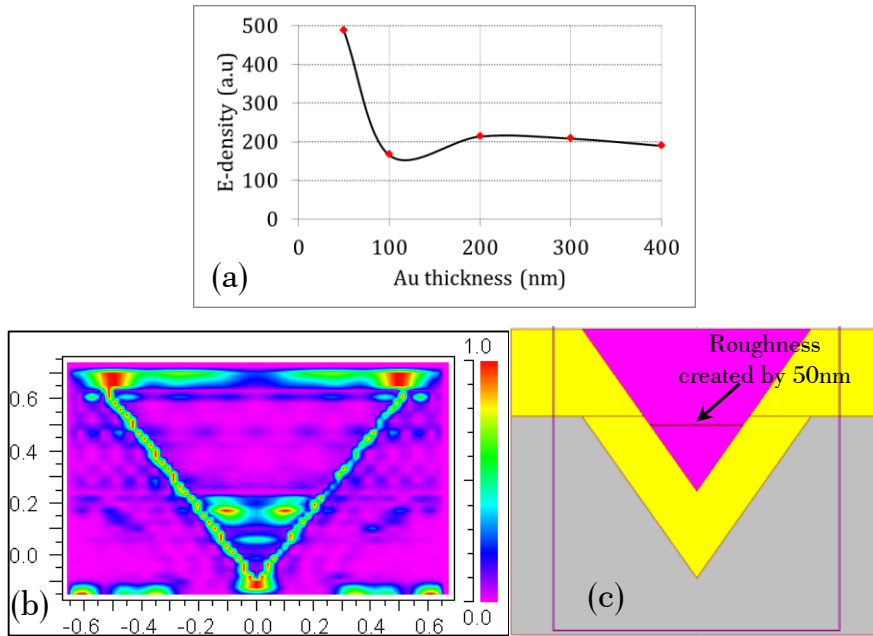


Figure 7.5 (a) Line graph shows that the field density as a function of gold thickness. (b) Normalized field distribution plot for 400nm gold thickness with the created roughness at the height of 300nm by using the 50nm sphere. (c) Illustration of the simulated design with the roughness at 300nm height.

7.2 Effect of non-conformality gold deposition on Plasmonic properties

In chapter 5, a comprehensive three dimensional computational model based on Rigorous Coupled Wave Analysis (RCWA) has been developed to investigate the properties of surface plasmons resident on metal coated arrays of inverted pyramidal pits used for SERS sensing applications in the form of 'KlariteTM'. This simulation tool allows the identification of a variety of dispersive features including propagating and localized surface plasmons as well as simple diffraction relating to the influence of geometrical features. In this chapter, the influence of non-conformality of the gold coating over the internal surfaces of the inverted pyramidal pits on plasmon dispersion was investigated. Modeling reveals very strong changes in plasmon behavior as a function of gold layer conformality. Dependent upon conformality of the gold coating indicates that the nano-textured metallic surface can behave either as an efficient broadband mirror-like reflector or as an efficient broadband, wide angle absorber at infrared wavelengths. Creation of a broadband wide angle absorbing surface such as this has important implications for photovoltaic cells. For sensing applications, understanding the effect of metal layer conformality on plasmon dispersion gives clear insight into how to further improve SERS enhancement factor.

Plasmonics are currently seeking widespread applications in the area of plasmonic surface-enhanced Raman scattering sensors [13,116,122], plasmonic lasers [134-136], surface-plasmon-enhanced light-emitting diodes [137], plasmonic light trapping [138-143], plasmonic integrated circuits [144,145], plasmonic imaging below diffraction limit [146], nanoscale plasmonic wave- guiding and optical antennas. All these applications require the extreme confinement of light and its related nonlinear effects which can be achieved by guiding and concentration light using plasmonic nanostructures. But the question is how to advantageously use Plasmon excitation and localization in all these opportunities. Therefore, a lot of research has been expanded in area for materials, device geometries, nanoscale fabrication and characterization to understand the behavior and ability of Plasmon which in turn open up developments and new approaches in nanophotonic application. As a result, in Surface Enhanced Raman Scattering (SERS) technology, enhancement is increased ten-fold through the use of plasmonic substrates. In photovoltaic devices, plasmonic metal nanoparticles can be used either as efficient scatters or to

enhance the generation of photo carriers through local field enhancement around the metal nanoparticles. Plasmonic waveguide have enabled transmission of light through holes smaller than its wavelength. Studies are just beginning to appear exploring contributions from plasmonic coupling. This section investigates the effect of metal layer conformality on plasmon behavior for three dimensional arrays of inverted rectangular pyramidal pits. It is observed that by tailoring the non-conformality of the gold coating it is possible to tune the absorption in the infrared (IR) wavelength range which might be useful for applications in silicon solar cells where broadband absorption over the IR range is challenging. In addition to that, a nano-textured metallic surface with a non-conformal metal coating can behave as an efficient broadband reflector.

7.2.1 Design variation and discussion on results

To study the non-conformality effect on plasmonic properties, the optimum design for 780-800nm excitation (pyramidal pits 1250P1000D with Au200nm gold coating thickness) which has been demonstrated to show high SERS enhancement factor [122]. The measured pit size after glancing angle deposition shows 961nm instead of 1000nm in fabrication. Therefore, simulated pit size is designed as 961nm. Sample-1250P961D with the conformal metal coating is from now on defined as non-conformality“0”. In this case sidewalls of the pits have a uniform coating of even thickness (170nm). The taper factor for the sidewall coatings of the pits is changed to simulate the effect of different angular deposition conditions. In the simulation we are therefore able to gradually increase the non-conformality of metallization. Gold coating thickness on the pit sidewalls at the top of the pyramids is varied in steps of 100nm, whilst maintaining the same gold coating thickness (170nm) at the bottom of the pits as shown in Table 7.1. In this case, the effective width of the neck of the pyramid decreases in proportion, and the apex angle of the pyramid decreased by the average value of 7° (seen in Table 7.1). In this section, this type is defined as ‘apex angle decreased non-conformal’ coating. Conversely the ‘backward non-conformal’ coating causes an increase in apex angle and pit neck size.

Table 7-1 List of pyramidal geometric data with ‘apex angle decreased non-conformality’ condition

Degree of Non-conformality	0	1	2	3	4	5	6	7
Simulated pitch (P) and pit size (D)	1250P-961D	1250P-861D	1250P-761D	1250P-661D	1250P-561D	1250P-461D	1250P-361D	1250P-261D
Apex angle	70.6	62.74	56.63	50.16	43.33	36.15	28.68	20.94

Figure 7.6 shows the results of index profiles and dispersion maps of the respective non-conformality condition. In figures of index profiles, the purple region is the gold coated area and the red region is the air. Since the pitch length of the underlying pyramid (normally formed in silicon) is fixed at 1250nm, the diffraction behaviour of all designs is same for zero order diffraction mode as this is determined by pit to pit periodicity. Therefore, simple diffraction modes are not affected by the effect of conformality of metal coating (as shown in Fig 7.6(f)). The change in the formation of gold coating can be seen more clearly in the index profile plots (upper in Fig 7.6(a, b, c, d, and e)). Results presented in Fig 7.6(a, b, and c) show that gradual reduction in coating conformality directly affects localized plasmons confined within the pit in such a way that broadband localized plasmons (Fig 7.6(a) – shown by white dotted circle) are split into either the narrower localized Plasmon (Fig 7.6(b) - shown by yellow arrows) or sharp propagating plasmons modes (Fig 7.6(c) –short yellow arrow). The split plasmon band can again affect nearby plasmons behaviour and energy levels. The evolution of plasmon process can be seen briefly in the dispersion maps of noncon-0, 1 and 2 shown by drawing of yellow arrows and white-dotted circles (Fig 7.6(a, b and c)). The arrows show the way of plasmon split and the white-dotted circle indicates the evolved plasmon. The detailed plasmon behaviour relating to non-conformality effect is studied with the individual incident angle as shown in Fig 7.7. Figure 7.7 shows the normalized reflectivity spectra for a range of metal non-conformality for specific example incident angle of 5°, 10°, 15° and 20°. The fact that broadband localized plasmons are independent from the incident light is observed and shown by red circle in Fig7.7 (a, b, c and d) results for non-conformality ‘0’. When the non-conformality changes, the plasmons modes become shifted. In 600nm-700nm range and 950nm-1250nm range, the broadband localized plasmons become divided into two or three localized plasmon modes (as shown by black arrows in Fig 7.7 (a, b and c)) and plasmon absorption

efficiencies are decreased to 80%-90% from 90%-99% corresponding to the effect of non-conformality.

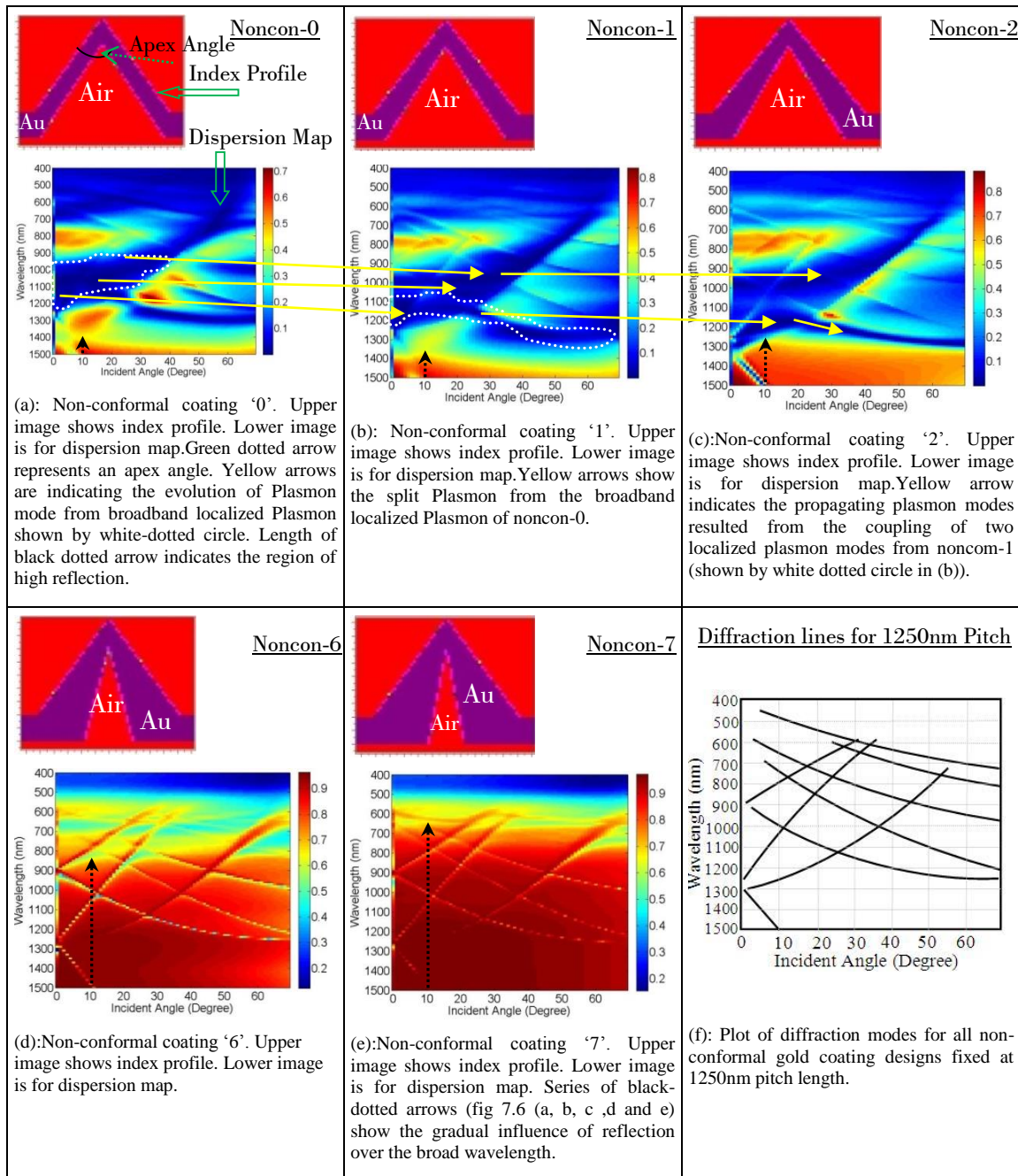


Figure 7.6 Simulation results shows the effect of non-conformal gold coating resulted from decrease in apex angle of pyramid

The high energy plasmon can be formed till noncon-4 condition due to the limitation of pitch length, the plasmons could not couple to incident and reflected photon in the higher forward non-conformality gold coating. Due to the reduced apex angle of the pyramid, instead of plasmon absorption the high reflection is overtaken and shifted from 1500nm to

700nm range. Within the infrared region, reflection efficiency is achieved from 84% to 96% at noncon-7 condition. Therefore, for the noncon-7 design reducing the pitch from 1250nm by 250nm and 200nm consecutively it is possible to harness the Plasmon absorption in the visible and near infra-red region as well as high reflection in infra-red region. Figure 7.8(a) and 7.8(b) are the results of 900nm pitch-261nm pit size and 700nm pitch-261nm pit size, respectively. As expected, the localized plasmons are gradually shifted to near infra-red region (600nm-700nm) and the plasmon energy also become stronger while maintaining the efficient broadband mirror-like reflection with wider angular spread in infrared region.

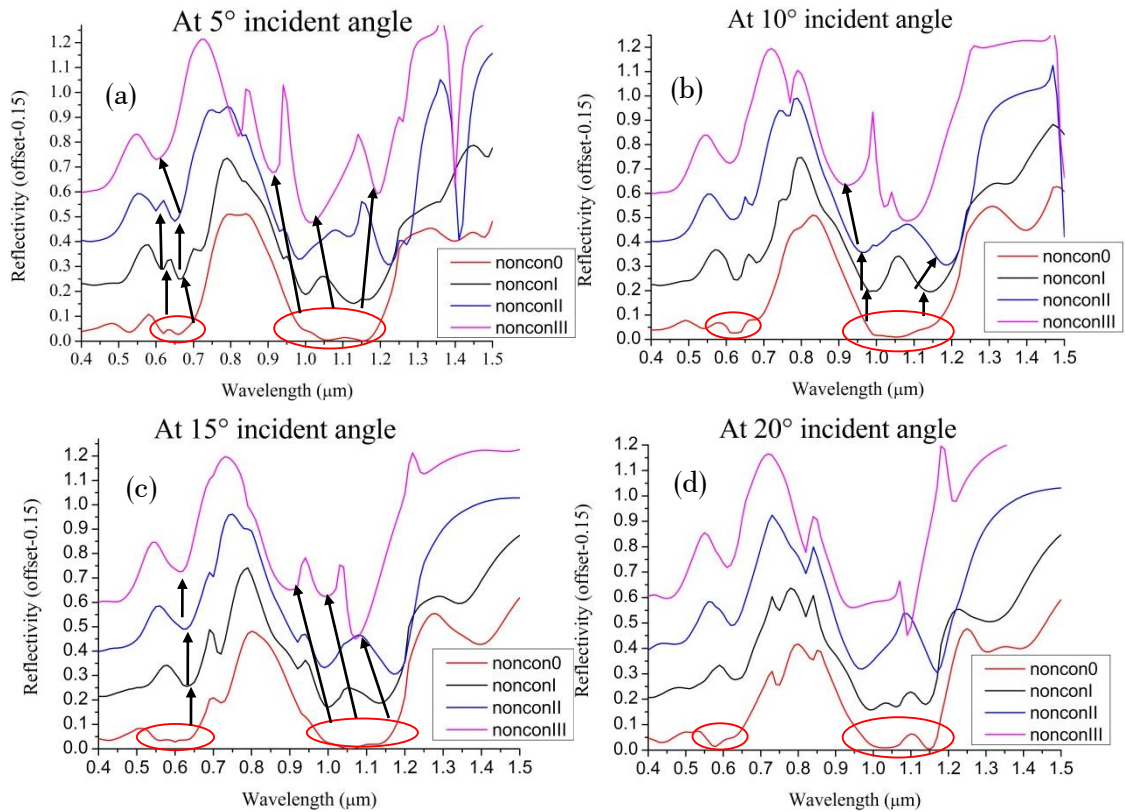


Figure 7.7 Normalized reflectivity spectra for non-conformal gold coating shows the changes in Plasmon behavior and its energy at (a) 5° incident angle (b) 10° incident angle (c) 15° incident angle (d) 20° incident angle.

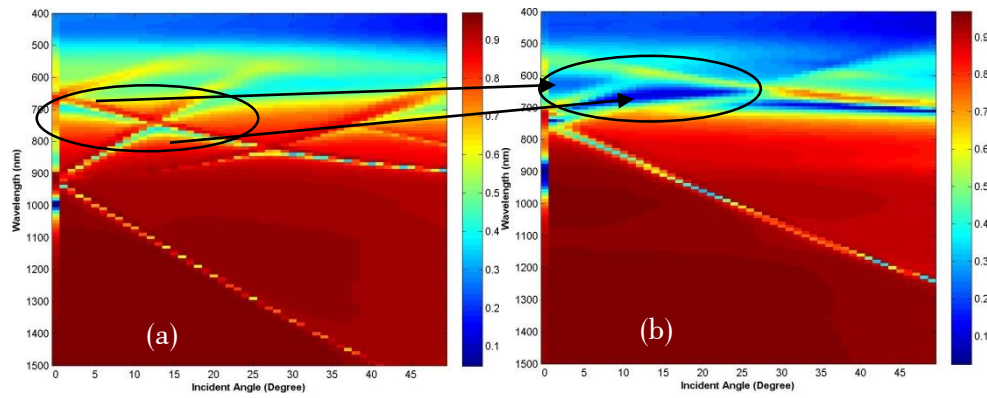


Figure 7.8 Dispersion maps for reducing pith length by 200nm at noncon-7 condition at TM polarization (a) 900P261D (b) 700P261D

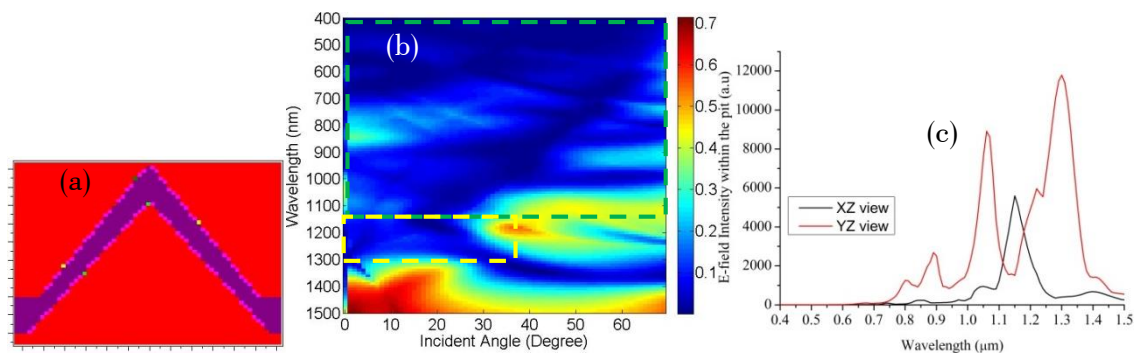


Figure 7.9 Effect of apex angle increased non-conformality coating on Plasmon properties: (a) index profile (b) dispersion map. Green box shows the high plasmon absorption over wide angular spectrum in visible and near infrared region and yellow box shows the high energy plasmons in part of infrared region. (c) e-field energy within the pit.

When the conformal coating called noncon-0 is modified with the apex angle increased non-conformal coating, the pit size become slightly larger to 1150nm with 1250nm pitch length as shown in Fig 7.9(a). Interestingly, the higher plasmon energy modes are formed as wider angular spectrum over broadband wavelength (shown by green box) including most of the infrared region (shown by yellow box) as shown in Fig 7.9(b). This large amount of plasmon confinement is partly due to the increased apex angle and larger pit size formed by non-conformally. Moreover, in the simulation the e-field energy within the pit is observed by two monitors: one for XZ view and other for YZ view (Fig 7.9(c)). Both monitors show that high energy is trapped within the pit over the infra-red wavelength range although e-field is larger in YZ view due to the TM incident polarization state.

7.2.2 Conclusion

This section studies the effect of non-conformality of gold coating (due to angled deposition) on behavior of surface plasmons for SERS enhancing inverted pyramidal pit arrays. Non-conformal metal coating affects the pit size and shape which in turn affect surface plasmon, resonance and energy. Two types of geometries are defined ('decreased and increased apex angle' non-conformal coating). The former makes the pit size smaller at the top resulting in thinner metal thickness at the region near the tip of the pyramid after metal coating. The latter causes a thicker metal at the region near the tip of the pyramid. In 'decreased apex angle' non-conformal coating, wider broadband localized plasmon separated into narrower localized plasmon bands with lower plasmon energy. Therefore broadband reflection is more efficient over the near-infrared and infrared region. After fixing the pitch length to 900nm and 700nm, the high plasmon absorption energy is appointed in the near-infrared region while the efficient wider reflection spectrum is in infrared region. In 'increased apex angle' non-conformal coating, the plasmonic energy is higher and the plasmonic bands are preferentially wider and occupy in the visible, near-infrared and part of the infrared region of the spectrum. Understanding the effect of metal layer conformality on plasmon dispersion provides the clear insight into how to further improve SERS enhancement factor in sensing applications. Moreover, dependent upon conformality of the gold coating the nano-textured metallic surface could be suitable to act either as an efficient broadband mirror-like reflector or as an efficient broadband, wide angle absorber at infrared wavelengths. Creation of a broadband wide angle absorbing surface such as this has important implications for photovoltaic cells.

Chapter 8. Next generation designs

This chapter introduces a further generation of SERS substrates. The substrate is designed as a 3D grating like array with 90° straight sidewalls (90SW) instead of the sloped sidewall of the inverted pyramids described in chapter 5. The reason of considering the 90SW nanostructure as a free-space SERS sensor in this thesis is it provides the ease of fabrication in integrating with waveguide which it will be considered as an integrated SERS sensor in future work. Here the plasmonic behaviour and SERS effects are considered for nanostructures which have high aspect ratio nanostructure and surface. As conclusion, this chapter discusses pros and cons of different geometries between the 90SW devices and the inverted pyramids devices.

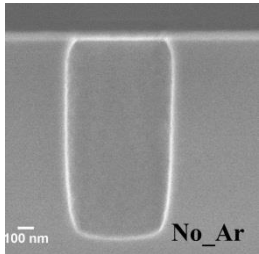
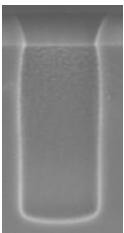
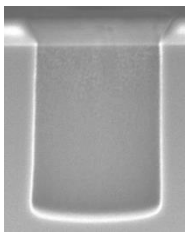
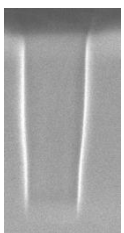
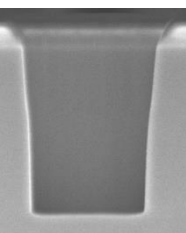
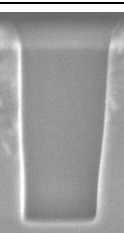
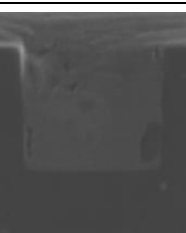
8.1 Consideration of surface abilities with straight sidewalls

In order to fabricate 90°straight sidewalls (90SW) nanostructures composed of rectangular trenches with the same lithographic pattern as used for the inverted pyramid design described in chapter 5 but a different etching step was applied. The 90SW nanostructure was created by dry etching via opening in the hard mask (silicon dioxide layer). The dry etch is achieved by using an Oxford Instruments “Plasmalab System 100” where the etching plasma is formed by a reactive ion etching (RIE) using a RF source and a RF induction magnetic coil to produce high plasma densities. In plasma etching, ions are first generated which can then remove the atoms from the substrate surface either chemically or mechanically. For the ICP tool, the three physical parameters including the forward power, ICP power and pressure, are utilized to achieve the anisotropic etch profile. Increasing the forward power can increase in the bias voltage which provides higher energy to the ions, notably as momentum in the normal direction of the substrate, which in turn, results in the ion angular distribution function becomes narrower. Since the wider angular distribution function results in a higher flux of ions hitting the sidewalls, this distribution function strongly impacts on the sidewall profile. Increasing the ICP power generates an increase in the vertical magnetic field during the plasma to generate more ions resulting in the faster chemical etching. By controlling the pressure, the side wall profile can be controlled to 90°. For example, decreasing the pressure will result in a greater Debye length of the ions in the plasma which in turn allows the plasma to spread resulting in the

reduction of dark space leading to an increase of the e-field driving the ions. Thus the driving force reduces the ion angular distribution.

The gas chemistry is the most essential aspect of the RIE. To achieve a 90SW profile, here the passivated silicon etch chemistry was used due to the lateral etching of non-vertical ions becoming an issue by using an unpassivated silicon etch for the nanoscale etching. For silicon etching, sulphur-hexafluoride(SF_6) is used as an etch gas and octafluorocyclobutane (C_4F_8) as a passivation gas. Since the forward power mostly rules the milling rate and the ion angular distribution function which is controlled by the pressure, as well as controlling the gas ratio. The proposed profile is achieved with the high aspect ratio and high selectivity using a silicon dioxide hard mask. The parameters and the etching results are discussed in Table 8-1.

Table 8-1 Details of the fabricated parameters of the anisotropic dry etch for the straight sidewall cavities

Fixed Parameter	Varied Argon gas flow(sccm)	SEM Image		Comments
		500D	1000D	
RF=50W ICP=800W SF_6 =25 sccm C_4F_8 =48 sccm Etching time=4min Avg. Depth=1143nm Selectivity of SiO_2 to Si = 1:25 	20			slight under cut in small pit size narrow profile angle at larger pit size
	27			No-under cut, over opening at the large pit size, a bit bow shape in the small pit size
	23.5			Under-cut free profiles for both pit sizes and no over opening at the large pit size

The etching recipe has to be optimized for the different pit geometries on the same chip. Increasing the ICP power (to 1300 and 1500) could offer a better profile angle at 90° with the sacrifice in selectivity of the hard mask of silicon dioxide. The ICP power is therefore selected at 800W using the gas chemistry as mentioned in the Table 8-1, leading to a bow shaped etch with slight under cut for 500nm pit size. To overcome this issue mechanically, argon gas has been introduced with 20sccm flow rate, resulting in the desired profile structure at 90° with the slight under cut for the narrow pit size (500nm) and leading the narrow profile angle for the larger pit size (1000nm). Increasing the argon flow to 27sccm means that the undercut issue at the opening of the cavity does not occur but offers a bow profile for narrow pit size and over opening for the larger pit. Finally argon flow was fixed at 23.5 sccm and both structures give the undercut free profiles. Using this modified recipe, the nanostructures are etched for 2 and 3 minutes resulting in 598nm and 798nm depths respectively, followed by gold metallization with a 400nm thickness. The ‘glancing angle’ metallization is done using a LAB700 evaporator using the same recipe as used for the inverted pyramid described in chapter 5. The ‘glancing angle’ is fixed at 25° (which is the angle for the deposition of inverted pyramid) and 34° . Due to the different angle deposition, the sidewall gold thickness and morphologies can be seen in SEM images (Fig 8.1) showing that 25° deposition can deposit more gold on the structure compared to 34° deposition.

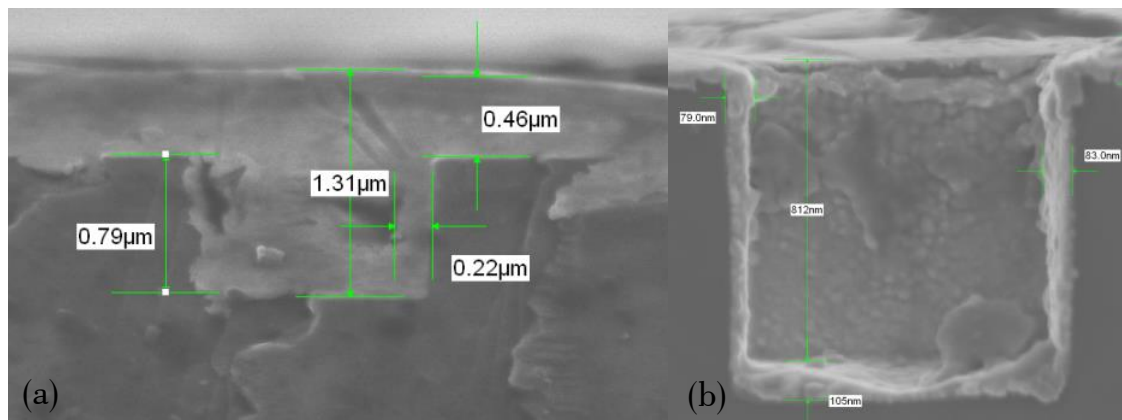


Figure 8.1 SEM images cleaved devices with different angle metallization of the straight sidewall cavities: (a) 25° glancing angle deposition provides gold of 220nm thickness on the sidewall and 180nm thickness at the bottom, (b) 34° glancing angle deposition provides that 83nm thick gold on the sidewall and 105nm thick at the bottom of the cavity.

8.1.1 Simulation studies

The 3D nanostructures with the 90SW profile are designed such that pit size was similar to the pyramidal cavities of chapter 5 except for that the geometry and depth of the cavity were different. The 90SW structures depth is not defined by opening size but is defined by an anisotropic dry etch. In designing the parameters, the depth of the structure after the surface is coated with gold is set at 782 nm (for 2 minute etching) and 1048nm (for 3minute etching). Here the simulation considers the effect of pitch length, pit size and depth of the straight sidewall structures. The effect of pitch on the plasmonic behavior was studied theoretically by varying the pitch from 1250nm to 2000nm whilst maintaining the pit scale to 1000nm, with a depth of 782nm and a gold thickness on the sidewall of 220nm conformally. The results are collected in terms of zero order reflection for the broadband excitation wavelength range for different incident angles till 70° and presented as the dispersion maps as mentioned in section 4.3.1. The dispersion maps (Fig 8.2) illustrates the overall reflection efficiencies and diffraction effects at different excitation wavelengths for the change in pitch length under TM-polarization. The diffraction features in the data are shifted to the longer wavelengths with the larger pitch length. This phenomenon was also observed for the inverted pyramid devices as described in chapter 5 and confirms how the shift of the diffraction pattern is dependent on scaling of the pitch length rather than the structural architecture. Under normal incidence, band gaps formed by the diffraction are also shifted to the longer wavelength while increasing the pitch however the shift of the band gap depends upon the incident angle and the excitation wavelength. The tuning/shift of plasmon resonance however is independent on the pitch length but it depends on the pit size. The subtle features resulting from diffraction effects as a function of the different pitch lengths are shown in Fig. 8.3(a). The diffraction lines are shifted to the longer wavelengths with the longer pitch length devices as indicated with the series of color arrows and also the shift of bandgap to the lower energy (shown by the red circle) is observed at the normal incidence.

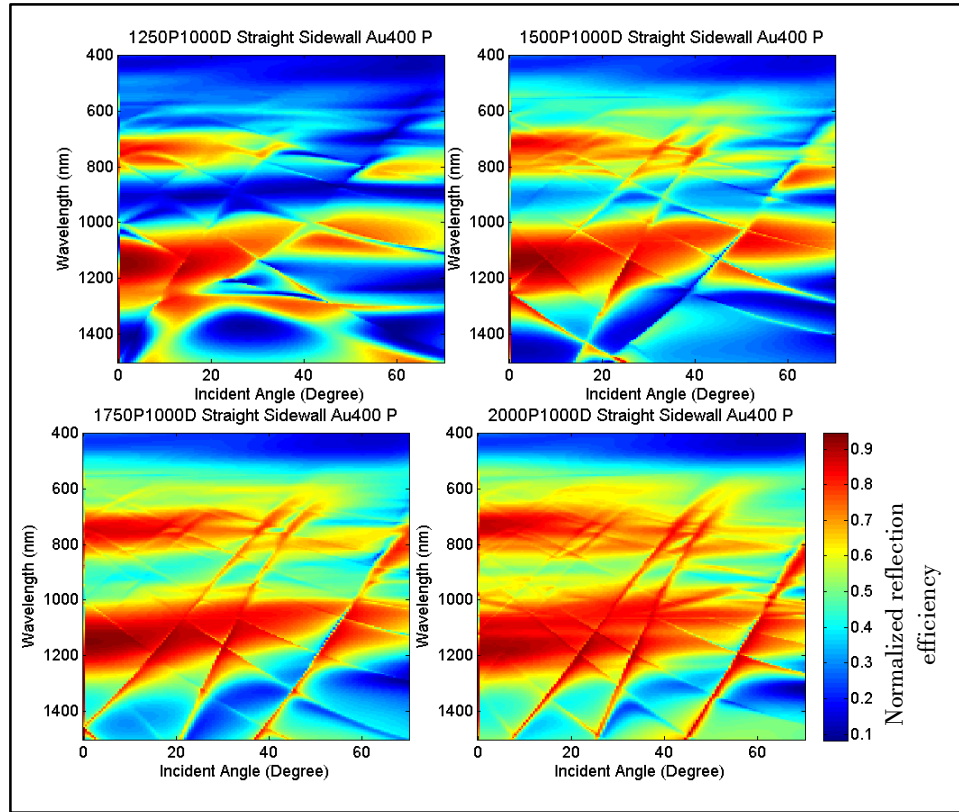


Figure 8.2 Dispersion maps of the normalized reflection efficiency for the nanostructure cavity composed of the straight sidewall profile, for the 1000nm pit size and 782nm depth with the different periods ranging from 1250nm to 2000nm by 250nm steps. The gold layer is deposited as 400nm thick on the flat surface and 220nm on the sidewall surface. The simulation is performed with TM-polarization for the specular measurement.

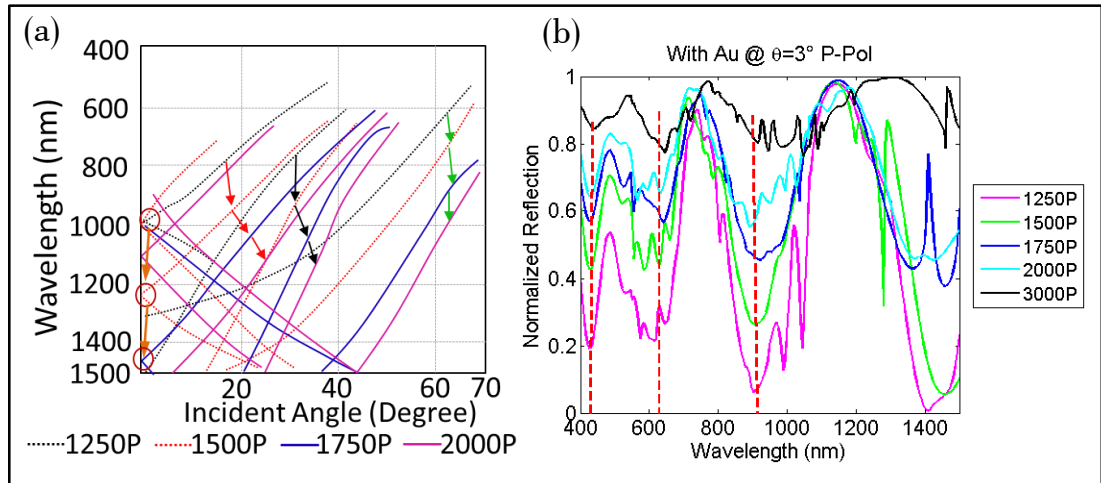


Figure 8.3(a).Distribution of zero order diffraction of 1000nm pit size along with various pitch length ranging from 1250nm to 2000nm. The colour arrows indicate to the shift of the diffraction lines and the red circles with arrows for the shift of bandgap. (b) Normalized reflection at 3° incident angle as a function of the excitation wavelength for pitch effect. The red dotted lines are guided to the plasmon resonance.

Since the pit size is constant and hence plasmon resonance energies confined at the specified excitation wavelength remain unchanged although their intensity is mostly suffered from the fill factor effect. This phenomenon is shown in Fig. 8.3(b) where the normalized reflection at a 3° incident angle as a function of excitation wavelength for the various pitch lengths is shown. Here the plasmon is localized at 425nm, 610nm and 900nm operation wavelengths with the broader bandwidth (shown by the red dotted line), the intensity is scaled by the fill factor. The profile is straight enough to mean that the plasmon is localized within the cavity over the range of incident angle.

The pit size effect on the interaction of incoming light with the 90SW structures was studied under TM-polarization while maintain the pitch at the 1500nm and pits are varied from the 500nm to 1250nm by 250nm step increases. Since the pitch is constant, the distribution of the diffraction patterns remains unchanged for the different pit sizes although the fill factor and hence on the absorption intensity is limited. From the dispersion maps shown in Fig 8.4, the change in the absorption efficiency corresponding to the pit and the fill factor can be seen clearly. The plasmon resonance (particularly the localized plasmon) is highly dependent on the pit size while the surface plasmon polariton depends upon the pitch related diffraction distribution in such a way that lower reflection efficiencies correlate with the diffraction lines as shown in the dispersion maps (Fig 8.4). The dispersive plasmon mode starts at low fill factors, 1500P750D while the localized plasmon modes are influenced at high fill factor, 1500P1250D. The correlation for surface with different pit geometries on the plasmonic behavior was performed at the 3° angle of incidence is shown in Fig 8.5(a). At a first glance, it can be clearly seen that the plasmon resonance is shifts to the longer wavelengths and also the absorption intensity increases with the increment of pit size. The different plasmon resonances named λ_1 , λ_2 and λ_3 are studied in detail as shown in Fig 8.5(b). Figure 8.5(b) is the double-y axis graph which represents the degree of shift of wavelength and change in absorption efficiency as a function of pit size. Although the plasmon resonance shifts to the longer wavelengths with pit size, the amount of wavelength shift is not linearly depend on the pit size with the maximum shift for 1000nm pit size. However for the 1000nm pit size, the increase in absorption intensity with wavelength is linearly related to the plasmon resonance in such a way that the longer wavelength can be used to tune the resonance.

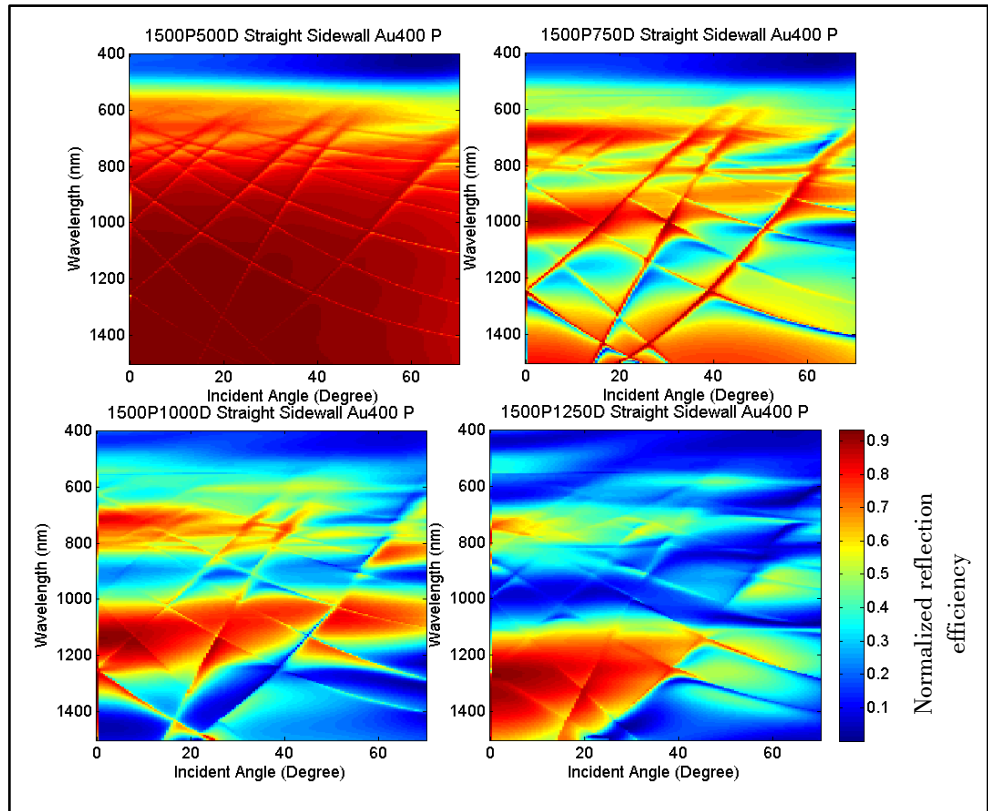


Figure 8.4 Dispersion maps for the 90SW cavity devices composed of the straight sidewall profiles, with the 1500nm pitch length and 782nm depth of a different pit size ranging from the 500nm to 1250nm by 250nm step. The gold layer is deposited 400nm on the flat surface and 220nm on the sidewalls. The simulation is performed under TM-polarization for the specular measurement.

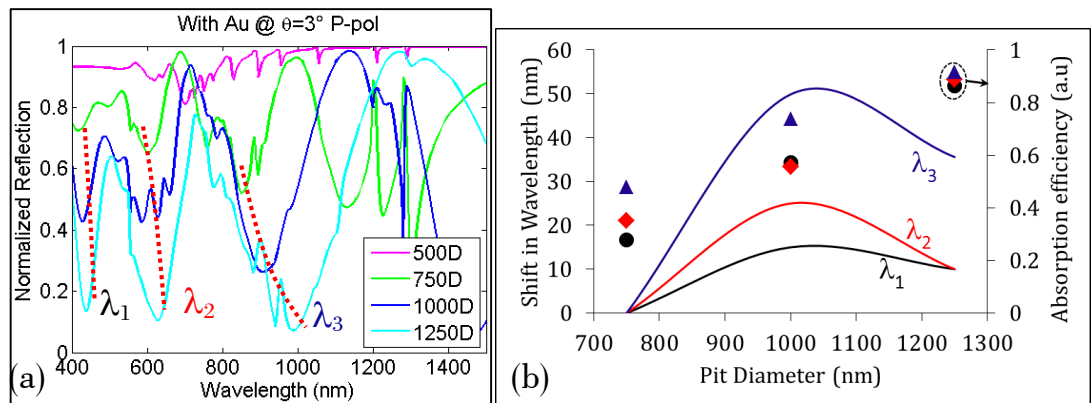


Figure 8.5 (a) Normalized reflection at a 3° incident angle as a function of the excitation wavelength for various pit sizes with a 1500nm pitch length. (b) A double-y axis graph shows that the amount of wavelength shift and the change in the absorption efficiency varied with pit size.

Absorption efficiencies are seen to be and directly proportional to the pit size (but not linearly dependent possibly due to the fill factor effect). The plasmon resonance, λ_3 in the

near infrared region (shown by blue triangle symbol in Fig 8.5(b)) has the highest absorption efficiency which is probably due to the fact that gold is used.

8.1.1.1 Dependence of the depth of the structures on the plasmon behaviour

The response of plasmon behavior as a function of a change in depth of the surface etched geometry. The studied depths are 782nm and 1048nm for the straight side wall structure, 1250P1000D at the aspect ratio 1:1.2 (width to length). The collected specular reflection as a function of excitation wavelength are plotted as a dispersion map in the same manner as in section 3.1, and shown in Fig 8.6.

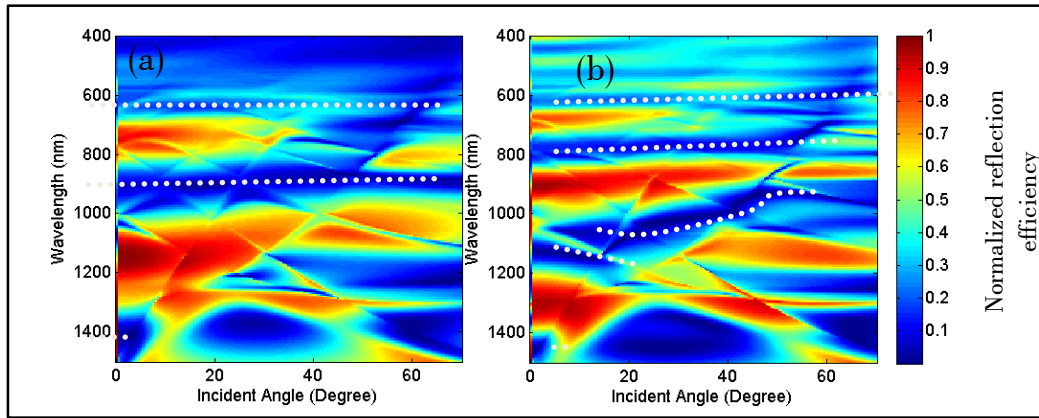


Figure 8.6 Dispersion maps of normalised reflection efficiency 1250P1000D straight sidewall structures of different depths, (a) Depth=782nm, (b) Depth=1048nm. The reflection efficiency is collected at TM-polarization and the scale bar is scaled from the dark blue to the dark red for the complete absorption to complete reflection of the light at each wavelength, respectively. White-dotted lines show the different plasmon modes between the two structures with different depths.

Since the pitch is same, the diffraction distribution remains unchanged irrespective of the depth of the structures as shown in Fig 8.6. However, unlike the pyramid cavities described in chapter 5 in which plasmon tuning is highly dependent on the pit size and depth, it is seen that the plasmon resonance is not fully dependent on the pit size for the 90° straight sidewall structures. In Fig 8.6, the effect of depth on plasmon behaviour of the fixed 1000nm pit sized structure can be observed clearly. The white-dotted lines in Fig 8.6 are guide lines that identify the difference in the distribution of the plasmon modes as a function of different depths. A deeper depth provides better confinement or more plasmon modes at the longer excitation wavelengths as compared to the structures with a shallower depth. To get a better understanding of the effect of depth on the plasmon absorption, the

reflection efficiency is extracted from the dispersion map at the normal incidence and plotted as shown in Fig 8.7(a) in which the red square box represents the region where the plasmon absorption is more influenced the change in depth of the cavity. The shallow depth, 782nm, gives one plasmon mode at $\lambda=900\text{nm}$ while the deeper depth, 1084nm, offers the plasmon modes at the operation wavelength of $\lambda=785\text{nm}$ and $\lambda=1130\text{nm}$. Apart from the differences illustrated in the red highlighted square box in Fig 8.7(a) in the visible and medium infra-red region, the increase in depth results in a shift in the reflection spectrum to higher energy.

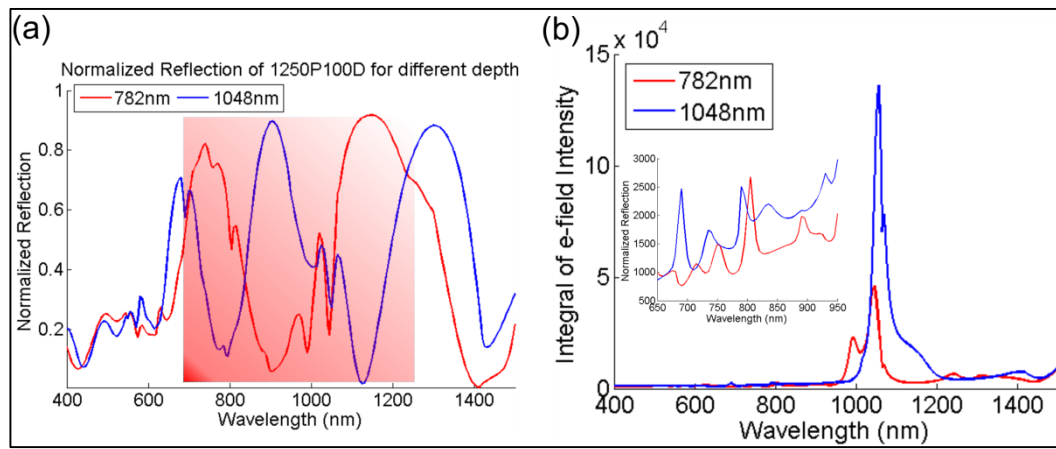


Figure 8.7 (a) Normalized Reflection spectrum of 1250P1000D with different depths as a function of wavelength. The coloured region refers to the range of wavelengths where the plasmon behaviour is distinctly affected by the change in device depth. (b) The line graph shows the total integral of the e-field intensity over the monitored area as a function of wavelength. The inset graph shows the close view of the field intensity at the near infrared region.

It is generally believed that the plasmon absorption is due to e-field confinement within the cavity at the boundary of the metal and dielectric medium. Therefore, the monitor is placed across the cavity at the center of the structure to record the e-field as a function of wavelength at the normal incidence. The monitor grid size is the same as the structure grid size. Figure 8.7(b) shows a plot of the total e-field energy integrated across the area of monitor, as a function of wavelength. The field intensity shows the highest value at the 1045nm and 1055nm for the shallow depth and the deeper depth respectively while the latter one provides a more intense field at all wavelengths of gold as shown in the inset of Fig 8.7(b). The field distribution within the cavity of different depths is also observed at the specific resonances such as 650nm, 785nm, 900nm and 1130nm as shown in Fig 8.8 from

which the field distribution and mode of each plasmon resonance can be examined. Figure 8.8 provides the information about the field distribution within the cavity for the different depth (1st column for shallow depth and 2nd column for deeper depth) at each plasmon resonance (650nm, 785nm, 900nm and 1130nm) observed in Fig 8.7(a). Generally, the deeper depth provides more confinement and more localized modes within the cavity. Although the highest field intensity due to the propagating plasmon occurs only at the corner of the openings rather than within the cavity, the field intensity of the plasmons is more intense at the longer wavelength/mid-infrared region (1130nm in Fig 8.8) as compared to the near infrared region. The field intensity varies with the height of the structure as extracted from the field distribution plot where the dotted yellow lines are guides plotted as a contour map for the different excitation wavelengths as shown in Fig 8.8. The bottom section of Fig 8.8 illustrates the field intensity as a function of height in the cavity for each operational wavelength. It is seen that the maximum field intensity is a predominantly at the height near the opening of the cavity structure possibly due to the coupling of the localized field to the dispersive field over the periodic domains. The field is more intense and confined at the longer wavelengths, particularly after the wavelength of 1000nm, regardless of the depth of the structure showing that the position of the field confinement is almost identical for both depths, for example at 1130nm the field greatest intensity is at the height of 350nm to 750nm. It can be concluded that the depth defines the number of modes and their intensity and hence, illustrates that it is possible to define either the pit size or the depth to tune the plasmon resonance and intensity. (How the plasmon resonance and the absorption intensity depend on the pit size and depth are shown in detail in the appendix (D.1.1).)

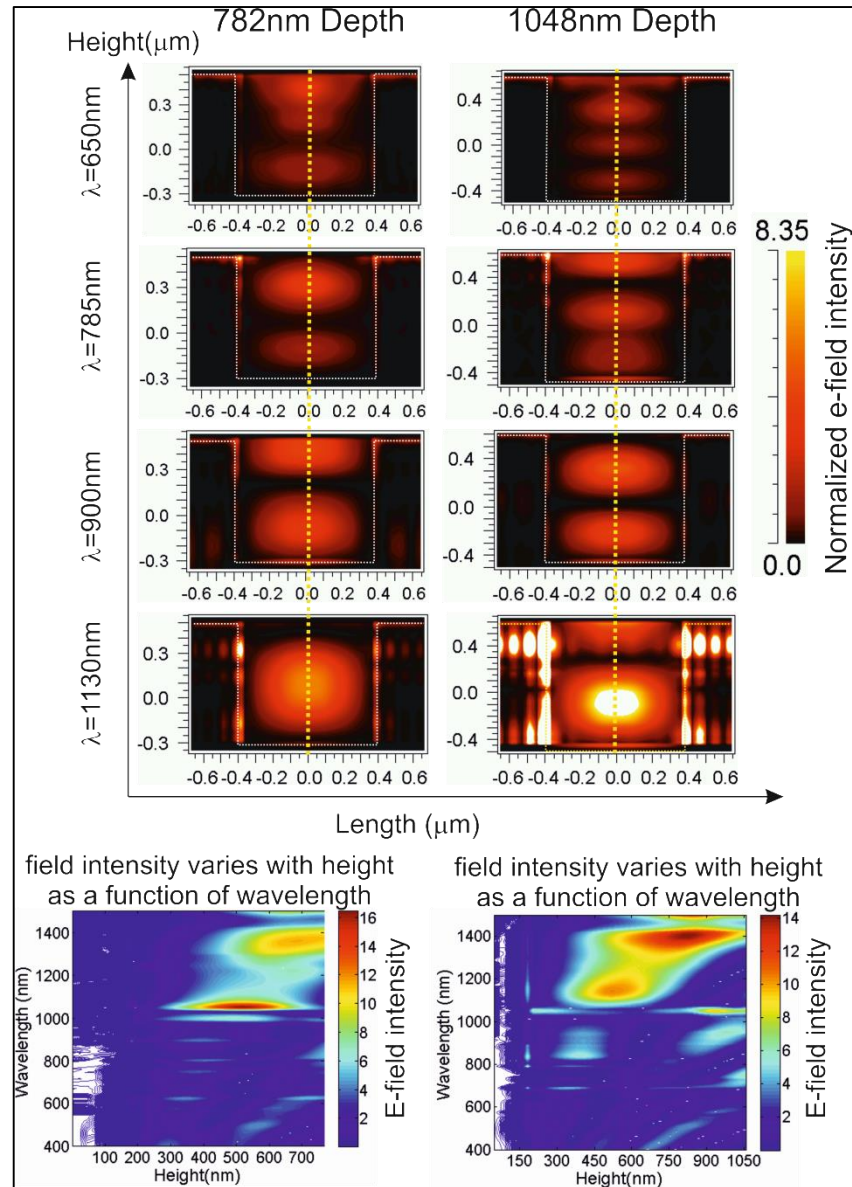


Figure 8.8 Field Distribution across the cavity as a function of height for the different depth, the 1st column represents the shallow depth 782nm, and the 2nd column refers to the deeper depth 1048nm. Each row represents the particular excitation wavelength where the plasmon absorption occurred, as shown Fig 8.7(a). The lower two plots are the high resolution contour maps for the variation of e-field intensity as a function of height for different excitation wavelengths. Left is for shallow depth and right is for the deeper depth.

8.1.2 Experimental studies using optical methods

This section provides data for the experimental evaluation of the effect of pitch length, pit size and the depth. Also provided is a dispersion of the difference in the optical properties of the 90SW devices as compared to the pyramidal cavities described in chapter 5.

First the effect of pit size on the plasmon was investigated using the dispersion maps as discussed in the section 4.1, and shown in Fig 8.9. Figure 8.9 illustrates the plasmon behavior with the pit size for different excitation wavelengths as a function of incident angle used for excitation. As expected the effect due to diffraction remain unchanged as the pitch length remains constant (Fig 8.9) and the plasmon resonances are shifted to the lower energy together with the larger pit sizes as shown in Fig 8.9 (e) (see the dotted line). Unlike the results seen for the pyramidal cavities in chapter 5, the devices with straight side walls maintain the broadband localized plasmon over the wider incident angle even though the fill factor defines the coupling between the plasmon mode and the intensity.

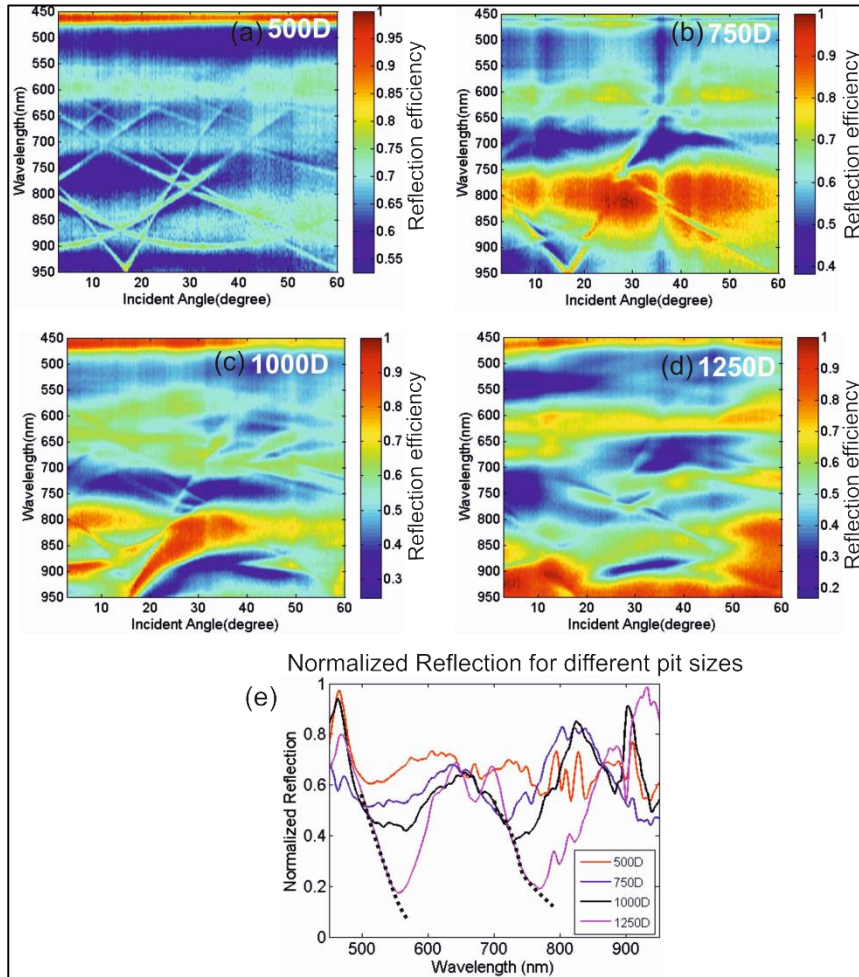


Figure 8.9 Dispersion maps for the various pit sizes at constant of pitch lengths and depths (a) 500nm, (b) 750nm, (c) 1000nm, (d) 1250nm (e) Normalized reflection as a function of wavelength at 3° incident angle illumination for different pit sizes. Dotted lines are present as guides for the shift of the plasmon resonance with the pit size.

As the pitch length changes, the distribution of the diffraction lines and the related band gaps vary with the scale of the period/pitch length. The plasmon resonance is fixed at the 535nm and 735nm (shown in Fig 8.10(e)) with the constant pit size. The dispersive propagating plasmon at around 900nm illustrated by the dark blue color region in the figures 8.10(a-d) is impacted by periodicity effect and thus the plasmon confinement is not constant with the pitch length and produces anti-crossing at 1750nm pitch lengths and gradually disappears at 2000nm pitch length. As expected, the plasmon absorption intensity is impacted by the fill factor in such a way that the plasmon absorption is generally higher (but not linearly proportional) with the high density fill factor meaning that the line spacing between the structures is narrower.

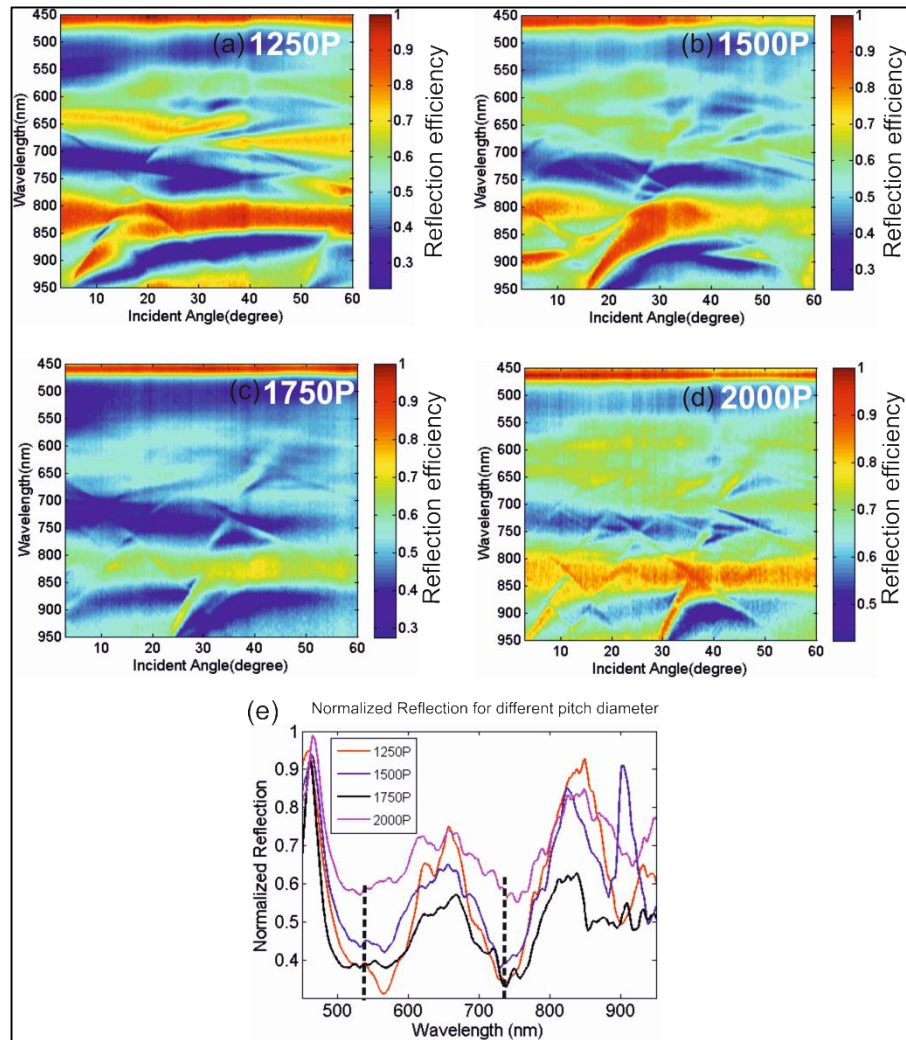


Figure 8.10 Dispersion maps of the normalized reflection efficiency for the different pitch length while maintaining the depth and pit size; (a) 1250nm, (b) 1500nm, (c) 1750P, (d) 2000nm, (e) line plot of the normalized reflection as a function of wavelength for different pitch length so that plasmon is confined at the fixed resonance due to the constant pit size (shown by the dotted line).

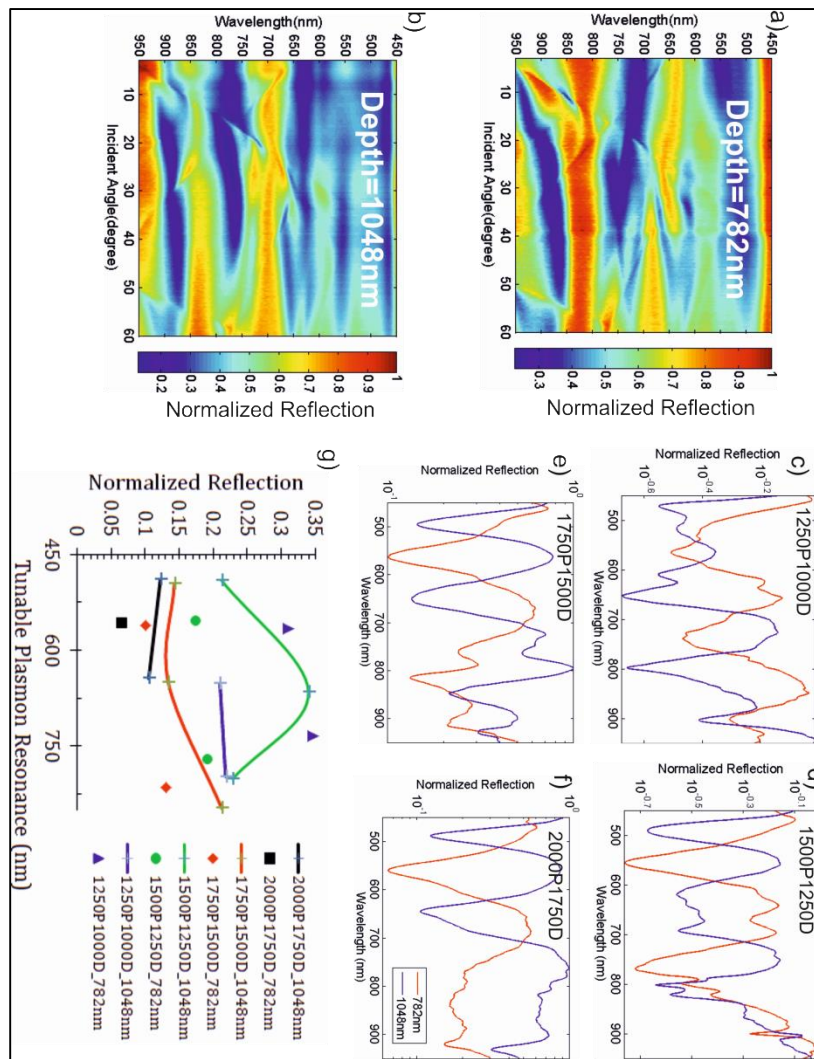


Figure 8.11 Reflection analysis for different depth. (a) Dispersion map for the depth of 782nm. (b) Dispersion map for the depth of 1048nm. Normalized Reflection at 3° incident angle for different depth with a separation distance of 250nm between adjacent structure such that (c) 1250P1000D, (d) 1500P1250D, (e) 1750P1500D, (f) 2000P1750D. (g) Comparison of normalized reflection (@ 3° incident angle) between different depths as a function of tuneable plasmon resonance for different pyramidal structures.

Unlike the KOH wet-etched pyramidal structures of chapter 5, this dry-etched straight sidewall structure has a greater level of variability in depth. Therefore, plasmon behavior as a function of the depth is studied. First the angular reflection from the structure of 1250P1000D with different depths are obtained and visualized as a dispersion map as shown in Fig 8.11 (a) and (b) where the color scale represents (from dark red to dark blue) is high reflection to high absorption. An important factor that can be distinctly observed from those dispersion maps is that the plasmon modes (dark blue regions) are highly dependent on the depth, even though the diffraction is unaffected because the pitch length

is constant at 1250nm. The plasmon modes are mainly impacted in the near-infrared region ($500\text{nm} < \lambda < 900\text{nm}$). For this phenomenon, to be scrutinized the comparison of normalized reflection at 3° incident angle must be compared for the structures or different depths with a separation distance of 250nm in respect to adjacent structures such as 1250P1000D, 1500P1250D, 1750P1500D and 2000P1750D as shown in Fig 8.11 (c-f). The reason to select these structures is that the relatively closed packed structural array can provide more plasmons by coupling the surface plasmon polaritons from the surface to the localized plasmon inside the cavity. From the figures, the plasmons are complementarily tuned to each depth within the near infra-red region regardless of the pit cross-sectional size. In Fig 8.11(g) it is shown how the depth of the cavity can be used to tune the plasmon resonance with the rest of geometrical parameters such as pitch and pit cross-sectional size. Figure 8.11(g) (which is analyzed from Fig 8.11(c-f)) is a line graph showing the normalized reflection intensity as a function of the tunable plasmon resonance for different depths. Moreover Fig 8.11(g) provides an information about how the plasmon resonance is also dependent on the pit and pitch length by comparing the various designs with different depths. It can be observed that the devices deeper of depth have more plasmon modes but lower plasmon absorption than the shallow depth devices, other than the 1250P1000D structure. The data presented have clearly illustrated that the straight sidewall optimized design parameters are different to the optimized pyramidal design, 1250P1000D in chapter 5. To confirm this experimental reflection analysis, the Raman measurement was carried out and will be discussed in the next section.

8.1.3 Raman measurement

The straight sidewall structure was coated with the same test molecule benzenethiol (BTh) as used for the pyramidal gold devices discussed in chapter 5. The structures were carried out using a Raman spectrometer using the 785nm excitation wavelength with the parameters: 44mW power, exposure time-10seconds, accumulation- 3times using the 20 times magnification (NA-0.4). The Raman measurements were taken for devices with different pit size and pitch length for different depths. The trigonal ring breathing mode ($990\text{-}1010\text{cm}^{-1}$) of BTh molecule was used for this analysis. 25 Raman measurements were carried out on each design of straight sidewall structures, averaged and plotted as shown in Fig 8.12 where the average Raman intensity of trigonal ring breathing mode of BTh(Fig

8.12 a-b) as a function of pit size for different depth and (Fig 8.12 c-d) as a function of pitch length for different depth are given.

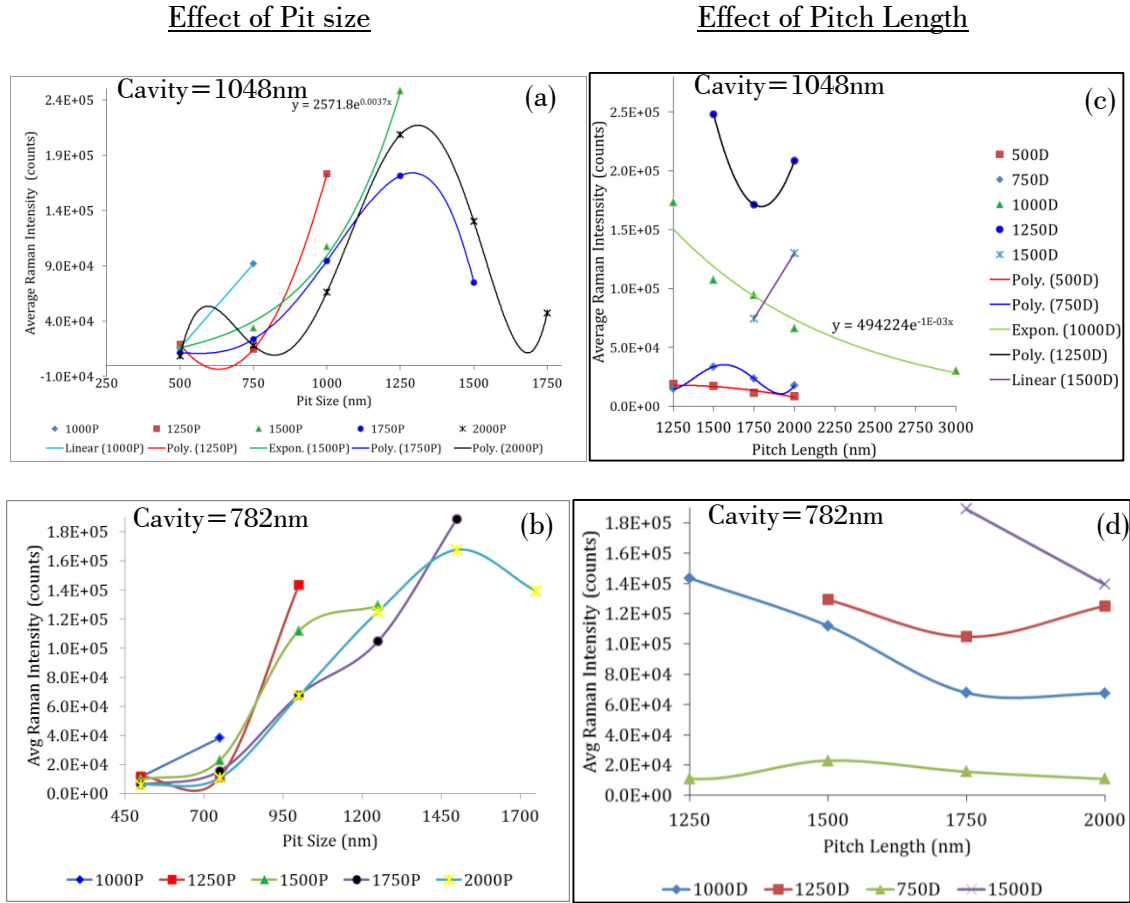


Figure 8.12 Comparison of average Raman intensity for trigonal ring breathing: (a) and (c) shows the effect of pit size and pitch length, for 1048nm depth respectively. (b) And (d) represents the effect of pit size and pitch length, for 782nm depth respectively.

From Fig 8.12, the effect of pit, pitch length at 1500nm and pitch at 1000nm pit size with a 1048nm depth of the 90SW structure is illustrated. The data illustrates that the same phenomenon to the pyramid structure (Fig 5.28) is seen. From figures 8.12 (a) and (c), the exponential functions of curve fitting provide $2571.8e^{0.0037x}$ and $4944224e^{-0.001x}$ for the pit and pitch effect respectively. The impact of the pitch is greater than that of pit size on the Raman signal intensities and this phenomenon is also related to the pyramid structure. Apart from 1500nm pitch length and pitch effect at 1000nm pit size, the remaining structures do not provide the same degree of Raman signal enhancement, where it is seen that the trend is polynomial and linear with geometry (pitch and pit). However, the effect of

the size of the pitch and pit (Fig 8.12 (b-d)) for the 782nm depth structures do not follow the exponential trend or enhancement at all. Regardless of the depth effect, the combination of pitch and pit with high fill factor can generally provide the increased plasmon absorption and hence enhance the Raman amplification of the molecule.

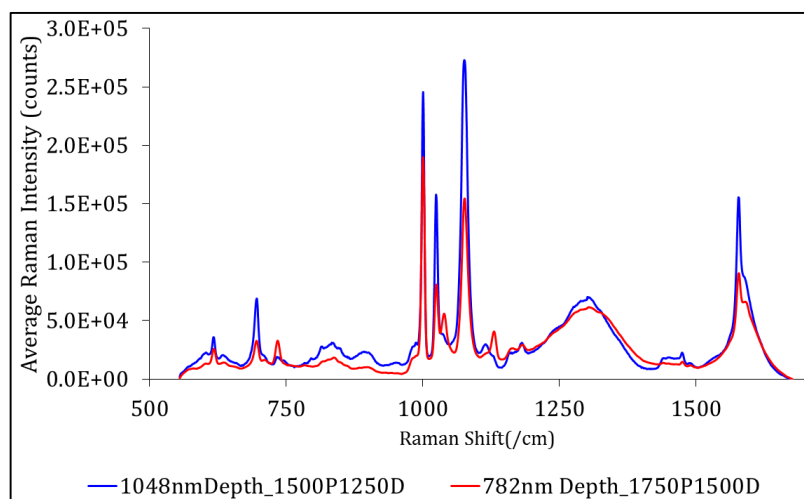


Figure 8.13 Comparison of average Raman intensity for BTh molecule between the optimized deeper depth structure (blue spectrum) and the optimized shallow one (red spectrum).

As observed in the previous section (the reflection analysis on the depth-Fig 8.11), the Raman measurement confirmed the optimized design of the 90SW structures for each depth such that 1500P1250D for 1048nm depth and 1750P1500D for 782nm depth. Also the deep depth of the device structure results in an improvement by a factor of 1.32 (for the trigonal ring breathing mode of BTh) compared to the optimized shallow depth structure of 782nm as shown in Fig 8.13. The enhancement factor of 9.2×10^7 is for the 1500P1250D device with a 1048nm depth, the enhancement factor of 1.01×10^8 is for the 1750P1500D device with a 782nm depth. The intra-sample reproducibilities in term of the relative standard deviation are 15.62% and 19.81% for the former and latter devices, respectively. These enhancement factors were calculated using the equation described in appendix B by substituting the area multiplication factor, $m = 2.41$ and 1.66 for 1500P1250D-1048nm Depth and 1750P1500D-782nm Depth respectively. Actually, the enhancement factor is not a precise parameter to compare the performance of the structure since the calculation depends on the area multiplier and the properties of test molecules rather than the solid standard reference. Therefore, the SERS performance of the structure depends on the

geometrical parameters, surface roughness and instrumental parameters and effects. However, these optimized straight sidewall substrates shows better enhancement compared to the benchmark substrate, Klarite and are comparable to the optimized pyramidal substrates described in chapter 5. Also they have better reliability for ease of integration with the waveguide.

8.2 Conclusion

This chapter discussed the plasmonic behaviour and SERS effects of 90SW devices. The motivation of studying the 90SW profile is to develop the fabrication process for integration with waveguide SERS sensor. The 90SW profile design can offer a direct fabrication approach and still produce similar performance to the inverted pyramid design. In the ‘glancing angle’ metallization process of creating the metal roughness (free from hot-spot), there is limitation to the 90SW aspect ratio. If it has a high aspect ratio, it will be challenging to achieve conformal coating in the sidewall as shown in Fig 8.14. However due to the advantage of dry etch method, the depth of 90SW profile is independent on the pit size of the cavity and hence tuning of plasmon modes can be achieved by varying three geometrical parameters including depth, pit size and periodicity. The depths of inverted pyramid devices depend on the pit size of the cavity when using KOH wet etch and the plasmon behaviour can only be tuned by the pit size and periodicity.

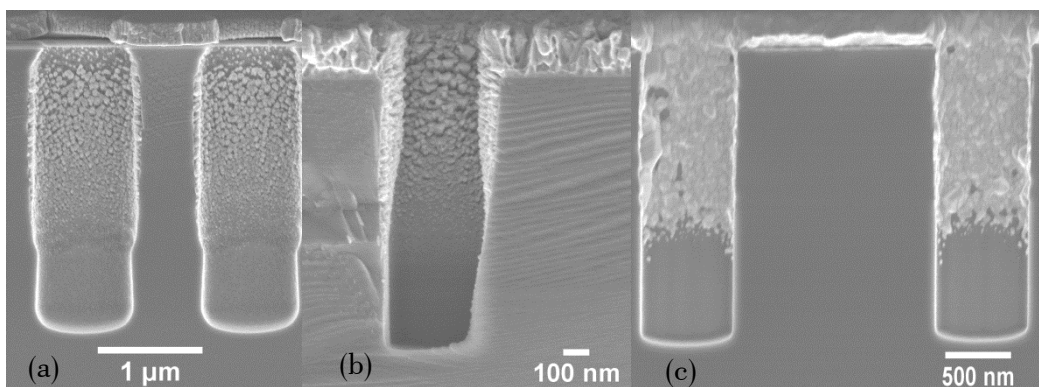


Figure 8.14 SEM images cleaved devices with different angle metallization of the straight sidewall cavities: (a) 28° glancing angle deposition of titanium, (b) 34° glancing angle deposition of titanium, (c) 37° glancing angle deposition of silver.

Another advantage of the 90SW high aspect ratio nanostructure is the ability to tune more plasmon modes at the same pit size of the inverted pyramids described in chapter 5. The 90° angle of sidewall profile provides more localized plasmon modes hence light energy of the near field plasmon mode. The 54.7° angle of inverted pyramid sidewall profile provides the coupling of propagating plasmon on the slope sidewall to resonated plasmons inside the cavity. It can be concluded that changing the angle of sidewall profile can tune the different plasmon energies and modes such that the cavities with steep sidewalls are favourable to the localized plasmons mode. The cavities with slope sidewalls are favourable to both localized and propagating plasmons inside the cavities. The optimized geometrical parameters of 90SW profiles are 1500P1250D with a 1048nm depth and 1750P1500D with 782nm depth. These optimized straight sidewall sensors provide approximately 10 fold improvement than the benchmark Klarite and are comparable to the optimized pyramidal SERS sensor described in chapter 5. However the reproducibility is lower compared to the optimized inverted pyramidal device.

Chapter 9. Conclusion and future work

9.1 Conclusion

The thesis has studied the plasmonic behaviour from a SERS active substrate which is comprised of gold coated inverted pyramid arrays fabricated on a silicon substrate using electron-beam lithography and an anisotropic wet etching. It has been shown that thereplication technique of nano-imprint lithography/nano-imprinting and angle-gold deposition can be used to produce low-cost, disposable and high throughput SERS plastic sensors. These gold coated SERS sensors have been thoroughly characterized to understand the geometrical properties of the sub-micron inverted pyramids. The inverted pyramidal structures have the physical parameters of pitch length, pit size, fill factor and aspect ratio (width to length) of the pyramidal base. Tuning of the geometrical properties gives an opportunity to optimize the plasmonic behaviour of inverted pyramid and hence achieve the highest enhancement factor. The disposable plastic sensor devices have been well demonstrated on thiol molecules by the project collaborator, Renishaw Diagnostics Ltd., Glasgow.

Both dispersive and non-dispersive surface plasmon modes have been found to occur on the structures. The plasmonic modes have been studied using modelling with the commercially available Photonic software, RSoft and verified experimentally using the bespoke computer controlled reflectometry system. Delocalized plasmons, so called Bragg plasmon have been shown to depend on the pitch length. Larger pitch length allows the more diffraction lines and then shifts to the lower energy (longer wavelength). Since these propagating surface plasmons depends on the incident angle and excitation wavelength, the polarization dependence of dispersive surface plasmon modes has also been observed. Although changes of pit size cannot dominate the order of diffraction, it mainly impacts on the trapping of localized plasmons of the selective excitation wavelength due to depth variation of pyramidal profile. Moreover the fill factor ($\frac{\text{pit size}}{\text{pitch length}} \times 100\%$) plays a major role to control the mix plasmon mode such as the coupling effect either between the delocalized to localized plasmon or between the same plasmon modes. These hypothesis are well agreed with both simulation and expmeriment results. Also the experimental results showed that the spacing between the adjacent pyramids, 250nm offers the highest

plasmon absorption and the spacing smaller than 250nm will not give any distinct improvement in plasmon absorption expect for the high fabrication cost. In addition to these geometrical parameters, the aspect ratio of inverted pyramid has shown that the inverted pyramid with the asymmetric lattice is highly sensitive to the polarization showing over 2-fold improvement in SERS counts under the input TM-polarized light compared to TE-polarized light while the symmetric has no dependence on polarization. Moreover, the rectangular based inverted pyramid has been observed to provide the polarization conversion via plasmon coupling and hence it could be a promising candidate in the optical applications such as polarization converter. The optimized inverted pyramidal SERS sensor on the silicon platform has average of 8 times improvement in Raman intensity of BTh molecules, compared to the benchmark standard Klarite.

For the purpose of the low-cost, mass-manufacturing and easy disposal, the sensor is transferred to plastic base platform using the silicon inverted pyramid as a stamp. Transfer is achieved using roll-to-roll and sheet-level nanoimprint fabrication techniques. The replicated plastic sensor also follows the same geometrical combination for highest SERS enhancement such as 1250nm pitch length and 1000nm pit size with rectangular aspect ratio (1:1.2). However, EF of the replicated plastic sensor is 10-fold lower than the silicon master. Analysis using AFM imaging gives the reason of lower in sensitivity such that the impairment in replication such as structural profile and depth accuracy and lack of waviness causing the difference in surface roughness of gold in the sidewall. The essential of gold roughness on the sidewall for SERS effect has also been proved. Nonetheless, the plastic sensor still can demonstrate for the real world application such as pharmaceutical cleaning using the ibuprofen and food monitoring using melamine in the milk even though they don't have super high enhancement compared to the optimized inverted pyramid on silicon platform. However the optimization of metallization makes the enhancement factor improved by the factor of 3.5. However the disposable plastic sensors have the potential for dual sensing applications using both SERS and SPR sensing configurations. In SPR sensing configuration, the optimized design, plastic sensor gives a wavelength of sensitivity 417nm/RIU.

Figure 9.1 gives the photograph of silicon stamp of the optimized design, the layout diagram for sensor chip showing the dimension and the roll of plastic substrate manufactured using R2R imprinting. Raman measurements were performed using a

Renishaw Invia Raman system at 785nm excitation wavelength with 44mW power, 3sec exposure time, 2 times accumulation, 5 times objective lens with NA=0.12. Measurements were taken at 45 random points over a chip across an area of 8mmx8mm. Table 9.1 gives the overall comparison of average Raman intensity of molecules among the SERS sensor devices such as enhanced inverted (IV) pyramid, Silicon, enhanced inverted (IV) pyramid, plastic and the benchmark standard Klarite for all vibrational modes. Table 9.2 gives the qualitative and quantitative performance of the different SERS substrates at C-C stretch mode of BTh. From Table 9.2, the enhanced design of pyramid produces the 10-fold increment in sensitivity and 4 times improvement in reproducibility compared to benchmark substrate “Klarite”. Transfer of enhanced design of pyramid to plastic platform was achieved although it could not give the same enhancement factor as its silicon master. However, the impairments occurred on the plastic design have been reported so that the plastic sensor can give the same sensitivity like master after overcoming those issues.

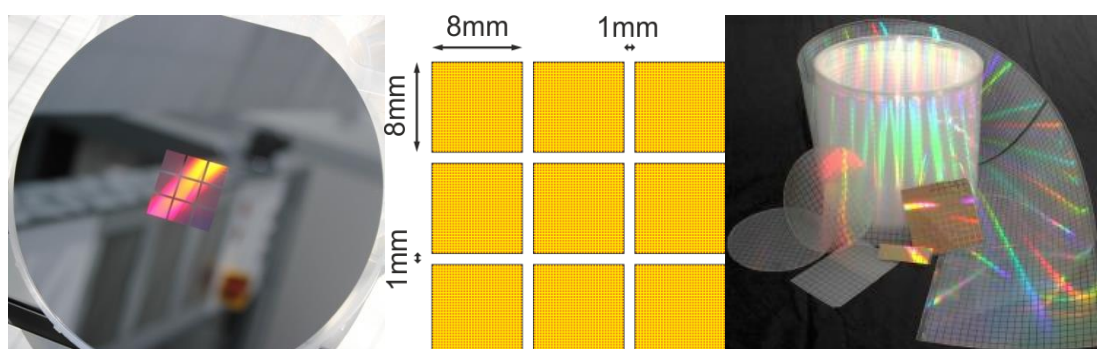


Figure 9.1 (a) photo of silicon stamp, (b) layout diagram, (c) replicated plastic substrate, using R2R imprinting.

The effect of gold thickness on the plasmonic behavior has been studied using the simulation where maintaining the geometrical parameters of the pyramid constant and varies only the gold thickness to observe only the plasmon response to gold thickness. The dependence of the shift in plasmon resonance, plasmon bandwidth and absorption energy on the gold thickness has been observed. Also the plasmon can be coupled on both interfaces of the metal layer when the thickness of gold is less than 100nm. The effect of metal conformality of the inverted pyramid corresponding to the interaction with incident light also has been studied. Non-conformal metal coating affects the pit size and shape which in turn impacts on the surface plasmon, resonance and energy. Understanding the

effect of metal layer conformality on plasmon dispersion provides the clear vision of the essential of the quality of metal coating in tuning plasmons resonance inside the cavity. Moreover, depending upon the conformality of gold coating the nano-textured metallic surface, the inverted pyramid could be used as an efficient broadband mirror-like reflector or as an efficient broadband, wide angle absorber at infrared wavelengths. Creation of a broadband wide angle absorbing surface such as this has important implications for photovoltaic cells.

Table 9-1 Comparison of average Raman intensity for the characteristic vibrational modes of BTh molecules on the different substrates

Characteristic Raman Vibrational frequencies of BTh molecules (/cm)	<i>Average Raman Intensity (Counts)</i>		
	<i>Enhanced IV-</i>	<i>IV-</i>	<i>Standard</i>
	<i>Pyramid, Si</i>	<i>Pyramid,</i>	<i>Klarite</i>
Ring deformation (615-630)	3215.08	173.73	1312.38
Trigonal ring breathing (990-1010)	37959.38	1483.73	10212.66
In-plane CH deformation (1015-1030)	26071.90	901.42	6494.39
CC stretches, 1075	44264.39	1554.25	10483.99
Ring stretches (1550-1630)	24942.85	700.65	5301.01

Table 9-2 Qualitative and quantitative performance of the different SERS substrates at C-C stretch mode of BThs

Substrates	<i>Enhancement Factor (EF)</i>	<i>Reproducibility (%)</i>
IV-pyramid, plastic (<i>EN</i>)	6.38×10^6	16.02
Standard Klarite	4.54×10^7	8.88
IV-pyramid, Si (<i>EN</i>)	1.82×10^8	2.37

"EN" refers to the enhanced design of Klarite.

Alternative geometry, 3D grating composed of straight sidewall profile, has also been studied for the plasmonic behavior and SERS effect relating to the physical variations. An advantage of 90SW profile is that depth of profile can be controlled by the anisotropic dry etch and in particular, the design is ease to integrate with waveguide underneath. The difference in plasmonic behavior between the slope sidewall and straight sidewall has been observed such that the straight sidewall mainly provides the localized plasmon while the slope side wall applies the mix plasmon mode to enhance Raman scattering. Controlling the depth, pit size and periodicity, the 90SW device was optimized at 785nm excitation wavelength for Raman spectroscopy measurement. The optimized geometrical parameters of 90SW devices are 1750P1500D at 728nm depth and 1500P1250D at 1048nm depth. The calculated enhancement factor using BTh molecules shows that 9.2×10^7 for 1500P1250D with 1048nm depth and 1.01×10^8 for 1750P1500D with 782nm depth. Actually, the enhancement factor is not a precise parameter to compare the performance of the different geometrical structures since its calculation depends on the area multiplier and the properties of test molecules rather than the solid standard reference. However, these optimized straight sidewall substrates shows better enhancement compared to the benchmark substrate, Klarite and are comparable to the optimized pyramidal substrate.

This thesis has given answers to many questions posed on the working principles of SERS mechanism on inverted pyramidal nanostructures. Of course, there are many questions still to be answered. Some of these questions have reached a more theoretical region of study, for example, the theoretical and mathematical understanding the inter-relationship between metal roughness and surface plasmon to SERS enhancement for Raman amplification because the study observed that SERS effect of Raman amplification could not be provided although there is either high plasmon energy/resonance or high metal surface roughness on the structures. Other questions require further experimental analysis to be performed. Towards, further application, there are a number of possible paths as discussed below.

9.2 Some suggestions for future work

9.2.1 Integrated SERS sensor

In this thesis, the free-space SERS sensor has demonstrated the sensitivity on the self-assembled molecules, Benzenethiol with the enhancement factor of 1.82×10^8 and

reproducibility of 2.37%, as shown in Fig 9.2. The free-space optics approach is most efficient due to the advantages of low losses, large area of interrogation and collection. However for a portable sensing system, the integrated optics is preferred because the waveguide can be integrated underneath of the sensor as shown in Fig 9.3. The straight sidewall structure is proposed instead of the slope sidewall structure due to the ease of fabrication when integrating the coupler and waveguide together as shown in Fig 9.4.

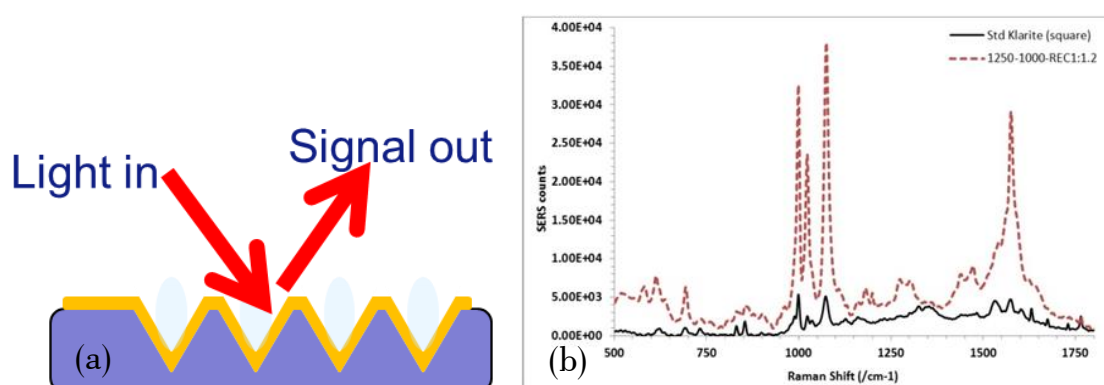


Figure 9.2 (a) Schematic diagram for free-space SERS sensor, (b) Raman spectra of BTh shows that an optimized inverted pyramid has higher enhancement compared to standard Klarite

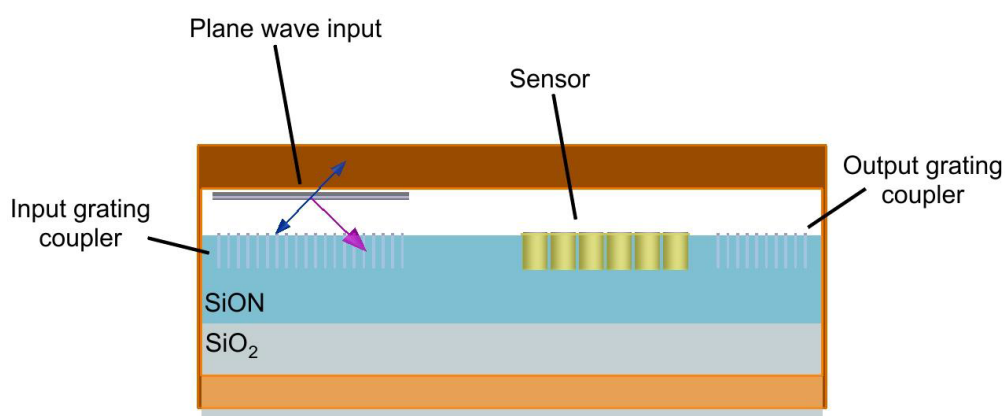


Figure 9.3 Schematic diagram for the proposed design of integrated SERS substrate

Figure 9.3 shows the schematic of the integrated waveguide and sensor device with input grating coupler. The grating input is used to couple the excitation light and assist guiding to SERS region. After interaction with analytes at the sensor region light is collected from the output grating coupler. For the losses waveguide, low frequency PECVD-deposited

silicon oxynitride (SiON) is considered due to its tuneable refractive index (1.46 to 2.1) and low optical loss ($<0.2\text{dB/cm}$ at 633nm)[147].

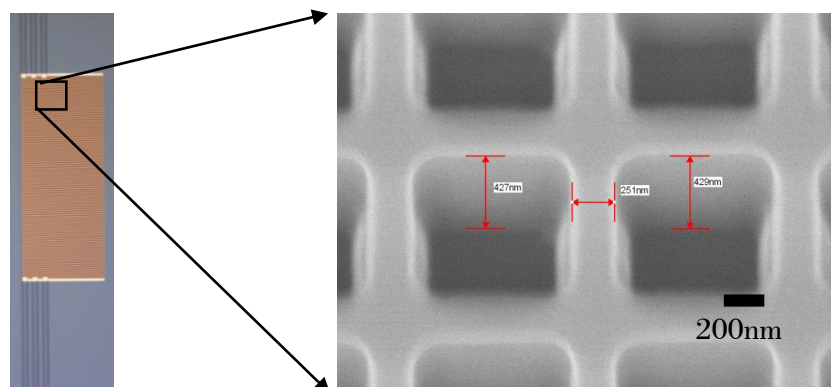


Figure 9.4 SEM image shows the fabricated integrated SERS sensor

9.2.2 Free standing inverted pyramid with nanopore leading to DNA sequencing via optical method

Current DNA sequencing by enzymes-based synthesis methods leaves its limitation and challenges [148]. These include long read-lengths time and require high accuracy. Although the single molecule sequencing method[149] based upon template-directed synthesis may provide valuable strategies for DNA sequencing, the application of nanoporous structures for the direct detection of DNA strands is an area of significant promise. This is the sequencing without the need for error-prone enzymes. Although the direct sequencing of DNA sequences through nanopores using electrical detection methods has been proposed[148], this has not yet been proven experimentally (in the literature). The most well developed and commercialized nanopore sequencing approach is that of Oxford Nanopore Technologies[150] where the α -hemolysin modified with cyclodextrin and an exonuclease is supported within a lipid bilayer within a pore. The challenges associated with this method are based around the lipid bilayer in which α -hemolysin is supported and sequences along the full DNA molecule length. Whilst this offers a direct sequencing can be achieved without the need for expensive reagents, the process is fast, cheap and provides high accuracy.

The slope sidewall inverted pyramid described in chapter 5 is designed for SERS sensing mechanism tuning the plasmon resonance to enhance the Raman scattering. Moreover, the plasmon enhancement near the tip of inverted pyramid provides an advantage to create a DNA sequencing approach based upon optical methods with potential for both sequencing and also optical trapping of protein functionalised nanoparticles. From this thesis, a free standing 3D gold inverted pyramid with a nanopore milled through the base whereby plasmon enhancement is greatest at the pore, is proposed. A developing strategy based upon 3D structured gold with nanopores through which the DNA strand is to be transported and enhanced as shown in Fig 9.5 and Fig 9.6.

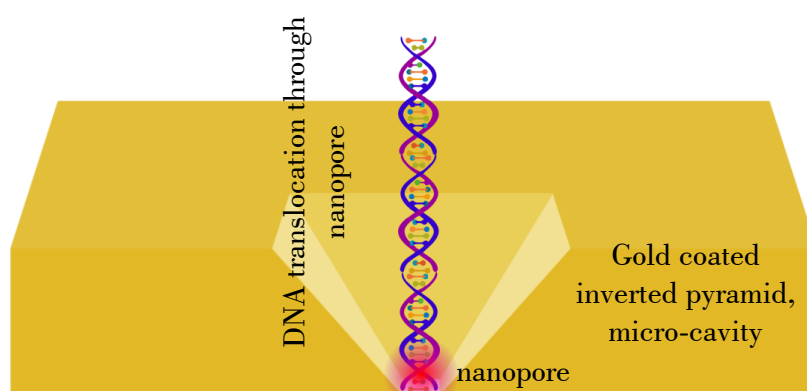


Figure 9.5 Schematic diagram shows that double stranded DNA passing through a nanopore of micro-cavity structure.

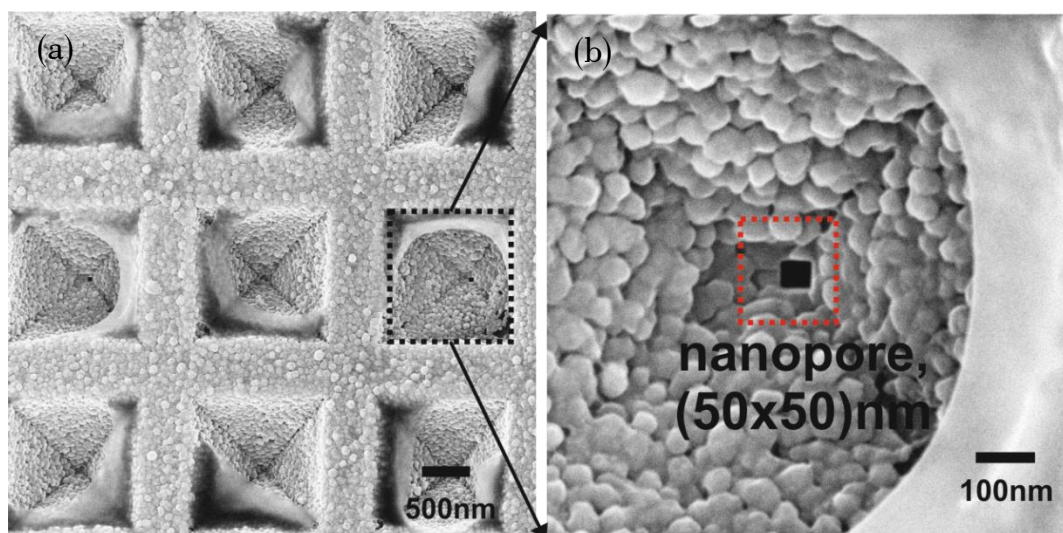


Figure 9.6(a) Helium ion microscope image of fabricated free standing microcavity with nanopore, (b) High magnification image highlights the nanopore structure with red box.

Free standing 3D-inverted pyramid with nanopore is designed to study the behavior of localized plasmon trapped inside the cavity. The geometrical parameters of the inverted pyramid is based from the commercial standard Klarite™ which is composed of 2000nm pitch length with 1500nm pit size followed by gold coating with 100nm thickness. In order to achieve a suitable size of a drilled square hole at the tip of the pyramid which will support the high localized e-field leading to high plasmon energy, different sizes of square hole will be conducted ranging from 10nm to 100nm via 10nm step. The height of the square hole is set at 100nm to penetrate the tip of the gold coated inverted pyramid. The simulation medium is first employed as air and then executed for water which is considered as the close environment for the fluidic system.

The design and simulation is carried out using a commercialized photonic suite, RSoft DiffractMOD, which employs Rigorous Coupled Wave Algorithm (RCWA) to obtain the backward diffraction efficiency using the periodic boundary condition. DiffractMOD treats a unit cell (each inverted pyramid) as the periodic array and transmission line formulation for boundary condition and the z-direction is defined as the launch field. The source will be a wide broadband range starting from 400nm to 1500nm and TM-polarization will be mainly applied since the plasmon is excited when the electric field perpendicular to the interface of the inverted pyramid. As a figure of merit, the zero order diffraction efficiency (specular reflection) can be observed. Since the concern is an effect of square hole on the plasmonic behavior, the e-field at around the drilled square hole however will be emphasized more using the spatial E-density monitor ruled by the equation:

$$E \text{ density}, U_E = \frac{1}{2} \int_V \text{Re}[\varepsilon(r')] |E|^2 dV \quad (9.1)$$

Where E is the electric field, ε is the spatially dependent permittivity and V is the volume of monitor set by length and height/width. Figure 9.7 gives a cross-sectional view of inverted pyramid with 100nm gold thickness where a square hole is drilled at the tip of the inverted pyramid and a monitor is placed in the middle of the square's height (50nm) while Fig 9.7(b) is a proof whether the hole is passed through the gold layer.

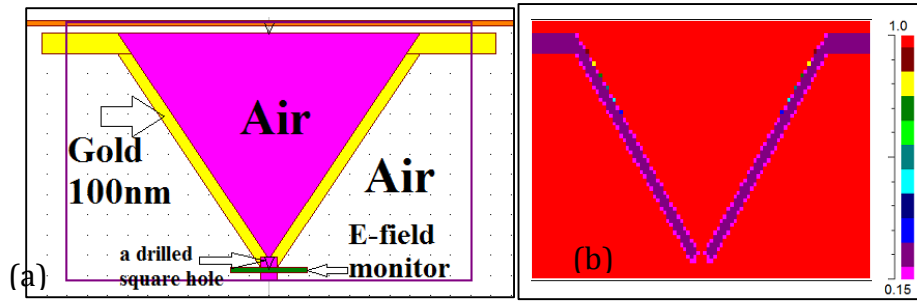


Figure 9.7 (a) a cross-sectional view of inverted pyramid indicating where a square hole and its spatial monitor are allocated; (b) a cross-sectional view of index profile where the red colour refers to the medium of air with RI=1

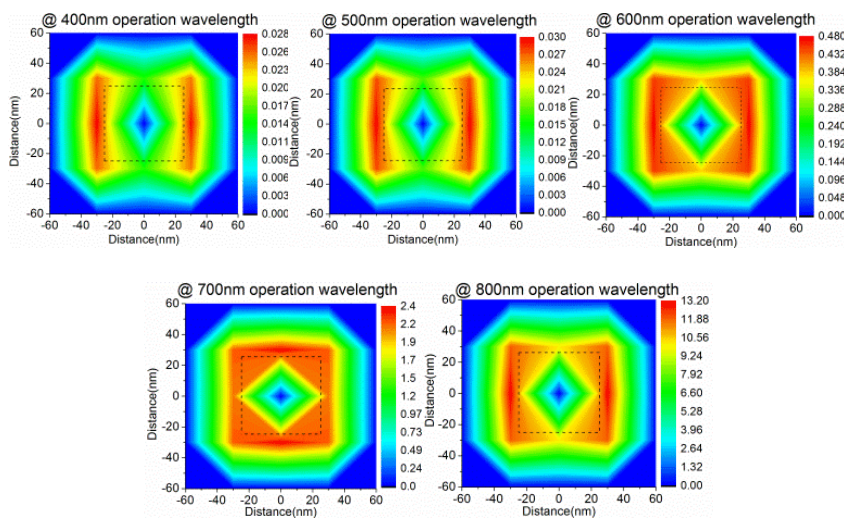


Figure 9.8 Calculated electric field above the nanopore within 3D gold microcavity for different excitation wavelength using the water background media.

A correct size of square hole will first be assessed changing the parameter from 10nm to 100nm at the medium of air and then change the medium to water and e-field profile will be examined to study the effect of square hole on the plamonic behavior. The e-field distribution is well confined around the nanopore (interface between the square and the end of the pyramid) for the 50nm square hole for both medium. Figure 9.8 gives the examples of electric field with the water medium. These are the preliminary results of the proposed nanopore technology for DNA sequencing based upon optical methods. After optimizing the size of inverted pyramid and nanopore for the intended excitation wavelength, the on-going studies including the microfluidic set-up along and the optical interrogation of the substrate need to be performed.

Appendices

Appendix A: Rigorous Coupled Wave Analysis (RCWA)

In numerical simulation of Plasmonic substrates, it is difficult to calculate Plasmon absorption bands directly. So it is wise to determine the diffraction efficiencies of structure and then find out the Plasmon bands from it. There are numerous simulation methods (finite-element simulation, finite difference time domain (FDTD) and RCWA method) to determine the diffraction efficiency, I here employ RCWA method.

Rigorous Coupled Wave Analysis (RCWA) method [151], represents electromagnetic fields as sum of coupled waves. The amplitude of coupled waves is solved by using state-variables method which determines the space-harmonic fields inside the structure in terms of eigen-vector and eigen-functions defined by RCWA equations. It uses complex periodic permittivity functions for materials, thus avoid perfect conductor (infinite conductivity) approximation. Latter approximation is applicable for microwave but leads to erroneous results for visible wavelength. All permittivity functions are represented in terms of Fourier harmonics. Each coupled wave is directly related to Fourier harmonics to perform full vectorial calculation of Maxwell's equation in Fourier domain. At the end of simulation, the diffraction efficiencies and spatial field distribution are calculated. When light (electromagnetic waves) is incident on a grating structure at an angle greater than normal of incidence, it results in both forward and backward diffracted waves as shown in figure 9.8.

For solving the electromagnetic field conveniently and determining coupled wave equation, the area of simulation region is split into three regions as shown in figure 13. Region 1 is a homogeneous dielectric medium with permittivity ϵ_1 , containing incident and backward diffracted wave. Region 3 is a homogeneous metallic medium with complex permittivity ϵ_3 . The forward diffracted waves get adsorbed as they propagate along the metallic medium. Region 2 includes the grating structure with both types of material.

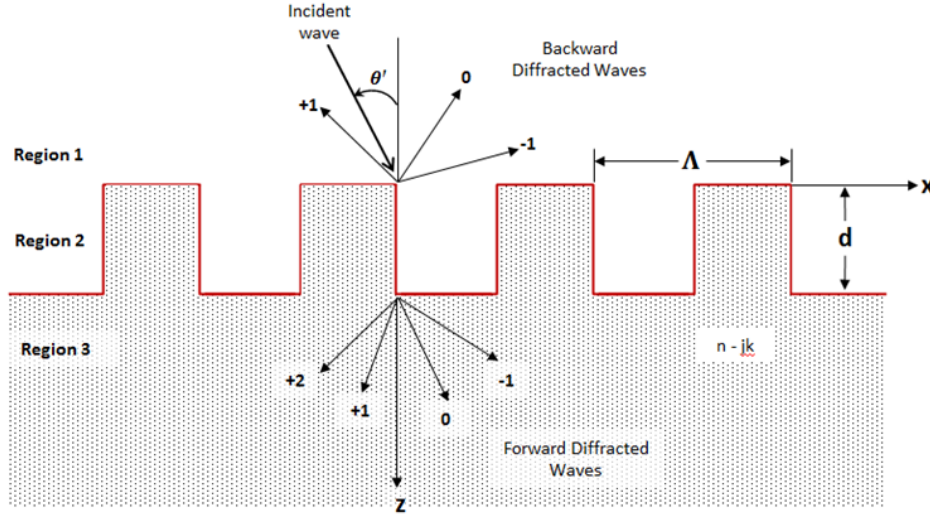


Figure 9.9 Geometry of metallic rectangular-groove grating [151]

The permittivity of region 2 can be determined by the equation:

$$\varepsilon(x, z) = \varepsilon(x + \Lambda, z) = \sum_p \varepsilon_p(z) \exp(jpKx) \quad (\text{A-1})$$

Where Λ is grating period, ε_p denotes Fourier component of grating permittivity, K represents magnitude of grating vector ($K = 2\pi/\Lambda$) and $j = (-1)^{1/2}$.

The total electric field in region 1 can be given as sum of incident and backward diffractive waves. The normalized field in region 1 is:

$$E_1 = \exp[-j(k_{x0}x + k_{z0}z)] + \sum_i R_i \exp[-j(k_{xi}x - k_{zi1}z)] \quad (\text{A-2})$$

where $k_{x0} = k\varepsilon_1^{1/2} \sin \theta'$, $k_{z0} = k\varepsilon_1^{1/2} \cos \theta'$, $k = 2\pi/\lambda$, θ' is angle of incidence, λ is free-space wavelength, $k_{xi} = k_{x0} - ik$ is vector Floquet condition and R_i is amplitude of i^{th} -order backward diffracted wave. Similarly, the normalized total electric-field in region 3 is:

$$E_3 = \sum_i T_i \exp\{-j[k_{xi}x + k_{zi3}(z - d)]\} \quad (\text{A-3})$$

where $k_{zi3} = (k^2\varepsilon_3 - k_{xi}^2)^{1/2}$. In the grating region (region 2), the field is expanded in terms of space harmonic components in periodic structure. The diffracted orders in region 1 and 3 are phase matched to the space harmonic components of grating structure. The normalized total electric-field in region 2 is:

$$E_2 = \sum_i S_i(z) \exp[-j(k_{xi}x + k_{z0}z)] \quad (A-4)$$

where $S_i(z)$ are field amplitude and in which i is space harmonic index. The electric-field in the grating region is related to its permittivity through the wave equation as shown in below:

$$\nabla^2 E_2 + k^2 \varepsilon(x, z) E_2 = 0 \text{ (TE polarization)} \quad (A-5)$$

On substitution of space harmonic field amplitude in to the above wave equation, I get the rigorous coupled wave equation:

$$\frac{d^2 S_i(z)}{dz^2} - j2k_{z0} \frac{dS_i(z)}{dz} = (k_{xi}^2 + k_{z0}^2) S_i(z) - k^2 \sum_p \varepsilon_p(z) S_{i-p}(z) \quad (A-6)$$

Finally, the rigorous coupled wave equation is solved using state variable method^[126] to obtain backward diffraction efficiency:

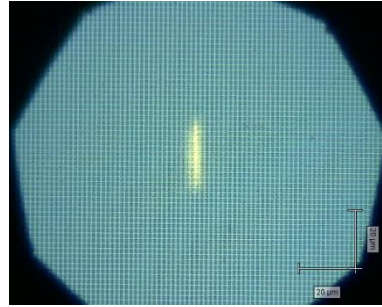
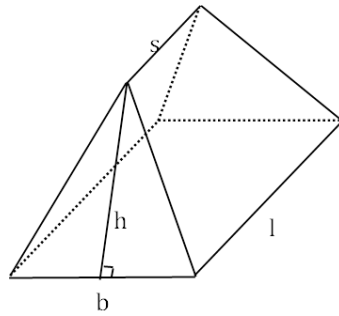
$$DE_i = |R_i|^2 \text{Re} \left(k_{zi} / k_{z0} \right) \quad (A-7)$$

Appendix B Calculation of enhancement factor

B.1 Area multiplication factor

Using the 50times objective lens without pin hole gives the illuminating area ($16.5\mu\text{m} \times 2\mu\text{m}$) including 10 inverted pyramids in the Raman measurement, the area multiplier will be

$$m = \frac{\text{Area}_{16.5 \times 2} - 10(\text{area of based rectangles}) + 10[(2 \times \text{area of triangular faces}) + (2 \times \text{area of trapezium})]}{\text{Area}_{16.5 \times 2}}$$



Getting the required parameters from the measurement such as $b = 1.05\mu\text{m}$, $l = 1.24\mu\text{m}$, $h = 0.741\mu\text{m}$ and $s = 0.222\mu\text{m}$ and the multiplier m becomes 1.17.

B.2 Enhancement factor

$$EF = \frac{I_{SERS}}{I_{RS}} \times \frac{N_{RS} \times L}{N_{SERS} \times m} \times \frac{1}{n^2} [152]$$

I_{SERS} = Raman intensity from SERS substrate

I_{RS} = Raman intensity from neat Benzene thiol = 124 [153]

N_{RS} = the molecular density of Benzene thiol

N_{SERS} = the real density of Benzene thiol on flat surface

L = the Raman scattering length = $450\mu\text{m}$

m = area multiplication factor

n = refractive index of benzene thiol = 1.56 [154]

$$\text{Molecular density} = N_{Av} \times \frac{\text{mass density (gcm}^{-3}\text{)}}{\text{molar mass (gmol}^{-1}\text{)}}$$

Where Avogadro's number, $N_{Av}=6.022 \times 10^{23} \text{ mol}^{-1}$

For BTh, since mass density is 1.077 gcm^{-3} and molar mass is 110.2 gmol^{-1} ,
 $N_{RS}=5.9 \times 10^{21} \text{ cm}^{-3}$

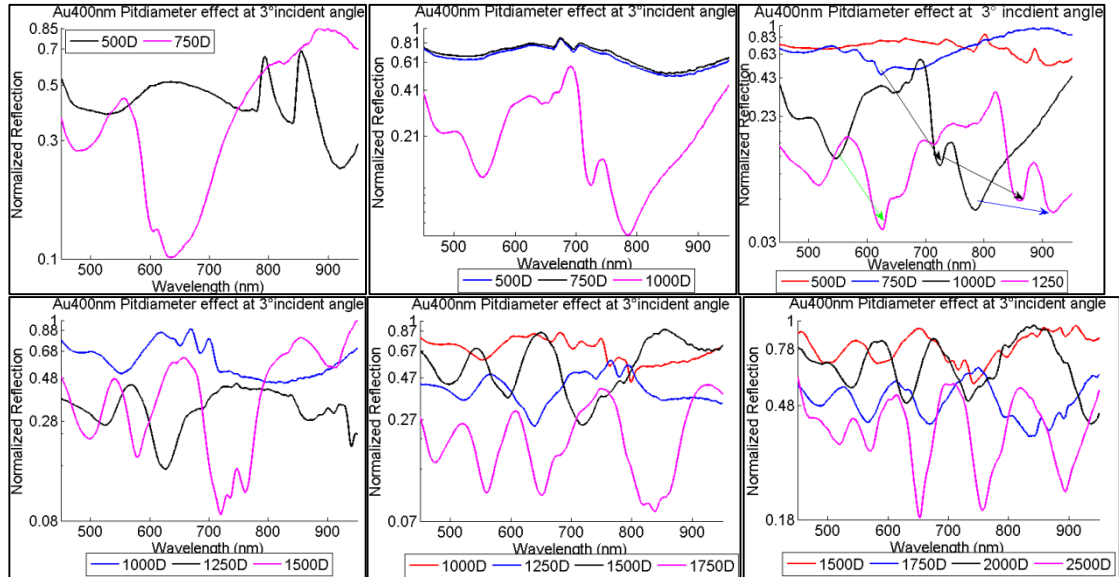
$N_{SERS}=0.544 \text{ nmolcm}^{-2}$ [155] and multiplied by N_{Av} becomes $N_{SERS}=3.3 \times 10^{14} \text{ cm}^{-2}$ on flat surface.

For an optimized design on silicon platform, the Raman intensity I_{SERS} is 1.7×10^5 counts and obtain a value of enhancement factor $EF=0.4 \times 10^9$. For an optimized design on R2R polymer replica, 4th generation, I_{SERS} is 1.13×10^4 counts and achieve a value of $EF=0.26 \times 10^8$. For an optimized design on R2R polymer, 5th generation (final demonstrator), $I_{SERS}=2.29 \times 10^4$ counts and give a value of $EF=0.523 \times 10^8$.

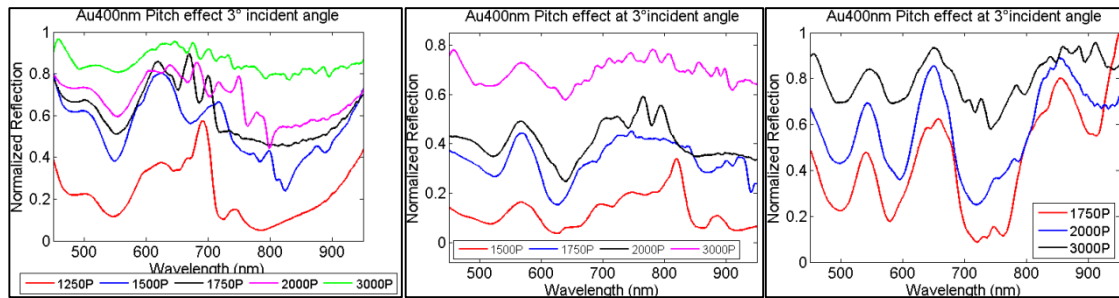
Appendix C Experimental Results

C.1 Analytical data from the Reflectometry measurement

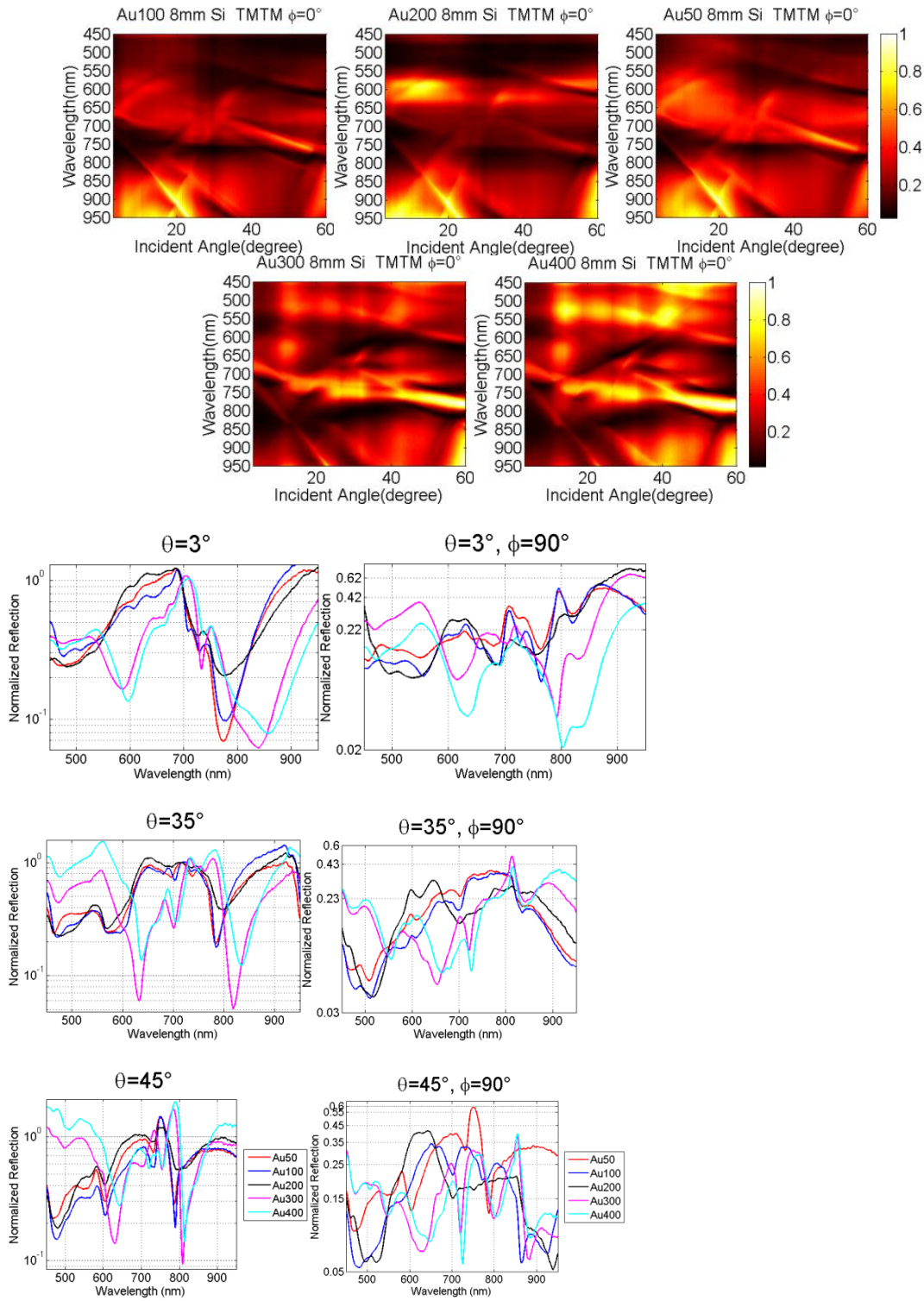
C.1.1 Pit size effect for Au 400nm



C.1.2 Pitch length effect for Au 400nm



C.1.3 Different Gold thickness



Appendix D Straight Sidewall Structure

D.1 Simulation Results

D.1.1 Difference in Depth together with pit size

Table 9-3 Plasmon response to the change in depth and pit size at the constant pitch, 1500nm

	Plasmon Behaviour varied with depth and pit size				
	Depth(nm)				
	782		1048		
	mode1				
Pit Size	Plasmon Resonance	Absorption	Plasmon Resonance	Absorption	(shift)
750	760	0.34	720	0.43	-40
1000	785	0.3033	735	0.59	-50
1250	775	0.46	765	0.992	-10
	mode2				
Pit Size	Plasmon Resonance	Absorption	Plasmon Resonance	Absorption	(shift)
750	850	0.48	940	0.46	90
1000	910	0.74	795	0.68	-115
1250	880	0.74	830	0.82	-50
	mode3				
Pit Size	Plasmon Resonance	Absorption	Plasmon Resonance	Absorption	(shift)
750	1130	0.53	1160	0.49	30
1000	1280	0.68	1210	0.47	-70

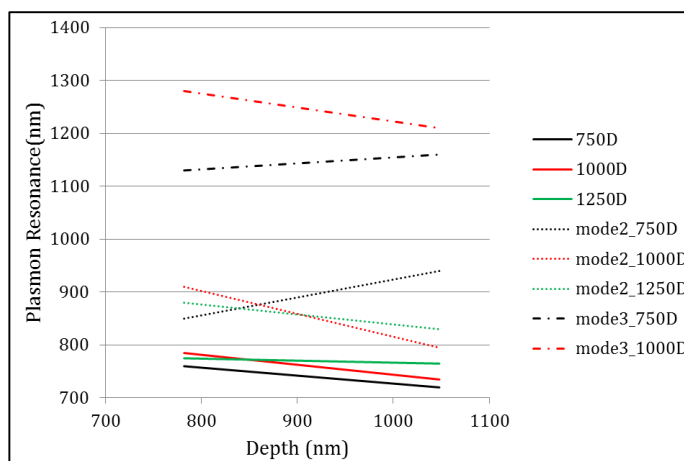


Figure 9.10 Line graph shows that the shift in plasmon resonance on the depth variation for different plasmon mode.

Bibliography

- [1] M. Fleischmann, P.J. Hendra, A.J. McQuillan, *Chemical Physics Letters* 26 (1974) 163.
- [2] R.G. Freeman, K.C. Grabar, K.J. Allison, R.M. Bright, J.A. Davis, A.P. Guthrie, M.B. Hommer, M.A. Jackson, P.C. Smith, D.G. Walter, M.J. Natan, *Science* 267 (1995) 1629.
- [3] T. Qiu, W. Zhang, P.K. Chu, *Recent Patents on Nanotechnology* 3 (2009) 10.
- [4] S.M. Prokes, O.J. Glembocki, R.W. Rendell, M.G. Ancona, *Applied Physics Letters* 90 (2007) 093105.
- [5] T. Vo-Dinh, *Selected Topics in Quantum Electronics*, *IEEE Journal of* 14 (2008) 198.
- [6] Y. Lu, G.L. Liu, J. Kim, Y.X. Mejia, L.P. Lee, *Nano Letters* 5 (2004) 119.
- [7] L. Qin, S. Zou, C. Xue, A. Atkinson, G.C. Schatz, C.A. Mirkin, *Proceedings of the National Academy of Sciences of the United States of America* 103 (2006) 13300.
- [8] J. Zhou, J. An, B. Tang, S. Xu, Y. Cao, B. Zhao, W. Xu, J. Chang, J.R. Lombardi, *Langmuir* 24 (2008) 10407.
- [9] M.E. Abdelsalam, S. Mahajan, P.N. Bartlett, J.J. Baumberg, A.E. Russell, *Journal of the American Chemical Society* 129 (2007) 7399.
- [10] L. Su, C.J. Rowlands, S.R. Elliott, *Opt. Lett.* 34 (2009) 1645.
- [11] J.P. Camden, J.A. Dieringer, Y. Wang, D.J. Masiello, L.D. Marks, G.C. Schatz, R.P. Van Duyne, *Journal of the American Chemical Society* 130 (2008) 12616.
- [12] S. Nie, S.R. Emory, *Science* 275 (1997) 1102.
- [13] N. Perney, F. García de Abajo, J. Baumberg, A. Tang, M. Netti, M. Charlton, M. Zoorob, *Physical Review B* 76 (2007).
- [14] D.A. Long, *The Raman Effect: A Unified Treatment of the Theory of Raman Scattering by Molecules*, John Wiley & Sons, Ltd, 2002.
- [15] C.A. Jennings, G.J. Kovacs, R. Aroca, *Langmuir* 9 (1993) 2151.
- [16] P.J.G. Goulet, R.F. Aroca, *Canadian Journal of Chemistry* 82 (2004) 987.
- [17] V. Deckert, D. Zeisel, R. Zenobi, T. Vo-Dinh, *Analytical Chemistry* 70 (1998) 2646.
- [18] B. Pettinger, B. Ren, G. Picardi, R. Schuster, G. Ertl, *Physical Review Letters* 92 (2004) 096101.
- [19] P. Hildebrandt, M. Stockburger, *The Journal of Physical Chemistry* 88 (1984) 5935.
- [20] K. Kneipp, H. Kneipp, I. Itzkan, R.R. Dasari, M.S. Feld, *Chemical Reviews* 99 (1999) 2957.
- [21] C.J.L. Constantino, T. Lemma, P.A. Antunes, R. Aroca, *Analytical Chemistry* 73 (2001) 3674.
- [22] J. Fang, S. Du, S. Lebedkin, Z. Li, R. Kruk, M. Kappes, H. Hahn, *Nano Letters* 10 (2010) 5006.
- [23] J.F. John, S. Mahurin, S. Dai, M.J. Sepaniak, *Journal of Raman Spectroscopy* 41 (2010) 4.
- [24] Z.Y. Zhang, Y.J. Liu, Q. Zhao, Y.P. Zhao, *Applied Physics Letters* 94 (2009) 143107.
- [25] T. Vo-Dinh, *TrAC Trends in Analytical Chemistry* 17 (1998) 557.
- [26] E.Z. Tan, P.G. Yin, T.T. You, H. Wang, L. Guo, *ACS applied materials & interfaces* 4 (2012) 3432.
- [27] S. Cataldo, J. Zhao, F. Neubrech, B. Frank, C. Zhang, P.V. Braun, H. Giessen, *ACS Nano* 6 (2011) 979.
- [28] X. Huang, Z. Zhao, J. Fan, Y. Tan, N. Zheng, *Journal of the American Chemical Society* 133 (2011) 4718.
- [29] N. Tian, Z.-Y. Zhou, S.-G. Sun, Y. Ding, Z.L. Wang, *Science* 316 (2007) 732.
- [30] J.W. Hong, S.-U. Lee, Y.W. Lee, S.W. Han, *Journal of the American Chemical Society* 134 (2012) 4565.
- [31] B. Liu, E.S. Aydil, *Journal of the American Chemical Society* 131 (2009) 3985.
- [32] Q. Zhang, N. Large, H. Wang, *ACS applied materials & interfaces* 6 (2014) 17255.
- [33] K.D. Osberg, M. Rycenga, N. Harris, A.L. Schmucker, M.R. Langille, G.C. Schatz, C.A. Mirkin, *Nano Letters* 12 (2012) 3828.

- [34] A.M. Gabudean, M. Focsan, S. Astilean, *The Journal of Physical Chemistry C* 116 (2012) 12240.
- [35] C. Liusman, H. Li, G. Lu, J. Wu, F. Boey, S. Li, H. Zhang, *The Journal of Physical Chemistry C* 116 (2012) 10390.
- [36] J.P. Singh, T.E. Lanier, H. Zhu, W.M. Dennis, R.A. Tripp, Y. Zhao, *The Journal of Physical Chemistry C* 116 (2012) 20550.
- [37] D. Correia-Ledo, K.F. Gibson, A. Dhawan, M. Couture, T. Vo-Dinh, D. Graham, J.-F. Masson, *The Journal of Physical Chemistry C* 116 (2012) 6884.
- [38] N.G. Tognalli, A. Fainstein, E.J. Calvo, M. Abdelsalam, P.N. Bartlett, *The Journal of Physical Chemistry C* 116 (2012) 3414.
- [39] C. Steuwe, C.F. Kaminski, J.J. Baumberg, S. Mahajan, *Nano Letters* 11 (2011) 5339.
- [40] S.H. Lee, K.C. Bantz, N.C. Lindquist, S.-H. Oh, C.L. Haynes, *Langmuir* 25 (2009) 13685.
- [41] J.R. Anema, A.G. Brolo, P. Marthandam, R. Gordon, *The Journal of Physical Chemistry C* 112 (2008) 17051.
- [42] A.G. Brolo, E. Arctander, R. Gordon, B. Leathem, K.L. Kavanagh, *Nano Letters* 4 (2004) 2015.
- [43] M.S. Goh, Y.H. Lee, S. Pedireddy, I.Y. Phang, W.W. Tjiu, J.M.R. Tan, X.Y. Ling, *Langmuir* 28 (2012) 14441.
- [44] L. Zhang, X. Gong, Y. Bao, Y. Zhao, M. Xi, C. Jiang, H. Fong, *Langmuir* 28 (2012) 14433.
- [45] C. Tian, C. Ding, S. Liu, S. Yang, X. Song, B. Ding, Z. Li, J. Fang, *ACS Nano* 5 (2011) 9442.
- [46] J.-L. Yao, J. Tang, D.-Y. Wu, D.-M. Sun, K.-H. Xue, B. Ren, B.-W. Mao, Z.-Q. Tian, *Surface Science* 514 (2002) 108.
- [47] A. Tao, F. Kim, C. Hess, J. Goldberger, R. He, Y. Sun, Y. Xia, P. Yang, *Nano Letters* 3 (2003) 1229.
- [48] S. Shanmukh, L. Jones, J. Driskell, Y. Zhao, R. Dluhy, R.A. Tripp, *Nano Letters* 6 (2006) 2630.
- [49] W.J. Cho, Y. Kim, J.K. Kim, *ACS Nano* 6 (2011) 249.
- [50] S. Mubeen, S. Zhang, N. Kim, S. Lee, S. Krämer, H. Xu, M. Moskovits, *Nano Letters* 12 (2012) 2088.
- [51] R. Olivares-Amaya, D. Rappoport, P.A. Munoz, P. Peng, E. Mazur, A. Aspuru-Guzik, *The Journal of Physical Chemistry C* 116 (2012) 15568.
- [52] R.L. Aggarwal, L.W. Farrar, S.K. Saikin, *The Journal of Physical Chemistry C* 116 (2012) 16656.
- [53] M. Banik, A. Nag, P.Z. El-Khoury, A. Rodriguez Perez, N. Guarrotxena, G.C. Bazan, V.A. Apkarian, *The Journal of Physical Chemistry C* 116 (2012) 10415.
- [54] N. Pazos-Perez, F.J. Garcia de Abajo, A. Fery, R.A. Alvarez-Puebla, *Langmuir* 28 (2012) 8909.
- [55] Y. Fang, N.-H. Seong, D.D. Dlott, *Science* 321 (2008) 388.
- [56] E. Albanesi, C. Okoye, C. Rodriguez, E. Peltzer y Blanca, A. Petukhov, *Physical Review B* 61 (2000) 16589.
- [57] A.G. Milekhin, N.A. Yeryukov, L.L. Sveshnikova, T.A. Duda, S.S. Kosolobov, A.V. Latyshev, N.V. Surovtsev, S.V. Adichtchev, C. Himcinschi, E.I. Zenkevich, W.-B. Jian, D.R.T. Zahn, *The Journal of Physical Chemistry C* 116 (2012) 17164.
- [58] T. Ming, W. Feng, Q. Tang, F. Wang, L. Sun, J. Wang, C. Yan, *Journal of the American Chemical Society* 131 (2009) 16350.
- [59] F. Wang, C. Li, L.-D. Sun, H. Wu, T. Ming, J. Wang, J.C. Yu, C.-H. Yan, *Journal of the American Chemical Society* 133 (2010) 1106.
- [60] G. Kumari, C. Narayana, *The Journal of Physical Chemistry Letters* 3 (2012) 1130.
- [61] A. Kudelski, S. Wojtysiak, *The Journal of Physical Chemistry C* 116 (2012) 16167.
- [62] M.C.S. Pierre, A.J. Haes, *Analytical Chemistry* 84 (2012) 7906.
- [63] D. Li, S. Wu, Q. Wang, Y. Wu, W. Peng, L. Pan, *The Journal of Physical Chemistry C* 116 (2012) 12283.

- [64] Y. Bu, S. Lee, *ACS applied materials & interfaces* 4 (2012) 3923.
- [65] L. Rivas, S. Sanchez-Cortes, J.V. García-Ramos, G. Morcillo, *Langmuir* 16 (2000) 9722.
- [66] E.S. Thrall, A.C. Crowther, Z. Yu, L.E. Brus, *Nano Letters* 12 (2012) 1571.
- [67] S. Huh, J. Park, Y.S. Kim, K.S. Kim, B.H. Hong, J.-M. Nam, *ACS Nano* 5 (2011) 9799.
- [68] G. Luo, L. Wang, H. Li, R. Qin, J. Zhou, L. Li, Z. Gao, W.-N. Mei, J. Lu, S. Nagase, *The Journal of Physical Chemistry C* 115 (2011) 24463.
- [69] P. Chen, Z. Yin, X. Huang, S. Wu, B. Liedberg, H. Zhang, *The Journal of Physical Chemistry C* 115 (2011) 24080.
- [70] J. Liu, H. Cai, X. Yu, K. Zhang, X. Li, J. Li, N. Pan, Q. Shi, Y. Luo, X. Wang, *The Journal of Physical Chemistry C* 116 (2012) 15741.
- [71] E. Nalbant Esenturk, A.R. Hight Walker, *Journal of Raman Spectroscopy* 40 (2009) 86.
- [72] M.K. Hossain, Y. Kitahama, G.G. Huang, X. Han, Y. Ozaki, *Analytical and bioanalytical chemistry* 394 (2009) 1747.
- [73] K. Kneipp, *Spectrochimica Acta Part a-Molecular and Biomolecular Spectroscopy* 51 (1995) 8.
- [74] G.V.P. Kumar, S. Shruthi, B. Vibha, B.A.A. Reddy, T.K. Kundu, C. Narayana, *The Journal of Physical Chemistry C* 111 (2007) 4388.
- [75] Y. Cui, B. Ren, J.-L. Yao, R.-A. Gu, Z.-Q. Tian, *The Journal of Physical Chemistry B* 110 (2006) 4002.
- [76] E. Antoniou, P. Voudouris, A. Larsen, B. Loppinet, D. Vlassopoulos, I. Pastoriza-Santos, L.M. Liz-Marzán, *The Journal of Physical Chemistry C* 116 (2011) 3888.
- [77] M.G. Blaber, A.-I. Henry, J.M. Bingham, G.C. Schatz, R.P. Van Duyne, *The Journal of Physical Chemistry C* 116 (2011) 393.
- [78] X. Liu, C.-H. Sun, N.C. Linn, B. Jiang, P. Jiang, *The Journal of Physical Chemistry C* 113 (2009) 14804.
- [79] W. Ahn, S.V. Boriskina, Y. Hong, B.M. Reinhard, *Nano Letters* 12 (2011) 219.
- [80] A.J. Pasquale, B.M. Reinhard, L. Dal Negro, *ACS Nano* 6 (2012) 4341.
- [81] J. Ye, F. Wen, H. Sobhani, J.B. Lassiter, P.V. Dorpe, P. Nordlander, N.J. Halas, *Nano Letters* 12 (2012) 1660.
- [82] C. Forestiere, A.J. Pasquale, A. Capretti, G. Miano, A. Tamburrino, S.Y. Lee, B.M. Reinhard, L. Dal Negro, *Nano Letters* 12 (2012) 2037.
- [83] D. Jana, A. Mandal, G. De, *ACS applied materials & interfaces* 4 (2012) 3330.
- [84] M. Kim, Y.W. Lee, D. Kim, S. Lee, S.-R. Ryoo, D.-H. Min, S.B. Lee, S.W. Han, *ACS applied materials & interfaces* 4 (2012) 5038.
- [85] D. Jana, G. De, *Journal of Materials Chemistry* 21 (2011) 6072.
- [86] X. Ling, J. Zhang, *The Journal of Physical Chemistry C* 115 (2011) 2835.
- [87] X. Wang, W. Shi, G. She, L. Mu, *Journal of the American Chemical Society* 133 (2011) 16518.
- [88] X. Wang, W. Shi, G. She, L. Mu, *Physical chemistry chemical physics : PCCP* 14 (2012) 5891.
- [89] F. Bonaccorso, Z. Sun, T. Hasan, A.C. Ferrari, *Nat Photon* 4 (2010) 611.
- [90] I. Meric, M.Y. Han, A.F. Young, B. Ozyilmaz, P. Kim, K.L. Shepard, *Nat Nano* 3 (2008) 654.
- [91] C. Lee, X. Wei, J.W. Kysar, J. Hone, *Science* 321 (2008) 385.
- [92] W. Kubo, S. Fujikawa, *Nano Letters* 11 (2010) 8.
- [93] Q. Yu, P. Guan, D. Qin, G. Golden, P.M. Wallace, *Nano Letters* 8 (2008) 1923.
- [94] S. Yang, F. Xu, S. Ostendorp, G. Wilde, H. Zhao, Y. Lei, *Advanced Functional Materials* 21 (2011) 2446.
- [95] J.C. Hulteen, D.A. Treichel, M.T. Smith, M.L. Duval, T.R. Jensen, R.P. Van Duyne, *The Journal of Physical Chemistry B* 103 (1999) 3854.
- [96] D. He, B. Hu, Q.-F. Yao, K. Wang, S.-H. Yu, *ACS Nano* 3 (2009) 3993.
- [97] H. Liang, Z. Li, W. Wang, Y. Wu, H. Xu, *Advanced Materials* 21 (2009) 4614.
- [98] J. Fang, S. Lebedkin, S. Yang, H. Hahn, *Chemical communications* 47 (2011) 5157.

- [99] R. Alvarez-Puebla, B. Cui, J.-P. Bravo-Vasquez, T. Veres, H. Fenniri, *The Journal of Physical Chemistry C* 111 (2007) 6720.
- [100] S.-W. Lee, K.-S. Lee, J. Ahn, J.-J. Lee, M.-G. Kim, Y.-B. Shin, *ACS Nano* 5 (2011) 897.
- [101] M. Hu, F.S. Ou, W. Wu, I. Naumov, X. Li, A.M. Bratkovsky, R.S. Williams, Z. Li, *Journal of the American Chemical Society* 132 (2010) 12820.
- [102] N.L.-G. Maximilien Cottat, Inga Tijunelyte, Gregory Barbillon, Frederic Hamouda, Philippe Gogol, Abdelhanin Aassime, Jean-Michel Lourtioz, Bernard Bartenlian and Marc Lamy de la Chapelle, *Nanoscale Research Letters* 9 (2014) 6.
- [103] K.M. Nazrin Kooy, Lee Tze Pin and Ooi Su Guan, *Nanoscale Research Letters* 9 (2014) 13.
- [104] H. Zhang, C.A. Mirkin, *Chemistry of Materials* 16 (2004) 1480.
- [105] A. Santos, T. Kumeria, D. Losic, *Materials* 7 (2014) 4297.
- [106] B. Liedberg, C. Nylander, I. Lunström, *Sensors and Actuators* 4 (1983) 299.
- [107] S.A. Maier, H.A. Atwater, *Journal of Applied Physics* 98 (2005) 011101.
- [108] O.A. Sadik, A.O. Aluoch, A. Zhou, *Biosensors & bioelectronics* 24 (2009) 2749.
- [109] D. Shankaran, K. Gobi, N. Miura, *Sensors and Actuators B: Chemical* 121 (2007) 158.
- [110] J.N. Anker, W.P. Hall, O. Lyandres, N.C. Shah, J. Zhao, R.P. Van Duyne, *Nat Mater* 7 (2008) 442.
- [111] R.L. Rich, D.G. Myszka, *Journal of molecular recognition : JMR* 15 (2002) 352.
- [112] L.B.N.a.T.S. Lars Lading, *Sensors, proceedings of IEEE* 2 (2002) 4.
- [113] F.V. Matthew F. Peters, Madeleine Heroux, Manon Valiquette and Clay W. Scott. , *Assay and Drug Development Technologies* 8 (2010) 10.
- [114] M.A. Arugula, A. Simonian, *Measurement Science and Technology* 25 (2014) 032001.
- [115] J. Homola, S.S. Yee, G. Gauglitz, *Sensors and Actuators B: Chemical* 54 (1999) 3.
- [116] T.M. Chinowsky, S.D. Soelberg, P. Baker, N.R. Swanson, P. Kauffinan, A. Mactutis, M.S. Grow, R. Atmar, S.S. Yee, C.E. Furlong, *Biosensors & bioelectronics* 22 (2007) 2268.
- [117] G.G. Nenninger, P. Tobiška, J. Homola, S.S. Yee, *Sensors and Actuators B: Chemical* 74 (2001) 145.
- [118] R. Slavík, J. Homola, *Sensors and Actuators B: Chemical* 123 (2007) 10.
- [119] L.S. Live, O.R. Bolduc, J.-F.o. Masson, *Analytical Chemistry* 82 (2010) 3780.
- [120] J.H. Sim, Y.H. Kwak, C.H. Choi, S.-H. Paek, S.S. Park, S. Seo, *Sensors and Actuators B: Chemical* 173 (2012) 752.
- [121] P.K. Maharana, R. Jha, *Sensors and Actuators B: Chemical* 169 (2012) 161.
- [122] S.Z. Oo, M.D.B. Charlton, D. Eustace, R.Y. Chen, S.J. Pearce, M.E. Pollard, Optimization of SERS enhancement from nanostructured metallic substrate based on arrays of inverted rectangular pyramids and investigation of effect of lattice non-symmetry, 2012, p. 823406.
- [123] S.Z. Oo, R.Y. Chen, S. Siitonen, V. Kontturi, D.A. Eustace, J. Tuominen, S. Aikio, M.D.B. Charlton, *Opt. Express* 21 (2013) 18484.
- [124] M. Moskovits, *Reviews of Modern Physics* 57 (1985) 783.
- [125] D. Pines, *Reviews of Modern Physics* 28 (1956) 184.
- [126] H. Raether, *Surface Plasmons on Smooth and Rough Surfaces and on Gratings*, Springer-Verlag, 1988.
- [127] E.C.L.R.a.P.G. Etchegoin, *Principles of Surface-Enhanced Raman Spectroscopy and related plasmonic effects*, ELSEVIER, 2009.
- [128] A. Campion, P. Kambhampati, *Chemical Society Reviews* 27 (1998) 241.
- [129] e.E.D.Palik, *Handbook of optical constants of solids III*, New York, 1998.
- [130] P.G.E.E.C.L. Ru, *Principles of Surface-enhanced Raman spectroscopy and related plasmonic effects*, ELSEVIER, 2009.
- [131] G. MA, K. MJ, *Progress in Photovoltaics: Research and Applications* 3 (1995) 189.
- [132] T.A.Kelf, D.Phil, University of Southampton, 2006.
- [133] T. Inagaki, M. Motosuga, K. Yamamori, E. Arakawa, *Physical Review B* 28 (1983) 1740.
- [134] R. Colombelli, K. Srinivasan, M. Troccoli, O. Painter, C.F. Gmachl, D.M. Tennant, A.M. Sergent, D.L. Sivco, A.Y. Cho, F. Capasso, *Science* 302 (2003) 1374.

- [135] R.F. Oulton, V.J. Sorger, T. Zentgraf, R.-M. Ma, C. Gladden, L. Dai, G. Bartal, X. Zhang, *Nature* 461 (2009) 629.
- [136] M.T. Hill, Y.-S. Oei, B. Smalbrugge, Y. Zhu, T. de Vries, P.J. van Veldhoven, F.W.M. van Otten, T.J. Eijkemans, J.P. Turkiewicz, H. de Waardt, E.J. Geluk, S.-H. Kwon, Y.-H. Lee, R. Notzel, M.K. Smit, *Nat Photon* 1 (2007) 589.
- [137] K. Okamoto, I. Niki, A. Shvartsner, Y. Narukawa, T. Mukai, A. Scherer, *Nat Mater* 3 (2004) 601.
- [138] J. Müller, B. Rech, J. Springer, M. Vanecek, *Solar Energy* 77 (2004) 917.
- [139] S. Pillai, K.R. Catchpole, T. Trupke, M.A. Green, *Journal of Applied Physics* 101 (2007) 093105.
- [140] D. Derkacs, W.V. Chen, P.M. Matheu, S.H. Lim, P.K.L. Yu, E.T. Yu, *Applied Physics Letters* 93 (2008).
- [141] D.M. Schaadt, B. Feng, E.T. Yu, *Applied Physics Letters* 86 (2005).
- [142] K. Nakayama, K. Tanabe, H.A. Atwater, *Applied Physics Letters* 93 (2008).
- [143] D. Derkacs, S.H. Lim, P. Matheu, W. Mar, E.T. Yu, *Applied Physics Letters* 89 (2006).
- [144] S.I. Bozhevolnyi, V.S. Volkov, E. Devaux, J.-Y. Laluet, T.W. Ebbesen, *Nature* 440 (2006) 508.
- [145] H. Ditlbacher, J.R. Krenn, G. Schider, A. Leitner, F.R. Aussenegg, *Applied Physics Letters* 81 (2002) 1762.
- [146] J. Pendry, *Physical Review Letters* 85 (2000) 3966.
- [147] S.J. Pearce, M.E. Pollard, S.Z. Oo, R. Chen, M.D.B. Charlton, *Applied Physics Letters* 105 (2014) 181101.
- [148] D. Branton, D.W. Deamer, A. Marziali, H. Bayley, S.A. Benner, T. Butler, M. Di Ventra, S. Garaj, A. Hibbs, X. Huang, S.B. Jovanovich, P.S. Krstic, S. Lindsay, X.S. Ling, C.H. Mastrangelo, A. Meller, J.S. Oliver, Y.V. Pershin, J.M. Ramsey, R. Riehn, G.V. Soni, V. Tabard-Cossa, M. Wanunu, M. Wiggin, J.A. Schloss, *Nat Biotech* 26 (2008) 1146.
- [149] J. Eid, A. Fehr, J. Gray, K. Luong, J. Lyle, G. Otto, P. Peluso, D. Rank, P. Baybayan, B. Bettman, A. Bibillo, K. Bjornson, B. Chaudhuri, F. Christians, R. Cicero, S. Clark, R. Dalal, A. deWinter, J. Dixon, M. Foquet, A. Gaertner, P. Hardenbol, C. Heiner, K. Hester, D. Holden, G. Kearns, X. Kong, R. Kuse, Y. Lacroix, S. Lin, P. Lundquist, C. Ma, P. Marks, M. Maxham, D. Murphy, I. Park, T. Pham, M. Phillips, J. Roy, R. Sebra, G. Shen, J. Sorenson, A. Tomaney, K. Travers, M. Trulson, J. Vieceli, J. Wegener, D. Wu, A. Yang, D. Zaccarin, P. Zhao, F. Zhong, J. Korlach, S. Turner, *Science* 323 (2009) 133.
- [150] G.F. Schneider, C. Dekker, *Nat Biotech* 30 (2012) 326.
- [151] M.G. Moharam, T.K. Gaylord, *J. Opt. Soc. Am. A* 3 (1986) 1780.
- [152] R.L. Aggarwal, L.W. Farrar, E.D. Diebold, D.L. Polla, *Journal of Raman Spectroscopy* 40 (2009) 1331.
- [153] M.R. Gartia, Z. Xu, E. Behymer, H. Nguyen, J.A. Britten, C. Larson, R. Miles, M. Bora, A.S. Chang, T.C. Bond, G.L. Liu, *Nanotechnology* 21 (2010) 395701.
- [154] S. Mathias, E.d.C. Filho, R.G. Cecchini, *The Journal of Physical Chemistry* 65 (1961) 425.
- [155] J.Y. Gui, D.A. Stern, D.G. Frank, F. Lu, D.C. Zapien, A.T. Hubbard, *Langmuir* 7 (1991) 955.